Dissertation zur Erlangung des Doktorgrades

der Fakultät für Chemie und Pharmazie

der Ludwig-Maximilians-Universität München

$(CaFeAs)_{10}Pt_zAs_8$ superconductors

and related compounds

Tobias Stürzer

aus

München, Deutschland

2015

Erklärung

Diese Dissertation wurde im Sinne von § 7 der Promotionsordnung vom 28. November 2011 von Herrn Prof. Dr. Dirk Johrendt betreut.

Eidesstattliche Versicherung

Diese Dissertation wurde eigenständig und ohne unerlaubte Hilfe erarbeitet.

München, 23.01.2015

_____

Tobias Stürzer

Dissertation eingereicht am	23.01.2015
1. Gutachter:	Prof. Dr. Dirk Johrendt
2. Gutachter:	Prof. Dr. Oliver Oeckler
Mündliche Prüfung am	13.04.2015

Meiner Familie

Danksagung

Es kommt nicht darauf an, mit dem Kopf durch die Wand zu rennen,

sondern mit den Augen die Tür zu finden.

(Werner von Siemens)

Table of Contents

1   Introduction

"The experiment left no doubt that, as far as accuracy of measurement went, the resistance disappeared. At the same time, however, something unexpected occurred. The disappearance did not take place gradually but abruptly. [...] Thus the mercury at 4.2 K has entered a new state, which [...] can be called the state of *superconductivity*."[1] With these words *Heike Kamerlingh Onnes* described the discovery of superconductivity in his Nobel lecture.

Although more than one century has passed since *Onnes*' ground breaking discovery,[2-3] the fascination of this phenomenon has not diminished. This is perfectly reasonable since the superconducting state overcomes the barrier of electrical resistance which has been taken for granted until then. Thus, in our modern society where electronic components and energy issues play an indispensable key role, the prospect of lossless electrical conductivity still inspires scientists and visionaries alike. Imaginable applications frequently suggested range from strong electro magnets allowing for unprecedented high flux densities to lossless super-conducting generators, motors, transportation networks, quantum computers and frictionless levitation trains. Nevertheless, applications based on superconductivity are no "pie in the sky". Already today wires of A-15 phase superconductors are used in scientific and medical NMR technology or the LHC at CERN for example, whereas *Josephson* contacts are applied as ultrafast switches, single electron transistors and sensible field detectors. Since super-conductivity is generally recognized to be a "technology of the 21. century with strategic importance"[4] also enormous efforts are in progress worldwide for the development of new superconductor technologies to meet future energy generation, transportation, conversion, and storage issues.

Despite their potential the vast application of superconductors is yet to come. The main draw-backs so far are the material specific critical values temperature (T_c), current density (J_c), and magnetic field (H_c), above which the superconducting state is destroyed. Thus, possible applications are restricted to temperatures below 40 K, and therewith requiring liquid helium cooling. However, with liquid helium prices 10 – 20 times higher than for liquid nitrogen any potential technological advantage using state-of-the-art superconductors is outweighed by economic interests. Nevertheless, the discovery of high temperature superconductivity in cuprates up to 140 K in the 1980s proved[5-6] that this remarkable effect can be shifted to applicable temperature ranges. Unfortunately, the high anisotropy renders these cuprates extremely difficult for processing into coils and wires. These examples show that there is still

hope and a tremendous economic demand for high temperature superconductors but the appropriate materials are yet to be found.

Although the phenomenon of superconductivity is fascinating, the theory and history of superconductor research is no less so. Since more than 100 years this effect persistently survives among the biggest challenges of solid-state chemistry and physics. Five Nobel prizes of physics for research in the field of superconductivity were awarded so far, but a thorough understanding of the effect is still missing to the present day. *Bardeen*, *Cooper*, and *Schrieffer* developed a first generally accepted theory of conventional superconductivity. They suggested an effective attractive interaction between conduction electrons meditated by phonons. Bosonic *Cooper* pairs are formed with the same quantum state, so that they cannot be scattered by the crystal lattice and the electrical resistance vanishes.[7] Concluding from that, the superconducting state is restricted below critical temperatures, current densities, and magnetic fields, above which the *Cooper* pairs would break apart. Experimental evidence for the BCS theory was provided by the correct prediction of the isotope effect,[8-9] a super-conducting band gap,[10-12] the field penetration depth[13], and the *Meissner-Ochsenfeld-*effect.[14] Moreover, the BCS theory reliably reproduces T_c of elementary metals and many simple alloys.[15] Although the development of this basic theory completely describing all that was known about superconductivity in this early period of research was an immense progress, it had a bitter aftertaste. The BCS model restricted superconductivity below a fundamental limit of $T_c \approx 30 - 40$ K destroying all hopes for room temperature superconductors.[7] At that time *Matthias* formulated his six rules for a successful search for new superconductors: (1) A high symmetry is good, cubic symmetry is the best. (2) A high density of electronic states is good. (3) Stay away from oxygen. (4) Stay away from magnetism. (5) Stay away from insulators. (6) Stay away from theorists.[16-17]

Ironically most of these assumptions were later not only proved incorrect, but their exact opposite seems to be true, which became obvious with the discovery of unconventional super-conductivity at temperatures up to 140 K in cuprates after 1986.[5-6] These strong anisotropic compounds containing $CuO_{4/2}$ and metal ion layers are *Mott* insulators with an antiferro-magnetic ground state at low temperatures. Oxygen deficiency or intermediate layer metal substitution can destabilize the magnetic ordering and superconductivity arises. At first the euphoria was high of breaking the BCS limit and finally gaining control over superconduc-tivity (Figure 1). However, the cuprates' brittleness and their strong anisotropy were the big drawbacks in terms of technical applicability and the initial enthusiasm gradually ceased. In

the following years many superconductors were (re)discovered in fields never expected before,[17] among them MgB_2 (T_c = 40 K), $(Ba_{1-x}K_x)BiO_3$ ($T_{c,max}$ = 35 K), C_3Cs_{60} (T_c = 40 K), YPd_2B_2C (T_c = 23 K), and Na_xHfNCl ($T_{c,max}$ = 25 K). The steadily growing number also indicated, that the effect of superconductivity is not so scarce in nature as initially assumed, but could appear in any class of materials with mobile electrons.[16, 18]

However, it was not until 2008, when a new gold rush took the scientific world by the discovery of superconductivity in iron pnictides heralding the "iron age" of superconductivity.[19-20] Although many of the new iron pnictide superconductors were known for years, they were never investigated in the scope of superconductivity. For decades iron had been ruled out as a potential candidate for superconductors since iron was associated with ferromagnetism, which was known to be detrimental to superconductivity. A wrong generalization, which may have effectively obstructed the progress in superconductor research.
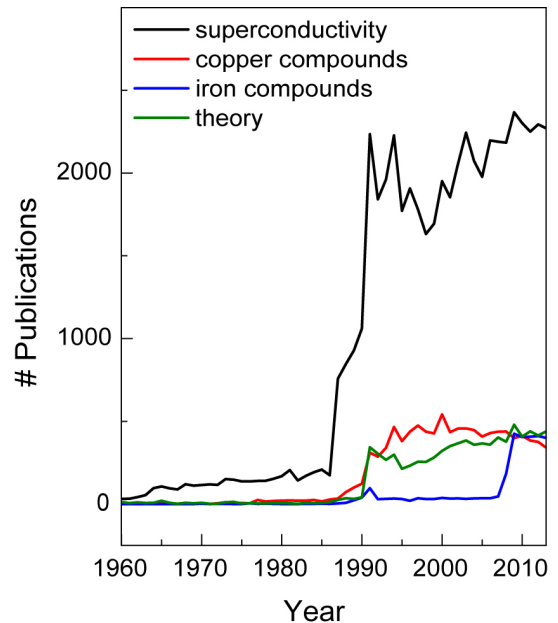
Figure 1. Number of publications covering superconductivity (SC) (black), SC in copper compounds (red) or iron compounds (blue), and theory of SC (green).

Superconductivity in iron arsenides was first found in stoichiometric LaFePO (T_c ≈ 4 K),[21] which was soon followed by $RE(O_{1-x}F_x)FeAs$ featuring critical temperatures as high as 55 K.[22-26] It was not long before superconducting properties were also found in many other iron arsenides and chalcogenides. Today a variety of related compounds are reported that can be derived from the *anti*-PbO,[27] *anti*-PbFCl,[28] $ThCr_2Si_2$,[29] or ZrCuSiAs structure types.[30] A structural classification of these superconductors can be achieved based on the stoichiometry of the parent compounds. Besides $REOFePn$ (1111 type; RE = La, Ce, Pr, Nd, Sm, Gd; Pn = P, As)[22-26] also FeSe and $Fe(Se_{1-x}Te_x)$ (11 type),[31-32] AFeAs (111 type; A = Li, Na),[33-34] AEFeAsF (another 1111 type; AE = Ca, Sr, Eu),[35-39] AFe_2As_2 (122 type; A = Na, K, Rb, Cs, Ca, Sr, Ba, Eu),[33, 40-45] and AE_2MO_3FeAs (21311 type, AE = Sr, Ba; M = Sc, V, Cr)[46-47] are reported (Figure 2).

Structurally the new superconductors consist of layers of edge-sharing $FeAs_{4/4}$ or $FeSe_{4/4}$ tetrahedra, respectively. Interlayers, ranging from vacancies (11 type) to complex perovskite

like blocks (21311 type), are sandwiched in between, resulting in an alternating stacking and giving rise to the different branches in the iron arsenide/chalcogenide family.

11	111	1111	122	21311
FeSe	NaFeAs	LaOFeAs	$BaFe_2As_2$	Sr_2VO_3FeAs
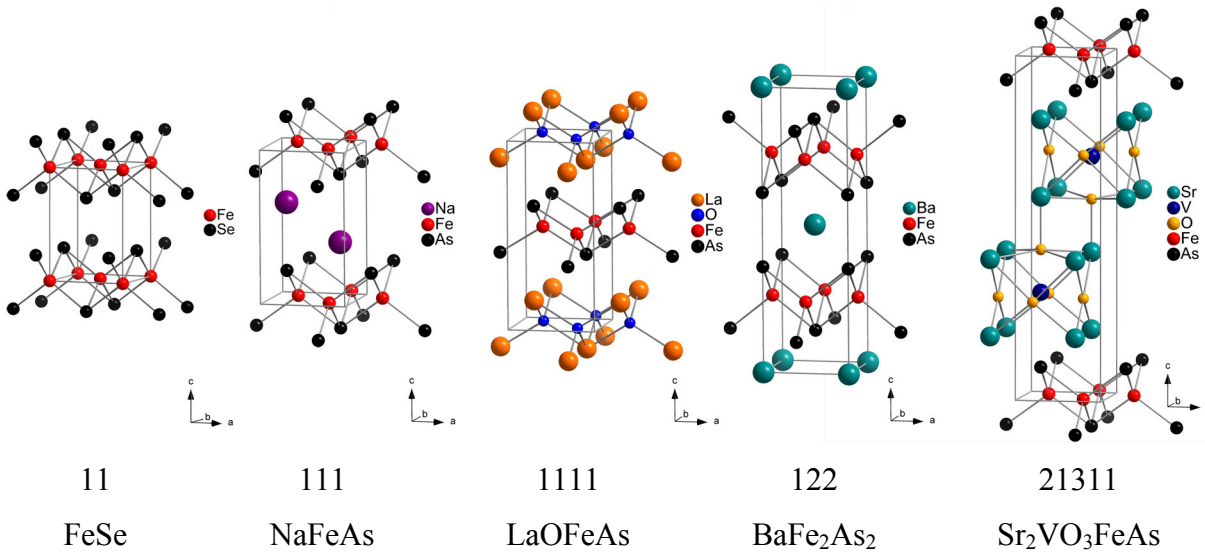
Figure 2. Crystal structures of the most famous iron-based superconductors.

Featuring exclusively Fe-$3d$ states at the Fermi energy (E_F) the properties of these compounds are dominated by the FeAs sheets, taking the role of the CuO_2 layers in the cuprate family. In contrast to the cuprates, however, the iron arsenides are metals instead of insulators, a property very auspicious in the scope of technical workability.[18]

Most of the stoichiometric iron arsenide compounds (parent compounds) are not super-conducting, *Pauli* paramagnetic poor metals with a formal iron valence state of Fe^{+2}. At lower temperatures an in-plane lattice distortion from tetragonal to orthorhombic crystal system ($t2$), accompanied with a spin density wave (SDW) ordering to an antiferromagnetic ground state occurs.[18, 48] Neutron diffraction, NMR, and μSR investigations found a stripe type antiferro-magnetism equal in all parent compounds.[49-51] Thereby the iron spins are antiferromagnetic aligned along the longer orthorhombic axis b, with ferromagnetic interactions along a (Figure 3b). In c direction different magnetic orderings are possible as was found comparing LaOFeAs and SmOFeAs.[16, 50]

Upon chemical doping and/or physical pressure the SDW transition can be gradually shifted to lower temperatures, finally suppressed and superconductivity arises (Figure 3a). Thereby most remarkably also substitutions within the iron arsenide layers itself are applicable, in contrast to the cuprate family. To the present day nearly all conceivable possibilities have been studied as shown by the example $A(Fe_{1-x}M_x)_2Pn_2$ (A = Na, K, Rb, Cs, Ca, Sr, Ba, Eu; M = Co, Ni, Ru, Rh, Pd, Ir, Pt; Pn = P, As).[42, 52-62] Enormous effort was taken to find correla-

tions between high T_c and structural or electronic changes empirically. Highest T_c 122 and 1111 superconductors were found to have almost ideal tetrahedra angles and optimal pnictide height in the FeAs layer.[18, 63] However, such supposedly optimal values were also found in LiFeP superconductor for example with T_c below 10 K.[64] Another approach argued the importance of increased anisotropy like in the cuprates, which can be realized by larger spacing layers.[65] Also a contribution of rare earth magnetic moments in present record holders *RE*OFeAs was discussed.[50]

The enormous experimental progress that has been made so far along with recent results emphasize the importance of charge modification, whereas structural details in terms of bond length and angles were assigned a subsidiary role.[66] Removing or inserting charge carriers in the FeAs sheets, which is referred to as hole or electron doping, was found repeatedly to be the most effective route to achieve T_c as high as 38 K in $(Ba_{1-x}K_x)Fe_2As_2$ or 55 K in $Sm(O_{1-x}F_x)FeAs$ for example.[26, 67] Also initially puzzling compounds like stoichiometric *A*FeAs (*A* = Li, Na) and Sr_2VO_3FeAs being superconducting without additional doping can be understood phenomenologically in the context of doping. Investigations on 111 compounds identified intrinsic hole doping caused by alkaline metal deficiency as possible reason,[33, 42] whereas V^{3+}/V^{4+} valence mixing is discussed as origin of electron doping in 21311.[68]
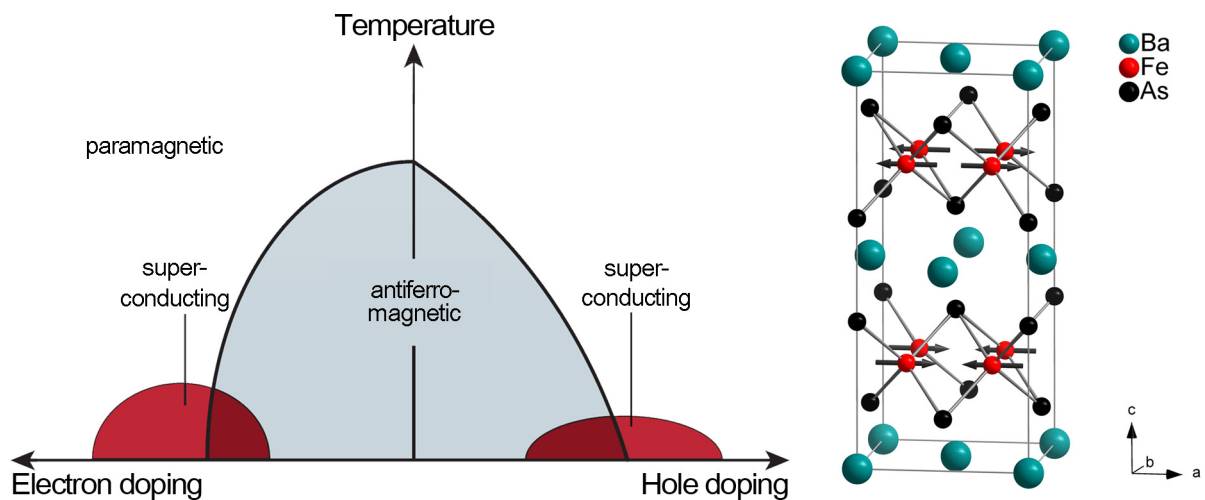
Figure 3. Schematic phase diagram illustrating the emergence of superconductivity upon doping in iron arsenides (left).[16] Magnetic structure of parent compound $BaFe_2As_2$ (right).[69]

So far critical temperatures remain below 25 K upon direct substituting the iron sites, whereas site mixing with transition metals left of iron in the periodic system induces no superconductivity at all. To this present day there is still no final consensus whether direct doping influences the SDW ordering by charge doping or dilution of the iron arsenide layers by magnetic impurities. So far experiments substantiate highest T_c to emerge only in compounds with

clean FeAs layers. A schematic phase diagram is depicted in Figure 3, illustrating the emergence of superconductivity upon doping in iron pnictide compounds. Also shown is the magnetic structure of $BaFe_2As_2$ in the parent state below 140 K.

A detailed understanding of the mechanism of superconductivity in iron arsenide compounds is still missing. All iron-based superconductors share the same crystallographic motif, with the main component being a square lattice of iron atoms sandwiched between two square lattices of pnictogen or chalcogen. Thus, the crucial role of this building block is more than obvious. Theoretical studies and ARPES measurements revealed the iron arsenides being semi metals. They are characterized by valence and conduction bands shifted in momentum space, but exhibiting an overlap in energy (Figure 4a).[18, 70-71] Electrons are transferred in order to equalize E_F forming electron and hole pockets. Furthermore the electronic structure of these compounds was found to be quasi two-dimensional featuring cylinder like sheets,[72] originating from the previously described hole-like and electron-like bands. A nesting vector $q = (\pi, \pi, 0)$ was evidenced in iron arsenide parent compounds connecting coplanar planes of the Fermi surface.[18] This nesting indicates the close proximity of the iron arsenides to an electronic and/or magnetic instability. If the nesting is "good", charge density wave (CDW) or spin density wave (SDW) instabilities can occur.[73] It is assumed that this instability causes the antiferromagnetic ordering in the parent compounds, while the resulting magnetic frustration is ultimately lifted by the orthorhombic distortion of the plane. However, structural and magnetic transitions occur nearly simultaneously in the 122 systems and within several Kelvin of each other for the 1111 systems.[74] Thus the issue of cause and consequence in the scope of these two transitions is not settled yet, but on the contrary was even extended by recent experimental indication of nematic ordering in $BaFe_2As_2$.[75-77]

Upon chemical doping the Fermi surface nesting can be gradually destroyed and the SDW transition is suppressed.[16, 18] Though the long-range magnetic order is removed then, short-range spin fluctuations could still be present which might act as mediating glue in the formation of *Cooper* pairs as it was suspected for the cuprates as well.[74] The importance of magnetism in this family was also demonstrated by recent results on underdoped $(Ba_{1-x}K_x)Fe_2As_2$ revealing a microscopic coexistence of superconductivity and magnetism, which indicates that both states compete for the same electrons.[78] Experiments on the isotope effect moreover found strong evidence for phonons and magnetism being intimately coupled in the iron arsenides.[79] Thus at the present stage a combination of magnetic fluctuations and lattice vibrations is assumed to mediate superconductivity in iron arsenides. Excellent reviews about

chemistry, physics, and superconductivity in iron arsenides are given by *Mazin*,[16] *Johrendt*,[18] *Hinks*,[74] *Johnston*,[80] and *Stewart*.[81]

But what can be concluded from the insights into iron arsenide superconductivity in the context of the cuprate and conventional superconductors? On the first glance it is tempting to see a close resemblance to the cuprates due to the proposed pairing based on magnetic fluctuations. However, the more they are studied, the less they seem to look like copper oxides. Iron arsenides are metals with $s^{\pm}$ symmetry of the pair wave function featuring multi-band superconductivity (Figure 4b). In contrast to that single-band superconductivity with d symmetry of the order parameter is found in cuprates, which are *Mott* insulators in the parent state. On the other side iron arsenides can definitely not be classified being conventional superconductors like MgB_2, although at least they are metals with s symmetry in the superconducting state, but without sign change.[16] Therefore the iron arsenides probably have to be put somewhere in between these two extremes suggesting that high T_c superconductivity is not limited to any particular class. Following the example of *Matthias*,[17] *Mazin* formulated a new set of guidelines for the search for high T_c superconductors taking into account recent results from iron arsenide and copper oxide superconductors. (1) Layered structures are good. (2) The carrier density should not be too high. (3) Transition metals of the fourth period are good. (4) Magnetism is essential. (5) Proper Fermi surface geometry is essential. (6) Materials of interest are likely to be complex chemical compounds.[16]
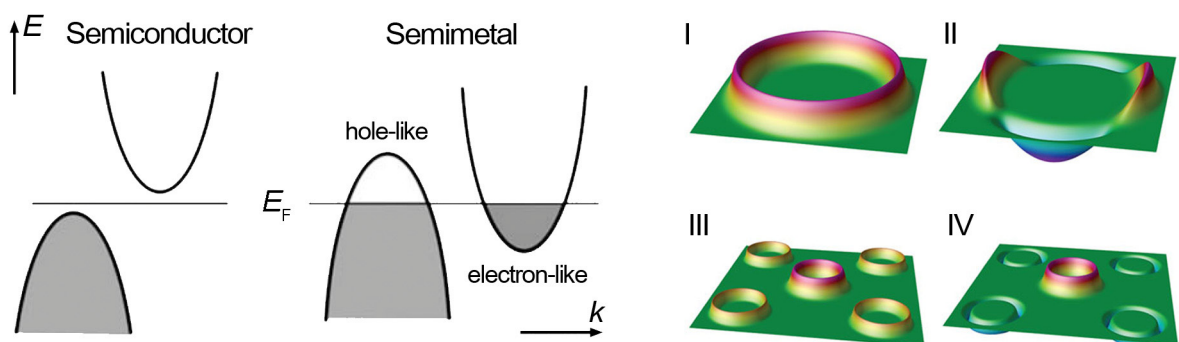
Figure 4. Sketch of the electronic structure of a semimetal developing from a semiconductor. Shaded areas represent filled electronic states (left).[18] (b) Schematic representation of the superconducting order parameter with (I) simple s wave (e.g. Al), (II) d wave (e.g. copper oxides), (III) multi-band s wave with the same sign (e.g. MgB_2), and (IV) multi-band $s^{\pm}$ wave with sign change superconductors, assumed for iron arsenides (right).[16]

The explorative search for new superconductors as well as the detailed structure investigation of known compounds is therefore a task for solid-state chemists and crystallographers alike. The immense progress made in the field of analytical methods over the last decades allows for very sensitive measurements. Therefore, high quality samples are indispensable, requiring

ongoing optimization of established preparation procedures and exploration of new synthesis strategies. Since no reliable predictions of new superconductors are available yet, the most promising route to uncover new pieces of the puzzle of superconductivity is the close investigation of unusual representatives in known material classes. In the iron arsenides the 122 compounds are plainly one of the most studied model systems featuring previously described typical properties. The little brother $CaFe_2As_2$, however, was discovered much later and was found to exhibit some peculiarities which render this 122 representative unique among the iron arsenide family.[41] A second phase transition competes with the familiar SDW ordering at higher pressures giving rise to a "collapsed" tetragonal phase with As–As single bonds between neighboring FeAs layers. Established doping scenarios of the 122 system were found to be violated in $CaFe_2As_2$ which is referred to as "breakdown of chemical scaling".[82] These results along with recent controversial reports about one[83] or two superconducting phases[84] or no superconductivity at all[85] in electron doped $(Ca_{1-x}RE_x)Fe_2As_2$ as well as the discovery of the new iron arsenides $CaFe_4As_3$[86] and potentially superconducting layered $(Ca_{1-x}RE_x)FeAs_2$[87-88] shifted the attention of many groups worldwide to the auspicious Ca–Fe–As system (Figure 5).
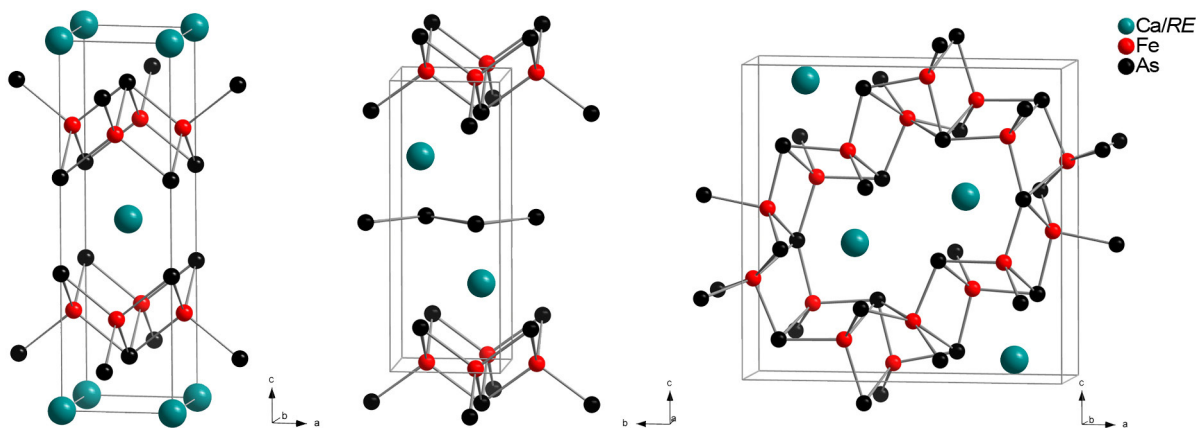
Figure 5. Crystal structures of calcium iron arsenides $(Ca_{1-x}RE_x)Fe_2As_2$ (left), $(Ca_{1-x}RE_x)FeAs_2$ (middle), and $CaFe_4As_3$ (right).

The complex structures of highest T_c copper oxides and reported structural flexibility of $CaFe_2As_2$, inspired the general idea of exploring the existence of more complex stacking structures in a potential Ca–Fe–M–As system. Therefore M would need to be so similar to Fe to form layered structures on the one side, but different enough on the other side to not just mix with Fe. In this context Pt turned out to be an ideal candidate. Soon after first indication of superconductivity was reported in the system Ca–Fe–Pt–As, but both structure and composition could not be determined at this stage.[89]

The main topic of this dissertation is the identification of new compounds, structure determination, and substitution dependent investigation of properties in this new branch of the family of iron arsenide superconductors (Chapter 2). Chapter 2.1 presents the identification of the superconducting compounds and the corresponding structure elucidation identifying two different species $(CaFeAs)_{10}Pt_3As_8$ and $(CaFeAs)_{10}Pt_4As_8$ in this family (abbreviated as 1038 and 1048 according to their stoichiometry). However, a closer look revealed a more challenging structure chemistry which is covered in Chapter 2.2. The following two Chapters 2.3 and 2.4 are devoted to $(CaFeAs)_{10}Pt_3As_8$ and more detailed investigations on this parent compound of the new superconductor family. Furthermore, transition metal substitution series $(CaFe_{1-x}M_xAs)_{10}Pt_3As_8$ were synthesized to investigate the resemblance to model systems $Ba(Fe_{1-x}M_x)_2As_2$ and $LaO(Fe_{1-x}M_x)As$ in the scope of structural changes and superconductivity as described in Chapter 2.5. Initially amazing differences in superconducting properties comparing 1038 and 1048 compounds are analyzed in Chapter 2.6 establishing an universal doping model in the $(CaFe_{1-x}M_xAs)_{10}Pt_zAs_8$ family. Additionally substituent dependent properties upon rare earth substitution in electron doped $(Ca_{1-y}RE_yFeAs)_{10}Pt_3As_8$ are investigated in Chapter 2.7, while a detailed study of superconducting properties and magnetism in $(Ca_{1-y}La_yFeAs)_{10}Pt_3As_8$ by the local μSR technique is presented in Chapter 2.8. In Chapter 2.9 a comparison of direct and electron doping is discussed based on codoping experiments in $(Ca_{1-y}La_yFe_{1-x}Pt_xAs)_{10}Pt_3As_8$ and $(CaFe_{1-x}Pt_xAs)_{10}Pt_4As_8$. Finally, in Chapter 2.10 electron doping in stoichiometric 1048 is studied by charge compensation experiments in $(Ca_{1-y}Na_yFeAs)_{10}Pt_4As_8$.

Chapter 3 is dedicated to a new family of calcium iron arsenides featuring frameworks of interconnected iron arsenide layers. The first subchapter presents the structure elucidation as well as a systematic structural characterization. Investigations on the complicated properties as well as theoretical consideration of selected compounds are given in section 3.2.

Last but not least, Chapter 6 is dedicated to the description of a variety of different tools developed during this thesis with the objective to accelerate data procession, automatize standard procedures and simplify structure solution as well as complex twinning issues.

References

[1]   H. K. Onnes, *Nobel Lectures in Physics 1901-1921* **1913**, *333*.

[2]   H. K. Onnes, *Commun. Phys. Lab. Univ. Leiden* **1911**, *120b*.

[3]   H. K. Onnes, *Commun. Phys. Lab. Univ. Leiden. Suppl.* **1911**, *29*.

[4]   J. Rüttgers, quoted by *Deutsche Kommission Elektrotechnik Elektronik Informations-technik* **2009**.

[5]   J. G. Bednorz, K. A. Müller, *Z. Physik B - Condensed Matter* **1986**, *64*, 189.

[6]   G. F. Sun, K. W. Wong, B. R. Xu, Y. Xin, D. F. Lu, *Phys. Lett. A* **1994**, *192*, 122.

[7]   J. Bardeen, L. N. Cooper, J. R. Schrieffer, *Phys. Rev.* **1957**, *108*, 1175.

[8]   C. A. Reynolds, B. Serin, L. B. Nesbitt, *Phys. Rev.* **1951**, *84*, 691.

[9]   B. Serin, C. A. Reynolds, C. Lohman, *Phys. Rev.* **1952**, *86*, 162.

[10]   W. S. Corak, B. B. Goodman, C. B. Satterthwaite, A. Wexler, *Phys. Rev.* **1954**, *96*, 1442.

[11]   M. A. Biondi, M. P. Garfunkel, A. O. McCoubrey, *Phys. Rev.* **1956**, *101*, 1427.

[12]   R. E. Glover, M. Tinkham, *Phys. Rev.* **1956**, *104*, 844.

[13]   F. London, H. London, *Proc. R. Soc. Lond. A* **1935**, *149*, 71.

[14]   W. Meissner, R. Ochsenfeld, *Naturwissenschaften* **1933**, *21*, 787.

[15]   I. Giaever, K. Megerle, *Phys. Rev.* **1961**, *122*, 1101.

[16]   I. I. Mazin, *Nature* **2010**, *464*, 183.

[17]   W. E. Pickett, *Physica B: Condensed Matter* **2001**, *296*, 112.

[18]   D. Johrendt, *J. Mater. Chem.* **2011**, *21*, 13726.

[19]   P. M. Grant, *Nature* **2008**, *453*, 1000.

[20]   C. Xu, S. Sachdev, *Nat. Phys.* **2008**, *4*, 898.

[21]   Y. Kamihara, H. Hiramatsu, M. Hirano, R. Kawamura, H. Yanagi, T. Kamiya, H. Hosono, *J. Am. Chem. Soc.* **2006**, *128*, 10012.

[22]   Y. Kamihara, T. Watanabe, M. Hirano, H. Hosono, *J. Am. Chem. Soc.* **2008**, *130*, 3296.

[23]   G. F. Chen, Z. Li, D. Wu, G. Li, W. Z. Hu, J. Dong, P. Zheng, J. L. Luo, N. L. Wang, *Phys. Rev. Lett.* **2008**, *100*, 247002.

[24]   Z. A. Ren, J. Yang, W. Lu, W. Yi, G. C. Che, X. L. Dong, L. L. Sun, Z. X. Zhao, *Mater. Res. Innovations* **2008**, *12*, 105.

[25]   Z.-A. Ren, J. Yang, W. Lu, W. Yi, X.-L. Shen, Z.-C. Li, G.-C. Che, X.-L. Dong, L.-L. Sun, F. Zhou, Z.-X. Zhao, *Europhys. Lett.* **2008**, *82*, 57002.

[26]   Z.-A. Ren, W. Lu, J. Yang, W. Yi, X.-L. Shen, C. Zheng, G.-C. Che, X.-L. Dong, L.-L. Sun, F. Zhou, Z.-X. Zhao, *Chin. Phys. Lett.* **2008**, *25*, 2215.

[27]   W. J. Moore, L. Pauling, *J. Am. Chem. Soc.* **1941**, *63*, 1392.

[28]   W. Nieuwenkamp, J. M. Bijvoet, *Z. Kristallogr.* **1985**, *171*, 23.

[29]   Z. Ban, M. Sikirica, *Acta Crystallogr.* **1965**, *18*, 594.

[30]   V. Johnson, W. Jeitschko, *J. Solid State Chem.* **1974**, *11*, 161.

[31]   F.-C. Hsu, J.-Y. Luo, K.-W. Yeh, T.-K. Chen, T.-W. Huang, P. M. Wu, Y.-C. Lee, Y.-L. Huang, Y.-Y. Chu, D.-C. Yan, M.-K. Wu, *Proc. Natl. Acad. Sci.* **2008**, *105*, 14262.

[32]   Y. Kuo-Wei, H. Tzu-Wen, H. Yi-lin, C. Ta-Kun, H. Fong-Chi, M. W. Phillip, L. Yong-Chi, C. Yan-Yi, C. Chi-Lian, L. Jiu-Yong, Y. Der-Chung, W. Maw-Kuen, *Europhys. Lett.* **2008**, *84*, 37002.

[33]   D. R. Parker, M. J. Pitcher, P. J. Baker, I. Franke, T. Lancaster, S. J. Blundell, S. J. Clarke, *Chem. Commun. (Cambridge, U. K.)* **2009**, 2189.

[34]   J. H. Tapp, Z. Tang, B. Lv, K. Sasmal, B. Lorenz, P. C. W. Chu, A. M. Guloy, *Phys. Rev. B* **2008**, *78*, 060505.

[35]   C. Peng, S. Bing, M. Gang, Z. Xiyu, H. Fei, Z. Bin, W. Hai-Hu, *Europhys. Lett.* **2009**, *85*, 67003.

[36]   M. Tegel, S. Johansson, V. Weiß, I. Schellenberg, W. Hermes, R. Pöttgen, D. Johrendt, *Europhys. Lett.* **2008**, *84*, 67007.

[37]   S. Matsuishi, Y. Inoue, T. Nomura, M. Hirano, H. Hosono, *J. Phys. Soc. Jpn.* **2008**, *77*, 113709.

[38]   S. Matsuishi, Y. Inoue, T. Nomura, H. Yanagi, M. Hirano, H. Hosono, *J. Am. Chem. Soc.* **2008**, *130*, 14428.

[39]   X. Zhu, F. Han, P. Cheng, G. Mu, B. Shen, B. Zeng, H.-H. Wen, *Physica C: Superconductivity* **2009**, *469*, 381.

[40]   M. Pfisterer, G. Nagorsen, *Z. Naturforsch. B* **1980**, *35*, 703

[41]   N. Ni, S. Nandi, A. Kreyssig, A. I. Goldman, E. D. Mun, S. L. Bud'ko, P. C. Canfield, *Phys. Rev. B* **2008**, *78*, 014523.

[42]   G. M. Friederichs, I. Schellenberg, R. Pöttgen, V. Duppel, L. Kienle, J. Schmedt auf der Günne, D. Johrendt, *Inorg. Chem.* **2012**, *51*, 8161.

[43]   S. Rózsa, H.-U. Schuster, *Z. Naturforsch.* **1981**, *36b*, 1668.

[44]   M. Noack, H.-U. Schuster, *Z. Anorg. Allg. Chem.* **1994**, *620*, 1777.

[45]   R. Marchand, W. Jeitschko, *J. Solid State Chem.* **1978**, *24*, 351.

[46]   X. Zhu, F. Han, G. Mu, P. Cheng, B. Shen, B. Zeng, H.-H. Wen, *Phys. Rev. B* **2009**, *79*, 220512.

[47]   M. Tegel, F. Hummel, S. Lackner, I. Schellenberg, R. Pöttgen, D. Johrendt, *Z. Anorg. Allg. Chem.* **2009**, *635*, 2242.

[48]   M. Rotter, M. Tegel, D. Johrendt, I. Schellenberg, W. Hermes, R. Pöttgen, *Phys. Rev. B* **2008**, *78*, 020503.

[49]   C. de la Cruz, Q. Huang, J. W. Lynn, J. Li, W. R. Ii, J. L. Zarestky, H. A. Mook, G. F. Chen, J. L. Luo, N. L. Wang, P. Dai, *Nature* **2008**, *453*, 899.

[50]   H. Maeter, H. Luetkens, Y. G. Pashkevich, A. Kwadrin, R. Khasanov, A. Amato, A. A. Gusev, K. V. Lamonova, D. A. Chervinskii, R. Klingeler, C. Hess, G. Behr, B. Büchner, H.-H. Klauss, *Phys. Rev. B* **2009**, *80*, 094524.

[51]   H. Fukazawa, K. Hirayama, K. Kondo, T. Yamazaki, Y. Kohori, N. Takeshita, K. Miyazawa, H. Kito, H. Eisaki, A. Iyo, *J. Phys. Soc. Jpn.* **2008**, *77*, 093706.

[52]   M. Rotter, M. Pangerl, M. Tegel, D. Johrendt, *Angew. Chem. Int. Ed.* **2008**, *47*, 7949.

[53]   S. Peschke, T. Stürzer, D. Johrendt, *Z. Anorg. Allg. Chem.* **2014**, *640*, 830.

[54] A. F. Wang, B. Y. Pan, X. G. Luo, F. Chen, Y. J. Yan, J. J. Ying, G. J. Ye, P. Cheng, X. C. Hong, S. Y. Li, X. H. Chen, *Phys. Rev. B* **2013**, *87*, 214509.

[55] M. Tegel, M. Rotter, V. Weiß, F. M. Schappacher, R. Pöttgen, D. Johrendt, *J. Phys.: Condens. Matter* **2008**, *20*, 452201.

[56] A. S. Sefat, R. Jin, M. A. McGuire, B. C. Sales, D. J. Singh, D. Mandrus, *Phys. Rev. Lett.* **2008**, *101*, 117004.

[57] F. Han, X. Zhu, P. Cheng, G. Mu, Y. Jia, L. Fang, Y. Wang, H. Luo, B. Zeng, B. Shen, L. Shan, C. Ren, H.-H. Wen, *Phys. Rev. B* **2009**, *80*, 024506.

[58] A. S. Sefat, M. A. McGuire, R. Jin, B. C. Sales, D. Mandrus, F. Ronning, E. D. Bauer, Y. Mozharivskyj, *Phys. Rev. B* **2009**, *79*, 094508.

[59] N. Ni, A. Thaler, A. Kracher, J. Q. Yan, S. L. Bud'ko, P. C. Canfield, *Phys. Rev. B* **2009**, *80*, 024511.

[60] M. Rotter, C. Hieke, D. Johrendt, *Phys. Rev. B* **2010**, *82*, 014513.

[61] S. R. Saha, T. Drye, K. Kirshenbaum, N. P. Butch, P. Y. Zavalij, P. Johnpierre, *J. Phys.: Condens. Matter* **2010**, *22*, 072204.

[62] Y. Nishikubo, S. Kakiya, M. Danura, K. Kudo, M. Nohara, *J. Phys. Soc. Jpn.* **2010**, *79*, 095002.

[63] C.-H. Lee, A. Iyo, H. Eisaki, H. Kito, M. T. Fernandez-Diaz, T. Ito, K. Kihou, H. Matsuhata, M. Braden, K. Yamada, *J. Phys. Soc. Jpn.* **2008**, *77*, 083704.

[64] Z. Deng, X. C. Wang, Q. Q. Liu, S. J. Zhang, Y. X. Lv, J. L. Zhu, R. C. Yu, C. Q. Jin, *Europhys. Lett.* **2009**, *87*, 37004.

[65] H. Ogino, S. Sato, K. Kishio, J.-I. Shimoyama, *Phys. Procedia* **2012**, *36*, 722.

[66] V. Zinth, T. Dellmann, H.-H. Klauss, D. Johrendt, *Angew. Chem. Int. Ed.* **2011**, *50*, 7919.

[67] M. Rotter, M. Tegel, D. Johrendt, *Phys. Rev. Lett.* **2008**, *101*, 107006.

[68] F. Hummel, Y. Su, A. Senyshyn, D. Johrendt, *Phys. Rev. B* **2013**, *88*, 144517.

[69] M. Martin, *Dissertation*, Ludwig-Maximilians-Universität München, **2010**.

[70]   F. Ma, Z.-Y. Lu, *Phys. Rev. B* **2008**, *78*, 033111.

[71]   A. A. Kordyuk, V. B. Zabolotnyy, D. V. Evtushinsky, A. N. Yaresko, B. Büchner, S. V. Borisenko, *J. Supercond. Novel Magn.* **2013**, *26*, 2837.

[72]   J. Dong, H. J. Zhang, G. Xu, Z. Li, G. Li, W. Z. Hu, D. Wu, G. F. Chen, X. Dai, J. L. Luo, Z. Fang, N. L. Wang, *Europhys. Lett.* **2008**, *83*, 27006.

[73]   G. Grüner, *Density Waves in Solids* **1994**, Perseus Publishing.

[74]   D. G. Hinks, *Nat. Phys.* **2009**, *5*, 386.

[75]   R. M. Fernandes, A. V. Chubukov, J. Schmalian, *Nat. Phys.* **2014**, *10*, 97.

[76]   A. E. Böhmer, P. Burger, F. Hardy, T. Wolf, P. Schweiss, R. Fromknecht, M. Reinecker, W. Schranz, C. Meingast, *Phys. Rev. Lett.* **2014**, *112*, 047001.

[77]   E. Wiesenmayer, *private communication*, Ludwig-Maximilians-Universität München, **2015**.

[78]   E. Wiesenmayer, H. Luetkens, G. Pascua, R. Khasanov, A. Amato, H. Potts, B. Banusch, H.-H. Klauss, D. Johrendt, *Phys. Rev. Lett.* **2011**, *107*, 237001.

[79]   R. H. Liu, T. Wu, G. Wu, H. Chen, X. F. Wang, Y. L. Xie, J. J. Ying, Y. J. Yan, Q. J. Li, B. C. Shi, W. S. Chu, Z. Y. Wu, X. H. Chen, *Nature* **2009**, *459*, 64.

[80]   D. C. Johnston, *Adv. Phys.* **2010**, *59*, 803.

[81]   G. R. Stewart, *Rev. Mod. Phys.* **2011**, *83*, 1589.

[82]   K. Kudo, M. Kobayashi, S. Kakiya, M. Danura, M. Nohara, *J. Phys. Soc. Jpn.* **2012**, *81*, 035002.

[83]   S. R. Saha, N. P. Butch, T. Drye, J. Magill, S. Ziemak, K. Kirshenbaum, P. Y. Zavalij, J. W. Lynn, J. Paglione, *Phys. Rev. B* **2012**, *85*, 024525.

[84]   Y. Sun, W. Zhou, L. J. Cui, J. C. Zhuang, Y. Ding, F. F. Yuan, J. Bai, Z. X. Shi, *AIP Advances* **2013**, *3*, 102120.

[85]   R. Pobel, *private communication*, Ludwig-Maximilians-Universität München, **2014**.

[86] I. Todorov, D. Y. Chung, C. D. Malliakas, Q. Li, T. Bakas, A. Douvalis, G. Trimarchi, K. Gray, J. F. Mitchell, A. J. Freeman, M. G. Kanatzidis, *J. Am. Chem. Soc.* **2009**, *131*, 5405.

[87] N. Katayama, K. Kudo, S. Onari, T. Mizukami, K. Sugawara, Y. Sugiyama, Y. Kitahama, K. Iba, K. Fujimura, N. Nishimoto, M. Nohara, H. Sawa, *J. Phys. Soc. Jpn.* **2013**, *82*, 123702.

[88] H. Yakita, H. Ogino, T. Okada, A. Yamamoto, K. Kishio, T. Tohei, Y. Ikuhara, Y. Gotoh, H. Fujihisa, K. Kataoka, H. Eisaki, J.-I. Shimoyama, *J. Am. Chem. Soc.* **2014**, *136*, 846.

[89] M. Nohara, S. Kakiya, K. Kudo, *international workshop on novel superconductors and super materials* **2011**, Tokyo.

2 New Iron Arsenide Superconductors (CaFeAs)$_{10}$Pt$_z$As$_8$

2.1 Superconductivity up to 35 K in the Iron Platinum Arsenides (CaFe$_{1-x}$Pt$_x$As)$_{10}$Pt$_{4-y}$As$_8$ with Layered Structures

C. Löhnert, T. Stürzer, M. Tegel, R. Frankovsky, G. Friederichs, D. Johrendt
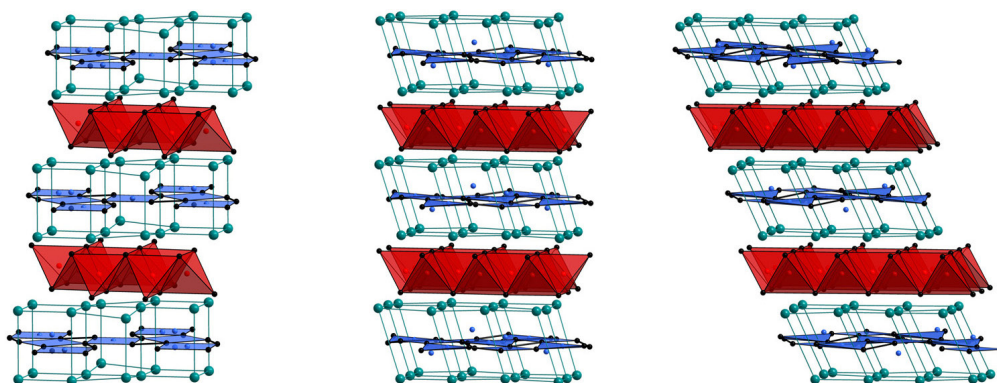
Abstract

The family of iron arsenide superconductors is expanded by the new iron platinum compounds (CaFe$_{1-x}$Pt$_x$As)$_{10}$Pt$_{4-y}$As$_8$ with novel crystal structures. Layers of FeAs$_{4/4}$ tetrahedra and of nearly planar PtAs$_{4/2}$ squares with (As$_2$)$^{4-}$ dumbbells are stacked in different ways, resulting in polytypes with triclinic or tetragonal symmetry. Superconductivity up to 35 K is induced either by Pt doping of the Fe site or by electron transfer from PtAs to FeAs layers.

2.1.1 *Introduction*

The discovery of high-temperature superconductivity in iron arsenides in 2008[1] has arguably been the biggest breakthrough in this field since the appearance of the copper oxide superconductors in 1986. In iron arsenides, superconductivity up to 55 K[2] originates in layers of edge-sharing $^{2}_{\infty}$[FeAs$_{4/4}$] tetrahedra. Meanwhile, a series of different structure types has been identified, but the family of superconducting iron arsenide compounds is still small in comparison with the cuprates. Its members are mainly derivatives of the relatively simple and long-known *anti*-PbFCl-[1,3,4] and ThCr$_2$Si$_2$-type structures.[5,6] Thus, extending the crystal

chemistry of iron-based superconductors is a foremost task of solid-state chemistry. Compounds like Sr_2VO_3FeAs with thick perovskite-like oxide blocks between the FeAs layers were derived from known copper sulfides and showed superconductivity up to 37 K. However, the combination of the metallic iron arsenide layers with transition metal oxides caused difficulties.[8, 9]

Another approach is the combination of iron arsenide layers with other intermetallic building blocks. We considered the fact that a second transition metal should be one that can adopt coordination geometries other than tetrahedral. Platinum appeared promising, because Pt is known to be very flexible and forms arsenides with octahedral, tetrahedral, trigonal, and square coordination in compounds like $PtAs_2$,[10] $SrPt_2As_2$,[11] $SrPtAs$,[12] and Cs_2PtAs_2,[13] respectively. Recently, *Nohara* and co-workers[14] mentioned superconductivity in the system Ca–Fe–Pt–As, but the detailed structure and composition of the compound were not reported. With these points in mind, we started explorative syntheses in the system Ca–Fe–Pt–As and found three new platinum iron arsenides $(CaFe_{1-x}Pt_xAs)_{10}Pt_4As_8$, $(CaFe_{1-x}Pt_xAs)_{10}Pt_3As_8$, and $(CaFeAs)_{10}Pt_4As_8$. These compounds crystallize in to date unknown structure types, where iron arsenide and platinum arsenide layers alternate. We have detected superconductivity up to 35 K, which is probably either induced by Pt doping of the FeAs layers in $(CaFe_{1-x}Pt_xAs)_{10}Pt_3As_8$ or by indirect electron doping in $(CaFeAs)_{10}Pt_4As_8$ owing to additional Pt^{2+} in the platinum arsenide layers. However, the concrete phase relationships are not yet completely resolved. Herein, we report the synthesis, crystal structures, preliminary property measurements, and density functional (DFT) calculations of these new superconductors.

2.1.2 *Experimental Details*

The compounds were synthesized by heating stoichiometric mixtures of pure elements at 700 – 1100 °C in alumina crucibles, sealed under argon in silica tubes. Powder diffraction data were measured using either a HUBER G670 Guinier imaging plate (Co Kα_1 or Cu Kα_1 radiation) or a STOE Stadi P diffractometer (Mo Kα_1 or Cu Kα_1 radiation, Ge [111] monochromator). Rietveld refinements were performed with the TOPAS package.[15] Crystals were selected from the polycrystalline samples. X-ray intensity data were measured with a STOE IPDS-I imaging plate or a Nonius-κ-CCD (Mo Kα radiation). The structures were solved using the charge flipping method included in the JANA2006 program package.[16] The latter was also used for structure refinement. Further details on the crystal structure investigations may be obtained from the Fachinformationszentrum Karlsruhe, 76344 Eggenstein-

Leopoldshafen (Fax: (+49) 7247-808-666; e-mail: crysdata@ fiz-karlsruhe.de), on quoting the depository numbers CSD-423398 (Ca$_5$Fe$_{4.75}$Pt$_{1.75}$As$_9$; 1038), 423399 (Ca$_5$Fe$_5$Pt$_{1.82}$As$_9$; α-1048), and 423400 (Ca$_5$Fe$_{4.35}$Pt$_{2.65}$As$_9$; β-1048). AC susceptibility data were measured at 1333 Hz and 2 G. DFT calculations were performed with the LMTO47c package.[17]

2.1.3 Results and Discussion

The polycrystalline samples were mostly inhomogeneous and contained plate-shaped as well as needle-shaped crystals with metallic luster. X-ray powder patterns could initially not be indexed, and the plate-like crystals easily exfoliated. Their diffraction patterns showed clean square motifs but a disturbed periodicity of the third dimension, which indicated stacking disorder. Only some crystals were of fairly sufficient quality for X-ray structure determinations. Finally, we found three different but closely related crystal structures, whose compositions and lattice parameters are compiled in Table 1. The rather high R values reflect the poor crystal quality and still not completely resolved twinning and/or intergrowth issues.

Table 1. Crystal data of the platinum iron arsenides.

Formula	(CaFe$_{1-x}$Pt$_x$As)$_{10}$Pt$_3$As$_8$		(CaFe$_{1-x}$Pt$_x$As)$_{10}$Pt$_4$As$_8$
Label	1038	α-1048	β-1048
SG	$P\bar{1}$	$P4/n$	$P\bar{1}$
a (Å)	8.776(1)	8.716(1)	8.7382(4)
b (Å)	8.781(1)	a	8.7387(4)
c (Å)	10.689(2)	10.462(2)	11.225(1)
α (°)	75.67(1)	90	81.049(3)
β (°)	85.32(1)	90	71.915(3)
γ (°)	89.97(1)	90	89.980(3)
$R_{F>3\sigma(F)}$	0.064	0.099	0.069

(CaFe$_{1-x}$Pt$_x$As)$_{10}$Pt$_3$As$_8$, hereafter referred to as the 1038 compound, crystallizes in the triclinic crystal system and consists of iron arsenide layers separated by calcium ions and slightly puckered Pt$_3$As$_8$ layers. The crystal structure is shown in Figure 1. Platinum atoms either lie in the centers of the corner sharing As$_4$-squares or are shifted slightly above it. Arsenic forms As$_2^{4-}$ dumbbells with typical As–As bond lengths of approximately 2.48 Å. The combination of As$_2$ dumbbells with square coordinated Pt atoms is known from the pyrite like compound BaPt$_4$As$_6$, which also contains octahedrally coordinated platinum.[18] Assuming divalent Pt^{2+} ($5d^8$) in the present compound, charge neutrality is achieved according to (Ca^{2+}Fe^{2+}As^{3-})$_{10}$(Pt^{2+})$_3$[(As$_2$)$^{4-}$]$_4$. Thus, the electronic situation of the (FeAs)$^{1-}$ layer is iden-

tical to that in the known parent compounds BaFe$_2$As$_2$ and LaFeAsO. Subsequent refinements of the crystal structure revealed Pt substitution at the Fe site. The final composition has been determined to be (CaFe$_{0.95(1)}$Pt$_{0.05(1)}$As)$_{10}$Pt$_3$As$_8$.
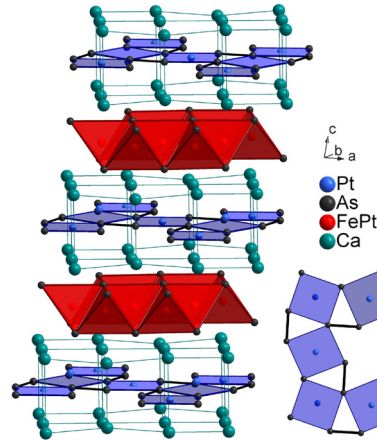
Figure 1. Crystal structure of triclinic (CaFe$_{1-x}$Pt$_x$As)$_{10}$Pt$_3$As$_8$ (1038 compound) and details of the Pt$_3$As$_8$ layer (right).

A second type of plate-like crystals from the polycrystalline samples showed tetragonal symmetry, and the structure could be solved in the space group *P*4/*n*. The tetragonal structure contains building blocks very similar to the triclinic phase as described above. No Pt doping was detected at the iron site, even though the refined composition (CaFeAs)$_{10}$Pt$_{3.58(2)}$As$_8$ (*α*-1048) contains even more platinum than triclinic (CaFe$_{0.95(1)}$Pt$_{0.05(1)}$As)$_{10}$Pt$_3$As$_8$. Finally, the structure of the needle-shaped crystals could also be solved and refined in the space group *P*$\overline{1}$. Their composition is (CaFe$_{0.87(1)}$Pt$_{0.13(1)}$As)$_{10}$Pt$_4$As$_8$ (*β*-1048), which is the platinum-richest phase so far. In this case, all Pt sites in the Pt$_4$As$_8$ layer are fully occupied, and additionally about 13 % iron in the FeAs layer is substituted by platinum.
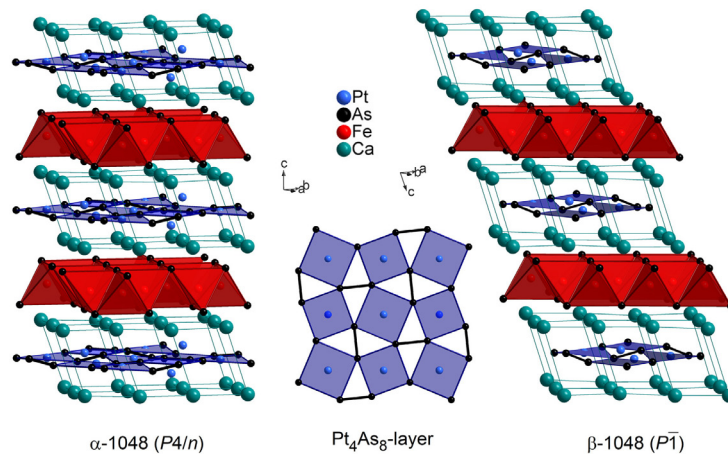
Figure 2. Crystal structures of (CaFeAs)$_{10}$Pt$_{3.58}$As$_8$ (left, *α*-1048) and (CaFe$_{0.87(1)}$Pt$_{0.13(1)}$)$_{10}$Pt$_4$As$_8$ (right, *β*-1048). The Pt$_{4-y}$As$_8$ layer of both structures is shown in the middle.

Figure 2 shows the crystal structures of both 1048 compounds. Additional Pt atoms occupy the voids in the Pt$_3$As$_8$ layer of the 1038 structure (cf. Figure 1), which gives a layer formula of Pt$_4$As$_8$. But also the stacking of Pt$_4$As$_8$ and FeAs layers is different from the 1038 compound. This situation becomes clear when the arrangements of the calcium atoms in the 1038 and 1048 structures are compared. While the Ca layers are mirror-symmetric above and below the Pt$_3$As$_8$ layers in the 1038 compound (see Figure 1), they are shifted by half the diagonal of one CaFeAs subcell in the 1048 structures. In contrast, the FeAs layers are congruently stacked in the 1048 structures, but not in the 1038 structure. Thus, α- and β-1048 are polymorphs with the same stacking of the Ca and FeAs layers. But while consecutive Pt$_4$As$_8$ layers are congruent in α-1048, they are shifted by one period of the CaFeAs layer (3.89 Å) along [120] in β-1048 (Figure 2). This shift by [0.2,0.4,0] is incompatible with the positions of the fourfold axis at (0,0,z) and (1/2,1/2,z), therefore the structure becomes triclinic. The crystal structures are compatible with the X-ray powder patterns that could be fitted by using both the 1038 and the α-1048 phases in roughly 60 : 40 weight ratio. Figure 3 shows the measured data and the Rietveld fit.
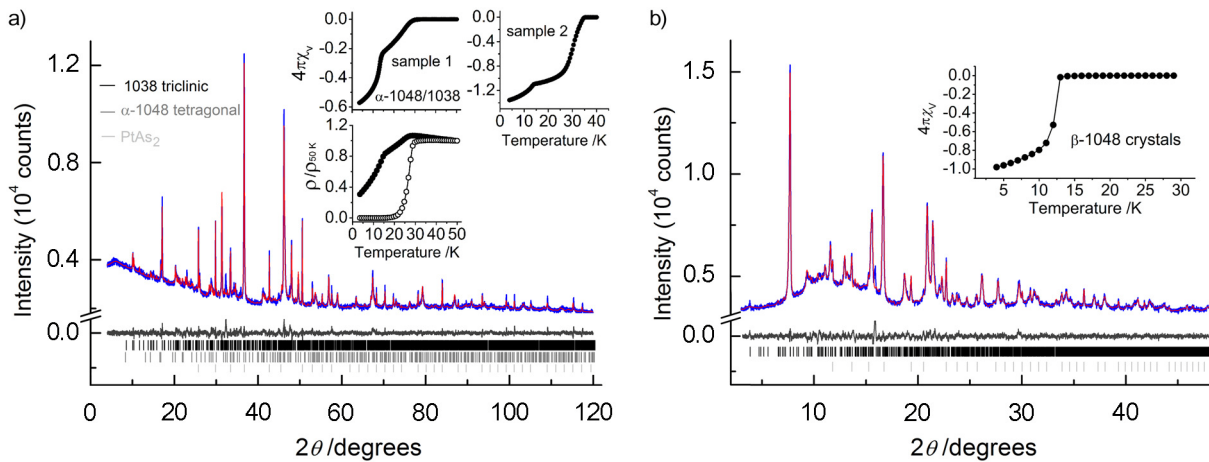
Figure 3. (a) X-ray powder pattern and Rietveld fit using the structures of the triclinic 1038 and the tetragonal α-1048 compounds. Inset: AC susceptibility and DC resistivity measurements. The latter shows data of a cold-pressed pellet (filled circles) and after annealing at 1000°C (open circles). (b) X-ray powder pattern and Rietveld fit of the needle-shaped β-1048 crystals. Inset: AC susceptibility measurement.

AC susceptibility measurements of different samples always revealed two superconducting transitions. A lower onset temperature around 15 K was found in both samples, while the higher T_c is at 31 K in sample 1 and at 35 K in sample 2 (insets in Figure 3a). The shielding fraction of about 60 % at 4 K in sample 1 can be subdivided in two roughly equal amounts of the two phases, which is in agreement with the Rietveld data, but allows no assignment of the different phases to the superconducting transitions. The resistivity of a cold-pressed pellet of sample 1 shows the same two transitions as the susceptibility, but zero resistivity is not

achieved owing to grain boundary effects. After annealing the pellet at 1000 °C for five hours, we observe one rather sharp drop at approximately 30 K (open circles in Figure 3a), while the magnetic susceptibility of the annealed pellet (not shown) still reveals two transition temperatures. As expected, the fraction of the 30 K superconductor is sufficient to achieve zero resistivity.

Both compounds show electronic structure features typical for iron arsenide superconductors that may allow an at least probable assignment of the 1038 and 1048 compounds to the observed transitions. The 1038 phase formally represents a parent compound with $(FeAs)^{1-}$ layers like undoped $BaFe_2As_2$ or $LaOFeAs$, neither of which is superconducting. Pt doping at the Fe site is known to induce superconductivity in $SrFe_{2-x}Pt_xAs_2$,[19] and we suggest that $(CaFe_{1-x}Pt_xAs)_{10}Pt_3As_8$ is superconducting because of Pt doping of the FeAs layers. In contrast, indirect electron doping of clean FeAs layers induces superconductivity in $La(O_{1-x}F_x)FeAs$ and $(Ca_{1-x}RE_x)Fe_2As_2$ (RE = rare earth metal).[20] The tetragonal α-1048 compound may be considered as indirectly electron doped owing to the approximately 0.6 additional Pt^{2+} atoms in the $Pt_{3.58}As_8$ layer, which formally reduce the charge at the Fe atom. It has generally been observed that indirect electron or hole doping of clean FeAs layers leads to higher T_c values than substitution of Fe by other metals (direct doping), for example in $Ba_{0.6}K_{0.4}Fe_2As_2$ (38 K)[6, 21] and $BaFe_{1.86}Co_{0.14}As_2$ (22 K).[22] One possible reason may be the additional disorder in the latter case.

From these considerations, we suggest that the indirectly electron doped α-1048 compound with clean FeAs layers has a higher T_c value than the Pt doped 1038 compound. We have also synthesized samples of the 1038 phase with lower Pt concentrations (no Pt at the Fe site) that were not superconducting, which is in line with our arguments. Our assignment is compatible with the properties of the β-1048 compound. Owing to the needle-like shape of the crystals, we were able to manually select an amount sufficient for AC measurements and powder diffraction, but not for resistivity measurements. The pattern was fitted using the crystal structure of β-1048 (Figure 3b). Small amounts of $PtAs_2$ were included in the refinement. The peak at $2\theta = 16°$ is an unidentified impurity, but nevertheless the pattern is well described by the structure of the β-1048 phase obtained from X-ray single crystal data.

The AC susceptibility of the crystals is shown in the inset of Figure 3. A sharp superconducting transition at 13 K with almost 100 % shielding at 4 K is observed, in agreement with the single-phase refinement of the X-ray powder data. Owing to the tiny amount of these crystals, this 13 K transition is not visible in the AC measurement and in the powder pattern

of the whole sample (Figure 3a). The lower critical temperature is plausible, because the crystals of the β-1048 compound can be considered as overdoped. Indeed, *Nishikubo* et al.[19] observed superconductivity at 17 K in Sr(Fe$_{1-x}$Pt$_x$)$_2$As$_2$ at 12.5 % Pt doping. Our β-1048 single crystals contain about the same amount of Pt at the iron site (13 %) and are additionally indirectly electron doped owing to the completely Pt filled Pt$_{4-y}$As$_8$ layer.

DFT calculations were conducted to check for certain features of the electronic structure that were considered essential. In FeAs superconductors, the electronic states near the Fermi level (E_F) are dominated by iron $3d$ bands. These generate a special topology of the Fermi surface, referred to as nesting between so-called electron and hole like sheets.[23] It has been argued that this nesting plays a certain role in the pairing mechanism;[24] however, the recently discovered iron selenide superconductors gave rise to doubts about this concept.[25] The question that arises here is whether the electronic subsystem of the Pt$_{4-y}$As$_8$ layer contributes to the Fermi surface. If not, we can probably apply the concept of the other iron arsenide materials; otherwise, a different scenario has to be considered. From the chemical point of view, we may expect that the Pt $5d_{x^2-y^2}$ orbitals are pushed above the Fermi level by the square ligand field. If the Fermi level in the FeAs bands is just inside this gap, we have a pure FeAs Fermi surface. The 1038 compound is charge-neutral by using the Zintl concept according to (Ca^{2+}Fe^{2+}As^{3-})$_{10}$(Pt^{2+})$_3$[(As$_2$)$^{4-}$]$_4$, while two additional electrons have to be placed in the 1048 structure that may be written as (Ca^{2+}Fe^{2+}As^{3-})$_{10}$(Pt^{2+})$_4$[(As$_2$)$^{4-}$]$_4 \cdot 2\,e^-$. However, it is not yet clear where to ascribe these extra electrons. Figure 4 shows the partial density of states (PDOS) of the Pt-$5d$ and Fe-$3d$ orbitals. We also show the crystal orbital Hamilton populations (COHP) of the Pt–As bonds in the Pt$_{4-y}$As$_8$ layers, which provide information about the bonding/antibonding character of the corresponding electronic states. The Fe-$3d$ PDOS (Figure 4a, c) of both compounds are very similar to those of other FeAs superconductors. The Fermi levels at the rising edges of the Fe-$3d$ peaks reveal that mostly iron states contribute to the Fermi surfaces in both the α-1048 and 1038 compounds. In contrast, the contribution of platinum at E_F is very small. The Pt-$5d$ PDOS of α-1048 has nearly a gap, which means that the Fermi surface of this compound consists of states from the FeAs layer only, as in the known FeAs superconductors. This situation is also consistent with the Pt–As bonding. The COHP plot (Figure 4b) reveals that the majority of the Pt–As bonding states are well below and the antibonding states are mainly well above the Fermi energy, respectively. In other words, Pt–As bonding removes most of the Pt states from the Fermi surface in α-1048.
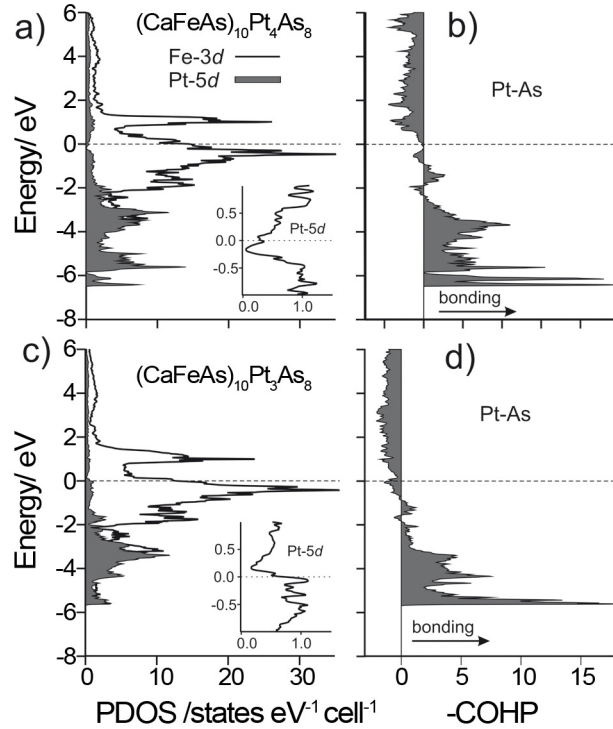
Figure 4. Partial density of states (PDOS) and crystal orbital Hamilton population (COHP) of the Pt–As bonds in a,b) tetragonal α-1048 and c,d) triclinic 1038. Insets: Details of the Pt-5d PDOS near E_F.

The situation is surprisingly similar in the 1038 compound (Figure 4c, d). The Pt contribution at E_F again is very small, while these states are slightly Pt–As antibonding (Figure 4d). Details of the Pt-5d PDOS are shown in the insets of Figure 4. The Fermi level is just above the gap in the α-1048 compound (which contains one more Pt^{2+} ion) but just below this gap in the 1038 phase. Thus, band filling across this gap in the Pt states mainly fills Fe states that contribute most of the energy levels in this range, which is equivalent to electron doping. This finding strongly suggests that the FeAs layer of the α-1048 compound is indirectly doped by two electrons from the Pt$_4$As$_8$ layer. Assuming Pt^{2+}, the amount of transferred charge is 0.2 e^- / FeAs, which is close to the typical values where other indirectly electron doped iron arsenide superconductors like LaO$_{1-x}$F$_x$FeAs[1] or the recently discovered Ca$_{1-x}RE_x$Fe$_2$As$_2$[20] achieve the highest critical temperatures.

2.1.4   *Conclusion*

In summary, we have found three new superconducting iron platinum arsenides with the general formula (CaFe$_{1-x}$Pt$_x$As)$_{10}$Pt$_{4-y}$As$_8$. The crystal structures are stacking variants of FeAs and slightly puckered Pt$_{4-y}$As$_8$ layers with square coordinated platinum, separated by calcium layers. Arsenic atoms in the Pt$_{4-y}$As$_8$ layers form As$_2^{4-}$ dumbbells according to the Zintl concept, providing charge balance in (Ca^{2+}Fe^{2+}As^{3-})$_{10}$(Pt^{2+})$_3$[(As$_2$)$^{4-}$]$_4$. Superconductivity was

observed at $13 - 35$ K. We suggest that the highest T_c value (above 30 K) occurs in the α-1048 phase with clean FeAs layers that are indirectly electron doped according to $(Ca^{2+}Fe^{2+}As^{3-})_{10}(Pt^{2+})_4[(As_2)^{4-}]_4 \cdot 2\, e^-$. We also suggest that the lower critical temperatures occur in the 1038- and β-1048 phases owing to Pt doping at the Fe site. Such direct electron doping has not achieved a T_c value above 25 K in any other iron-based material. DFT band structure calculations suggest that the contribution of the $Pt_{4-y}As_8$ layers to the Fermi surface is small and the Fermi energy is slightly either below or above a quasi-gap in the Pt states of the 1038 and α-1048 compounds, respectively. The latter clearly supports the suggested indirect electron doping of the FeAs layer in the α-1048 compound with the highest critical temperature. The platinum iron compounds represent the first iron-based superconductors with new crystal structures and can serve as a new platform for further studies that go beyond the known systems. Note: During the submission of this manuscript, we noticed a preprint by *Ni* et al.[26] that reports similar results. The authors confirm two of the crystal structures reported herein and observed superconductivity up to 27 K.

2.1.5 *References*

[1]   Y. Kamihara, T. Watanabe, M. Hirano, H. Hosono, *J. Am. Chem. Soc.* **2008**, *130*, 3296.

[2]   Z.-A. Ren, W. Lu, J. Yang, W. Yi, X.-L. Shen, Z.-C. Li, G.-C. Che, X.-L. Dong, L.-L. Sun, F. Zhou, Z.-X. Zhao, *Chin. Phys. Lett.* **2008**, *25*, 2215.

[3]   M. J. Pitcher, D. R. Parker, P. Adamson, S. J. C. Herkelrath, A. T. Boothroyd, R. M. Ibberson, M. Brunelli, S. J. Clarke, *Chem. Commun.* **2008**, 5918.

[4]   F. C. Hsu, J. Y. Luo, K.W. Yeh, T. K. Chen, T. W. Huang, P. M. Wu, Y. C. Lee, Y. L. Huang, Y. Y. Chu, D. C. Yan, M. K. Wu, *Proc. Natl. Acad. Sci. USA* **2008**, *105*, 14262.

[5]   M. Rotter, M. Tegel, I. Schellenberg, W. Hermes, R. Pöttgen, D. Johrendt, *Phys. Rev. B* **2008**, *78*, 020503.

[6]   M. Rotter, M. Tegel, D. Johrendt, *Phys. Rev. Lett.* **2008**, *101*, 107006.

[7]   X. Zhu, F. Han, G. Mu, P. Cheng, B. Shen, B. Zeng, H.-H. Wen, *Phys. Rev. B* **2009**, *79*, 220512.

[8] M. Tegel, F. Hummel, Y. Su, T. Chatterji, M. Brunelli, D. Johrendt, *Europhys. Lett.* **2010**, *89*, 37006.

[9] M. Tegel, T. Schmid, T. Stürzer, M. Egawa, Y. Su, A. Senyshyn, D. Johrendt, *Phys. Rev. B* **2010**, *82*, 140507.

[10] L. Thomassen, *Z. Phys. Chem.* **1929**, *2*, 349.

[11] A. Imre, A. Hellmann, G. Wenski, J. Grap, D. Johrendt, A. Mewis, *Z. Anorg. Allg. Chem.* **2007**, *633*, 2037.

[12] G. Wenski, A. Mewis, *Z. Anorg. Allg. Chem.* **1986**, *535*, 110.

[13] A. Czybulka, M. Noack, H.-U. Schuster, *Z. Anorg. Allg. Chem.* **1992**, *609*, 122.

[14] M. Nohara, S. Kakiya, K. Kudo*, International workshop on novel superconductors and super materials*, Tokyo, Japan, March 6 – 8. **2011**.

[15] A. Coelho, TOPAS-Academic, Version 4.1, Coelho Software, Brisbane, **2007**.

[16] V. Petricek, M. Dusek, L. Palatinus, Jana2006 *Structure Determination Software Programs*, Institute of Physics, Praha, Czech Republic, **2009**.

[17] O. K. Andersen, O. Jepsen, *Tight-Binding LMTO*, Max-Planck-Institut für Festkörperforschung, Stuttgart, **1994**.

[18] G. Wenski, A. Mewis, *Z. Naturforsch. B* **1987**, *42*, 507.

[19] Y. Nishikubo, S. Kakiya, M. Danura, K. Kudo, M. Nohara*, J. Phys. Soc. Jpn.* **2010**, *79*.

[20] S. R. Saha, N. P. Butch, T. Drye, J. Magill, S. Ziemak, K. Kirshenbaum, P. Y. Zavalij, J. W. Lynn, J. Paglione, *Phys. Rev. B* **2012**, *85*, 024525.

[21] M. Rotter, M. Pangerl, M. Tegel, D. Johrendt, *Angew. Chem.* **2008**, *120*, 8067; *Angew. Chem. Int. Ed.* **2008**, *47*, 7949.

[22] A. S. Sefat, R. Jin, M. A. McGuire, B. C. Sales, D. J. Singh, D. Mandrus, *Phys. Rev. Lett.* **2008**, *101*, 117004.

[23] I. I. Mazin, D. J. Singh, M. D. Johannes, M. H. Du, *Phys. Rev. Lett.* **2008**, *101*, 057003.

[24]   I. I. Mazin, *Nature* **2010**, *464*, 183.

[25]   I. Mazin, *Physics* **2011**, *4*, 26.

[26]   N. Ni, J. M. Allred, B. C. Chan, R. J. Cava, *Proc. Natl. Acad. Sci. USA* **2011**, *108*, E1019.

2.2 Stacking Disorder in the System (CaFeAs)$_{10}$Pt$_z$As$_8$
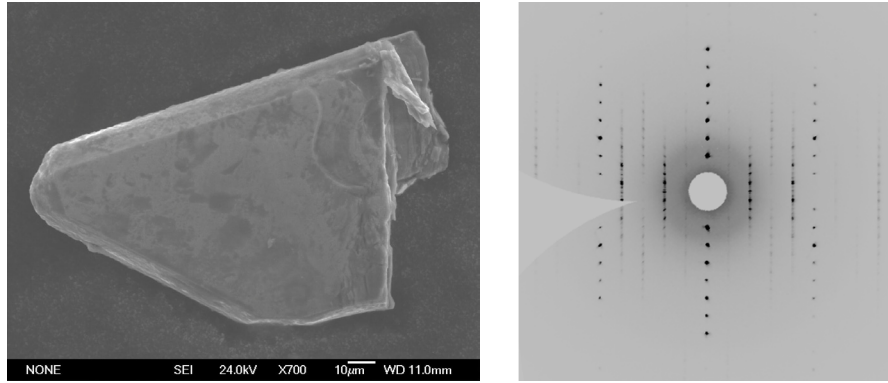
2.2.1 *Introduction*

Diffuse intensities at odd *Bragg* intensities in X-ray scattering experiments originate from broken three-dimensional translation symmetry in a crystal. This lack of atomic long range order can occur as site, one, two, or three-dimensional disorder, whereby the latter corresponds to glasses and amorphous compounds. One dimensional or stacking disorder, can be found in a variety of layered compounds such as silicates or halogenides with CdI$_2$- and BiI$_3$-type structures. Thereby faults in their stacking sequence are caused by different possible layer arrangements. The influence of stacking disorder on the X-ray diffraction pattern strongly depends on the frequency of these faults. Rare occurrences ($\sim10^{-5}$) yield polysynthetic twins, whereas more frequent faults cause reflection broadening. Domain sizes below the range of X-ray radiation coherence length result in diffuse scattering contributions along the stacking direction often accompanied with additional intensity maxima. Finally vast intensity distributions without reasonable maxima are found for complete arbitrarily stacked structures. For structure determination relying on focused *Bragg* reflections, the effects of disorder can be disastrous. Since an accurate measurement of separated *hkl* intensities is not possible for those systems, conventional structure determination often results in average structure models. Nevertheless a detailed insight into such structures and their local order can still be gained by an empirical evaluation of diffraction data as was shown for Sr$_{0.5}$Ba$_{0.5}$Si$_2$O$_2$N$_2$[1] for example.

Discovering superconductivity in the Ca–Fe–Pt–As system, especially the structure determination of the corresponding 1048 compounds revealed to be unexpectedly problematic. Strong reflections accompanied with diffuse contributions were found for all crystals, complicating the development of a structure model. Nevertheless the structures of the tetragonal α- and the

triclinic β-polymorphs[2-4] were found soon followed by a monoclinic γ-polymorph[5]. However, all attempts to isolate the polymorphs in form of bulk material failed. Instead all crystals revealed complex twinning, high residual electron density in the Pt_4As_8 layers, and diffuse scattering contributions often accompanied with additional intensity maxima along c^*. In this chapter the structure of the 1048 phase, being so far unique among the iron arsenides, will be discussed in detail. A disorder model will be presented giving an easy understanding for the diffuse contributions, twinning, and the existence of the polymorphs found. The model will be substantiated by DFT calculations, also giving an insight how superconducting properties may be affected by this special form of disorder. Although stacking disorder also exists in the 1038 structure, this section will focus on the 1048 system, where the identification of different structures raised the most confusion.

2.2.2 *Experimental Details*

Polycrystalline samples of $(CaFeAs)_{10}Pt_4As_8$ were prepared by heating stoichiometric mixtures of the elements (Ca: 99.99 %, Fe: 99.9 %, Pt: 99.95 %, As: 99.999 %) for 20 h at 800 – 1000 °C in alumina crucibles sealed in silica tubes. The product was grounded, reheated to 1200 °C for 120 h, slowly cooled to 900 °C and quenched with water. Single crystals were synthesized heating stoichiometric mixtures of the elements with an excess of Pb (600 wt%, Pb: 99.999 %) 72 h at 1000 °C and slow cooling to 400 °C. Subsequently the batches were turned upside down and kept another 60 min at 400 °C to remove the main part of the flux material. Plate-like and needle-shaped single crystals of $(CaFeAs)_{10}Pt_4As_8$ were isolated by dissolving remaining Pb in diluted HCl and washed with water. High resolution powder diffraction data were collected on a STOE Stadi P diffractometer (Cu-Kα_1 radiation, Ge(111) monochromator, position sensitive detector) in transmission geometry and at the ID31 synchrotron beam line at ESRF, Grenoble. Single crystal intensity data was measured on a STOE IPDS-I or a BRUKER D8 Quest diffractometer both using Mo-Ka radiation. Semiempirical absorption correction based on equivalent reflections was applied.[6-8]. The structures were solved using the charge flipping method included in the JANA2006 program package.[9] Powder pattern and selected area diffraction patterns of disordered polytypes including diffuse scattering were calculated using DIFFaX.[10-11] Structure relaxation and volume dependent total energy calculations were performed using the VASP 4.6 package.[12-14] Heat of formation and phonon spectra calculations were performed by the workgroup Dronskovski, RWTH Aachen.

2.2.3 *Single Crystal Data*

Single crystal X-ray diffraction investigations on $(CaFe_{1-x}Pt_xAs)_{10}Pt_4As_8$ revealed the polymorphic nature of the 1048 system. Three polytypes with the space groups $P4/n$, $P2_1/n$, and $P\bar{1}$ were identified. Deviations of the basal unit cell parameters a and b are based on Fe/Pt mixing and Pt deficiency.

Table 2. Unit cell parameters of 1048 polytypes.

Label	α-1048	β-1048	γ-1048
Space group	$P4/n$	$P\bar{1}$	$P2_1/n$
a (Å)	8.7145(1)	8.7382(4)	8.7032(14)
b (Å)	$= a$	8.7387(3)	8.7032(14)
c (Å)	10.462(2)	11.225(5)	21.010(6)
α (°)	90	81.049(3)	90
β (°)	90	71.915(3)	90
γ (°)	90	89.980(3)	90
Volume (Å³)	794.51(1)	803.79(6)	1591.4(6)

In *hk* cross sections of all crystals exclusively sharp *Bragg* reflections occur. Primitive tetragonal basis cells of approximately 3.9 Å × 3.9 Å were evident from the strongest reflections originating from the $CaFe_2As_2$ substructure of the 1048 phases. Additional reflections were assigned to the $\sqrt{5} \times \sqrt{5}$ supercell resulting from the symmetry of the Pt_4As_8 layers.

In c^* direction strong diffuse contributions were found for $2h + k \neq 5n$ ($n \in \mathbb{N}$), indicating stacking disorder in the $\sqrt{5} \times \sqrt{5}$ superstructure of the 1048 compounds. The absence of diffuse scattering for $2h + k = 5n$, however, accounts for an ordered CaFeAs substructure (Figure 1). No influence of synthesis conditions on the magnitude of disorder was found experimentally. This indicates the disorder being an intrinsic property of the 1048 system rather than a problem of crystal growth conditions.
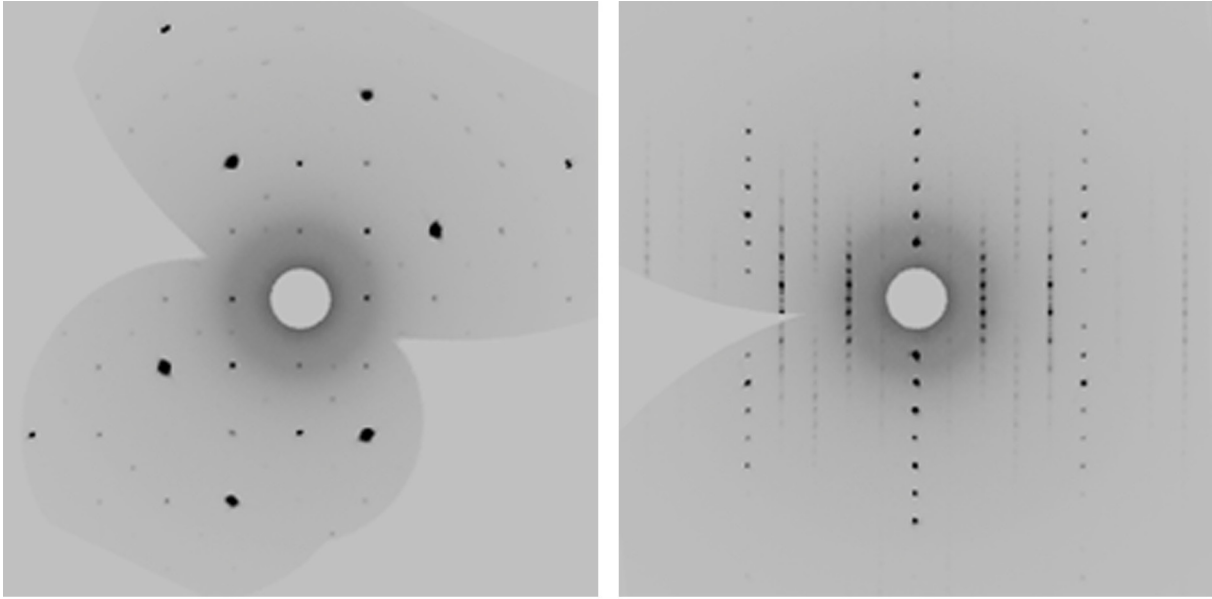
Figure 1. *hk0* (left) and *h0l* (right) cross sections of γ-1048 crystal.

The average structure of the crystals were determined by integration with the $\sqrt{5} \times \sqrt{5}$ super-cell and neglecting diffuse contributions. For all three polymorphs identical layers of CaFeAs and Pt_4As_8 were found, however, with different arrangements of the platinum arsenide layers to each other. This finding substantiates, that the diffuse intensity is a consequence of stacking disorder of the Pt_4As_8 layers. Nevertheless, in several crystals additional intensity maxima were found on diffuse streaks with fractional indices, which could be assigned to twinning (triclinic case) or presumably superstructure domains. These features substantiated, that the layer stacking in the 1048 compounds is not completely arbitrary but shows ordered domains on the length scale of X-ray radiation coherence length. In diffraction experiments those small domains are detectable as twin or polytype domains whereas smaller domains contribute as diffuse intensity in stacking direction. Although the application of different synthesis strategies in the system Ca–Fe–Pt–As showed hardly any effect on the magnitude of disorder, two ordered α-1048 derivatives were found by way of partial substitution in $(CaFe_{0.87}Ru_{0.13}As)_{10}Pt_{2.9}Ru_{1.1}As_8$ and $(Ca_{0.88}Na_{0.12}FeAs)_{10}Pt_{3.6}As_8$. The reduction of the electron count in the Pt_4As_8 layer either by Ru substitution or Pt deficiency appears to favor the higher symmetrical α-polymorph, whereas a detailed understanding is still missing.

2.2.4 Powder Data

Powder data of $(CaFeAs)_{10}Pt_4As_8$ obtained from laboratory powder diffraction instruments revealed sharp reflections together with anisotropically broadened reflections which could be indexed with the $\sqrt{5} \times \sqrt{5}$ supercell of the 1048 phases. However, a precise assignment to the

particular polymorphs was not possible. The presence of diffuse superstructure reflections accompanied by sharp subcell reflections even in high resolution powder data obtained from synchrotron beam line ID31 at ESRF, Grenoble, substantiates the model of stacking disorder in the 1048 system, rather than a mixture of different distinct polymorphs.

2.2.5 Theoretical Considerations

The 1048 structures consist of an alternating stacking of the two metal pnictide layers CaFeAs and Pt$_4$As$_8$. Assuming statistical stacking of these layers, the three-dimensional periodicity of the 1048 structures is broken and a structure description using space group systematic fails. However, within the layers two-dimensional translation symmetry is retained which allows for the application of layer symmetry.[15] Both metal pnictide layers feature tetragonal layer symmetry. The CaFeAs subcell shows *p4mm* (# 11) layer symmetry whereas *p4* (# 10) was found for the Pt$_4$As$_8$ layer.

Analyzing the stacking of CaFeAs and Pt$_4$As$_8$ sheets, the Ca and Pt sites are relevant in such way that a deflected Pt must always be arranged in *c** direction above a Ca site. Neighboring Ca sheets are shifted by (0.3, 0.1, 0) at every FeAs layer with respect to the supercell, and (0.3, 0.1, 0) at every Pt$_4$As$_8$ layer. Taking into account all combination of both shifts together with previously determined tetragonal layer symmetry five possible arrangements of neighboring Pt$_4$As$_8$ layers can be realized: A(0, 0, 0), B_0(0.2, 0.4, 0), B_{90}(0.4, -0.2, 0), B_{180}(-0.2, -0.4, 0), and B_{270}(-0.4, 0.2, 0) (Figure 2). It is noteworthy that the B_x shift corresponds to the translation symmetry of the CaFeAs subcell. Therefore neighboring FeAs layers reveal no shift, resulting in a tetrahedra layer arrangement as found in PbFCl-type structures for all A, B_x. Among this set of shifts (A, B_x) only A features a coincidence of fourfold rotation axes of the layers, whereas all other stacking possibilities break this symmetry in the superstructure. In the context of this systematic the three polymorphs experimentally found can be understood as mere A-stacking (α-1048), mere B_x-stacking (β-1048), and alternated B_0/B_{180}- or B_{90}/B_{270}-stacking (γ-1048), respectively (Figure 2). Thereby the ubiquitous presence of twin domains found in the majority of 1048 crystals can be traced back to broken fourfold and twofold rotation axes of the CaFeAs subsystem in the space group symmetry of the superstructure.
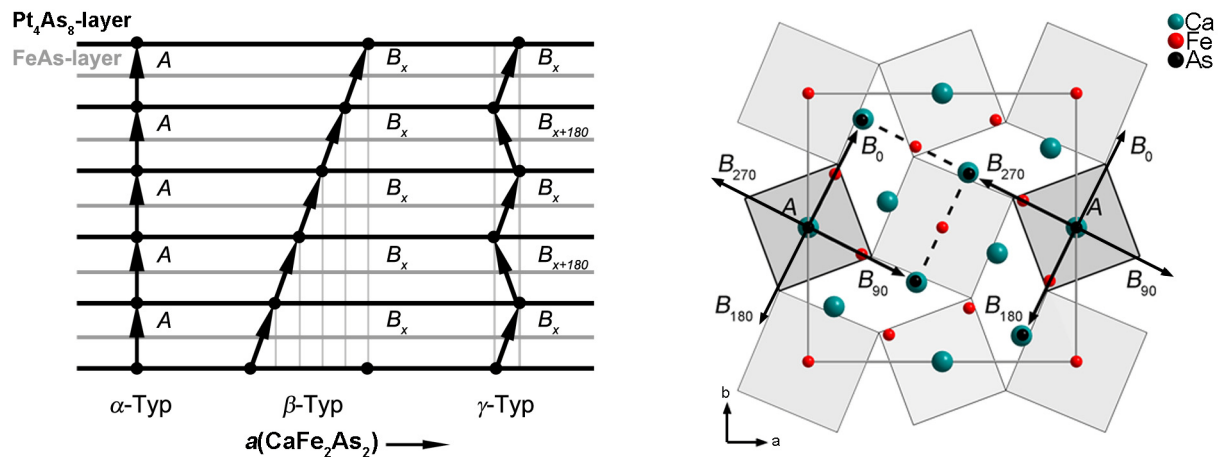
Figure 2. Schematic illustration of the three polymorphs identified based on the layer translation vectors A and B_x (left). Origin of the five layer translation vectors A, B_0, B_{90}, B_{180}, and B_{270} (right).

2.2.6   *DIFFaX Simulations*

Applying the previously developed disorder model to the 1048 structure allows for a more detailed understanding of the diffraction data. Figure 3 compares high-resolution X-ray powder data and a DIFFaX simulation based on a partly disordered stacking model. Sharp reflections as well as anisotropic broadened reflections affected by disorder are well described. Minor differences in intensity can be ascribed to Fe/Pt mixing and Pt deficiency which was not refined for this purpose.
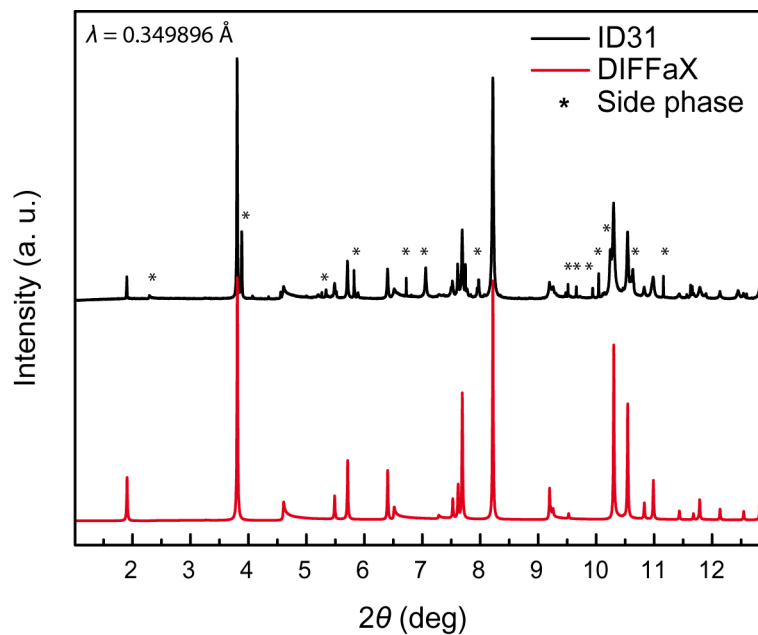
Figure 3. High-resolution powder X-ray diffractogram of (CaFeAs)$_{10}$Pt$_4$As$_8$ (black) and DIFFaX simulation of 1048 structure based on a partly disordered stacking model (red).

Analyzing single crystal diffraction data, diffuse intensity of reflections complying with $2h + k \neq 5n$ as well as sharp substructure reflections are well described within the stacking disorder model (Figure 4). More detailed information about the mean domain size, however, is accessible from a closer analysis of additional reflections. Figure 4 depicts the intensity distribution along the (10l) streak for stacking scenarios with full α-1048 order, small but equally probable domains, strong preference for an A domain, and full disorder. Best reproduction of the additional intensity maxima experimentally observed at $l = 0.2, 0.4, 0.6,$ and 0.8 is gained for the scenario of small but ordered domains. A reoccurrence probability of the last layer shift of $80 - 90$ % was used for this simulation, meaning that ordered domains are in the range of 5 to 10 unit cells. This finding substantiates, that the 1048 system features no complete arbitrary random stacking disorder but ordered domains in the range of X-ray coherence length. However, for the related compound (CaFeAs)$_{10}$Pd$_3$As$_8$ even stronger diffuse contributions were found without features at odd indices, thus suggesting enhanced disorder in these compounds.[16]

It should be mentioned that from powder data often unreasonable high Pt substitution on the iron sites could be refined. This effect can also be ascribed to stacking disorder. While *Bragg* intensity of reflections with $2h + k \neq 5n$ ($n \in \mathbb{N}$) is generally too low, CaFeAs substructure reflections appear to have too strong scattering intensity compared to the latter. Refinement software interprets this intensity mismatch as higher electron density in the substructure, thus higher Pt substitution.
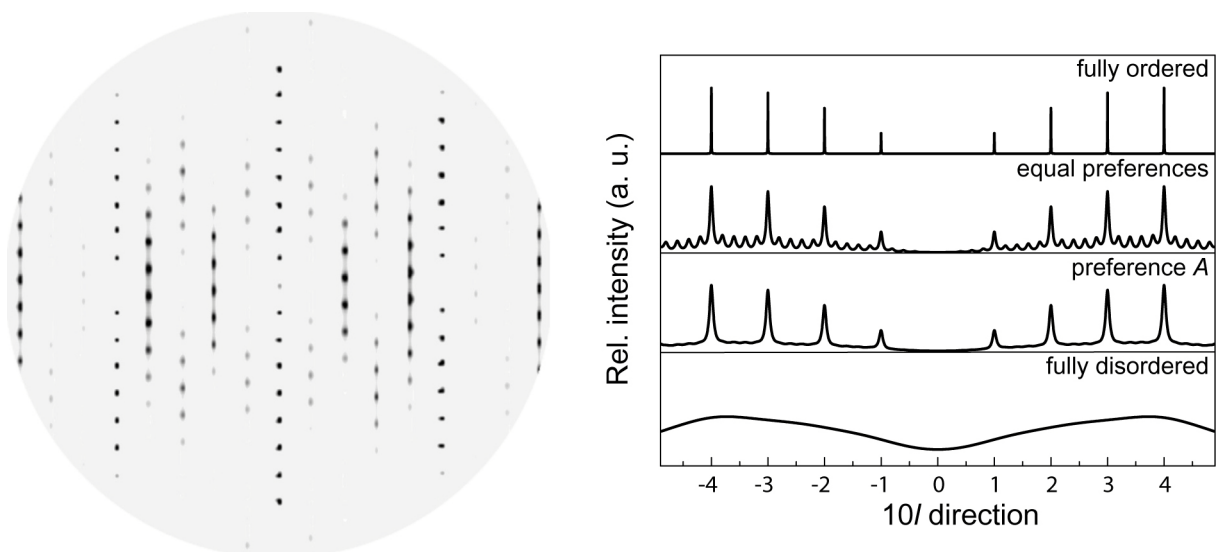
Figure 4. Simulated selected area diffraction pattern based on the partly disordered stacking model (left). Simulation of (10l) streaks based on models with full order, full disorder, preference for a domain, and equal probability for ordered domains (right).

2.2.7 *DFT Calculations*

Full structure relaxation, including volume, cell shape, and atomic coordinates revealed almost identical ground state energies (α-type: $\Delta E = 0$ eV, β-type: $\Delta E = -0.004$ eV, γ-type: $\Delta E = 0.001$ eV) for all three polymorphs. Volume dependent relaxations simulating external pressure yielded analogous *p-E*-correlations, excluding possible pressure induced phase transitions between the polytypes. Contemplating about thermally induced transitions, temperature dependent heat of formation calculations showed no significant energy differences in the scope of accuracy and applicable temperatures. This finding is in line with the previously established model of stacking disorder with the limit structures α-, β-, and γ-1048, rather than a picture of polymorphism.

Accepting the presence of partial stacking disorder in the 1048 structure, this compound is the first iron arsenide superconductor featuring limited three-dimensional order. Thus, the question was raised about the influence on the superconducting properties. Generally superconductivity in highly anisotropic iron arsenides is ascribed to phonon and magnon interactions in FeAs layers, but also interlayer coupling is discussed frequently. Phonon calculations comparing α- and β-polytype revealed identical spectra (Figure 5). This finding along with the ordered FeAs sublattice of the 1048 structures reduces the relevance of the Pt$_4$As$_8$ layer to a mere structural and electron reservoir function, whereas superconductivity itself is not affected by the arrangement of Pt$_4$As$_8$ layers. Although a systematic investigation of the influence of disorder on superconducting properties is difficult in this system, these conclusions are in line with the results on the 1048 compounds so far.
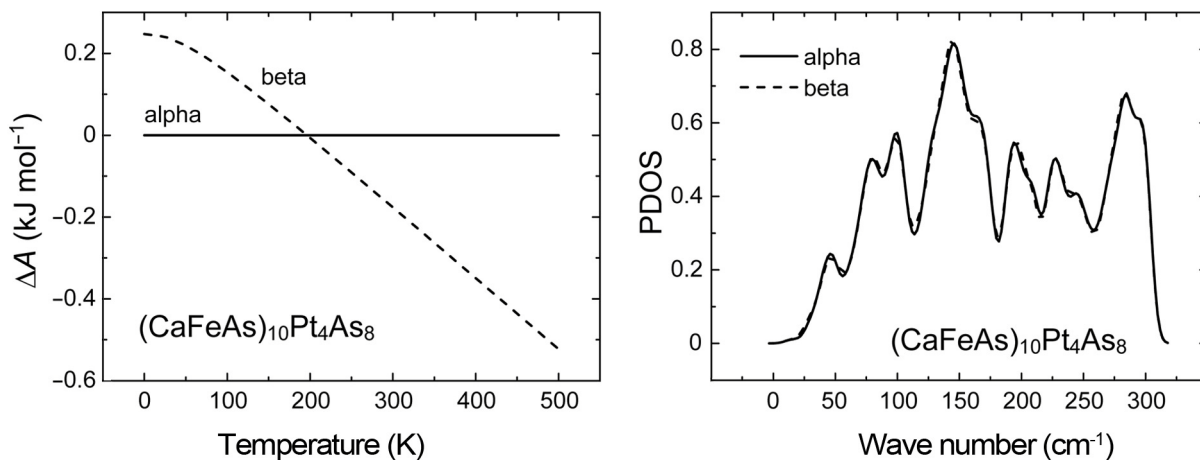
Figure 5. Heat of formation calculation (left) and calculated phonon density of states by DFT-methods, comparing α- and β-polytype of (CaFeAs)$_{10}$Pt$_4$As$_8$ (right).

2.2.8 *Annotation to Disorder in the 1038 Structure*

As mentioned in the introduction, stacking disorder in Ca–Fe–Pt–As is not restricted to the 1048 system but is also present in the 1038 compound. As in 1048, only $\sqrt{5} \times \sqrt{5}$ superstructure reflections are affected, featuring varying diffuse contributions along c^*. Layer symmetry *p4mm* (# 11) can be assigned to the CaFeAs subcell whereas *p4* (# 10) was found for the Pt_3As_8 layer. The presence of an additional mirror plane within the Pt_3As_8 layer, however, forces a different arrangement of neighboring Pt_3As_8 layers than in Pt_4As_8. The relevant point to determine the stacking order is again the Ca layer. While the Pt_3As_8 layer shifts the Ca sheet by (0, 0, 0), the FeAs layer adds a shift of (0.3, 0.1, 0), with respect to the $\sqrt{5} \times \sqrt{5}$ supercell. Together with fourfold rotational symmetry of the layers five possible arrangements of neighboring Pt_3As_8 layers are generated, being A(0.5, 0.5, 0), B_0(0.3, 0.1, 0), B_{90}(0.1, -0.3, 0), B_{180}(-0.3, -0.1, 0), and B_{270}(-0.1, 0.3, 0) with respect to the supercell. Again the FeAs sublattice remains ordered for all possible shifts, with the CaFeAs substructure in a $ThCr_2Si_2$-type stacking. Most remarkably a constant A shift would also allow a tetragonal 1038 limit structure ($P4_2/n$) like in the 1048 system. However, none of such could be identified so far. Although the disorder effects, being observable in diffraction data of 1038 compounds, are well described within this model, it remains disputable how much further disorder is added to this system by a potential partial ordering of the deflected Pt split site. A comparison of determined unit cell parameters of 1038 and 1048 compounds with calculated ones based on disorder models is given in Chapter 7.4 of the appendix.

2.2.9 *Conclusion*

It could be shown that the initially occurring problems concerning structure solution and reliable refinement were not based on "poor" crystal quality or bad growth properties, but be ascribed to stacking disorder in this system. The structure and symmetry of the two layers CaFeAs and Pt_4As_8 allow for five possible arrangements of neighboring Pt_4As_8 layers, in first approximation energetically equivalent. However, for all arrangements the CaFeAs sublattice remains unchanged in a PbFCl-like stacking. Assuming small ordered domains with defined layer shift diffuse scattering contributions as well as the additional intensity maxima found for the superstructure reflections $2h + k \neq 5n$ along the stacking direction c^* are well described. Moreover this model also describes the anisotropically broaden reflections in powder data satisfactory. In the context of this investigations the three polytypes α-, β-, and γ-1048 identified so far by single crystal X-ray methods were characterizes not as only existing structures

in the 1048 system, but limit cases of the disorder model. Twinning occurs in this system due to the broken tetragonal layer symmetry in the superstructure . A similar stacking model was also presented briefly for disorder in 1038 compounds.

DFT calculation gave no indication for possible pressure or temperature induced phase transitions, substantiating the disorder model. Finally, based on phonon calculations and the presence of the ubiquitous ordered FeAs sublattice it was concluded, that the influence of stacking disorder on the superconducting properties should be very small. Thus, the 1048 compounds might present a very interesting system to investigate the influence of broken translation symmetry in the stacking direction on the properties experimentally and why order is retained in the 1048 derivatives (CaFe$_{0.87}$Ru$_{0.13}$As)$_{10}$Pt$_{2.9}$Ru$_{1.1}$As$_8$ and (Ca$_{0.88}$Na$_{0.12}$FeAs)$_{10}$Pt$_{3.6}$As$_8$ with hole doped Pt$_z$As$_8$ layers.

2.2.10 *References*

[1]   M. Seibald, O. Oeckler, V. R. Celinski, P. J. Schmidt, A. Tücks, W. Schnick, *Solid State Sci.* **2011**, *13*, 1769.

[2]   C. Löhnert, T. Stürzer, M. Tegel, R. Frankovsky, G. Friederichs, D. Johrendt, *Angew. Chem. Int. Ed.* **2011**, *50*, 9195.

[3]   N. Ni, J. M. Allred, B. C. Chan, R. J. Cava, *Proc. Natl. Acad. Sci. USA* **2011**, *108*, E1019.

[4]   S. Kakiya, K. Kudo, Y. Nishikubo, K. Oku, E. Nishibori, H. Sawa, T. Yamamoto, T. Nozaka, M. Nohara, *J. Phys. Soc. Jpn.* **2011**, *80*, 093704.

[5]   T. Stürzer, G. Derondeau, D. Johrendt, *Phys. Rev. B* **2012**, *86*, 060516.

[6]   *XRED32*, Version 1.03, STOE & CIE GMBH, Darmstadt, Germany, **2002**.

[7]   *XSHAPE*, Version 2.07, STOE & CIE GMBH, Darmstadt, Germany, **2005**.

[8]   *SADABS*, BRUKER AXS, Karlsruhe, Germany, **2012**.

[9]   V. Petricek, M. Dusek, L. Palatinus, *Jana2006 Structure Determination Software Programs*, Institute of Physics, Praha, Czech Republic, **2009**.

[10]   M. M. J. Treacy, *DIFFaX* **2005**, Version 1.812.

[11] M. M. J. Treacy, J. M. Newsam, M. W. Deem, *Proc. R. Soc. London Ser. A* **1991**, *433*, 499.

[12] G. Kresse, J. Furthmüller, *Comp. Mat. Sci.* **1996**, *6*, 15.

[13] G. Kresse, J. Furthmüller, *Phys. Rev. B* **1996**, *54*, 11169.

[14] J. P. Perdew, K. Burke, M. Ernzerhof, *Phys. Rev. Lett.* **1996**, *77*, 3865.

[15] U. Müller, *Anorganische Strukturchemie* **2006**, *5*, Teubner Verlag.

[16] C. Hieke, J. Lippmann, T. Stürzer, G. Friederichs, F. Nitsche, F. Winter, R. Pöttgen, D. Johrendt, *Philos. Mag.* **2013**, *93*, 3680.

2.3 Structural and Magnetic Phase Transitions in triclinic $(CaFeAs)_{10}Pt_3As_8$

T. Stürzer, G. M. Friederichs, H. Luetkens, A. Amato, H.-H. Klauss, D. Johrendt
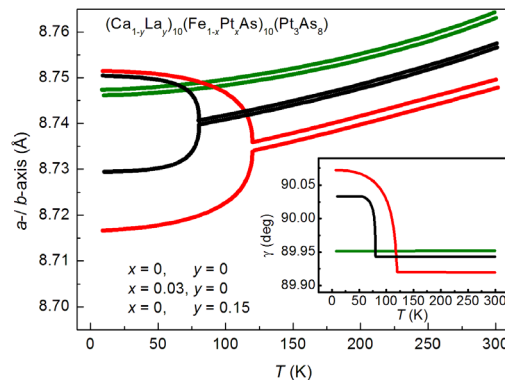
Abstract

We report the structural and magnetic phase transitions of triclinic $(CaFeAs)_{10}Pt_3As_8$, which is the parent compound of the 1038 type iron arsenide superconductors. High-resolution X-ray diffraction reveals splitting of the in-plane (a, b) lattice parameters at $T_s = 120$ K. Platinum doping weakens the distortion and shifts the transition temperature to 80 K in $(CaFe_{1-x}Pt_xAs)_{10}Pt_3As_8$ with $x = 0.03$. μSR experiments show the onset of magnetic order near T_s and a broad magnetic phase transition. The structural transition involves no reduction of the space group symmetry in contrast to the other parent compounds of iron arsenide superconductors; nevertheless the local fourfold symmetry of the FeAs layers in $(CaFeAs)_{10}Pt_3As_8$ is broken.

2.3.1 *Introduction*

Superconductivity in iron arsenides emerges from stoichiometric parent compounds in the course of the destabilization of antiferromagnetic ground states by chemical doping or pressure[1, 2]. The stripe-type antiferromagnetic ordering of the 1111-, 122-, and 111-type iron arsenides is linked to an orthorhombic distortion of the tetragonal lattice, which occurs at a temperature T_s slightly above the Néel-point T_N [3–7]. This proximity of superconductivity to the structural and magnetic phase transition was not clearly evidenced in the more complex

iron arsenide superconductors (CaFe$_{1-x}$Pt$_x$As)$_{10}$Pt$_3$As$_8$.[8–10] Their crystal structures contain alternating layers of iron arsenide and platinum arsenide, each separated by calcium atoms as shown in Figure 1. The compound, referred to as the 1038 phase, contains Pt$_3$As$_8$ layers, while in the 1048 phase one more platinum atom is located in Pt$_4$As$_8$ layers. Superconductivity in 1038/1048 compounds is controlled by Pt doping at the iron sites or by doping with excess electrons either from the Pt$_4$As$_8$ layer or from La doping at the Ca sites. High critical temperatures up to 38 K only occur with clean FeAs layers, while T_c remains below 15 K with Pt doped layers.[11] This doping behavior is similar to the other FeAs superconductors, where transition metal doping induces significantly lower critical temperatures than electron or hole doping outside the FeAs layers. Electronic structure calculations[8] as well as angle-resolved photoemission experiments[12] have shown that the Fermi surface of the 1038/1048 superconductors exhibits features very similar to the simpler FeAs compounds. Thus far there is every indication that the 1038/1048 materials act according to the same principle as known FeAs superconductors. Therefore a non-superconducting parent compound with antiferromagnetic ordering and a structural phase transition should exist. Recently we have proposed the stoichiometric 1038 phase (CaFeAs)$_{10}$Pt$_3$As$_8$ as the parent compound.[11] By assigning the usual ionic charges according to (Ca^{2+})$_{10}$[(FeAs)$_{10}$]$^{10-}$(Pt$_3$As$_8$)$^{10-}$ we obtain the identical charge for the FeAs layer (–1) as in the 1111- or 122-type parent compounds.
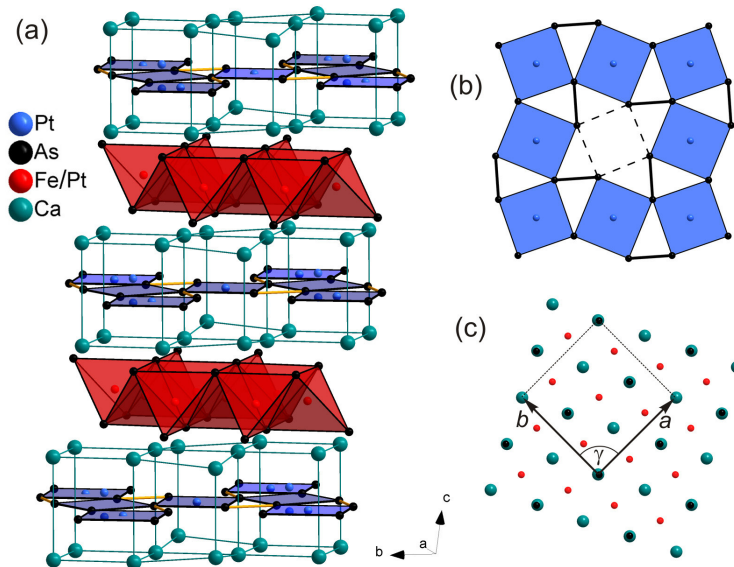
Figure 1. (a) Crystal structure of (CaFe$_{1-x}$Pt$_x$As)$_{10}$Pt$_3$As$_8$ (x = 0, 0.03), (b) Pt$_3$As$_8$ layer, (c) FeAs layer with the in-plane lattice translations *a*, *b*.

Moreover, we found that superconductivity is induced from this stoichiometric 1038 phase by La doping at the Ca site.[11] Thus one also expects an antiferromagnetic ground state of non-superconducting (CaFeAs)$_{10}$Pt$_3$As$_8$ and consequently a structural distortion of the FeAs layer.

The latter was also suggested on the base of polarized light imaging.[13] A recent preprint[14] reported the phase diagram of the La doped 1038 phase and assumed the existence of structural and magnetic transitions from weak features in the magnetic susceptibility, specific heat, and kinks in the derivative of the electrical resistivity. Another preprint[15] reported evidence for antiferromagnetic ordering in the 1038 phase from ^{75}As NMR data. All reports so far generally support the existence of a structural transition in the 1038 compound, but none of them gives clear experimental evidence of a lattice distortion. In this letter we show that the non-superconducting 1038 phase undergoes a structural phase transition near 120 K. The splitting of the equal in-plane lattice parameters a, b in the triclinic crystal structure is observed by high-resolution X-ray diffraction. Concomitant magnetic ordering is proved by means of μSR data showing an onset of magnetic ordering near T_s, followed by a broad magnetic transition.

2.3.2 *Experimental Details*

Polycrystalline samples of platinum iron arsenides were synthesized as described in [11], and characterized by X-ray powder diffraction using the Rietveld method with TOPAS[16]. Compositions were determined within errors of ±10 % by refining occupation parameters and by X-ray spectroscopy (EDX). Temperature-dependent X-ray powder diffraction data were collected using a HUBER G670 Guinier imaging plate diffractometer (Co $K\alpha_1$ radiation, Ge-111 monochromator) equipped with a close-cycle He-cryostat. *Dc*-resistivity was measured on a cold pressed pellet which had been annealed at 1073 K for 20 h. Magnetic susceptibility was measured using a QUANTUM DESIGN MPMS-XL5 SQUID magnetometer. μSR measurements were performed using the GPS and Dolly spectrometers located at the πM3 and πE1 beam lines of the Swiss Muon Source at the Paul Scherrer Institut, Switzerland. The data were analyzed using the MUSRFIT package[17].

2.3.3 *Results and Discussion*

Figure 2(a) shows the X-ray powder pattern of $(CaFeAs)_{10}Pt_3As_8$ measured at 10 K together with the Rietveld fit. Only small amounts of FeAs (4 %) were detected as impurities. Temperature-dependent changes in the pattern are tiny, and the splitting of the lattice parameters a, b becomes visible only at certain high angle reflections. The inset in Figure 2(a) shows a double peak, mainly generated by the (262) and ($\overline{6}$20) reflections. While the position of the ($\overline{6}$20) peak is almost constant near 80.55 °, the (262) peak begins to shift to higher angles as the temperature drops below 100 K, and is clearly discernible to the right of the ($\overline{6}$20) reflection at

10 K. Figure 2(b) shows the temperature dependency of the lattice parameters refined from X-ray powder data for $(CaFe_{1-x}Pt_xAs)_{10}Pt_3As_8$ with $x = 0$ and 0.03, and optimally La doped $(Ca_{0.85}La_{0.15}FeAs)_{10}Pt_3As_8$ for comparison.
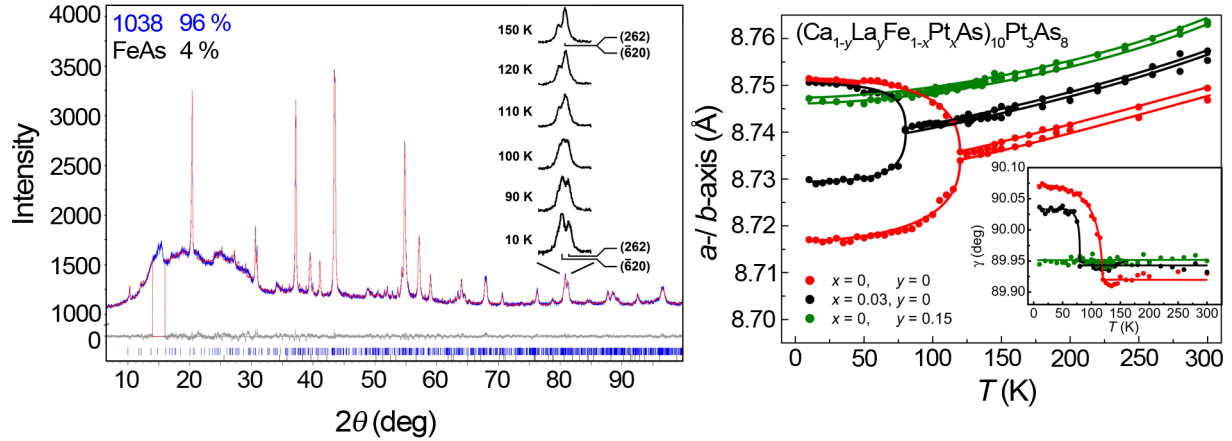
Figure 2. X-ray powder pattern (blue) and Rietveld fit (red) of $(CaFeAs)_{10}Pt_3As_8$ at 10 K (the high background between 10 ° and 30 ° is an artifact of the sample holder). The inset shows the shift of the (262)-reflection relative to the ($\bar{6}$20) (left). Lattice parameters of $(CaFe_{1-x}Pt_xAs)_{10}Pt_3As_8$ (x = 0, 0.03) and $(Ca_{0.85}La_{0.15}FeAs)_{10}Pt_3As_8$. The inset shows the angle between a, b (right).
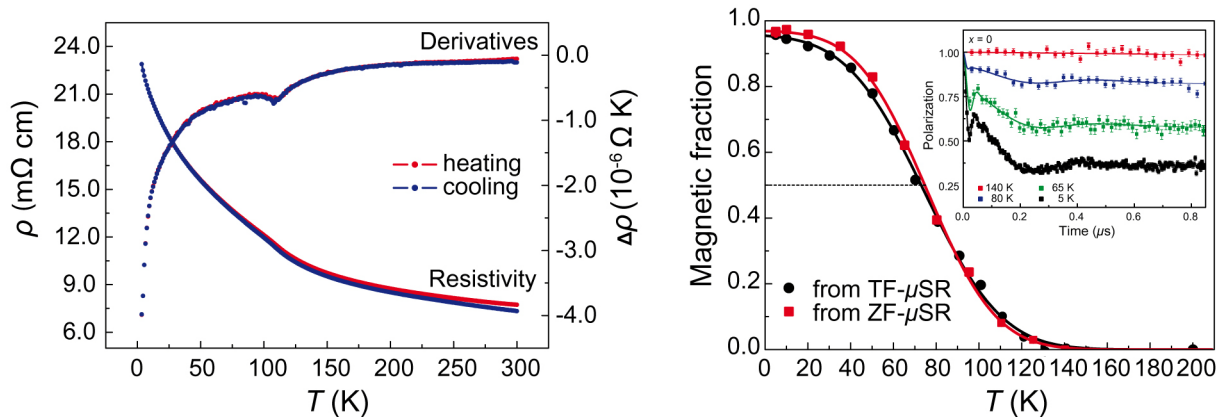
Figure 3. DC-resistivity of $(CaFeAs)_{10}Pt_3As_8$; The derivatives emphasize the anomaly at 120 K (left). Magnetic phase fraction of $(CaFeAs)_{10}Pt_3As_8$ obtained from transverse field (TF) and zero field (ZF) μSR data. Inset: ZF-μSR spectra of $(CaFeAs)_{10}Pt_3As_8$ at different temperatures (right).

Within the accuracy of the method, the lattice parameters a and b are equal at ambient temperature, due to the square base planes of both the FeAs and Pt_3As_8 layers. The c-axis decreases monotonically with cooling, while the angles remain nearly constant. The stoichiometric and underdoped 1038 compounds exhibit lattice distortions at 120 K and 80 K, respectively. Similar properties are known for a variety of iron arsenide compounds like $BaFe_2As_2$, where the phase transition results in a symmetry reduction from tetragonal $I4/mmm$ to orthorhombic $Fmmm$,[5] or LaOFeAs with a transition from $P4/nmm$ to $Cmme$.[18] The triclinic structure of the 1038 compounds precludes further reduction of the lattice symmetry, thus the transformation is isostructural. Nevertheless, the phase transition is tied to the loss of

the local fourfold symmetry in the FeAs layer, which is the crucial effect with respect to the physical properties.

The resistivity measurement is displayed in Figure 3(a). The semiconductor-like development to low temperatures is in contradiction to known iron arsenides, but was recently also observed by *Xiang* et al.[19] Absolute resistivity values are in the typical range for iron pnictides. The derivatives of resistivity data with respect to temperature reveal an anomaly near 120 K, coinciding for heating and cooling measurements. Muon spin rotation experiments with stoichiometric $(CaFeAs)_{10}Pt_3As_8$ detected three different muon precession frequencies with constant ratios, which accounts for three different muon sites in the magnetic unit cell of the homogeneous phase. The onset of long-range magnetic order below 130 K was found in transverse field (TF) and zero field (ZF) modes. Thereby the magnetic order develops gradually, reaching 100 % at 5 K, as shown in Figure 3(b). The sample is 100 % static magnetically ordered at 5 K, which is evident from the so-called 1/3-tail of the spectra, which is not damped (Inset in Figure 3(b)). Interestingly the μSR frequency is almost independent of temperature, which may indicate a first-order phase transition.
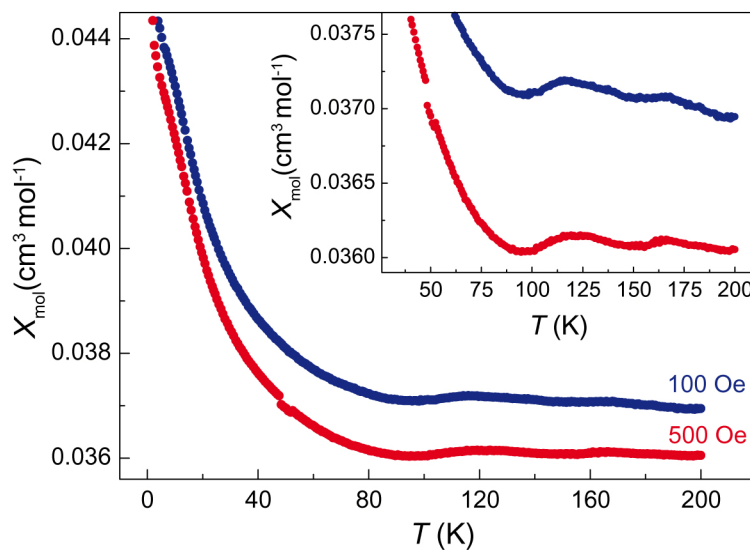
Figure 4. Magnetic susceptibility of $(CaFeAs)_{10}Pt_3As_8$.

The magnetic susceptibility of $(CaFeAs)_{10}Pt_3As_8$ (Figure 4) shows a weak and broad anomaly in the temperature region of the structural transition, in agreement with [14], thus substantiating a gradual development of magnetic order. The origin of the additional feature near 170 K is still unclear and has also been observed in [14]. The linear magnetization isotherm at 1.8 K (not shown) is compatible with antiferromagnetic order. The field dependency and the upturn of the susceptibility at low temperatures indicates a trace of ferromagnetic impurity in the sample, which is not detectable in the X-ray powder pattern. From the results so far, we

suggest a magnetic ordered state similar to the parent compounds $BaFe_2As_2$ or LaOFeAs. However, the low space group symmetry allows deviations from the stripe-type pattern, which remains to be seen.

2.3.4 Conclusion

In summary, our results give clear evidence for the magnetic and structural phase transition of $(CaFeAs)_{10}Pt_3As_8$ to an antiferromagnetic low-temperature phase at $T_s = 120$ K. In contrast to the 1111- and 122-type iron arsenides, the phase transition involves no reduction of the space group symmetry. Nevertheless the local tetragonal symmetry in the FeAs layers is broken. The magnitude of the lattice distortion is roughly half that observed in $BaFe_2As_2$ in terms of the order parameter $\delta = (a - b) / (a + b)$, and decreases with Pt doping on the Fe sites, as expected. Finally the transition is completely suppressed in optimally doped La-1038. The onset of long-range magnetic order in $(CaFeAs)_{10}Pt_3As_8$ coincides with the structural distortion at $T_s = 120$ K. In contrast to $BaFe_2As_2$, the magnetic fraction develops gradually and does not reach 100 % until 5 K. Taking this together with the temperature-independent μSR frequencies, a gradual increase of the structurally distorted compound at the expense of the ambient temperature phase should be observable below 130 K. However, our low-temperature structural data suggest a rather sharp structural change in the whole sample, without coexistence with the undistorted phase. While the detailed nature of the phase transition necessitates further investigations, our results demonstrate that the 1038 material acts according to the same principle as the known FeAs superconductors with $(CaFeAs)_{10}Pt_3As_8$ as the parent compound.

2.3.5 References

[1]   G. R. Stewart, *Rev. Mod. Phys.* **2011**, *83*, 1589.

[2]   D. Johrendt, *J. Mater. Chem.* **2011**, *21*, 13726.

[3]   C. de la Cruz, Q. Huang, J. W. Lynn, J. Li, W. Ratcliff II, J. L. Zarestky, H. A. Mook, G. F. Chen, J. L. Luo, N. L. Wang, P. Dai, *Nature* **2008**, *453*, 899.

[4]   M. Tegel, S. Johansson, V. Weiss, I. Schellenberg, W. Hermes, R. Pöttgen, D. Johrendt, *Europhys. Lett.* **2008**, *84*, 67007.

[5]   M. Rotter, M. Tegel, I. Schellenberg, W. Hermes, R. Pöttgen, D. Johrendt, *Phys. Rev. B* **2008**, *78*, 020503.

[6]   M. Tegel, M. Rotter, V. Weiss, F. Schappacher, R. Pöttgen, D. Johrendt, *J. Phys.: Condens. Matter* **2008**, *20*, 452201.

[7]   D. R. Parker, M. J. Pitcher, P. J. Baker, I. Franke, T. Lancaster, S. J. Blundell, S. J. Clarke, *Chem. Commun.* **2009**, *16*, 2189.

[8]   C. Löhnert, T. Stürzer, M. Tegel, R. Frankovsky, G. Friederichs, D. Johrendt, *Angew. Chem. Int. Ed.* **2011**, *50*, 9195.

[9]   N. Ni, J. M. Allred, B. C. Chan, R. J. Cava, *Proc. Natl Acad. Sci. USA* **2011**, *108*, E1019.

[10]   S. Kakiya, K. Kudo, Y. Nishikubo, K. Oku, E. Nishibori, H. Sawa, T. Yamamoto, T. Nozaka, M. Nohara, *J. Phys. Soc. Jpn.* **2011**, *80*, 093704.

[11]   T. Stürzer, G. Derondeau, D. Johrendt, *Phys. Rev. B* **2012**, *86*, 060516.

[12]   M. Neupane, C. Liu, S.-Y. Xu, Y.-J. Wang, N. Ni, J. M. Allred, L. A. Wray, N. Alidoust, H. Lin, R. S. Markiewicz, A. Bansil, R. J. Cava, M. Z. Hasan, *Phys. Rev. B* **2012**, *85*, 094510.

[13]   K. Cho, M. A. Tanatar, H. Kim, W. E. Straszheim, N. Ni, R. J. Cava, R. Prozorov, *Phys. Rev. B* **2012**, *85*, 020504.

[14]   N. Ni, W. E. Straszheim, D. J. Williams, M. A. Tanatar, R. Prozorov, E. D. Bauer, F. Ronning, J. D. Thompson, R. J. Cava, *Phys. Rev. B* **2012**, *87*, 060507(R).

[15]   T. Zhou, G. Koutroulakis, J. Lodico, N. Ni, J. D. Thompson, R. J. Cava, S. E. Brown, *J. Phys.: Condens. Matter* **2013**, *25*, 122201.

[16]   A. Coelho, *TOPAS-Academic*, Version 4.1, Coelho Software, Brisbane, Australia, **2007**.

[17]   A. Suter, B. M. Wojek, *Phys. Procedia* **2012**, *30*, 69.

[18]   T. Nomura, S. W. Kim, Y. Kamihara, M. Hirano, P. V. Sushko, K. Kato, M. Takata, A. L. Shluger, H. Hosono, *Supercond. Sci. Technol.* **2008**, *21*, 125028.

[19]   Z. J. Xiang, X. G. Luo, J. J. Ying, X. F. Wang, Y. J. Yan, A. F. Wang, P. Cheng, G. J. Ye, X. H. Chen, *Phys. Rev. B* **2012**, *85*, 224527.

2.4 ^{57}Fe-Mössbauer Study on $(CaFeAs)_{10}Pt_3As_8$
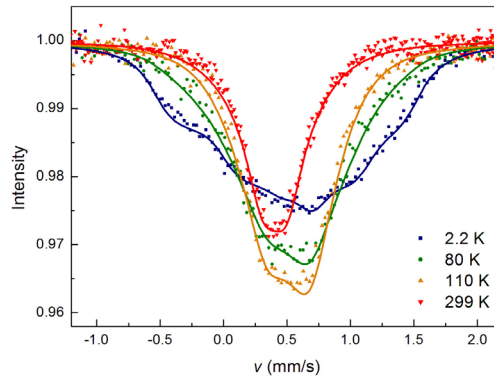
2.4.1   *Introduction*

In the last chapter stoichiometric $(CaFeAs)_{10}Pt_3As_8$ was shown to be a typical iron arsenide parent compound, despite its low symmetry and more complex structure. An isomorphic structural transition was evidenced by high resolution X-ray powder diffraction which breaks tetragonal FeAs layer symmetry.[1] Indication for this was also found in conductivity measurement on powder samples[1] and previously by polarized light investigations on single crystals[2]. An associated magnetic transition to an antiferromagnetic ground state was identified by μSR and SQUID[1] investigations. Indication for this was also reported based on ^{75}As NMR studies.[3] Angle-resolved photoemission studies supported by band structure and phonon spectra calculations have shown that the electronic structure is quite similar to the one observed for $BaFe_2As_2$,[4-8] while neutron scattering studies on single crystals demonstrated that magnetic fluctuations occur at the same stripe-like antiferromagnetic wave vector as observed in other Fe-based high-temperature superconductors.[9-11] Thus so far all results indicate $(CaFeAs)_{10}Pt_3As_8$ being a typical iron arsenide system, whereas the low symmetry and additional metal pnictide layer do not significantly influence the compounds properties dominated by the iron arsenide layer. Nevertheless, a complete temperature dependent phase diagram of $(CaFeAs)_{10}Pt_3As_8$ is not reported yet. So far also the reason for broadening of the magnetic transition is unclear. For the systems $AEFe_2As_2$ (AE = Sr, Ba, Eu) or LaOFePn (Pn = P, As) ^{57}Fe Mössbauer spectroscopy was demonstrated to be an excellent tool for investigations of the magnetic environment of iron.[12-15] The following chapter presents a temperature dependent ^{57}Fe Mössbauer study on stoichiometric $(CaFeAs)_{10}Pt_3As_8$. Results clearly show the magnetic ordering in the 1038 compound and give strong indication for the existence of a nematic magnetic phase above T_N.

2.4.2   Experimental Details

A polycrystalline sample of $(CaFeAs)_{10}Pt_3As_8$ was prepared from the elements (Ca: 99.99 %, Fe: 99.9 %, Pt: 99.95 %, As: 99.999 %) using the ration 10.5 : 10 : 2.9 : 18. The sample was sealed in an argon filled silica tube, heated to 600 °C for 10 h followed by 10 h at 1000 °C. The crude product was homogenized, encapsulated in a silica tube, reheated to 1000 °C for 25 h, then pelletized and heated to 1000 °C for 25 h again. For ^{57}Fe-Mössbauer measurements the sample was mixed with sugar. Measurements were performed on two spectrometers with WissEL setup (KETEX Axas SSD detector/ Kr-proportional counter, Co/Rh source) in the temperature range of 2.2 K to 299 K and additionally in the paramagnetic range of 99 K to 303 K.

2.4.3   Results and Discussion

Figure 1 shows Mössbauer spectra of $(CaFeAs)_{10}Pt_3As_8$ for $T = 299$ K, 110 K, 80 K, and 2.2 K and selected spectra from the paramagnetic range above T_N. Room temperature data can be satisfactory fitted assuming one iron site in accordance with the five symmetry independent but chemically identical Fe sites in $(CaFeAs)_{10}Pt_3As_8$. Moreover one additional Fe site was included to the fit which can be ascribed to the FeAs impurity phase, with values in good agreement with reported ones.[16] For the 1038 compound a single signal is observed at 299 K with an isomer shift of 0.41 mm/s. Values found for V_{ZZ}, Θ_{Debye}, and M_{eff} are in the typical range reported for iron in FeAs tetrahedral layers. Below the reported Néel temperature at 120 K[1] strong signal broadening can be observed, but without distinct signal splitting. A hyperfine field of 3.9(1) T was determined for 2.2 K, being smaller than B_{hyp} for reported compounds LaOFeAs ($B_{hyp} = 4.9$ T)[17] and $BaFe_2As_2$ ($B_{hyp} = 5.5$ T)[12]. A magnetic moment at the iron site could not be estimated, due to reasons discussed in reference [18]. The magnetic order parameter being associated with Mössbauer line width (Gauss broadening) clearly shows a magnetic transition to an ordered state at $T_N = 111(4)$ K (Figure 2, left), being in good accordance with reported transition temperature.[1, 11]

Measurements in the paramagnetic regime of the 1038 phase diagram also revealed significant signal broadening. Additional anisotropy in the peak shape gives indication for magnetic interactions already above T_N. These results point to the evolution of a nematic phase previous to antiferromagnetic ordering, being consistent with the course of magnetic fraction derived from measurements.
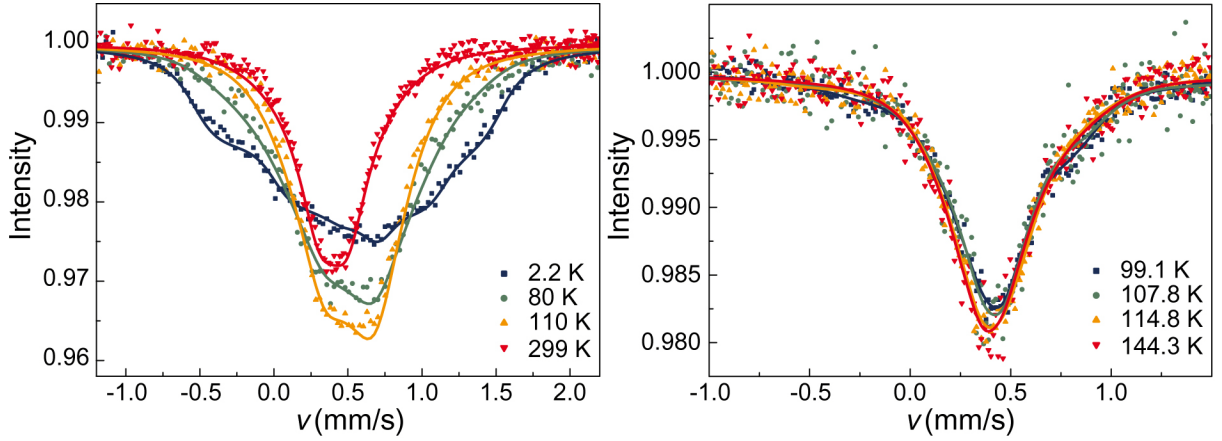
Figure 1. Mössbauer spectra illustrating spectrum change over full range (left) and paramagnetic range (right).
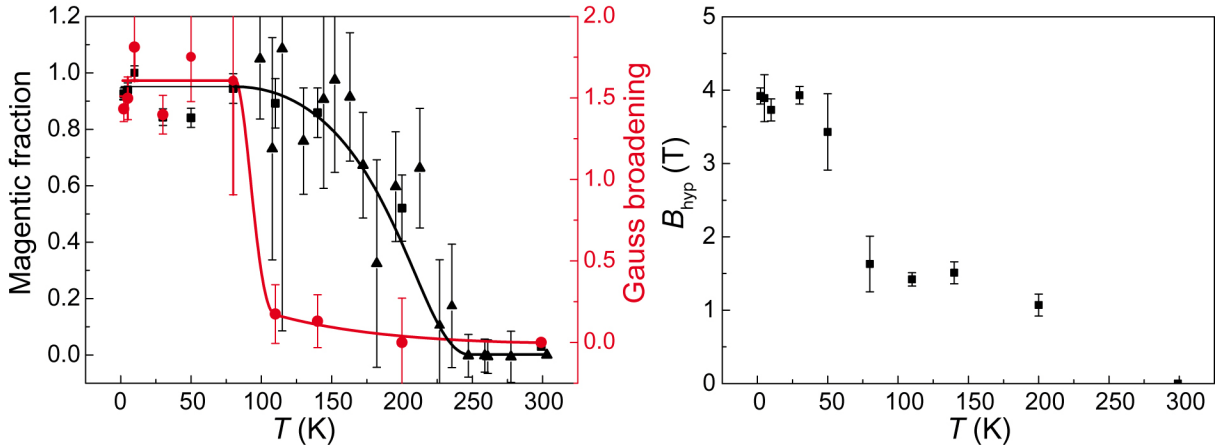
Figure 2. Magnetic fraction and Gauss broadening (left) as well as hyperfine field (right) derived from Mössbauer measurements. Black and red lines are guides to the eye. Magnetic fraction data was combined from full range (squares) and paramagnetic range (triangles) measurements.

Evidence for the existence of nematic fluctuations and ordering above T_N is already reported for several iron pnictide compounds.[19] The transition temperature to the nematic phase in (CaFeAs)$_{10}$Pt$_3$As$_8$ was determined to $T_{nem} = 245(10)$ K. Figure 2 shows the development of the magnetic fraction already before the formation of the antiferromagnetic state. Previously discussed μSR measurements on parent (CaFeAs)$_{10}$Pt$_3$As$_8$ gave no indication of magnetic fractions above ~140 K, but also revealed a gradual onset of magnetism just before T_N. This divergence of results from both measurements could be rationalized by the different time-scale of μSR (10 μs)[20] and Mössbauer (100 ns)[21], indicating fast nematic fluctuations between 140 and 245 K.

2.4.4 *Conclusion*

The magnetic phase transition found in stoichiometric (CaFeAs)$_{10}$Pt$_3$As$_8$ was confirmed by Mössbauer measurements.[1] The transition temperature was determined to $T_N = 111(4)$ K

with a hyperfine field of B_{hyp} of 3.9(1) T being smaller than reported for other iron arsenide parent compounds. Strong spectral broadening occurred below T_N revealing a rather sharp magnetic transition. However, minor broadening along with signal anisotropy was also conspicuous above T_N, giving strong indication for the presence of a nematic phase in $(CaFeAs)_{10}Pt_3As_8$ similar to the one found in $BaFe_2As_2$.[19, 22] This finding renders the 1038 parent compound an interesting system to study the necessity of magnetic fluctuations for the emergence of superconductivity.

2.4.5 *References*

[1]   T. Stürzer, G. M. Friederichs, H. Luetkens, A. Amato, H.-H. Klauss, D. Johrendt, *J. Phys.: Condens. Matter* **2013**, *25*, 122203.

[2]   K. Cho, M. A. Tanatar, H. Kim, W. E. Straszheim, N. Ni, R. J. Cava, R. Prozorov, *Phys. Rev. B* **2012**, *85*, 020504.

[3]   T. Zhou, G. Koutroulakis, J. Lodico, N. Ni, J. D. Thompson, R. J. Cava, S. E. Brown, *J. Phys.: Condens. Matter* **2013**, *25*, 122201.

[4]   M. Neupane, C. Liu, S.-Y. Xu, Y.-J. Wang, N. Ni, J. M. Allred, L. A. Wray, N. Alidoust, H. Lin, R. S. Markiewicz, A. Bansil, R. J. Cava, M. Z. Hasan, *Phys. Rev. B* **2012**, *85*, 094510.

[5]   H. Nakamura, M. Machida, *Physica C: Superconductivity* **2013**, *484*, 39.

[6]   X. P. Shen, S. D. Chen, Q. Q. Ge, Z. R. Ye, F. Chen, H. C. Xu, S. Y. Tan, X. H. Niu, Q. Fan, B. P. Xie, D. L. Feng, *Phys. Rev. B* **2013**, *88*, 115124.

[7]   S. Thirupathaiah, T. Stürzer, V. B. Zabolotnyy, D. Johrendt, B. Büchner, S. V. Borisenko, *Phys. Rev. B* **2013**, *88*, 140505.

[8]   T. Berlijn, *Phys. Rev. B* **2014**, *89*, 104511.

[9]   M. Sato, T. Kawamata, Y. Kobayashi, Y. Yasui, T. Iida, K. Suzuki, M. Itoh, T. Moyoshi, K. Motoya, R. Kajimoto, M. Nakamura, Y. Inamura, M. Arai, *J. Phys.: Conf. Ser.* **2012**, *400*, 022105.

[10]   K. Ikeuchi, M. Sato, R. Kajimoto, Y. Kobayashi, K. Suzuki, M. Itoh, P. Bourges, A. D. Christianson, H. Nakamura, M. Machida, *JPS Conf. Proc.* **2014**, *3*, 015043.

[11]   A. Sapkota, G. S. Tucker, M. Ramazanoglu, W. Tian, N. Ni, R. J. Cava, R. J. McQueeney, A. I. Goldman, A. Kreyssig, *Phys. Rev. B* **2014**, *90*, 100504.

[12]   M. Rotter, M. Tegel, D. Johrendt, I. Schellenberg, W. Hermes, R. Pöttgen, *Phys. Rev. B* **2008**, *78*, 020503.

[13]   M. Tegel, M. Rotter, V. Weiß, F. M. Schappacher, R. Pöttgen, D. Johrendt, *J. Phys.: Condens. Matter* **2008**, *20*, 452201.

[14]   M. Tegel, I. Schellenberg, R. Pöttgen, D. Johrendt, *Z. Naturforsch. B* **2008**, *63*, 1057.

[15]   S. Kitao, Y. Kobayashi, S. Higashitaniguchi, M. Saito, Y. Kamihara, M. Hirano, T. Mitsui, H. Hosono, M. Seto, *J. Phys. Soc. Jpn.* **2008**, *77*, 103706.

[16]   A. Błachowski, K. Ruebenbauer, J. Żukrowski, Z. Bukowski, *J. Alloys Compd.* **2014**, *582*, 167.

[17]   H.-H. Klauss, H. Luetkens, R. Klingeler, C. Hess, F. J. Litterst, M. Kraken, M. M. Korshunov, I. Eremin, S. L. Drechsler, R. Khasanov, A. Amato, J. Hamann-Borrero, N. Leps, A. Kondrat, G. Behr, J. Werner, B. Büchner, *Phys. Rev. Lett.* **2008**, *101*, 077005.

[18]   P. Bonville, F. Rullier-Albenque, D. Colson, A. Forget, *Europhys. Lett.* **2010**, *89*, 67008.

[19]   R. M. Fernandes, A. V. Chubukov, J. Schmalian, *Nat. Phys.* **2014**, *10*, 97.

[20]   S. J. Blundell, *Contemp. Phys.* **1999**, *40*, 175.

[21]   P. Gütlich, H. A. Goodwin, *Spin Crossover in Transition Metal Compounds II* **2004**, Springer Science & Business Media.

[22]   R. M. Fernandes, L. H. VanBebber, S. Bhattacharya, P. Chandra, V. Keppens, D. Mandrus, M. A. McGuire, B. C. Sales, A. S. Sefat, J. Schmalian, *Phys. Rev. Lett.* **2010**, *105*, 157003.

2.5 Superconductivity by Transition Metal doping in (CaFe$_{1-x}$M$_x$As)$_{10}$Pt$_3$As$_8$ (*M* = Co, Ni, Cu)

T. Stürzer, F. Kessler, D. Johrendt

published in: *Philos. Mag.* **2014**, *94*, 3632 – 3639.

Abstract

We report the successful substitution of cobalt, nickel, and copper for iron in the 1038 phase parent compound (CaFeAs)$_{10}$Pt$_3$As$_8$ yielding (CaFe$_{1-x}$Co$_x$As)$_{10}$Pt$_3$As$_8$, (CaFe$_{1-x}$Ni$_x$As)$_{10}$Pt$_3$As$_8$, and (CaFe$_{1-x}$Cu$_x$As)$_{10}$Pt$_3$As$_8$, respectively. Superconductivity is induced in Co and Ni doped compounds reaching critical temperatures up to 15 K, similar to known Pt substituted (CaFe$_{1-x}$Pt$_x$As)$_{10}$Pt$_3$As$_8$, whereas no superconductivity was detected in (CaFe$_{1-x}$Cu$_x$As)$_{10}$Pt$_3$As$_8$. The obtained $T_c(x)$ phase diagrams are very similar to those of other iron arsenide superconductors indicating rather universal behavior despite the more complex structures of the 1038-type compounds, where the physics is primarily determined by the FeAs layer.

2.5.1 *Introduction*

Superconductivity in iron arsenides emerges from antiferromagnetic metallic parent compounds in the course of suppressing the magnetic ordering by chemical doping or pressure,[1-6] resulting critical temperatures (T_c) up to 55 K in Sm(O$_{1-x}$F$_x$)FeAs.[7] Relationships between the magneto-structural phase transition and superconductivity in iron arsenides have intensively been studied.[5,8-14] In 2011, the new superconductors (CaFe$_{1-x}$Pt$_x$As)$_{10}$Pt$_3$As$_8$ (1038

phase, space group $P\bar{1}$) and polymorphic $(CaFeAs)_{10}Pt_4As_8$ (1048 phases, space groups $P4/n$, $P21/n$, $P\bar{1}$) with critical temperatures up to 35 K were discovered.[15-17] This new class recently expanded by analogous compounds with iridium (Ir1048)[18] and palladium (Pd1038)[19] instead of platinum. Due to the presence of the second metal pnictide layer Pt_zAs_8 ($z = 3, 4$) next to FeAs, as well as the low symmetry of these compounds (space group $P\bar{1}$), they were initially considered as rather peculiar representatives of the iron arsenide family. However, recent low-temperature X-ray structural data together with μSR spectra[20] as well as neutron diffraction[21] revealed a lattice distortion and magnetic phase transition at 120 K, proving that $(CaFeAs)_{10}Pt_3As_8$ is the parent compound of this branch of the iron arsenide family. Thereby, closely related superconductors like $(CaFe_{1-x}Pt_xAs)_{10}Pt_3As_8$ ($T_{c,max} = 14$ K), $(CaFeAs)_{10}Pt_4As_8$ ($T_{c,max} = 35$ K) and $(Ca_{1-x}RE_xFeAs)_{10}Pt_3As_8$ ($T_{c,max} = 35$ K) can be derived from this common parent by direct, indirect, and electronic doping, respectively.[22-24] Figure 1 depicts the structure of the 1038 parent compound as well as a section of the Pt_3As_8 layer. In this paper, we report the crystal structures and superconductivity of transition metal doped $(CaFe_{1-x}M_xAs)_{10}Pt_3As_8$ with $M = $ Co, Ni, and Cu with critical temperatures up to 15 K. Our results clearly establish that the 1038/1048 superconductors are more than an exotic exception, but another, even structurally more complex, branch of the iron arsenide family.
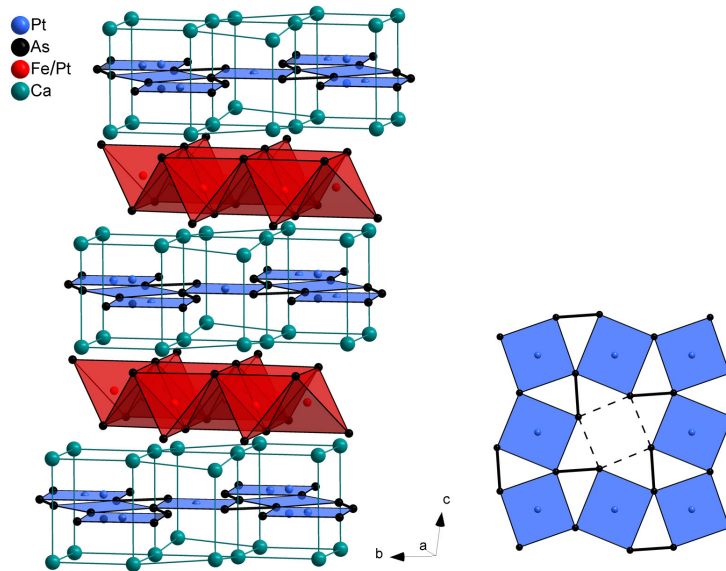
Figure 1. Crystal structure of the 1038 parent compound $(CaFeAs)_{10}Pt_3As_8$.

2.5.2 *Experimental Details*

Polycrystalline samples of Co, Ni, and Cu doped calcium platinum iron arsenides were synthesized from the elements as described in reference [15], and characterized by X-ray powder

diffraction using the Rietveld method with TOPAS[25]. Compositions were determined within errors of 10 % by X-ray spectroscopy (EDX). Superconducting properties were determined using an *ac*-susceptometer at 1333 Hz in the temperature range of 3.5 – 300 K at 3 Oe. Magnetic measurements were additionally performed on a QUANTUM DESIGN MPMS XL5 SQUID magnetometer which allowed for measurements with fields up to 50 kOe at temperatures between 1.8 and 300 K. Temperature dependent resistivity measurements between 3.5 and 300 K were carried out using a standard four-probe method.
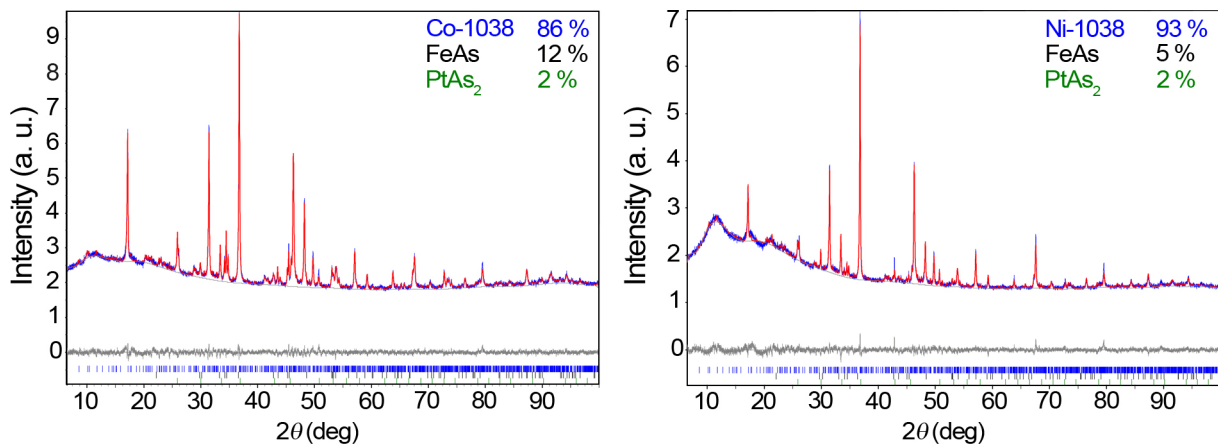
Figure 2. X-ray powder patterns (blue lines) with Rietveld fits (red lines) of (CaFe$_{1-x}$M$_x$As)$_{10}$Pt$_3$As$_8$ with M = Co (left) and Ni (right).
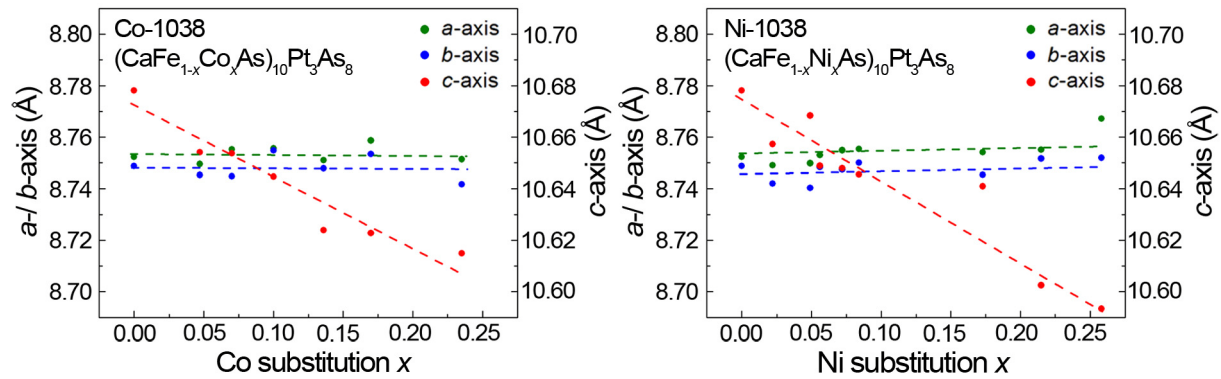
Figure 3. Lattice parameters of (CaFe$_{1-x}$M$_x$As)$_{10}$Pt$_3$As$_8$ with M = Co (left) and Ni (right) obtained from Rietveld fits.

2.5.3   Results and Discussion

Figure 2 shows X-ray powder patterns with Rietveld fits of (CaFe$_{1-x}$M$_x$As)$_{10}$Pt$_3$As$_8$ samples with M = Co, Ni and x = 0.1. The diffraction patterns are completely described with the 1038 phase structure model[15] and minor amounts of impurity phases FeAs and PtAs$_2$. The high sample quality implies smooth incorporation of cobalt, nickel, and copper into the 1038 structure. The amount of impurity phases increase at higher doping levels, which indicates

solubility limits of $x \approx 0.25$ for Co and Ni as well as $x \approx 0.12$ for Cu, respectively, in the 1038-type structure. Thus, the fully substituted compounds (CaCoAs)$_{10}$Pt$_3$As$_8$, (CaNiAs)$_{10}$Pt$_3$As$_8$, (CaCuAs)$_{10}$Pt$_3$As$_8$, and (CaFeAs)$_{10}$Ni$_3$As$_8$ were not accessible by solid-state synthesis, although the Pd analogue (CaFeAs)$_{10}$Pd$_3$As$_8$ was recently reported.[19] Figure 3 illustrates the dependency of the lattice parameters on Co- or Ni-substitution from X-ray powder data refinement, revealing similar behavior of both Co- and Ni-1038 to the 122-type compounds Ba(Fe$_{1-x}$Co$_x$)$_2$As$_2$[26] and Ba(Fe$_{1-x}$Ni$_x$)$_2$As$_2$.[11] The in-plane axes a and b as well as the unit cell angles (not shown) remain nearly constant within experimental accuracy, whereas c decreases by about 0.8 % in the range $0 \leq x \leq 0.25$, accompanied with shrinking of the cell volume by approximately 0.8 %. At this point it should be noted, that, even if small, the analogous effects of Co and Ni doping to the 1038 structure may be indicative for a similar $3d$ electron count localized at Co and Ni when doped to FeAs layers. An interesting aspect arises from the chemical similarity of platinum and nickel. Although the targeted position of Co when doped into the 1038 structure is the FeAs layer, the situation is more complicated in the case of Ni. In this system, Fe/Ni mixing is expected, but Ni substitution to the Pt sites is as well imaginable as Ni occupancy at the Pt vacancies in the Pt$_3\square$As$_8$ layer. However, modifications of the Pt$_3\square$As$_8$ layers by additional Ni incorporation were supposed to produce 1048 type impurity phases, or at least changes of the a, b lattice parameters. Susceptibility measurements would be a sensitive probe to detect even minimal traces of the 1048 phase due to its high T_c well above 30 K. However, none of these phenomena have been observed. Moreover, additional EDX measurements gave no indication for Pt/Ni mixing. All these results clearly indicate that no modifications of the Pt$_3$As$_8$ layers occur, tantamount with Co, Ni, or Cu doping taking place only in the FeAs layers.
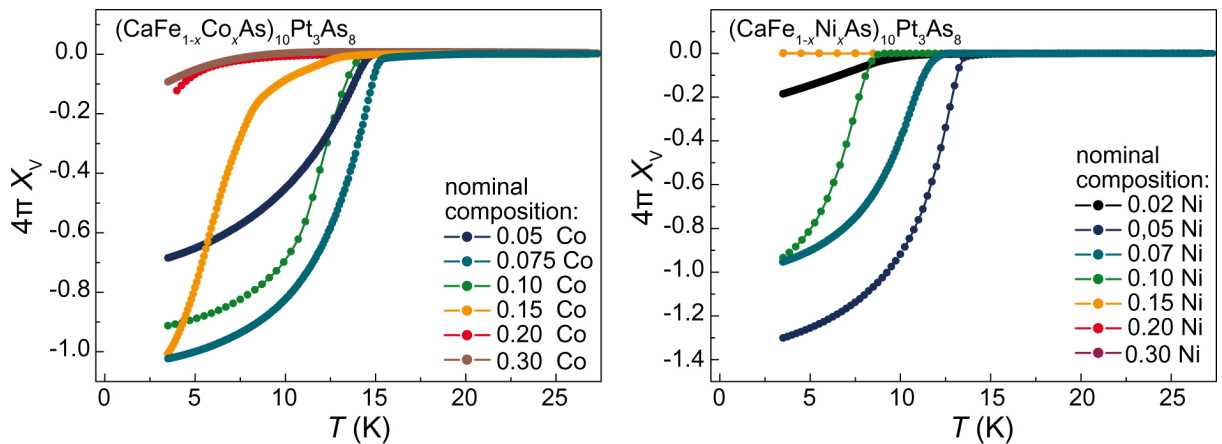
Figure 4. *Ac*-susceptibilities of (CaFe$_{1-x}$Co$_x$As)$_{10}$Pt$_3$As$_8$ (left) and (CaFe$_{1-x}$Ni$_x$As)$_{10}$Pt$_3$As$_8$ (right).

Figure 4 shows *ac*-susceptibility data of (CaFe$_{1-x}$M$_x$As)$_{10}$Pt$_3$As$_8$ (*M* = Co, Ni). Critical temperatures of Co-1038 reach 15.3 K at the optimal Co concentration *x* = 0.075, whereas Ni-1038 maximum T_c settles at 13.4 K for a doping level of *x* = 0.05. Superconducting volume fractions indicate bulk superconductivity. In contrast to this finding, no superconductivity was detected in (CaFe$_{1-x}$Cu$_x$As)$_{10}$Pt$_3$As$_8$, except of traces at the lowest doping level synthesized of *x* = 0.02. Figure 5 shows *dc*-electrical resistivity and low field *dc*-susceptibility data. The left panel (Figure 5) displays resistivity measurements performed with the maximum T_c samples (CaFe$_{0.925}$Co$_{0.075}$As)$_{10}$Pt$_3$As$_8$ and (CaFe$_{0.95}$Ni$_{0.05}$As)$_{10}$Pt$_3$As$_8$. A steep drop to zero resistance is observed for both samples which coincide with critical temperatures from susceptibility measurements, respectively. The absolute values of the specific resistivity are in the range of poor metals as typical for iron arsenides in the normal state. Remarkably, in our case, the normal state resistivity increases with decreasing temperature resembling a semiconductor like behavior. This temperature dependence of the specific resistivity is different from 1111- and 122-type iron arsenide superconductors, but was also found for the parent compound (CaFeAs)$_{10}$Pt$_3$As$_8$. Similar results have also been reported for (CaFe$_{1-x}$Pt$_x$As)$_{10}$Pt$_3$As$_8$.[27]
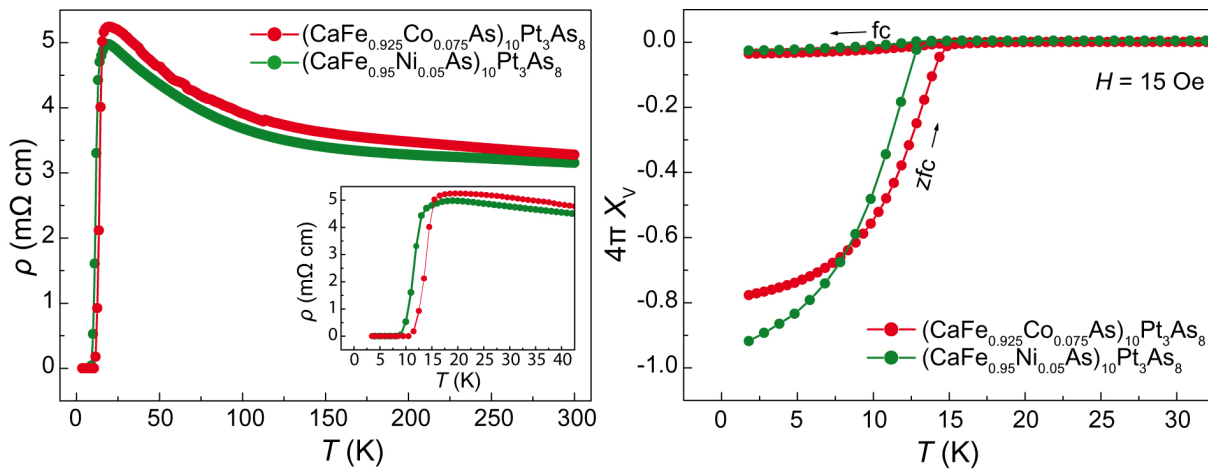
Figure 5. *Dc*-**resistivity (left) and low-field** *dc*-**susceptibilities (right) of (CaFe$_{1-x}$Co$_x$As)$_{10}$Pt$_3$As$_8$ and (CaFe$_{1-x}$Ni$_x$As)$_{10}$Pt$_3$As$_8$.**
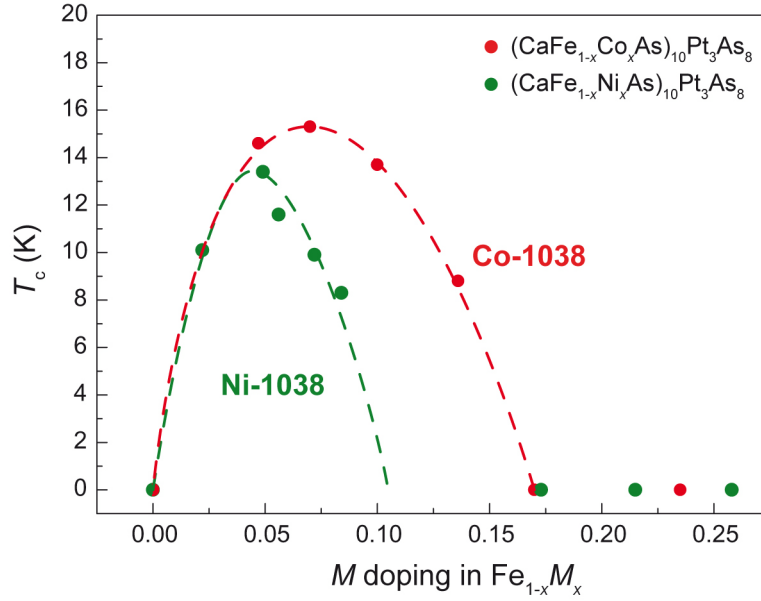
Figure 6. $T_c(x)$ **phase diagrams of (CaFe$_{1-x}$Co$_x$As)$_{10}$Pt$_3$As$_8$ and (CaFe$_{1-x}$Ni$_x$As)$_{10}$Pt$_3$As$_8$.**

The right panel of Figure 5 shows the low-field *dc*-susceptibility of Co- and Ni-1038 samples with the highest T_c. Almost 100 % shielding at low temperatures proves bulk superconductivity, while the *Meissner*-signal is rather small. Doping dependent critical temperatures for both Co- and Ni-1038 are compiled in Figure 6. Superconductivity is induced by small transition metal doping to the iron sites. (CaFe$_{1-x}$Co$_x$As)$_{10}$Pt$_3$As$_8$ reveals a dome like $T_c(x)$ dependency, reaching a maximum of 15.3 K for the optimal doping level $x = 0.075$. The critical temperature distinctly drops if x exceeds 0.075. However, full suppression of superconductivity upon high Co concentrations could not be achieved within the solubility limit of Co. Samples with a nominal composition of $x = 0.2$ and $x = 0.3$ show only traces of superconductivity which may come from inhomogeneously distributed cobalt. Therewith, the superconducting dome of Co-1038 is remarkably similar to the Co doped 122 compounds Ba(Fe$_{1-x}$Co$_x$)$_2$As$_2$[26,28]. The Ni-1038 compounds reveal narrower dependency of the critical temperatures from the substitution level, featuring a maximum T_c of 13.4 K at $x = 0.05$. This finding is in line with the additional electron of Ni with respect to Co, giving rise of an increased electron doping at same transition metal substitution[28]. T_c rapidly decreases at higher Ni concentrations until superconductivity is completely suppressed at 17 % Ni. Thus, (CaFe$_{1-x}$Ni$_x$As)$_{10}$Pt$_3$As$_8$ reveals very similar properties than its homologue (CaFe$_{1-x}$Pt$_x$As)$_{10}$Pt$_3$As$_8$. In this context, Ni-1038 is supposed to be a more suitable system to study its properties in the overdoped regime due to the higher solubility of Ni.

2.5.4 Conclusion

In conclusion, we have demonstrated bulk superconductivity in the 1038 compounds (CaFe$_{1-x}$M$_x$As)$_{10}$Pt$_3$As$_8$ doped by M = Co or Ni, with critical temperatures up to 15.3 K in Co-1038 (x = 0.075) and 13.4 K in Ni-1038 (x = 0.05), respectively. Superconducting properties in both compounds were evidenced by *ac*- and *dc*-susceptibility as well as *dc*-resistivity data. Moreover, no superconductivity was evident in Cu doped samples (CaFe$_{1-x}$Cu$_x$As)$_{10}$Pt$_3$As$_8$. The dependency of T_c of the substitution level x reveals similar behavior than in known directly doped 122-type iron arsenides Ba(Fe$_{1-x}$M$_x$)$_2$As$_2$ with M = Co, Ni, Cu, whereas the comparatively narrow superconducting dome of Ni-1038 is indicative for an increased electron doping contribution of Ni with respect to Co-1038. Our results clearly show the close resemblance of calcium platinum iron arsenides to other iron arsenide compounds, giving evidence that established doping methods to induce superconductivity are abundantly applicable also to more complex systems like the 1038 and 1048 materials.

2.5.5 References

[1]   Y. Kamihara, T. Watanabe, M. Hirano, H. Hosono, *J. Am. Chem. Soc.* **2008**, *130*, 3296.

[2]   M. Rotter, M. Tegel, D. Johrendt, *Phys. Rev. Lett.* **2008**, *101*, 107006.

[3]   P. L. Alireza, Y. T. C. Ko, J. Gillett, C. M. Petrone, J. M. Cole, G. G. Lonzarich, S. E. Sebastian, *J. Phys.: Condens. Matter* **2009**, *21*, 012208.

[4]   D. C. Johnston, *Adv. Phys.* **2009**, *59*, 803.

[5]   D. Johrendt, *J. Mater. Chem.* **2009**, *21*, 13726.

[6]   G. R. Stewart, *Rev. Mod. Phys.* **2011**, *83*, 1589.

[7]   Z. A. Ren, W. Lu, J. Yang, W. Yi, X. L. Shen, Z. C. Li, G. C. Che, X. L. Dong, L. L. Sun, F. Zhou, Z. X. Zhao, *Chin. Phys. Lett.* **2008**, *25*, 2215.

[8]   J. Paglione, R. L. Greene, *Nat. Phys.* **2010**, *6*, 645.

[9]   R. M. Fernandes, A. V. Chubukov J. Schmalian, *Nat. Phys.* **2014**, *10*, 97.

[10] M. A. McGuire, A. D. Christianson, A. S. Sefat, B. C. Sales, M. D. Lumsden, R. Y. Jin, E. A. Payzant, D. Mandrus, Y. B. Luan, V. Keppens, V. Varadarajan, J. W. Brill, R. P. Hermann, M. T. Sougrati, F. Grandjean, G. J. Long, *Phys. Rev. B* **2008**, *78*, 094517.

[11] L. J. Li, Y. K. Luo, Q. B. Wang, H. Chen, Z. Ren, Q. Tao, Y. K. Li, X. Lin, M. He, Z. W. Zhu, G. H. Cao, Z. A. Xu, *New J. Phys.* **2009**, *11*, 025008.

[12] C. de la Cruz, Q. Huang, J. W. Lynn, J. Y. Li, W. Ratcliff, J. L. Zarestky, H. A. Mook, G. F. Chen, J. L. Luo, N. L. Wang, P. C. Dai, *Nature* **2008**, *453*, 899.

[13] J. Zhao, Q. Huang, C. de la Cruz, S. L. Li, J. W. Lynn, Y. Chen, M. A. Green, G. F. Chen, G. Li, Z. Li, J. L. Luo, N. L. Wang, P. C. Dai, *Nat. Mater.* **2008**, *7*, 953.

[14] M. Rotter, M. Tegel, I. Schellenberg, W. Hermes, R. Pöttgen, D. Johrendt, *Phys. Rev. B* **2008**, *78*, 020503.

[15] C. Löhnert, T. Stürzer, M. Tegel, R. Frankovsky, G. Friederichs, D. Johrendt, *Angew. Chem. Int. Ed.* **2011**, *50*, 9195.

[16] N. Ni, J. M. Allred, B. C. Chan, R. J. Cava, *Proc. Nat. Acad. Sci. U.S.A.* **2011**, *108*, E1019.

[17] S. Kakiya, K. Kudo, Y. Nishikubo, K. Oku, E. Nishibori, H. Sawa, T. Yamamoto, T. Nozaka, M. Nohara, *J. Phys. Soc. Jpn.* **2011,** *80*, 093704.

[18] K. Kudo, D. Mitsuoka, M. Takasuga, Y. Sugiyama, K. Sugawara, N. Katayama, H. Sawa, H. S. Kubo, K. Takamori, M. Ichioka, T. Fujii, T. Mizokawa, M. Nohara, *Sci. Rep.* **2013**, *3*, 3101.

[19] C. Hieke, J. Lippmann, T. Stürzer, G. Friederichs, F. Nitsche, F. Winter, R. Pöttgen, D. Johrendt, *Philos. Mag.* **2013**, *93*, 3680.

[20] T. Stürzer, G. M. Friederichs, H. Luetkens, A. Amato, H.-H. Klauss, D. Johrendt, *J. Phys.: Condens. Matter* **2013**, *25*, 122203.

[21] A. Sapkota, G. S. Tucker, M. Ramazanoglu, N. N. W. Tian, R. J. Cava, R. J. McQueeney, A. I. Goldman, A. Kreyssig, *Phys. Rev. B* **2014**, *90*, 100504.

[22] T. Stürzer, G. Derondeau, D. Johrendt, *Phys. Rev. B* **2012**, *86*, 060516(R).

[23] T. Stürzer, G. Derondeau, D. Johrendt, *Solid State Commun.* **2015**, *201*, 36-39.

[24] N. Ni, W. E. Straszheim, D. J. Williams, M. A. Tanatar, R. Prozorov, E. D. Bauer, F. Ronning, J. D. Thompson, R. J. Cava, *Phys. Rev. B* **2013**, *87*, 060507.

[25] A. Coelho, *TOPAS-Academic*, Version 4.1, Coelho Software, Brisbane, Australia, **2007**.

[26] A. S. Sefat, R. Jin, M. A. McGuire, B. C. Sales, D. J. Singh, D. Mandrus, *Phys. Rev. Lett.* **2008**, *101*, 117004.

[27] Z. J. Xiang, X. G. Luo, J. J. Ying, X. F. Wang, Y. J. Yan, A. F. Wang, P. Cheng, G. J. Ye, X. H. Chen, *Phys. Rev. B* **2012**, *85*, 224527.

[28] P. C. Canfield, S. L. Bud'ko, *Annu. Rev. Cond. Mat. Phys.* **2010**, *1*, 27.

2.6 Role of different negatively charged Layers in $(CaFeAs)_{10}Pt_4As_8$ and Superconductivity at 30 K in Electron doped $(Ca_{0.8}La_{0.2}FeAs)_{10}Pt_3As_8$

T. Stürzer, G. Derondeau, D. Johrendt
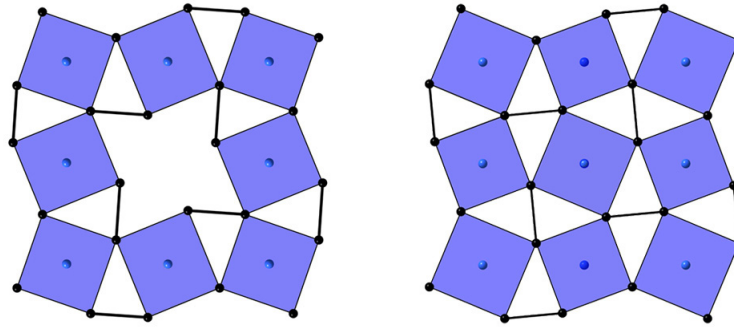
Abstract

The recently discovered compounds $(CaFe_{1-x}Pt_xAs)_{10}Pt_{3+y}As_8$ exhibit superconductivity up to 38 K, and contain iron arsenide (FeAs) and platinum arsenide ($Pt_{3+y}As_8$) layers separated by layers of calcium atoms. We show that $T_c > 15$ K only emerges by electron doping of pure FeAs layers, and not by platinum substitution in $(Fe_{1-x}Pt_x)As$ layers, as anticipated so far. Indeed, two different negatively charged layers $[(FeAs)_{10}]^{n-}$ and $(Pt_{3+y}As_8)^{m-}$ compete for the electrons provided by the Ca^{2+} ions. The charge between the layers is formally balanced to $(FeAs)^{1-}$ in the parent compound $(CaFeAs)_{10}Pt_3As_8$, and superconductivity emerges by electron doping, if this balance is shifted. The latter is achieved either by adding electrons as in $(Ca_{0.8}La_{0.2}FeAs)_{10}Pt_3As_8$ ($T_c = 30$ K), or intrinsically in $(CaFeAs)_{10}Pt_4As_8$ ($T_c \approx 38$ K), where the Pt_4As_8 layer itself provides extra electrons.

2.6.1 Introduction

The chemical complexity of iron arsenide superconductors has been increased by the recent discovery of the compounds $(CaFe_{1-x}Pt_xAs)_{10}Pt_{3+y}As_8$.[1–3] Their crystal structures contain alternating layers of iron arsenide and platinum arsenide, each separated by calcium atoms (Fig. 1). Platinum in the $Pt_{3+y}As_8$ layers is nearly planar fourfold coordinated by arsenic that forms As_2^{4-} Zintl ions. Two branches of the structural motif have been found, depending on

the composition of the platinum arsenide layers. The compound referred to as the 1038 phase contains Pt$_3$As$_8$ layers [Fig. 1(a)], while in the 1048 phase one more platinum atom is located in Pt$_4$As$_8$ layers [Fig. 1(b)]. The 1038 compound is triclinic, while we have identified three polymorphs of the 1048 phase with tetragonal (α-1048, $P4/n$), triclinic (β-1048, $P\overline{1}$), or monoclinic (γ-1048, $P2_1/n$) space group symmetries by single crystal X-ray diffraction. High critical temperatures (T_c) up to 38 K have been assigned to the 1048 variants, while T_c of the 1038 phase is below 15 K so far. Recent reports suggested that the critical temperatures are solely controlled by substitution of platinum for iron in the FeAs layers, as known from Sr(Fe$_{1-x}$Pt$_x$)$_2$As$_2$.[4] *Nohara* et al.[5] even proposed that "heavy Pt doping" is required to achieve high T_c in (CaFe$_{1-x}$Pt$_x$As)$_{10}$Pt$_{3+y}$As$_8$. Also *Ni* et al.[2] have suggested that platinum substitution controls T_c, but the higher values of the 1048 phases were associated with stronger interlayer coupling by Pt–As bonds between the Pt$_4$As$_8$ and FeAs layers. However, our band structure calculations have indicated that the Pt$_{3+y}$As$_8$ layers hardly contribute at the Fermi energy,[1] which has been supported by recent angle resolved photoemission experiments showing that the Fermi surface topology is similar to those of known FeAs materials.[6] Thereby it is extremely unlikely that critical temperatures as high as 38 K occur in Pt doped materials, while hitherto known transition metal doped FeAs superconductors remain well below 25 K. In this Rapid Communication we show that high critical temperatures in the iron platinum arsenides are not achieved by platinum substitution inside the iron layers, but by charge doping of FeAs layers. The $T_c(x)$ phase diagrams of the 1038 and 1048 compounds are quite different and reveal that platinum substitution induces superconductivity at low temperatures in the 1038 materials, but is detrimental to T_c in the 1048 compounds, where the FeAs layers are doped by electrons due to a shift of the charge balance between [(FeAs)$_{10}$]$^{n-}$ and (Pt$_{3+y}$As$_8$)$^{m-}$ to $n > m$. This interpretation is supported by the observation of superconductivity at 30 K in the electron doped 1038 compound (Ca$_{0.8}$La$_{0.2}$FeAs)$_{10}$Pt$_3$As$_8$.
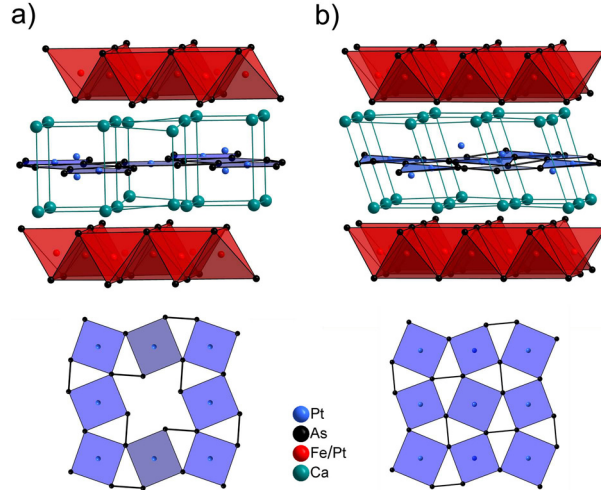
Figure 1. Crystal structures of (a) (CaFeAs)$_{10}$Pt$_3$As$_8$ (1038) and (b) (CaFeAs)$_{10}$Pt$_4$As$_8$ (1048).

2.6.2   *Experimental Details*

Polycrystalline samples of the platinum iron arsenides were synthesized by solid-state methods from the elements as described in Ref. [1], and characterized by X-ray powder diffraction (PXRD) using the Rietveld method with TOPAS.[7] Compositions were determined within errors of ±5 % by refining the occupation parameters and within ± 10 % by energy dispersive X-ray spectroscopy (EDX). *Ac* susceptibility measurements (3 Oe, 1333 Hz) were used to detect superconductivity and the critical temperatures. Full-potential density function theory (DFT) calculations using the WIEN2K package[8,9] along with the quantum theory of atoms in molecules (QTAIM) method[10] were used to calculate and analyze the electron density distribution of the tetragonal 1048 compound.

2.6.3   *Results and Discussion*

Figure 2 shows the critical temperatures of all samples plotted against the amount of platinum substitution at the iron site (*x*). Compounds with the 1048 structure are well separated from those with 1038 structure. The 1038 compounds are not superconducting below $x \approx 0.03$, and then T_c increases rapidly up to 15 K. This is very similar to known phase diagrams of other FeAs materials, where superconductivity emerges after suppression of a spin density wave (SDW) state of a parent compound by transition metal substitution at the iron site.[11]
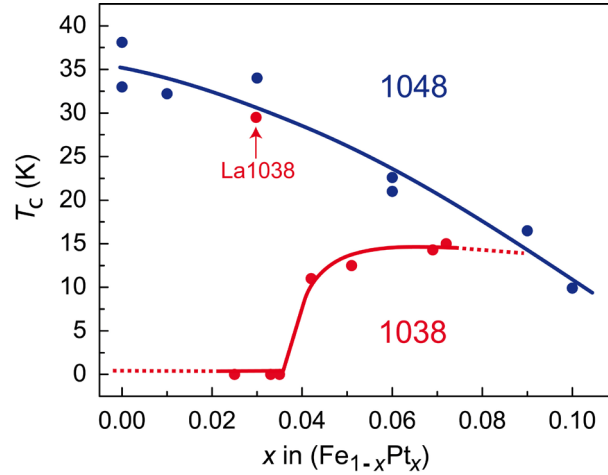
Figure 2. Critical temperatures of samples with 1048 structure (blue) and 1038 structure (red). Lines are guides to the eye.

Interestingly, $Ca(Fe_{1-x}Pt_x)_2As_2$ is reportedly not superconducting up to $x = 0.08$, which appears to be the solubility limit in $CaFe_2As_2$.[12] Our 1038 phase diagram agrees with those recently reported for 1038-type single crystals,[13] where low temperature structural transitions have been suggested at $x < 0.025$. Thus far, the 1038 compounds are in line with other FeAs compounds that become superconducting when doped with transition metals at the iron site, albeit at low T_c. We therefore refer to $(CaFeAs)_{10}Pt_3As_8$ as the parent compound. In contrast to this, the critical temperatures of the 1048 compounds are the highest without platinum at the iron site ($x = 0$), and decrease with the substitution level as shown in Figure 2. This reverse behavior of $T_c(x)$ clearly indicates a different electronic situation of the 1048 compound. Taking into account that $T_c > 25$ K has hitherto only been induced by charge doping of the FeAs layers as in $LnFeAs(O_{1-x}F_x)$[14] or $(Ba_{1-x}K_x)Fe_2As_2$,[15] but not by transition metal substitution at the iron site as in $Ba(Fe_{1-x}Co_x)_2As_2$,[16] we infer that charge doping of the FeAs layer would naturally explain the higher T_c of the 1048 compound. Also the decrease of T_c due to overdoping by additional platinum substitution at the iron site would be understandable. We point out that the platinum iron arsenides are the first compounds in the family of iron-based superconductors with two different negatively charged layers, because both the iron and platinum arsenide layers are negatively polarized. As suggested in previous studies,[1,2] the 1038 compound is perfectly charge balanced according to $(Ca^{2+})_{10}[(FeAs)_{10}]^{10-}(Pt_3As_8)^{10-}$, while in the 1048 compound the additional Pt^{2+} leads to $(Pt_4As_8)^{8-}$, and the question arises as to where are these electrons. Photoemission experiments[6] and DFT calculations[1] consistently suggest that the platinum arsenide layer hardly contributes to the Fermi surface, which is predominantly formed by states of the FeAs layer. Therefore the only choice of the excess electrons from the Pt_4As_8 layer is to occupy iron $3d$

states according to formally $(Ca_{10})^{20+}[(FeAs)_{10}]^{12-}(Pt_4As_8)^{8-}$. In other words, each FeAs in the 1048 compound is doped by 0.2 electrons, which is similar to the electron doped 1111 super-conductors $LnFeAs(O_{1-x}F_x)$, where the highest T_c likewise appears around $x = 0.2$. The suggested charge distribution is supported by the QTAIM analysis of the charge density in the tetragonal 1048 compound. The QTAIM charge of each atom is calculated by integration of the electron density bounded by the zero flux surface.[10] Summing up the charges of the layer atoms and normalizing to Ca^{2+} gives $(Ca_{10})^{20+}[(FeAs)_{10}]^{11.5-}(Pt_4As_8)^{8.5-}$, which is near to the above suggested charge distribution. We note that the atomic charge is not an observable quantity. Combining these results, the fundamentally different behavior of the critical temperatures in the 1038 and 1048 compounds presented in Fig. 2 becomes plausible. Super-conductivity in the 1038 phase is induced by platinum substitution of the FeAs layers, but thereby confined to lower T_c. On the other hand, there is every indication that intrinsic electron doping of pure FeAs layers is the reason for the higher T_c of the 1048 compounds. Finally, additional platinum substitution of the FeAs layers of the 1048 phase is overdoping, which decreases the critical temperature again.
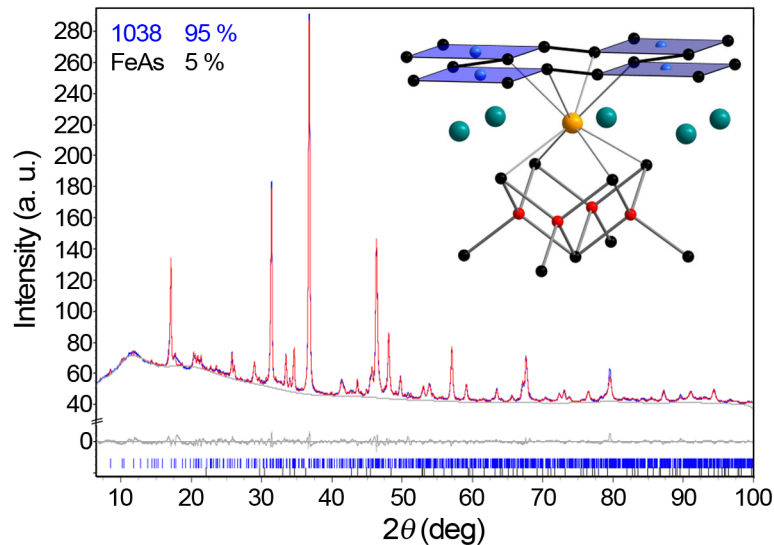
Figure 3. X-ray diffraction pattern and Rietveld fit of $(Ca_{0.8}La_{0.2}Fe_{1-x}Pt_xAs)_{10}Pt_3As_8$ (La1038; $P\bar{1}$, $a =$ 8.7493(3) Å, $b =$ 8.7533(2) Å, $c =$ 10.7139(3) Å, $\alpha =$ 75.877(3)°, $\beta =$ 85.295(3)°, $\gamma =$ 90.031(3)°, $R_{wp} =$ 0.016). Inset: Crystal structure of La1038 showing a preference for the lanthanum atom to the eightfold coordinated position.

If our idea of electron doped FeAs layers in the 1048 compound is correct, it should be possible to induce high T_c values above 15 K also in the 1038 compound by electron doping instead of platinum substitution in the FeAs layers. Indeed, we were able to synthesize the electron doped 1038 compound $(Ca_{0.8}La_{0.2}Fe_{1-x}Pt_xAs)_{10}Pt_3As_8$ with $x \approx 0.03$ (La1038). The small platinum substitution alone is not sufficient to induce superconductivity according to

the phase diagram (Fig. 2). The 1038 structure with La substitution at the Ca sites was confirmed by Rietveld refinement as shown in Figure 3. A special feature of the La1038 crystal structure is emphasized in the inset of Figure 3. The calcium atom just below and above the platinum vacancy in the $Pt_3\square As_8$ layer is eightfold coordinated by arsenic atoms, while all other calcium atoms are coordinated by seven arsenic atoms only. Lanthanum has a distinct preference for this site, where the higher charge of La^{3+} increases the lattice energy and stabilizes the structure. Figure 4 shows *ac*-susceptibility data of the 1038 compounds. No superconductivity emerges at low platinum substitution ($x < 0.035$), and T_c remains below 15 K at $x = 0.051$. In stark contrast to this, superconductivity is observed at 30 K in the La1038 compound, where the platinum substitution ($x = 0.03$) is much too small to induce superconductivity at all. Note also that the T_c of La1038 perfectly fits to the values expected for the 1048 compound with the same x in the phase diagram (Figure 2). This illustrates that only charge doping of the FeAs layer is crucial, regardless of whether the structure is of the 1038 or 1048 type. Given that platinum substitution reduces T_c in the 1048 compounds, we expect even higher values around 40 K for La1038 without platinum at the iron site, but we were not yet able to prepare this. However, the finding of superconductivity at 30 K in La1038 is a convincing proof that higher T_c (>15 K) in the 1038 materials emerge if the iron arsenide layers are free of platinum but charge doped.
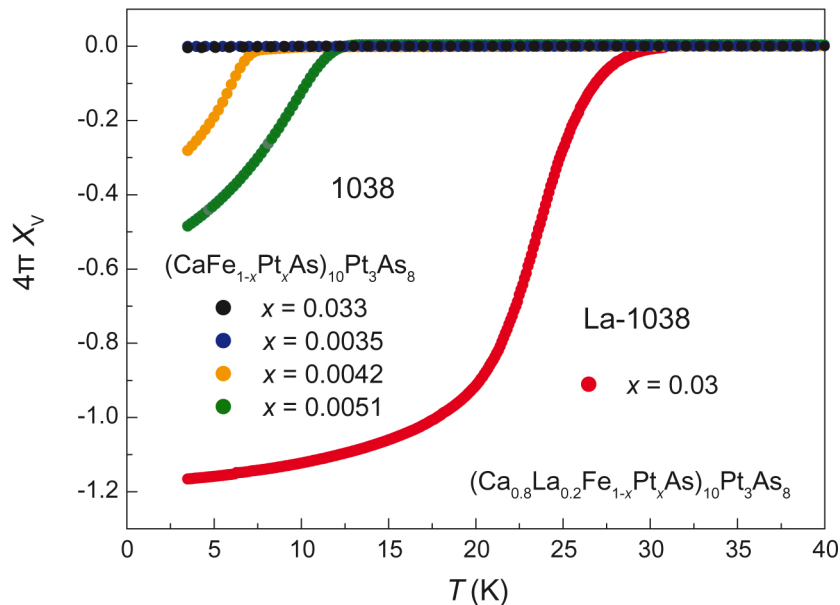
Figure 4. *Ac*-susceptibility measurements of 1038 compounds with different Pt substitutions and of La1038 with small Pt substitution that is not sufficient to induce superconductivity.

We have shown that three different doping scenarios of the 1038 parent compound are feasible. Two of them dope electrons to the FeAs layer and induce high critical temperatures

of 30 – 38 K. The third is platinum substitution of the FeAs layer, which also generates super-conductivity, albeit below 15 K. The three doping scenarios are compiled in the following scheme (Figure 5). Note the identical charge states of the FeAs layers in the 1048 and La1038 compounds, which likewise exhibit the highest critical temperatures:

$$(Ca_{0.8}^{2+}La_{0.2}^{3+})_{10}[(FeAs)_{10}]^{12-}(Pt_3As_8)^{10-}$$

La/Ca substitution

$$Ca_{10}^{2+}[(FeAs)_{10}]^{10-}(Pt_3As_8)^{10-}$$

Pt/Fe substitution

fill Pt into Pt$_3\square$As$_8$

$$Ca_{10}(Fe_{1-x}Pt_xAs)_{10}(Pt_3As_8)$$

$$Ca_{10}^{2+}[(FeAs)_{10}]^{12-}(Pt_4As_8)^{8-}$$
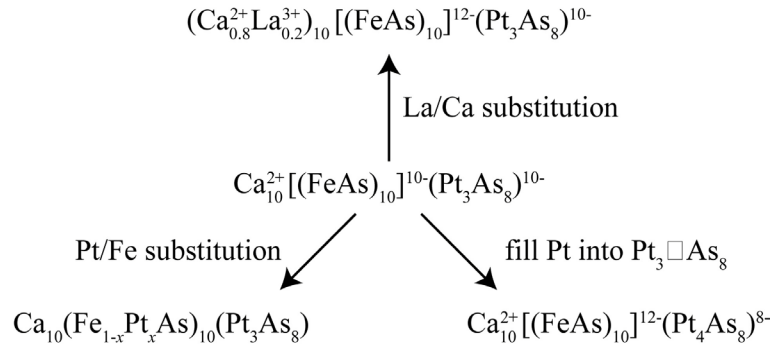
Figure 5. Schematic illustration of three doping scenarios based on 1038 parent compound.

2.6.4 *Conclusion*

In conclusion, our results emphasize the extraordinary role of the separating layers in the iron platinum arsenide superconductors with a second negatively charged layer $(Pt_3As_8)^{m-}$ beyond the known $[(FeAs)_{10}]^{n-}$. These layers compete for the electrons provided by the Ca^{2+} ions. The electronic situation of the FeAs layers in the 1038 compound is almost identical to the simpler iron arsenide superconductors, thus the Pt$_3$As$_8$ layer with its own particular structure attracts just the proper amount of electrons to establish the situation $n = m = 10$. This charge balance between the layers is delicate, and can be manipulated in various ways, but regardless the FeAs layer is much more susceptible to additional electrons, because the states close to the Fermi level are predominantly from FeAs. Thus extra electrons donated from La^{3+} ions in La1038 clearly move to the FeAs layer and cause electron doping. On the other hand, also the excess charge that intrinsically occurs in (CaFeAs)$_{10}$Pt$_4$As$_8$ shifts the charge balance to $n > m$ and transfers electrons to the FeAs layer, which induces high critical temperatures. Based on our results, we can satisfactory explain the at first sight puzzling behavior of the critical temperatures in these superconductors. These materials open perspectives for future studies, especially with respect to the detailed role and possible manipulations of the charge balance between the two negatively charged layers.

2.6.5   *References*

[1]   C. Löhnert, T. Stürzer, M. Tegel, R. Frankovsky, G. Friederichs, D. Johrendt, *Angew. Chem. Int. Ed.* **2011**, *50*, 9195.

[2]   N. Ni, J. M. Allred, B. C. Chan, R. J. Cava, *Proc. Natl. Acad. Sci. USA* **2011**, *108*, E1019.

[3]   S. Kakiya, K. Kudo, Y. Nishikubo, K. Oku, E. Nishibori, H. Sawa, T. Yamamoto, T. Nozaka, M. Nohara, *J. Phys. Soc. Jpn.* **2011**, *80*, 093704.

[4]   Y. Nishikubo, S. Kakiya, M. Danura, K. Kudo, M. Nohara, *J. Phys. Soc. Jpn.* **2010**, *79*, 095002.

[5]   M. Nohara, S. Kakiya, K. Kudo, Y. Oshiro, S. Araki, T. C. Kobayashi, K. Oku, E. Nishibori, H. Sawa, *Solid State Commun.* **2012**, *152*, 635.

[6]   M. Neupane, C. Liu, S.-Y. Xu, Y. J. Wang, N. Ni, J. M. Allred, L. Wray, N. Alidoust, H. Lin, R. Markiewicz, A. Bansil, R. J. Cava, M. Z. Hasan, *Phys. Rev. B* **2012**, *85*, 094510.

[7]   A. Coelho, *TOPAS-Academic*, Version 4.1, Coelho Software, Brisbane, Australia, **2007**.

[8]   P. Blaha, K. Schwarz, G. K. H. Madsen, D. Kvasnicka, J. Luitz, "WIEN2K-augmented plane wave+local orbitals program for calculating crystal properties," **2001**.

[9]   K. Schwarz, P. Blaha, *Comput. Mater. Sci.* **2003**, *28*, 259.

[10]   R. F. W. Bader, *Atoms in Molecules-A Quantum Theory*, Oxford University Press, London, **1990**.

[11]   D. Johrendt, *J. Mater. Chem.* **2011**, *21*, 13726.

[12]   K. Kudo, M. Kobayashi, S. Kakiya, M. Danura, M. Nohara, *J. Phys. Soc. Jpn.* **2012**, *81*, 035002.

[13]   K. Cho, M. A. Tanatar, H. Kim, W. E. Straszheim, N. Ni, R. J. Cava, R. Prozorov, *Phys. Rev. B* **2012**, *85*, 020504.

[14]   Z.-A. Ren, W. Lu, J. Yang, W. Yi, X.-L. Shen, Z.-C. Li, G.-C. Che, X.-L. Dong, L.-L. Sun, F. Zhou, Z.-X. Zhao, *Chin. Phys. Lett.* **2008**, *25*, 2215.

[15]   M. Rotter, M. Tegel, D. Johrendt, *Phys. Rev. Lett.* **2008**, *101*, 107006.

[16]   A. S. Sefat, R. Jin, M. A. McGuire, B. C. Sales, D. J. Singh, D. Mandrus, *Phys. Rev. Lett.* **2008**, *101*, 117004.

2.7 Superconductivity by Rare Earth doping in the 1038-type Compounds $(Ca_{1-y}RE_yFeAs)_{10}Pt_3As_8$ with RE = Y, La – Nd, Sm – Lu

T. Stürzer, G. Derondeau, E. Bertschler, D. Johrendt

Abstract

We report superconductivity in polycrystalline samples of the 1038-type compounds $(Ca_{1-y}RE_yFeAs)_{10}Pt_3As_8$ up to $T_c = 35$ K with RE = Y, La – Nd, Sm, Gd – Lu. The critical temperatures are nearly independent of the trivalent rare earth element used, yielding a common $T_c(y_{RE})$ phase diagram for electron doping in all these systems. The absence of super-conductivity in Eu^{2+} doped samples, as well as the close resemblance of $(Ca_{1-y}RE_yFeAs)_{10}Pt_3As_8$ to the 1048 compound substantiate that the electron doping scenario in the RE-1038 and 1048 phases is analogous to other iron-based superconductors with simpler crystal structures.

2.7.1 *Introduction*

Ever since the discovery of superconductivity in iron pnictides,[1] electronic doping is known to be an effective method to suppress the antiferromagnetic ground state of these compounds and induce high T_c superconductivity.[2–4] This was confirmed for many iron arsenides, examples are $La(O_{1-x}F_x)FeAs$,[1,5] $Ba(Fe_{1-x}Co_x)_2As_2$,[6] or $Sr_{1-x}La_xFe_2As_2$[7]. Recently the family of iron arsenide superconductors was enriched by the compounds $(CaFeAs)_{10}Pt_3As_8$ (1038, space group $P\bar{1}$) and polytypic $(CaFeAs)_{10}Pt_4As_8$ (1048, space groups $P\bar{1}$, $P2_1/n$, $P4/n$) which

have raised the chemical complexity.[8–10] This new class recently expanded by analogous compounds with iridium (Ir1048)[11] and palladium (Pd1038)[12] instead of platinum. The crystal structures of 1038 and 1048 compounds are closely related, and can be rationalized as alternating stacking of iron arsenide and platinum arsenide layers separated by calcium ions as depicted in Figure 1. Platinum in the Pt_3As_8 or Pt_4As_8 layer, respectively, is nearly planar fourfold coordinated by arsenic, forming a twisted edge-sharing $PtAs_4$ tile-pattern that contains As_2^{4-} Zintl anions.[13] The 1038 structure reveals one systematic Pt vacancy according to Pt_3As_8 (Figure 1) which is filled in the 1048 structure yielding Pt_4As_8 layers.

High critical temperatures up to 35 K were assigned to the 1048 compound, while Pt doping of the FeAs layers in the 1038 phase induces superconductivity with critical temperatures below 15 K. Although superconductivity induced by Pt doping is known from other iron arsenides, the very different critical temperatures of the 1038 and 1048 phases were matter of discussion. Based on DFT calculations we suggested intrinsic electron doping of the 1048 phase[8] caused by the electrons coming from the additional Pt^{2+} according to $[(Ca^{2+}Fe^{+1.8}As^{3-})_{10}]^{8+}[(Pt^{2+})_4(As^{2-})_8]^{8-}$ ($+0.2e^-$/Fe). In contrast, 1038 is a valence compound according to $[(Ca^{+2}Fe^{+2}As^{3-})_{10}]^{10+}[(Pt^{2+})_3(As^{2-})_8]^{10-}$ and not superconducting. We have found that electron doping of the 1038 phase is possible by lanthanum doping of the calcium site in $(Ca_{0.8}La_{0.2}FeAs)_{10}Pt_3As_8$ with critical temperatures above 30 K.[14] The phase diagram of La doped 1038 compounds is similar to those of the known iron arsenides.[15] Also the typical structural distortion of the 1038 parent compound $(CaFeAs)_{10}Pt_3As_8$ accompanied with magnetic ordering has recently been found.[16, 17] These results give clear evidence that electron doping of the FeAs layers in the 1038/1048 compounds can be realized either from the calcium layer or from the Pt_4As_8 layer. Hence, in spite of their structural complexity and low symmetry, these new superconductors turned out to be typical representatives of the iron arsenide family, with the 1038 phase as the magnetic non-superconducting parent compound.[16]
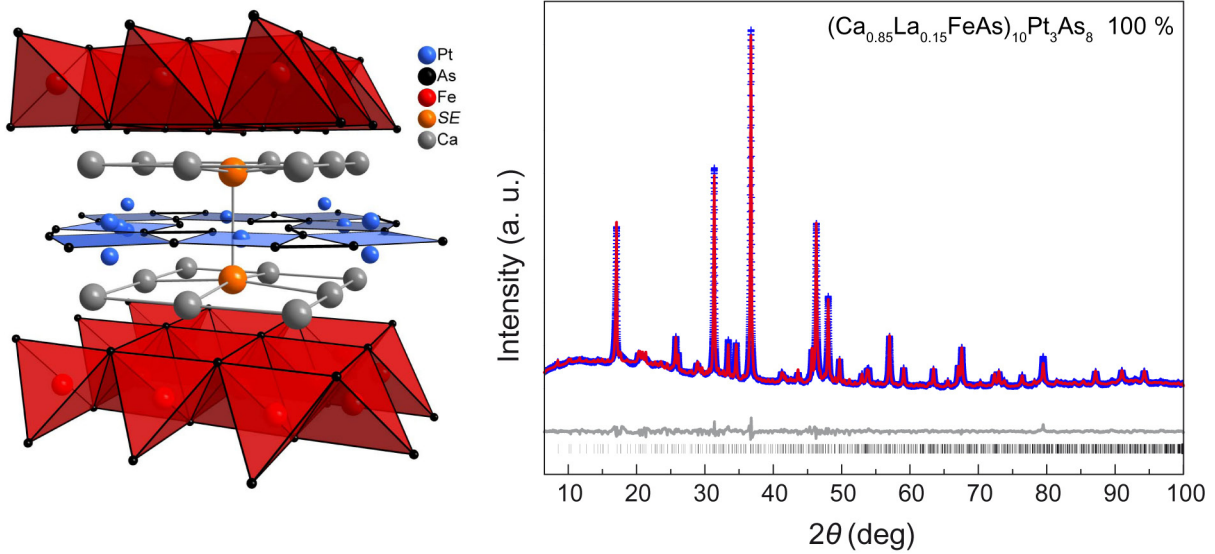
Figure 1. Crystal structure of $(Ca_{1-y}RE_yFeAs)_{10}Pt_3As_8$ (left). X-ray powder pattern (blue), Rietveld fit (red), and difference curve (gray) of $(Ca_{0.85}La_{0.15}FeAs)_{10}Pt_3As_8$ (right).

A special structural feature arises in the 1038 structure due to the missing platinum in the Pt_3As_8 layer. The calcium site just above and below the platinum vacancy is eightfold anti-prismatically coordinated by arsenic, while the other calcium positions are surrounded by seven arsenic atoms only (see Figure 1). This particular calcium site reveals a distinct preference for RE atoms, but with a remarkable size tolerance. These prerequisites render the 1038 phase an ideal system to probe the rare earth dependent response of the compound to different sized substitutes, electron doping, and strong magnetic impurities in $(Ca_{1-y}RE_yFeAs)_{10}Pt_3As_8$ with magnetic RE^{3+} ions.

In this letter we show that superconductivity in RE doped 1038 compounds can not only be induced by La doping,[14, 15] but also by the complete series of trivalent RE ions in spite of their different size. The $T_c(y_{RE})$ phase diagrams of varying rare earth ions reveal a universal correlation of electron doping and critical temperature, but are independent of the type of RE element. Furthermore the absence of superconductivity in $(Ca_{1-y}Eu_yFeAs)_{10}Pt_3As_8$ containing Eu^{2+} is in line with the above mentioned electron doping scenario. Finally the close similarity between 1048 and La-1038 are demonstrated by optimally doped La-1038 reaching the same T_c than 1048.

2.7.2 *Experimental Details*

Polycrystalline samples of rare earth calcium platinum iron arsenides were synthesized as described in reference [14], and characterized by X-ray powder diffraction using the Rietveld method with TOPAS.[18] Compositions were determined within errors of 10 % by refining

occupation parameters and by X-ray spectroscopy (EDX). The X-ray powder pattern of (Ca$_{0.85}$La$_{0.15}$FeAs)$_{10}$Pt$_3$As$_8$ together with the Rietveld fit is shown in Figure 1 as an example. Superconducting properties were measured using a *ac*-susceptometer at 1333 Hz in the temperature range of 3.5 to 300 K at a 3 Oe field. Gaussian magnetic units are used (molar susceptibility χ_{mol} in cm^3/mol; dimensionless volume susceptibility χ_V). Critical temperatures of bulk material were determined from strongest change of temperature dependent susceptibility slope. Magnetic susceptibility measurements of paramagnetic samples were performed on a QUANTUM DESIGN MPMS XL5 SQUID magnetometer which allowed for measurements with fields up to 50 kOe at temperatures between 1.8 K and 300 K.

2.7.3 *Results and Discussion*

Figure 2 shows the *ac*-susceptibility data for (Ca$_{1-y}$RE$_y$FeAs)$_{10}$Pt$_3$As$_8$ with *RE* = Y, La – Sm, and Gd – Lu with nominal compositions y = 0.1, 0.2 for the early and y = 0.2 for the late rare earth elements. Bulk superconductivity is detected in all samples. EDX measurements and Rietveld refinements confirmed the nominal composition of the early rare earth compounds La – Sm, whereas the structural tolerance towards rare earth substitution decreases with decreasing radii of the late rare earth elements Gd – Lu. Figure 3 depicts the maximum *RE* solubility in (Ca$_{1-y}$RE$_y$FeAs)$_{10}$Pt$_3$As$_8$. The red line marks the concentration level corresponding to a fully substituted eightfold coordinated calcium position (20 %). The gradual decrease of the superconducting volume fractions (Figure 2) for the late *RE* elements (Gd – Lu) is caused by their limited solubility and increasing fractions of impurity phases.
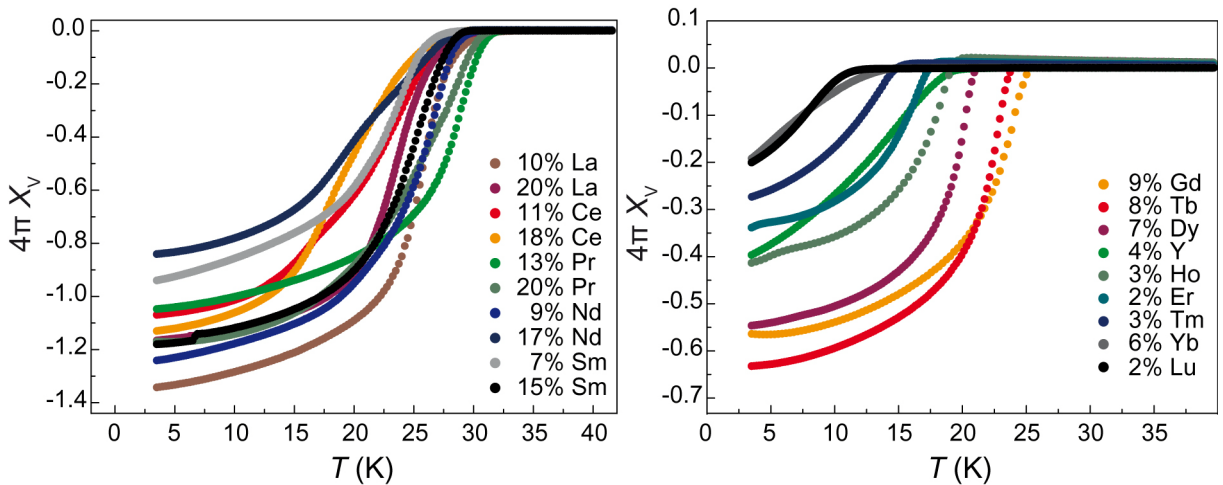
Figure 2. *Ac*-susceptibility of the *RE*-1038 samples with *RE* = La – Sm (left) and *RE* = Gd – Lu (right).

Recent publications reported superconductivity in the La doped compounds (Ca$_{1-y}$La$_y$FeAs)$_{10}$Pt$_3$As$_8$ with a maximum T_c of 30 K[14] and 26 K,[15] respectively. This finding was reasoned with a substitution of La^{3+} preferably to the eightfold antiprismatically coordinated Ca position in the structure, concomitant with electron doping to the FeAs layer similar to La(O$_{1-x}$F$_x$)FeAs.[14] A very similar doping scenario can be expected for the higher rare earth compounds, insofar the rare earth ions are trivalent. Notably, the critical temperatures of the compounds containing La, Ce, Pr, Nd, and Sm turned out to be independent of the rare earth used, whereas T_c drops significantly when the solubility limit restricts the RE concentration for the late rare earth metals. Taking this into account, neither the kind of rare earth element used, nor its magnetic properties or effects on the structure perceptibly influence the superconducting properties, but exclusively its electronic contribution, i.e. the electron transfer to the FeAs layers.

The critical temperatures of the (Ca$_{1-y}$$RE_y$FeAs)$_{10}Pt_3As_8$ samples and the determined RE concentrations are compiled in Figure 3. At $y = 0.13$ a maximum of the critical temperature up to $T_c \approx 35$ K is gained for La, Ce, and Pr substituted compounds, whereas corresponding samples with heavier rare earth elements were not available so far. This consideration yields a substituent independent, universal curve rendering the influence of electron doping in the system (Ca$_{1-y}$$RE_y$FeAs)$_{10}Pt_3As_8$ and featuring a maximum of T_c at $y = 0.13$. Small deviations in T_c may result from minor platinum substitution on the iron sites. The optimal electron doping level of 0.13 e^-/FeAs is comparable to the 1111 superconductors La(O$_{1-x}$F$_x$)FeAs ($x = 0.11$)[1] and Sm(O$_{1-x}$F$_x$)FeAs ($x = 0.1$).[19] The comparison with directly electron doped materials like Ba(Fe$_{1-x}$Co$_x$)$_2$As$_2$ appears not meaningful, since the extend of influence of chemical modification inside the FeAs layer is still not fully understood.[20, 21]
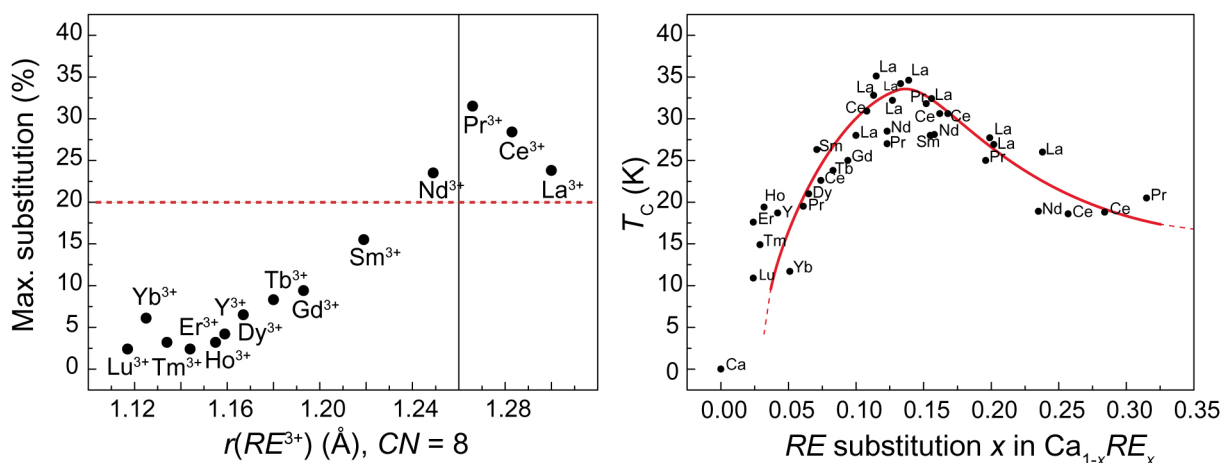
Figure 3. Solubility of RE dopants in (Ca$_{1-y}$$RE_y$FeAs)$_{10}Pt_3As_8$ against the ionic radius (left). The slashed line at 1.26 Å marks the radius of Ca^{2+}. Critical temperatures of (Ca$_{1-y}$$RE_y$FeAs)$_{10}Pt_3As_8$ (right).
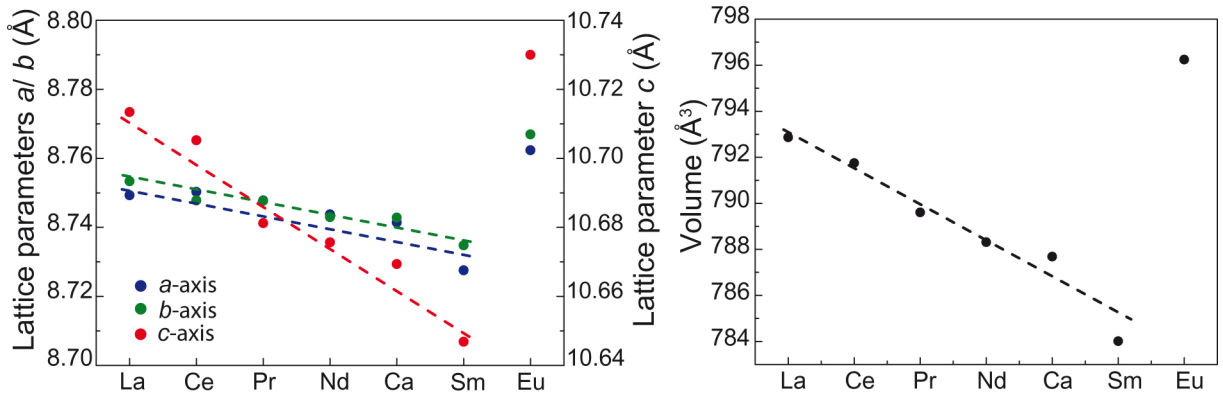
Figure 4. Lattice parameters (left) and cell volumes (right) of (Ca$_{1-y}$RE$_y$FeAs)$_{10}$Pt$_3$As$_8$ with y = 0.2.

It should be noted, that neglecting effects of size and magnetism of the rare earth elements on the superconducting properties appears oversimplified. One may expect at least an influence of strong magnetic moments present at the heavier elements like Holmium or Erbium affecting superconductivity. However, no suchlike was substantiated in our experiments. Even structural effects are minimal. Figure 4 depicts the evolution of the unit cell axes and volume for the compounds (Ca$_{1-y}$RE$_y$FeAs)$_{10}$Pt$_3$As$_8$ with RE = La, Ce, Pr, Nd, Sm, Eu with constant rare earth concentration y = 0.2. For comparison the values of the parent compound (CaFeAs)$_{10}$Pt$_3$As$_8$ were added at the position corresponding to the ionic radius of Ca^{2+}. Within the measurement accuracy the in-plane parameters a and b remain equal and both decrease gradually with decreasing rare earth radii. In the same direction the contraction of the stacking axis c increases more distinct, whereas all changes are well below 1 %.

The europium compounds (Ca$_{1-y}$Eu$_y$FeAs)$_{10}$Pt$_3$As$_8$ are special cases of the RE series due to the absence of superconductivity. The unit cell axis are significantly enlarged compared to the other RE (Figure 4) and magnetic measurements show paramagnetic behavior. Figure 5 displays the inverse magnetic susceptibilities of (Ca$_{1-y}$Eu$_y$FeAs)$_{10}$Pt$_3$As$_8$ with y = 0.1 and y = 0.2 measured at 20 kOe. Effective magnetic moments of 8.0 μ_B per rare earth atom in (Ca$_{0.9}$Eu$_{0.1}$FeAs)$_{10}$Pt$_3$As$_8$ and (Ca$_{0.8}$Eu$_{0.2}$FeAs)$_{10}$Pt$_3$As$_8$ were extracted from the Curie-Weiss fits, which are in excellent agreement with the effective moment of 7.94 μ_B expected for Eu^{2+}. Thus our data suggest divalent europium in line with the enhanced unit cell volume displayed in Figure 4. Given the presence of Eu^{2+}, the absence of superconductivity in (Ca$_{1-y}$Eu$_y$FeAs)$_{10}$Pt$_3$As$_8$ can clearly be referred to missing of electron doping of the FeAs layer.
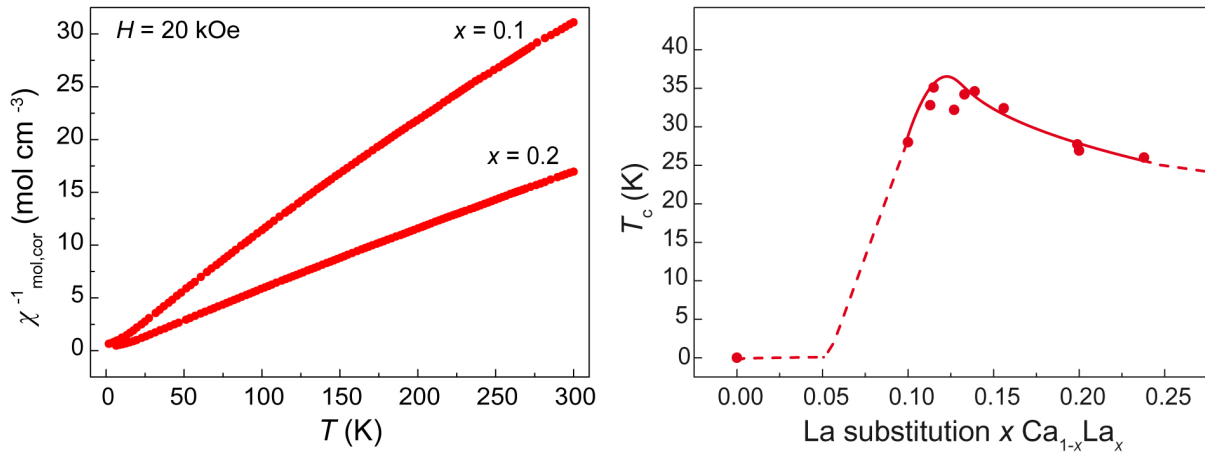
Figure 5. Magnetic susceptibilities of (Ca$_{1-y}$Eu$_y$FeAs)$_{10}$Pt$_3$As$_8$ with $y = 0.1$ and $y = 0.2$ (left). $T_c(y)$ phase diagram of (Ca$_{1-y}$La$_y$FeAs)$_{10}$Pt$_3$As$_8$ (right).

Figure 5 depicts the $T_c(y)$ phase diagram of (Ca$_{1-y}$La$_y$FeAs)$_{10}$Pt$_3$As$_8$ with $y = 0.1 - 0.3$. Analogous diagrams were obtained with Ce and Pr doping (not shown). The preparation of homogeneous powder samples for $0 \leq y \leq 0.1$ were not successful so far due to phase separation into (CaFeAs)$_{10}$Pt$_3$As$_8$ and (Ca$_{1-y}$La$_y$FeAs)$_{10}$Pt$_3$As$_8$ with $y \geq 0.1$. A similar phase diagram was reported recently[15] based on single crystal data, identifying the same optimal doping level, whereas the maximum T_c did not exceed 26 K due to considerable Pt mixing at the iron sites. (Ca$_{1-y}$La$_y$FeAs)$_{10}$Pt$_3$As$_8$ without Pt substitution features bulk superconductivity in the range investigated with a maximum T_c of 35 K for $y \approx 0.13$. Notably the critical temperature of 35 K coincides with T_c reported for the 1048 compound (CaFeAs)$_{10}$Pt$_4$As$_8$, as well as the electron doping level which was estimated by DFT calculation to be approximately 0.15 e^-/FeAs for the 1048 phase.[14] This finding is fully consistent with the two different electron doping scenarios we suggested earlier, and emphasizes the close electronic relation between (Ca$_{1-y}$La$_y$FeAs)$_{10}$Pt$_3$As$_8$ and (CaFeAs)$_{10}$Pt$_4$As$_8$ despite their different crystal structures.

2.7.4   *Conclusion*

In summary our results show that superconductivity in the 1038 phase does not only occur by substitution of lanthanum for calcium, but by the complete series of trivalent rare earth elements Y, La – Sm, and Gd – Lu with appropriate radius. Superconductivity arises in all compounds investigated and depends only on the *RE* concentration, but not on the type of *RE*. This gives proof for the electron donor function of the *RE* substitution. Other influences like lattice parameters and *RE* magnetism are minimal, and show no measurable effect on the superconducting critical temperatures. This finding yields an universal $T_c(y)$ phase diagram

for $(Ca_{1-y}RE_yFeAs)_{10}Pt_3As_8$ with a maximum T_c of 35 K at $y = 0.13$ independent of the kind of rare earth. Thereby the optimal doping level of $y = 0.13$ e^-/FeAs nearly coincides with known indirectly electron doped iron arsenides $La(O_{1-x}F_x)FeAs$ $(x = 0.11)$[1] and $Sm(O_{1-x}F_x)FeAs$ $(x = 0.1)$.[19] The absence of superconductivity in $(Ca_{1-y}Eu_yFeAs)_{10}Pt_3As_8$ is rationalized with divalent Eu^{2+} present in the structure and the absence of electron doping. Finally the close resemblance of electron doped $(Ca_{1-y}RE_yFeAs)_{10}Pt_3As_8$ and the 1048 phase $(CaFeAs)_{10}Pt_4As_8$ was demonstrated by featuring same $T_{c,max} \approx 35$ K coinciding at the same optimal doping level.

2.7.5 *References*

[1]   Y. Kamihara, T. Watanabe, M. Hirano, H. Hosono, *J. Am. Chem. Soc.* **2008**, *130,* 3296.

[2]   D. C. Johnston, *Adv. Phys.* **2010**, *59*, 803.

[3]   G. R. Stewart, *Rev. Mod. Phys.* **2011**, *83*, 1589.

[4]   D. Johrendt, *J. Mater. Chem.* **2011**, *21*, 13726.

[5]   H. Takahashi, K. Igawa, K. Arii, Y. Kamihara, M. Hirano, H. Hosono, *Nature* **2008**, *453*, 376.

[6]   A. S. Sefat, R. Jin, M. A. McGuire, B. C. Sales, D. J. Singh, D. Mandrus, *Phys. Rev. Lett.* **2008**, *101*, 117004.

[7]   Y. Muraba, S. Matsuishi, S.-W. Kim, T. Atou, O. Fukunaga, H. Hosono, *Phys. Rev. B* **2010**, *82*, 180512.

[8]   C. Löhnert, T. Stürzer, M. Tegel, R. Frankovsky, G. Friederichs, D. Johrendt, *Angew. Chem. Int. Ed.* **2011**, *50*, 9195.

[9]   N. Ni, J. M. Allred, B. C. Chan, R. J. Cava, *Proc. Natl. Acad. Sci. USA* **2011**, *108*, E1019.

[10] S. Kakiya, K. Kudo, Y. Nishikubo, K. Oku, E. Nishibori, H. Sawa, T. Yamamoto, T. Nozaka, M. Nohara, *J. Phys. Soc. Jpn.* **2011**, *80*, 093704.

[11] K. Kudo, D. Mitsuoka, M. Takasuga, Y. Sugiyama, K. Sugawara, N. Katayama, H. Sawa, H. S. Kubo, K. Takamori, M. Ichioka, T. Fujii, T. Mizokawa, M. Nohara, *Sci. Rep.* **2013**, *3*, 3101.

[12] C. Hieke, J. Lippmann, T. Stürzer, G. Friederichs, F. Nitsche, F. Winter, R. Pöttgen, D. Johrendt, *Philos. Mag.* **2013**, *93*, 3680.

[13] T. F. Fässler, *Zintl Phases: Principles and Recent Developments, Structure and Bonding*, Springer, Heidelberg, **2011**.

[14] T. Stürzer, G. Derondeau, D. Johrendt, *Phys. Rev. B* **2012**, *86*, 060516(R).

[15] N. Ni, W. E. Straszheim, D. J. Williams, M. A. Tanatar, R. Prozorov, E. D. Bauer, F. Ronning, J. D. Thompson, R. J. Cava, *Phys. Rev. B* **2013**, *87*, 060507.

[16] T. Stürzer, G. M. Friederichs, H. Luetkens, A. Amato, H.-H. Klauss, D. Johrendt, *J. Phys.: Condens. Matter* **2013**, *25*, 122203.

[17] T. Zhou, G. Koutroulakis, J. Lodico, N. Ni, J. D. Thompson, R. J. Cava, S. E. Brown, *J. Phys.: Condens. Matter* **2013**, *25*, 122201.

[18] A. Coelho, *TOPAS-Academic*, Version 4.1, Coelho Software, Brisbane, Australia, **2007**.

[19] Z.-A. Ren, W. Lu, J. Yang, W. Yi, X.-L. Shen, Z.-C. Li, G.-C. Che, X.- L. Dong, L.-L. Sun, F. Zhou, Z.-X. Zhao, *Chin. Phys. Lett.* **2008**, *25*, 2215.

[20] V. Zinth, T. Dellmann, H.-H. Klauss, D. Johrendt, *Angew. Chem. Int. Ed.* **2011**, *50*, 7919.

[21] H. Wadati, I. Elfimov, G. A. Sawatzky, *Phys. Rev. Lett.* **2010**, *105*, 157004.

2.8 Myon Spin Rotation Spectroscopy Study on $(Ca_{1-y}La_yFeAs)_{10}Pt_3As_8$
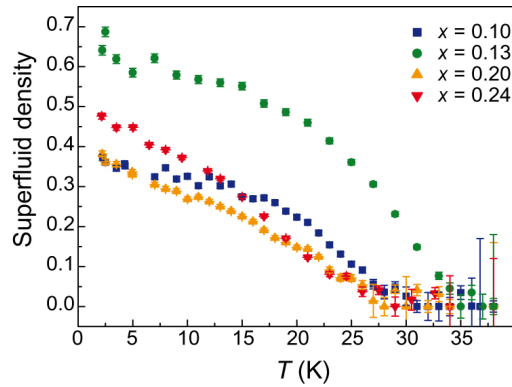
2.8.1 *Introduction*

Although the underlying mechanism of superconductivity in iron arsenides is not completely understood yet, it is generally accepted that magnetic fluctuations play an essential role in the formation of *Cooper* pairs.[1] Therefore detailed investigations on magnetism in the vicinity of superconductivity and in the superconducting phase are important. In the previous chapters stoichiometric $(CaFeAs)_{10}Pt_3As_8$ was demonstrated to be the parent compound of the $(CaFe_{1-x}M_xAs)_{10}Pt_zAs_8$ superconductor family.[2] A phase transition to a stripe-type antiferromagnetic ground state with broken local tetragonal symmetry was identified being typical for iron arsenide parents.[2-4] Analogous to other iron pnictide superconductors, this phase transition was found to be suppressed in the superconducting materials. Temperature dependent evolution of in-plane lattice parameters *a* and *b* as well as resistivity are depicted in Figure 1 comparing parent compound $(CaFeAs)_{10}Pt_3As_8$ and optimally electron doped superconductor $(Ca_{0.87}La_{0.13}FeAs)_{10}Pt_3As_8$.

This phase transition can be suppressed by direct substitution in $(CaFe_{1-x}M_xAs)_{10}Pt_3As_8$[5] as well as electron doping in $(Ca_{1-y}RE_yFeAs)_{10}Pt_3As_8$[6-7] and $(CaFeAs)_{10}Pt_4As_8$[8] giving rise to critical temperatures up to 35 – 38 K (Figure 1). Recent measurements on 122 systems gave evidence for spin nematicity above T_N and the formation of microscopic coexistence of magnetism and superconductivity below T_c in $(Ba_{1-x}K_x)Fe_2As_2$.[9] However, a thorough understanding of the magnetism in iron arsenides is still amiss. In contrast to other systems, measurements on stoichiometric $(CaFeAs)_{10}Pt_3As_8$ within this thesis evidenced a gradual formation of antiferromagnetic long range order instead of a spontaneous order like in 122 and 1111 compounds. Nevertheless also indication of a nematic phase preceding the SDW ordering was found by ^{57}Fe-Mössbauer studies (Chapter 2.4).

Therefore a closer investigation of the magnetism in the superconducting state of this family is of great interest. In this course (Ca$_{1-y}$La$_y$FeAs)$_{10}$Pt$_3$As$_8$ turned out to be especially suitable for further studies due to its high T_c and easy availability as bulk material. The following chapter presents results on (Ca$_{1-y}$La$_y$FeAs)$_{10}$Pt$_3$As$_8$ obtained by μSR spectroscopy being a very valuable tool to gain a deeper insight into temperature dependent local magnetism.
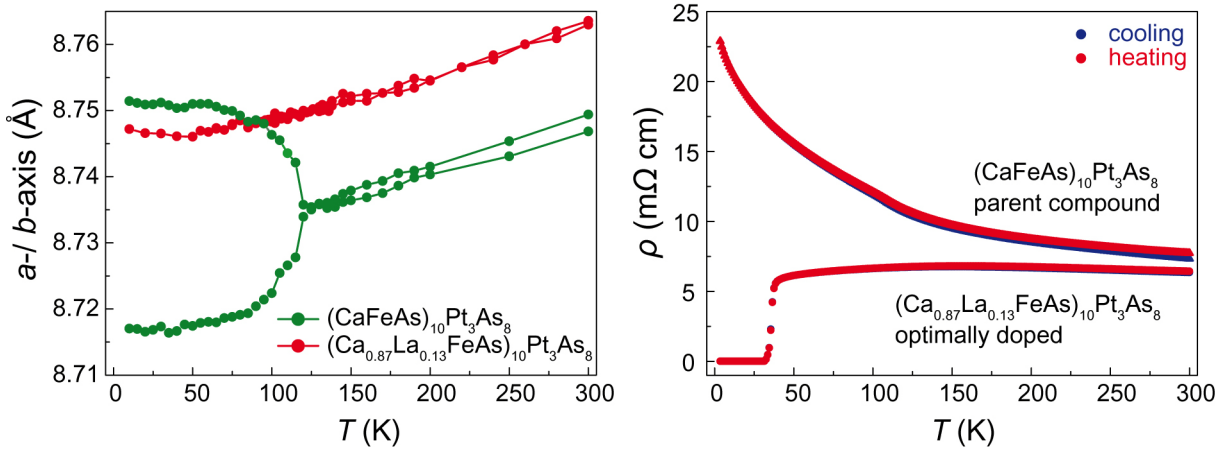
Figure 1. Comparison of temperature dependent in-plane lattice parameters *a* and *b* (left) and resistivity (right) of parent compound (CaFeAs)$_{10}$Pt$_3$As$_8$ and optimally electron doped superconductor (Ca$_{0.87}$La$_{0.13}$FeAs)$_{10}$Pt$_3$As$_8$.

2.8.2   *Experimental Details*

Powder samples of (Ca$_{1-y}$La$_y$FeAs)$_{10}$Pt$_3$As$_8$ were synthesized as described in Chapter 2.7 and reference [6]. Optimally doped sample ($y = 0.13$) was obtained phase pure, while under and over doped material contained minor impurities of FeAs ($y = 0.10$, 0.20, 0.24) and CaFe$_4$As$_3$ ($y = 0.24$). Sample compositions were refined based on X-ray powder diffraction data (HUBER G670 Guinier imaging plate, Cu Kα_1 radiation) using the Rietveld method with TOPAS.[10] Superconducting properties were determined using an *ac*-susceptometer at 1333 Hz in the temperature range of 3.5 – 300 K at 3 Oe. μSR measurements were performed using the GPS spectrometers located at the *M*3 beam line of the Swiss Muon Source at the Paul Scherrer Institut, Switzerland. Transverse field measurements were carried out applying a magnetic field of 700 Oe. The data was analyzed using the MUSRFIT package.[11]

2.8.3   *Results and Discussion*

Superconducting properties of the compounds (Ca$_{1-y}$La$_y$FeAs)$_{10}$Pt$_3$As$_8$ were measured in advance by *ac*-susceptibility yielding critical temperatures of 28 K ($y = 0.10$), 35 K ($y = 0.13$), 27 K ($y = 0.20$), and 26 K ($y = 0.24$) with shielding fractions over 90 %. μSR measurements

of the superfluid density (TF mode) confirmed superconductivity in the compounds (Ca$_{1-y}$La$_y$FeAs)$_{10}$Pt$_3$As$_8$ (Figure 4). Critical temperatures derived are in good agreement with those determined from *ac*-susceptibility measurement. The highest *Cooper* pair concentration was found for optimally doped (Ca$_{1-y}$La$_y$FeAs)$_{10}$Pt$_3$As$_8$ with $x = 0.13$.

Time dependent zero field μSR spectra of (Ca$_{1-y}$La$_y$FeAs)$_{10}$Pt$_3$As$_8$ taken above (~ 200 K, red) and below (2.2 K, black) T_c for $y = 0$, 0.10, 0.13, 0.20, and 0.24 are depicted in Figure 2 and 3. All samples show no magnetism at 200 K which is evident from the absence of oscillations and/or damping in polarization spectra. The parent compound (CaFeAs)$_{10}$Pt$_3$As$_8$ reveals the formation of static magnetism below 130 K as discussed in reference [2].
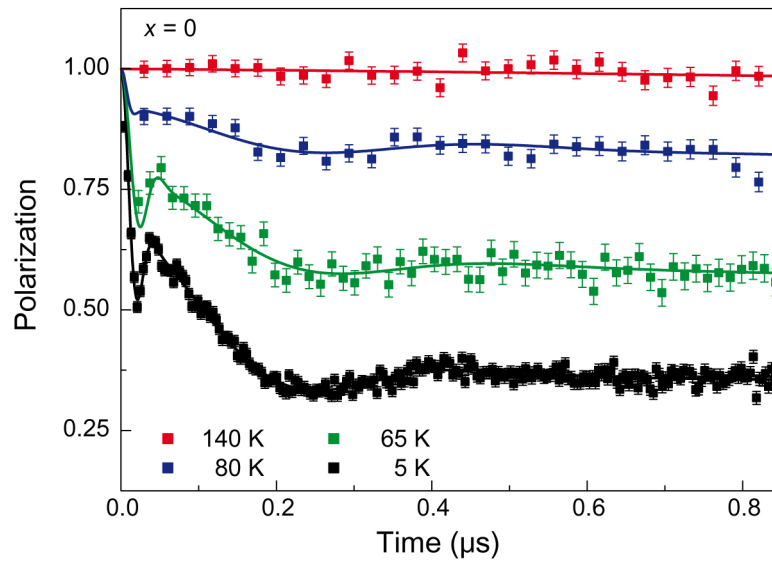
Figure 2. Zero field μSR spectra of parent compound (CaFeAs)$_{10}$Pt$_3$As$_8$ at different temperatures.[2]
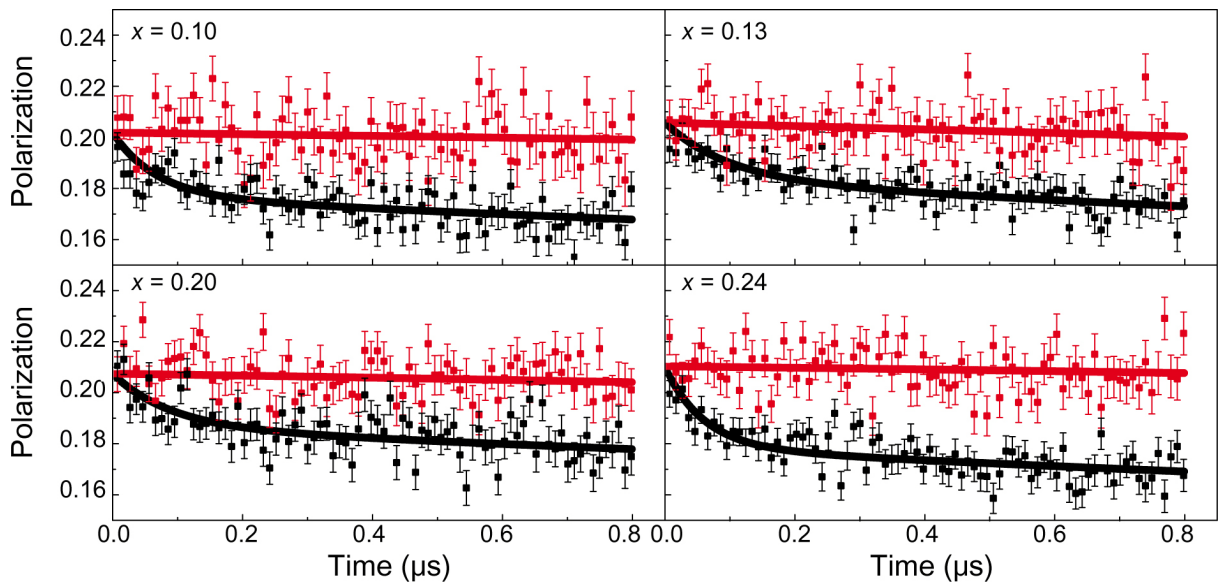
Figure 3. Zero field μSR spectra for characteristic temperatures above (red, ~ 200 K) and below (black, 2.2 K) T_c for (Ca$_{1-y}$La$_y$FeAs)$_{10}$Pt$_3$As$_8$ powder samples with $y = 0.10$, 0.13, 0.20, and 0.24.

In the superconducting state of La doped samples also strong damping of the μSR signal was detected being indicative for the presence of magnetism. Temperature dependent magnetic fractions derived from ZF measurements reveal a gradual increase of the magnetic fraction below about 90 K reaching approximately 20 % at 2.2 K for all La doped samples. Additional kinks were found in the vicinity of T_c, which was also reported recently for underdoped $(Ba_{1-x}K_x)Fe_2As_2$.[12]

What causes the magnetism in the superconducting state of $(Ca_{1-y}La_yFeAs)_{10}Pt_3As_8$ is still unclear. Impurity phase FeAs orders magnetically at 70 K,[13] while magnetic transitions in $CaFe_4As_3$ are reported at 25 K and 90 K.[14] Although slightly increased magnetic volume for $y = 0.24$ could be caused by minor $CaFe_4As_3$ impurity, it seems unreasonable to completely assign the magnetic phase to impurities. That is because side phase amounts were determined to be well below 10 % based on X-ray data, while the sample with $y = 0.13$ was pure phase. Furthermore susceptibility measurements revealed superconducting volume fractions of more than 90 % in all $(Ca_{1-y}La_yFeAs)_{10}Pt_3As_8$ samples. This reasoning together with the similar evolution of magnetic fraction and response to the onset of superconductivity indicate the magnetism being an intrinsic property of $(Ca_{1-y}La_yFeAs)_{10}Pt_3As_8$. Nevertheless, whether magnetism microscopically coexists with superconductivity like in $(Ba_{1-x}K_x)Fe_2As_2$[9] or is caused by inhomogeneity or phase separation cannot be settled based on this data.
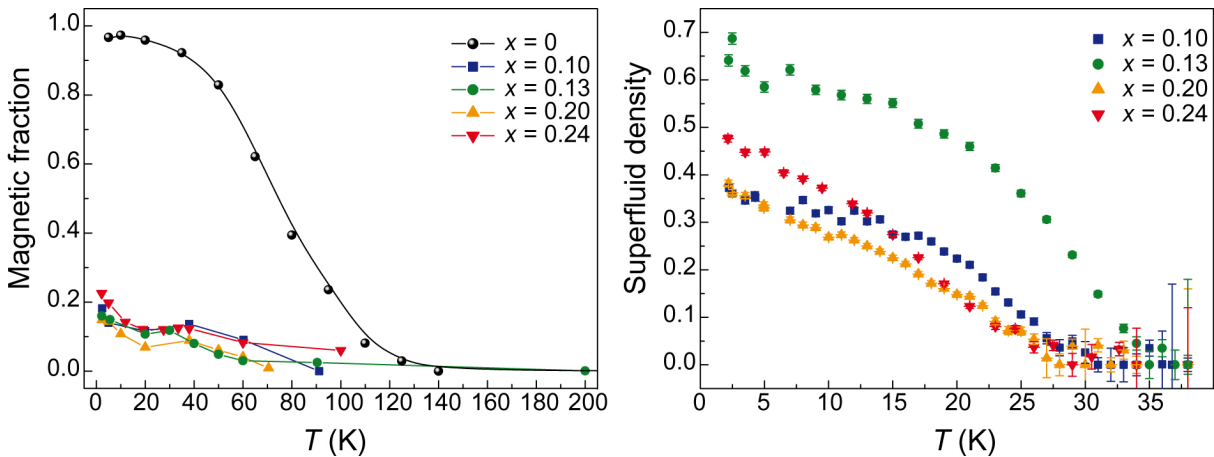
Figure 4. Temperature dependent magnetic fraction (left) and superfluid density (right) of $(Ca_{1-y}La_yFeAs)_{10}Pt_3As_8$ powder samples with $y = 0$, 0.10, 0.13, 0.20, and 0.24.

Interestingly similar magnetic contributions were also found for underdoped $(Ba_{1-x}K_x)Fe_2As_2$.[12] The presence of the magnetic fraction so far precludes more detailed investigations of $(Ca_{1-y}La_yFeAs)_{10}Pt_3As_8$ including the penetration depth or superconducting order parameter. Therefore further investigations are necessary to elucidate the origin of the magnetic phase in the superconducting state.

2.8.4 Conclusion

Temperature dependent superconducting and magnetic properties of electron doped $(Ca_{1-y}La_yFeAs)_{10}Pt_3As_8$ with $y = 0.10$, 0.13, 0.20, and 0.24 were investigated by μSR spectroscopy. Investigations of the superfluid density confirmed superconductivity in all samples with the highest T_c being 35 K in optimally doped $(Ca_{0.86}La_{0.13}FeAs)_{10}Pt_3As_8$, as was reported based on susceptibility data.[6] However, further investigations revealed a gradually developing magnetic fraction reaching about 20 % at 2.2 K, being equally present in all samples. X-ray scattering powder analysis and susceptibility measurements rendered impurity phases as only potential causes unlikely. Additional kinks in the temperature dependent magnetic fraction in the vicinity of T_c also indicate this feature being an intrinsic property of $(Ca_{1-y}La_yFeAs)_{10}Pt_3As_8$ samples. In this context inhomogeneous La doping was considered the most probable origin for the residual magnetism in $(Ca_{1-y}La_yFeAs)_{10}Pt_3As_8$ compounds. At this stage no detailed information about the superconducting state in La doped 1038 samples can be concluded, but further investigations are necessary to identify the origin of the magnetic signal.

2.8.5 References

[1]   D. G. Hinks, *Nat. Phys.* **2009**, *5*, 386.

[2]   T. Stürzer, G. M. Friederichs, H. Luetkens, A. Amato, H.-H. Klauss, D. Johrendt, *J. Phys.: Condens. Matter* **2013**, *25*, 122203.

[3]   T. Zhou, G. Koutroulakis, J. Lodico, N. Ni, J. D. Thompson, R. J. Cava, S. E. Brown, *J. Phys.: Condens. Matter* **2013**, *25*, 122201.

[4]   A. Sapkota, G. S. Tucker, M. Ramazanoglu, W. Tian, N. Ni, R. J. Cava, R. J. McQueeney, A. I. Goldman, A. Kreyssig, *Phys. Rev. B* **2014**, *90*, 100504.

[5]   T. Stürzer, F. Kessler, D. Johrendt, *Philos. Mag.* **2014**, *94*, 3632.

[6]   T. Stürzer, G. Derondeau, E.-M. Bertschler, D. Johrendt, *Solid State Commun.* **2015**, *201*, 36.

[7]   N. Ni, W. Straszheim, D. Williams, M. Tanatar, R. Prozorov, E. Bauer, F. Ronning, J. Thompson, R. Cava, *Phys. Rev. B* **2013**, *87*, 060507.

[8]   T. Stürzer, G. Derondeau, D. Johrendt, *Phys. Rev. B* **2012**, *86*, 060516.

[9]   E. Wiesenmayer, H. Luetkens, G. Pascua, R. Khasanov, A. Amato, H. Potts, B. Banusch, H.-H. Klauss, D. Johrendt, *Phys. Rev. Lett.* **2011**, *107*, 237001.

[10]   A. Coelho, *TOPAS-Academic*, Version 4.1, Coelho Software, Brisbane, Australia, **2007**.

[11]   A. Suter, B. M. Wojek, *Phys. Procedia*, to be published.

[12]   E. Wiesenmayer, *private communication*, Ludwig-Maximilians-Universität München, **2015**.

[13]   A. Błachowski, K. Ruebenbauer, J. Żukrowski, Z. Bukowski, *J. Alloys Compd.* **2014**, *582*, 167.

[14]   I. Todorov, D. Y. Chung, C. D. Malliakas, Q. Li, T. Bakas, A. Douvalis, G. Trimarchi, K. Gray, J. F. Mitchell, A. J. Freeman, M. G. Kanatzidis, *J. Am. Chem. Soc.* **2009**, *131*, 5405.

2.9 Phase Diagram of (CaFe$_{1-x}$Pt$_x$As)$_{10}$Pt$_z$As$_8$ and the Relation of (Ca$_{1-y}$La$_y$FeAs)$_{10}$Pt$_3$As$_8$ and (CaFeAs)$_{10}$Pt$_4$As$_8$
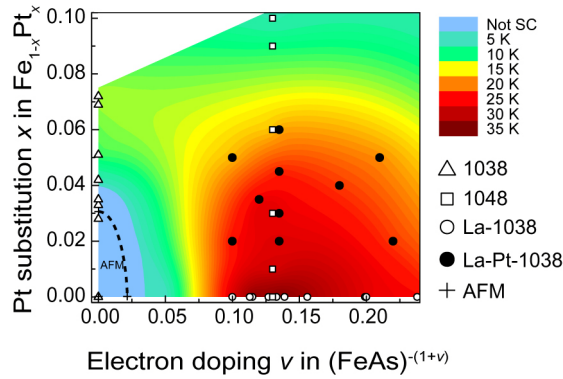
2.9.1 Introduction

Besides its unique structural complexity among iron arsenide superconductors the (CaFe$_{1-x}$Pt$_x$As)$_{10}$Pt$_z$As$_8$ system rendered itself exceptionally interesting because of an extreme difference in properties for $z = 3$ and 4. While (CaFeAs)$_{10}$Pt$_3$As$_8$ (1038 phase) is a typical iron arsenide parent compound with properties being reminiscent of a semiconductor, (CaFeAs)$_{10}$Pt$_4$As$_8$ (1048 phase) features high T_c superconductivity up to 35 K.[1] Moreover upon additional Pt doping to the Fe sites both compounds revealed opposing behavior. In the latter T_c is drastically diminished, while superconductivity was just induced in the 1038 compound upon Pt doping.[2] Structural parameters like Fe–As bond length or As–Fe–As angles, often discussed to essentially influence superconductivity, do not follow the trend found for other iron arsenide compounds (Chapter 7.6, appendix). Therefore *Ni* et al. assumed the reason for the discrepancy in 1038/1048 properties in enhanced interlayer coupling caused by the metallic nature of the 1048 phase as was suggested for cuprates.[3] *Nohara* et al. found high Pt mixing on the iron sites from X-ray data inconsistent with EPM analysis what might be an artifact from disorder in the structure (Chapter 2.2).[4] Based on this finding they suggested "heavy Pt doping"[5] as necessity for high T_c together with Pt states at E_F.[4] However, mixed crystal series of (CaFe$_{1-x}$Pt$_x$As)$_{10}$Pt$_z$As$_8$, together with DFT studies characterized the 1048 phase an ideally electron doped iron arsenide with an approximate doping level of 0.15 e$^-$/FeAs.[2] Furthermore this scenario was substantiated by the discovery of superconducting properties similar to the 1048 compounds in the electron doped 1038 derivative (Ca$_{1-y}$La$_y$FeAs)$_{10}$Pt$_3$As$_8$.[2, 6-7] In this context the change in 1038/1048 properties upon Pt/Fe mixing was explained as direct doping (1038 phase) and overdoping effects (1048 phase), respectively.[1-2] So far, in (CaFeAs)$_{10}$Pt$_4$As$_8$ the number of four Pt atoms per unit cell fixes

the electron doping. The electron doping in (Ca$_{1-y}$La$_y$FeAs)$_{10}$Pt$_3$As$_8$, however, can be changed by the La content, thus allowing for more detailed investigations concerning codoping in (Ca$_{1-y}$La$_y$Fe$_{1-x}$Pt$_x$As)$_{10}$Pt$_3$As$_8$, the relation of the two electronically doped compounds (CaFeAs)$_{10}$Pt$_4$As$_8$ and (Ca$_{1-y}$La$_y$FeAs)$_{10}$Pt$_3$As$_8$ and the relevance of structural differences comparing the 1038 and 1048 phase. For this purpose the mixed crystal series (Ca$_{1-y}$La$_y$Fe$_{1-x}$Pt$_x$As)$_{10}$Pt$_3$As$_8$ ($x = 0 - 0.07$; $y = 0 - 0.24$) was synthesized and characterized by X-ray powder diffraction, energy dispersive X-ray spectroscopy, and susceptibility measurements.

2.9.2 *Experimental Details*

Polycrystalline samples of (Ca$_{1-y}$La$_y$Fe$_{1-x}$Pt$_x$As)$_{10}$Pt$_3$As$_8$ were prepared by heating stoichiometric mixtures of the elements (Ca: 99.99 %, La: 99.9 %, Fe: 99.9 %, Pt: 99.95 %, As: 99.999 %) in alumina crucibles which were sealed in argon filled silica tubes. The samples were heated for 10 h at 600 °C followed by 10 h at 1000 °C and subsequent cooling to ambient temperature. Afterwards they were grounded, reheated to 1000 °C for 25 h, pelletized, and again treated for 25 h at 1000 °C. Crystalline powders obtained were characterized by X-ray powder diffraction using the Rietveld method with TOPAS[8]. Compositions were determined within errors of 10 % by refining occupation parameters and by X-ray spectroscopy (EDX). Superconducting properties were determined using an *ac*-susceptometer at 1333 Hz in the temperature range of 3.5 to 300 K at a 3 Oe field between 1.8 K and 300 K. Full-potential density function theory (DFT) calculations were performed using the WIEN2K package.[9-10]
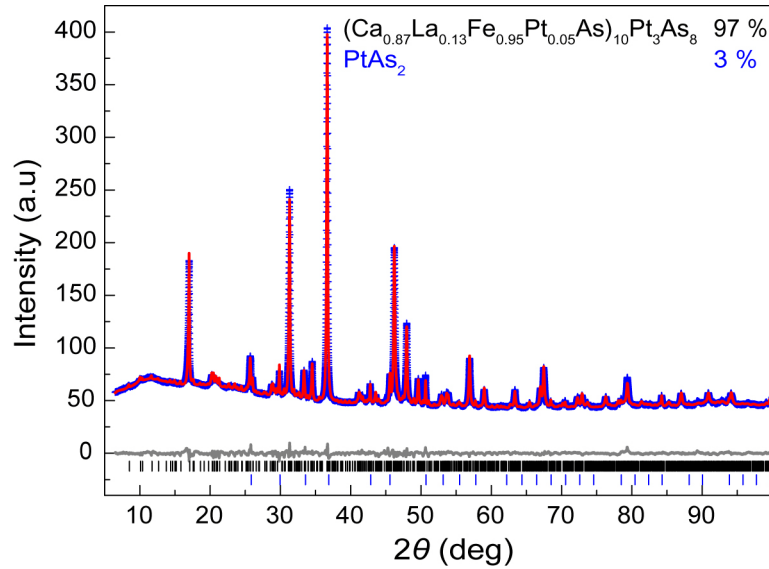
Figure 1. X-ray powder pattern (blue), Rietveld fit (red) and difference curve (gray) of $(Ca_{1-y}La_yFe_{1-x}Pt_xAs)_{10}Pt_3As_8$ with $x = 0.05$ and $y = 0.13$ (black tick marks) and minor impurity of $PtAs_2$ (blue tick marks).

2.9.3 Results and Discussion

The synthesis yielded almost phase pure polycrystalline samples (> 90 %) with minor side phases FeAs, $PtAs_2$, or $CaFe_2As_2$. Solubility limits for 1038 derivatives were found to be 7 % for Pt on iron sites and 24 % for La on Ca sites. Moreover samples $(Ca_{1-y}La_yFeAs)_{10}Pt_3As_8$ with $0 < y < 0.1$ revealed to be synthetically inaccessible because of phase separation. The course of unit cell axes upon Pt doping in $(Ca_{0.85}La_{0.15}Fe_{1-x}Pt_xAs)_{10}Pt_3As_8$ and La doping in $(Ca_{1-y}La_yFeAs)_{10}Pt_3As_8$ is depicted in Figure 2. Unit cell angles remained constant in the range investigated ($\pm 0.03°$). Anisotropic broadening of superstructure reflections can be ascribed to stacking disorder in the 1038 structure (Chapter 2.2). Pt substitution in the FeAs layer leads to an equal Fe/Pt mixing on all iron sites and a small increase of the *ab*-plane while the *c*-direction remains constant. This minor flattening of the FeAs layers is in line with the expectation for Fe site mixing with a d^8 element. In contrast La is not substituted equally to the Ca positions but reveals a strong preference for the eightfold, antiprismatically coordinated Ca position.[2, 6] Unit cell *c*-axis monotonically increases upon La substitution, while widening of the FeAs layer is far less pronounced. This increase can be ascribed to the bigger ionic radius of La^{3+} (1.30 Å) with respect to Ca^{2+} (1.26 Å).[11]
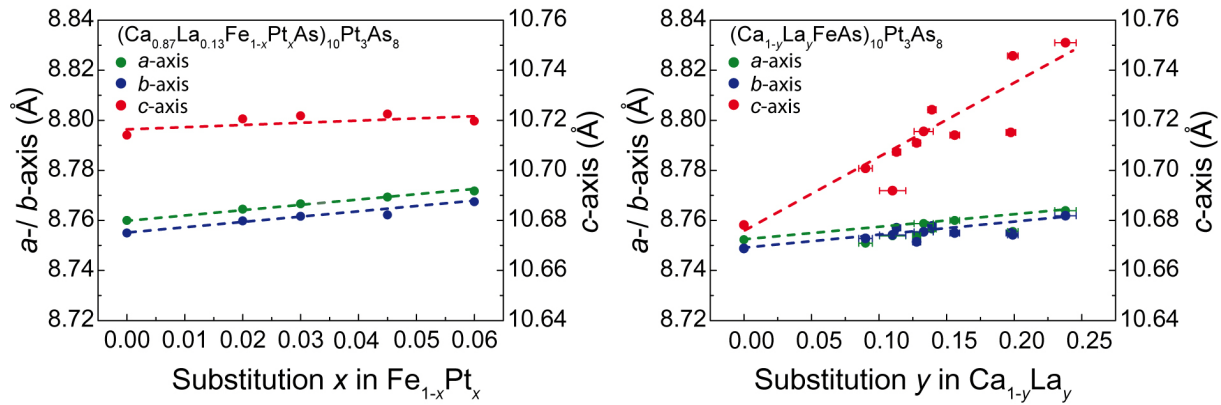
Figure 2. Changes of unit cell axes upon Pt doping in $(Ca_{0.87}La_{0.13}Fe_{1-x}Pt_xAs)_{10}Pt_4As_8$ (left) and La doping in $(Ca_{1-y}La_yFeAs)_{10}Pt_3As_8$ (right).

The highest reported critical temperature of the stoichiometric 1048 compounds is 35 – 38 K, whereby electron doping of 0.15 e^-/FeAs is assumed.[1-2] Same maximal critical temperatures were found for $(Ca_{1-y}La_yFeAs)_{10}Pt_3As_8$ with $x = 0.13$, thus at an comparable electron doping level.[6] Similar results on optimal doping in La-1038 were also reported by *Ni* et al.[7] Based on these results an electronic equivalence of the 1048 and La-1038 compounds was suggested, emphasizing the importance of the electronic structure in terms of superconducting properties. In this context the structural differences, however, appear to have minor relevance, at least in this system. Considering the differences in layer distance comparing ideally doped 1048 ($c \approx 10.5$ Å) and La-1038 ($c \approx 10.8$ Å) (Figure 2), also the discussed interlayer coupling seems to have negligible importance. The electronically equivalence of 1048 and La-1038 is illustrated in Figure 3. Therefore the La-1038 calculations were based on overdoped $(Ca_{0.8}La_{0.2}FeAs)_{10}Pt_3As_8$ instead of $(Ca_{0.85}La_{0.15}FeAs)_{10}Pt_3As_8$ to circumvent time consuming supercells. Both compounds feature a pseudo band gap of the Pt-$5d$ states at E_F, implying minor influence of the intermediate layer Pt_zAs_8 on the properties, despite its different structures for $z = 3$ and 4. The presence of almost exclusively Fe states at the Fermi level demonstrates why an introduction of additional electrons to the system by platinum (1048) or lanthanum (La-1038) causes electron doping of the iron centers. Therewith the peculiar electronic situation is formed where iron can be reduced in the presence of formally more electronegative platinum. Even if this scenario is against every chemical intuition, the consideration of isolated iron and platinum is not applicable here. Analogue Fermi surfaces were found illustrating the electron doped nature of the compounds by large electron pockets (Brillouin zone edge) with respect to small hole pockets (Brillouin zone center). It must be noted that the absence of the second hole pocket in La-1038 arises from the simplification of 20 % La doping applied, where this band is completely filled. A comparison of the relative E_F positions for both compounds is given in Chapter 7.5, appendix.
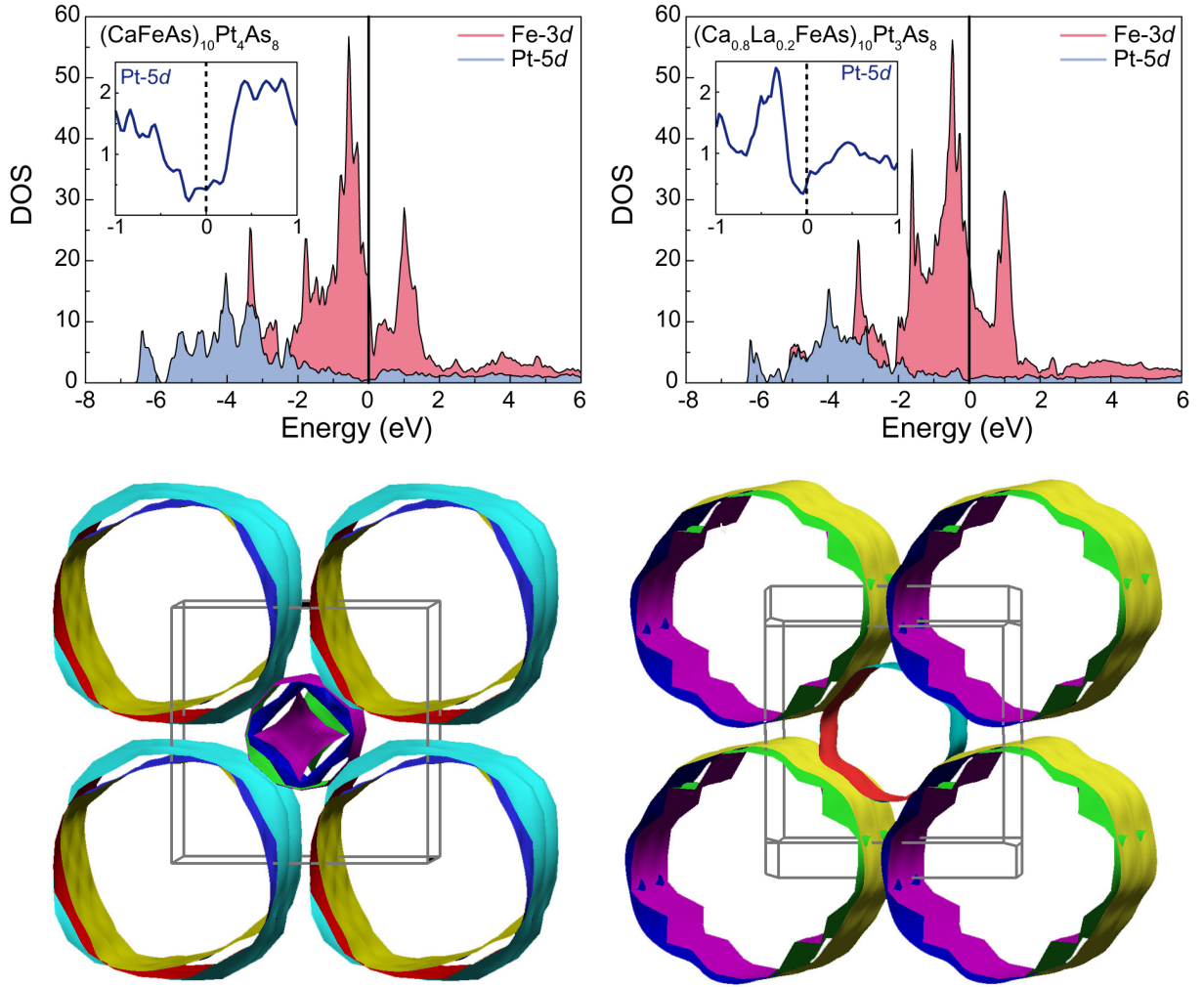
Figure 3. Density of states (DOS) and Fermi surfaces for (CaFeAs)$_{10}$Pt$_4$As$_8$ (left) and (Ca$_{0.8}$La$_{0.2}$FeAs)$_{10}$Pt$_3$As$_8$ (right).

The model of electronic equivalence of the 1048 and La-1038 system established so far, with negligible influence of the intermediate layer Pt$_z$As$_8$ and structural differences, allows for a direct comparison of these two system. Although ideal doping level was experimentally determined for La-1038, the intrinsic electron doping in stoichiometric is still an estimated value based on DFT calculations. Thus it seems reasonable to adjust the estimated $0.15\,e^-$ to $0.13\,e^-$/FeAs as experimentally found for La-1038.

Investigations on the effects of Ca/La and Fe/Pt codoping on the superconducting properties of (Ca$_{1-y}$La$_y$Fe$_{1-x}$Pt$_x$As)$_{10}$Pt$_3$As$_8$ revealed highest T_c only for La doped compounds with $x = 0$, whereas additional Fe/Pt mixing caused a rapid decrease of critical temperatures. An almost identical decline of T_c upon Pt substitution was also reported for (CaFe$_{1-x}$Pt$_x$As)$_{10}$Pt$_4$As$_8$, as is depicted in Figure 4. This result experimentally substantiate again the analogy of the 1048 and La-1038 systems despite their structural differences. The formal reduction of the 1038/1048 compounds to an iron arsenide system with the branches of direct doping (1038), electron

doping (1048, La-1038), and both combined (La-Pt-1038) allows for the construction of a preliminary phase diagram, revealing the different effects of chemical manipulation on superconductivity in this system. Data available so far is compiled in Figure 4.
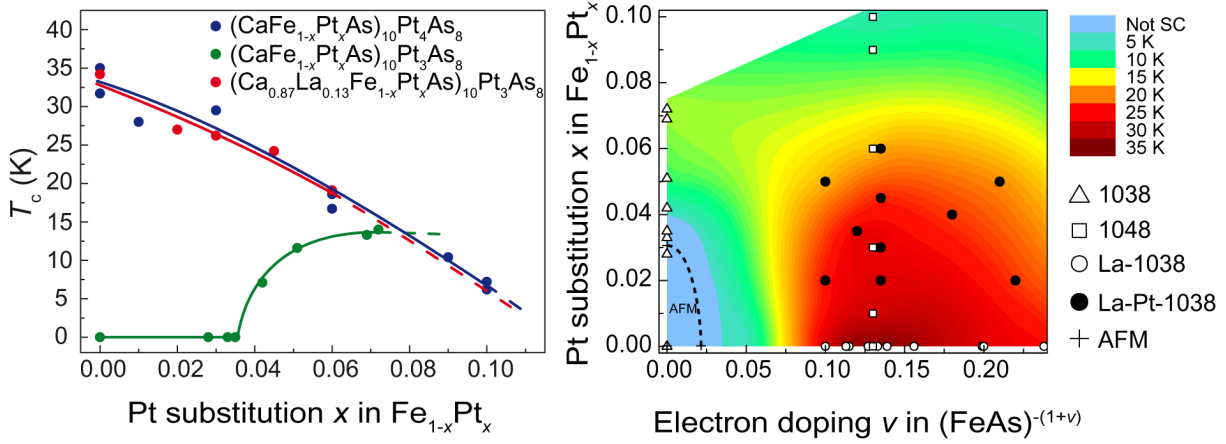
Figure 4. $T_c(x)$ **phase diagrams illustrating the influence of direct doping in (CaFe$_{1-x}$Pt$_x$As)$_{10}$Pt$_3$As$_8$, (CaFe$_{1-x}$Pt$_x$As)$_{10}$Pt$_4$As$_8$ and (Ca$_{0.87}$La$_{0.13}$Fe$_{1-x}$Pt$_x$As)$_{10}$Pt$_3$As$_8$ (left). $T_c(v,x)$ phase diagram of (CaFe$_{1-x}$Pt$_x$As)$_{10}$Pt$_z$As$_8$ superconductors with v being the formal charge of (FeAs)$^{(1+v)-}$ (right). Triangles: 1038 data from [2]. Squares: 1048 data from [2]. Circles: La-1038 data from [6]. Spots: Data of (Ca$_{1-y}$La$_y$Fe$_{1-x}$Pt$_x$As)$_{10}$Pt$_3$As$_8$. Crosses: Data of antiferromagnetic phase from [7, 12]. Dashed line: Tentative border of antiferromagnetic phase.**

The phase diagram clearly shows the effectivity of charge doping to induce high T_c superconductivity in (CaFe$_{1-x}$Pt$_x$As)$_{10}$Pt$_z$As$_8$ with an optimal electron doping of $v = 0.13$, thus being in good agreement with the one found for the analogue system La(O$_{1-x}$F$_x$)FeAs.[13] Superconductivity can also be induced by direct Pt doping in the 1038 phase, reaching T_c below 15 K which is consistent with results reported for Ba(Fe$_{1-x}$Pt$_x$)$_2$As$_2$.[14] However direct doping appears to be detrimental for superconductivity in (CaFe$_{1-x}$Pt$_x$As)$_{10}$Pt$_z$As$_8$ and (Ca$_{1-y}$La$_y$Fe$_{1-x}$Pt$_x$As)$_{10}$Pt$_3$As$_8$ in the charge doped regime, so that highest T_c only emerge in the presence of clean FeAs layers.

2.9.4 *Conclusion*

The suggested electronic similarity of (Ca$_{0.87}$La$_{0.13}$FeAs)$_{10}$Pt$_3$As$_8$ and (CaFeAs)$_{10}$Pt$_4$As$_8$[2, 6] was investigated by DFT calculations. A pseudo band gap of the Pt-5d states was found at E_F for both compounds, allowing for a charge transfer to iron. Although it is against chemical intuition on the first sight, a peculiar electronic situation is formed where iron is formally more electronegative than platinum. Comparable Fermi surfaces indicate similar electron doping levels in (Ca$_{0.87}$La$_{0.13}$FeAs)$_{10}$Pt$_3$As$_8$ and (CaFeAs)$_{10}$Pt$_4$As$_8$. Concluding from this theoretical aspects and the reported similar $T_{c,max} \approx 35$ K[1] a scenario of electronic equivalency in

$(Ca_{0.87}La_{0.13}FeAs)_{10}Pt_3As_8$ and $(CaFeAs)_{10}Pt_4As_8$ was established. Comparing structural differences between La-1038 and 1048 neither the different Pt_zAs_8 layers nor layer distances were found to have relevant influence on the properties. Accepting the secondary role of the structural differences together with the relation of $(CaFe_{1-x}Pt_xAs)_{10}Pt_3As_8$ and $(CaFe_{1-x}Pt_xAs)_{10}Pt_4As_8$ discussed in reference [2], this results allowed for a consolidation of the different compounds $(CaFe_{1-x}Pt_xAs)_{10}Pt_3As_8$, $(CaFe_{1-x}Pt_xAs)_{10}Pt_4As_8$, and $(Ca_{1-y}La_yFeAs)_{10}Pt_3As_8$ to one class of iron arsenides. From that a phase diagram was constructed combining T_c data for electron and direct doping. Moreover the codoped mixed crystal series $(Ca_{1-y}La_yFe_{1-x}Pt_xAs)_{10}Pt_3As_8$ was synthesized to investigate and complete the Ca–Fe–Pt–As phase diagram in the vicinity of $T_{c,max}$. Although it is reported that superconductivity can be induced upon direct Pt doping in 1038,[1, 3] this work substantiated, that substitutions on the Fe sites are detrimental to superconductivity in the regime of charge doping. Thus highest T_c can only be achieved by charge doping with clean FeAs layers as was also shown for $Ba_{1-x}K_x(Fe_{1-y}Co_y)_2As_2$ recently.[15]

2.9.5   *References*

[1]   C. Löhnert, T. Stürzer, M. Tegel, R. Frankovsky, G. Friederichs, D. Johrendt, *Angew. Chem. Int. Ed.* **2011**, *50*, 9195.

[2]   T. Stürzer, G. Derondeau, D. Johrendt, *Phys. Rev. B* **2012**, *86*, 060516.

[3]   N. Ni, J. M. Allred, B. C. Chan, R. J. Cava, *Proc. Natl. Acad. Sci. USA* **2011**, *108*, E1019.

[4]   S. Kakiya, K. Kudo, Y. Nishikubo, K. Oku, E. Nishibori, H. Sawa, T. Yamamoto, T. Nozaka, M. Nohara, *J. Phys. Soc. Jpn.* **2011**, *80*, 093704.

[5]   M. Nohara, S. Kakiya, K. Kudo, Y. Oshiro, S. Araki, T. C. Kobayashi, K. Oku, E. Nishibori, H. Sawa, *Solid State Commun.* **2012**, *152*, 635.

[6]   T. Stürzer, G. Derondeau, E.-M. Bertschler, D. Johrendt, *Solid State Commun.* **2015**, *201*, 36.

[7]   N. Ni, W. E. Straszheim, D. J. Williams, M. A. Tanatar, R. Prozorov, E. D. Bauer, F. Ronning, J. D. Thompson, R. J. Cava, *Phys. Rev. B* **2013**, *87*, 060507.

[8]   A. Coelho, *TOPAS-Academic*, Version 4.1, Coelho Software, Brisbane, Australia, **2007**.

[9]   K. Schwarz, P. Blaha, *Comp. Mat. Sci.* **2003**, *28*, 259.

[10]   P. Blaha, K. Schwarz, G. K. H. Madsen, D. Kvasnicka, J. Luitz, *WIEN2K-augmented plane wave+local orbitals program for calculating crystal properties* **2001**.

[11]   N. Wiberg, E. Wiberg, A. F. Holleman, *Lehrbuch der Anorganischen Chemie* **2007**, de Gruyter.

[12]   T. Stürzer, G. M. Friederichs, H. Luetkens, A. Amato, H.-H. Klauss, D. Johrendt, *J. Phys.: Condens. Matter* **2013**, *25*, 122203.

[13]   Y. Kamihara, T. Watanabe, M. Hirano, H. Hosono, *J. Am. Chem. Soc.* **2008**, *130*, 3296.

[14]   S. R. Saha, T. Drye, K. Kirshenbaum, N. P. Butch, P. Y. Zavalij, P. Johnpierre, *J. Phys.: Condens. Matter* **2010**, *22*, 072204.

[15]   T. Goltz, V. Zinth, D. Johrendt, H. Rosner, G. Pascua, H. Luetkens, P. Materne, H.-H. Klauss, *arXiv:1402.0711 (unpublished),* **2014**.

2.10 Suppression of Superconductivity by Compensation of Charge doping in $(Ca_{1-y}Na_yFeAs)_{10}Pt_4As_8$
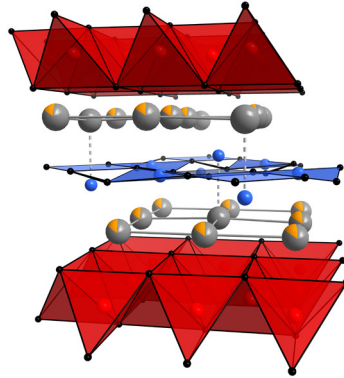
2.10.1 *Introduction*

Although the mechanism of superconductivity in iron based materials has not been finally clarified, it is generally accepted that the charge of the iron arsenide layer $(FeAs)^{v-}$ influencing Fermi surface nesting plays the dominant role for superconductivity.[1-5] While stoichiometric compounds like $BaFe_2As_2$[6-7] and $LaOFeAs$[8] are antiferromagnetic metals, critical temperatures up to 38 K[9] arise in hole doped $(Ba_{1-x}K_x)Fe_2As_2$ and 55 K[10] in electron doped $Sm(O_{1-x}F_x)FeAs$, respectively. Besides this (indirect) route to charge doping without manipulating the iron arsenide layer, also direct metal doping on the iron sites was found to induce superconductivity but with distinctly lower T_c. The reason for this difference remains unclear, although several aspects were discussed in literature.[11-13] *Zinth* et al. demonstrated the recovery of a parent-like state in charge compensated $(Ba_{1-x}K_x)(Fe_{0.93}Co_{0.07})_2As_2$ with $x = 0.2$ similar to the stoichiometric parent $BaFe_2As_2$.[11] This finding revealed, that Co acts as electron donor, whereby the additional charge can be fully compensated by hole doping. In this context structural differences induced by the chemical manipulation appeared to have minor relevance. Therewith this study demonstrated how electron doping and structural effects can be experimentally evidenced by codoping.

The origin for the drastic differences in properties comparing $(CaFeAs)_{10}Pt_3As_8$ and $(CaFeAs)_{10}Pt_4As_8$ was found in the different electronic situations present in both compounds. As discussed in Chapter 2.3 stoichiometric 1038 is a typical iron arsenide parent compound.[14] Stoichiometric 1048, however, can be characterized an electron doped superconductor whereby additional electrons originate from the fourth Pt in the Pt_zAs_8 layer.[15] This doping scenario combined the 1038 and 1048 compounds to one family

$(CaFeAs)_{10}Pt_zAs_8$ despite their considerable structural differences. Experimental substantiation was found in electron doped $(Ca_{1-y}RE_yFeAs)_{10}Pt_3As_8$ (Chapter 2.7) and codoped $(Ca_{1-y}La_yFe_{1-x}Pt_xAs)_{10}Pt_3As_8$ (Chapter 2.9) featuring properties analogue to the 1048 compound $(CaFe_{1-x}Pt_xAs)_{10}Pt_4As_8$. Thus so far investigations comparing 1038 and 1048 focused on the realization of a 1048-like state in compounds with 1038 structure. In this chapter the reverse reasoning will be discussed based on $(Ca_{1-y}Na_yFeAs)_{10}Pt_4As_8$ representing a system where the intrinsic electron doping of the Pt_4As_8 layer can be compensated by Na hole doping. The mixed crystal series was synthesized and characterized by means of ambient and low temperature powder diffraction, single crystal diffraction, *ac*-susceptibility, and SQUID measurements as well as DFT calculations to investigate a potential recovery of a parent-like state present in stoichiometric 1038.

2.10.2 *Experimental Details*

Powder samples of $(Ca_{1-y}Na_yFeAs)_{10}Pt_4As_8$ were prepared by mixing stoichiometric amounts of the elements (Ca: 99.99 %, Na: 99.8 %, La: 99.9 %, Fe: 99.9 %, Pt: 99.95 %, As: 99.999 %) in alumina crucibles, which were encapsulated in niobium tubes and then sealed in argon filled silica tubes. The samples were heated for 20 h at 800 °C, then cooled to ambient temperature. Afterwards they were grounded, sealed in niobium and silica tubes, reheated to 800 °C for 25 h, pelletized, and again treated for 25 h at 800 °C. Crystalline powders were characterized by X-ray powder diffraction using the Rietveld method with TOPAS[16] assuming the β-1048 structure as best approximation. Compositions were determined within errors of 10 % by X-ray spectroscopy (EDX). Singles crystals were selected from the polycrystalline samples and X-ray intensity data were measured on a BRUKER D8 QUEST diffractometer. Indexing, integration, data reduction and absorption correction was done using the APEX2 software package with SAINT and SADAPS.[17] Structure refinements were performed against F^2 using the JANA2006 package.[18] Superconducting properties were determined using a SQUID and an *ac*-susceptometer at 1333 Hz in the temperature range of 3.5 to 300 K at a 3 Oe field between 1.8 K and 300 K. Full-potential density function theory (DFT) calculations were performed using the WIEN2K package.[19-20] Owing to the complexity of the structure, calculations for Na substituted 1048 were based on $(Ca_{0.8}Na_{0.2}FeAs)_{10}Pt_4As_8$ to avoid even more computational expensive superstructures.

2.10.3 *Results and Discussion*

1048 bulk samples have been reported to be very difficult to synthesize,[21] which is conspicuous by the widely absence of investigations on powder samples in literature. Nevertheless in this study it turned out, that Na substitution immensely improves synthesis of 1048 compounds. Almost phase pure samples of (Ca$_{1-y}$Na$_y$FeAs)$_{10}$Pt$_4$As$_8$ (> 90 wt%) were obtained with minor side phases FeAs, PtAs$_2$, NaFeAs, Ca$_3$Fe$_8$PtAs$_6$, Ca$_6$Fe$_{11}$Pt$_3$As$_8$, or CaFe$_2$As$_2$ (Figure 1). The 1048 structures were confirmed for the Na doped mixed crystal series by powder X-ray diffraction. Anisotropically broadened reflections in powder diffraction data as well as strong diffuse contribution in single crystal X-ray data for reflections complying with $2h + k \neq 5n$ ($n \in \mathbb{N}$) give evidence for stacking disorder in the superstructure as was found for the 1048 phase (Chapter 2.2). Moreover enhanced reflection broadening was generally conspicuous in powder X-ray data, indicating inhomogeneous Na distribution, which could not be improved by varying synthesis conditions. Single crystal investigations revealed Na mixing among sevenfold coordinated Ca sites, whereas eightfold coordinated Ca positions remain unsubstituted. Although Ca^{2+} is listed in literature to have little smaller ionic radius than Na$^+$,[22] the divalent calcium ion preferentially occupies the higher coordinated cation site (Figure 1). This finding is in line with the site preference found for rare earth dopants in (Ca$_{1-y}$RE$_y$FeAs)$_{10}$Pt$_3$As$_8$ (Chapter 2.6 and 2.7).[15]

The course of unit cell axes upon Na doping in (Ca$_{1-y}$Na$_y$FeAs)$_{10}$Pt$_4$As$_8$ is depicted in Figure 2. *c*-axis and therewith interlayer distances monotonically increase probably due to a decreasing ionic attraction between the layers upon Na substitution. In the same course the *ab*-plane shows a small reduction in size, while cell angles remain constant. Therewith unit cell volume is slightly increased over the range $0 \leq y \leq 0.5$ by approximately 1 %. A solubility limit for Na in (Ca$_{1-y}$Na$_y$FeAs)$_{10}$Pt$_4$As$_8$ was found around $y = 0.5$, as depicted in Figure 2, comparing nominal and measured substitution level.
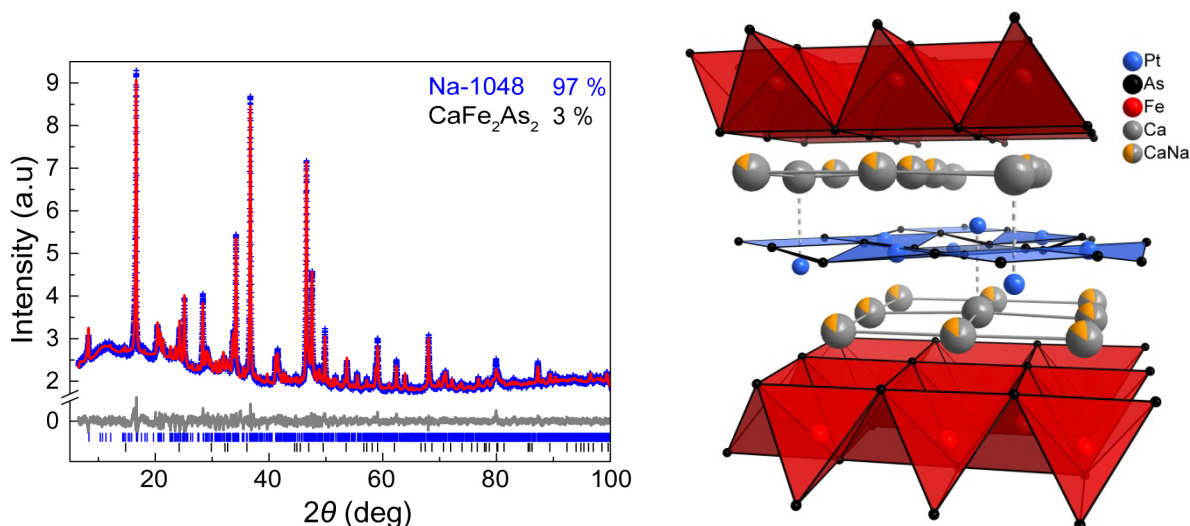
Figure 1. X-ray powder pattern (blue), Rietveld fit (red), and difference curve (gray) of (Ca$_{1-y}$Na$_y$FeAs)$_{10}$Pt$_4$As$_8$ with $y = 0.25$ (black tick marks) and minor impurity of CaFe$_2$As$_2$ (blue tick marks) (left). Structure section of (Ca$_{1-y}$Na$_y$FeAs)$_{10}$Pt$_4$As$_8$ illustrating sevenfold coordinated Na/Ca mixed sites (gray-orange) and unsubstituted eightfold coordinated Ca (gray). The special antiprismatic Ca position above/below the deflected Pt sites is emphasized by dashed lines (right).
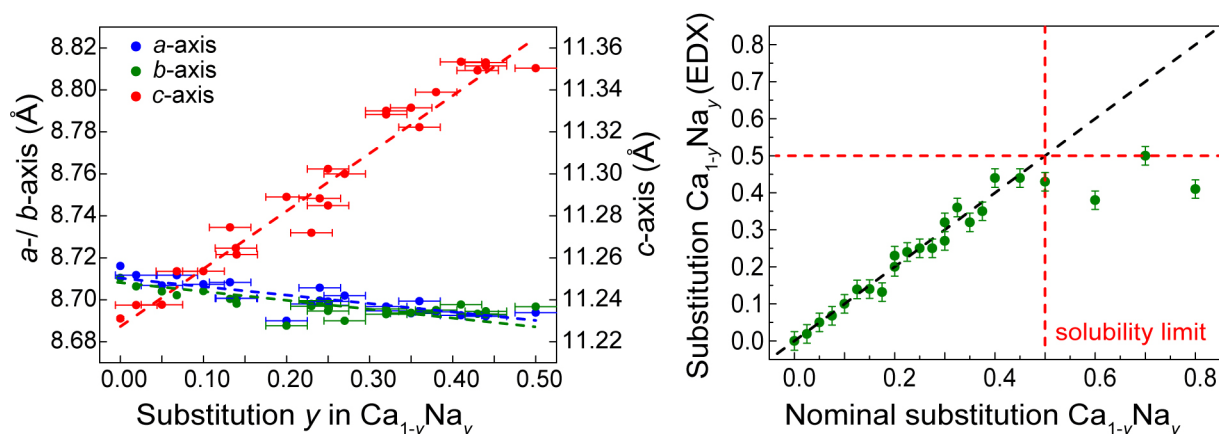
Figure 2. Course of unit cell axes of (Ca$_{1-y}$Na$_y$FeAs)$_{10}$Pt$_4$As$_8$ upon Na substitution y (left). Comparison of nominal and actual composition as determined by EDX spectroscopy indicating a Na solubility limit around $y = 0.5$ (right).

Susceptibility measurements of samples (Ca$_{1-y}$Na$_y$FeAs)$_{10}$Pt$_4$As$_8$ are shown in Figure 3 for $0 \leq y \leq 0.23$. Critical temperatures and superconducting volume fractions are drastically reduced upon Na doping, whereby only traces of superconductivity were detectable for $y = 0.23$. Thus Na substitution presents an effective tool to compensate intrinsic electron doping originating of the Pt$_4$As$_8$ layer. However, a further increase of Na substitution level beyond $y = 0.23$ gives rise to high superconducting volume fractions, along with a second transition. Whether this effect indicates a hole doped regime in the 1048 phase diagram, or originates from side phases is uncertain at this stage. Nevertheless, substitution depended unit cell axes substantiate Na inclusion to the 1048 structure up to $y = 0.5$ and amounts of minor side phases appear inconsistent with superconducting volume fractions measured so far. Thus,

further investigations are necessary in the high Na doped regime of the this system. Results obtained on (Ca$_{1-y}$Na$_y$FeAs)$_{10}$Pt$_4$As$_8$ are compiled in Figure 3.
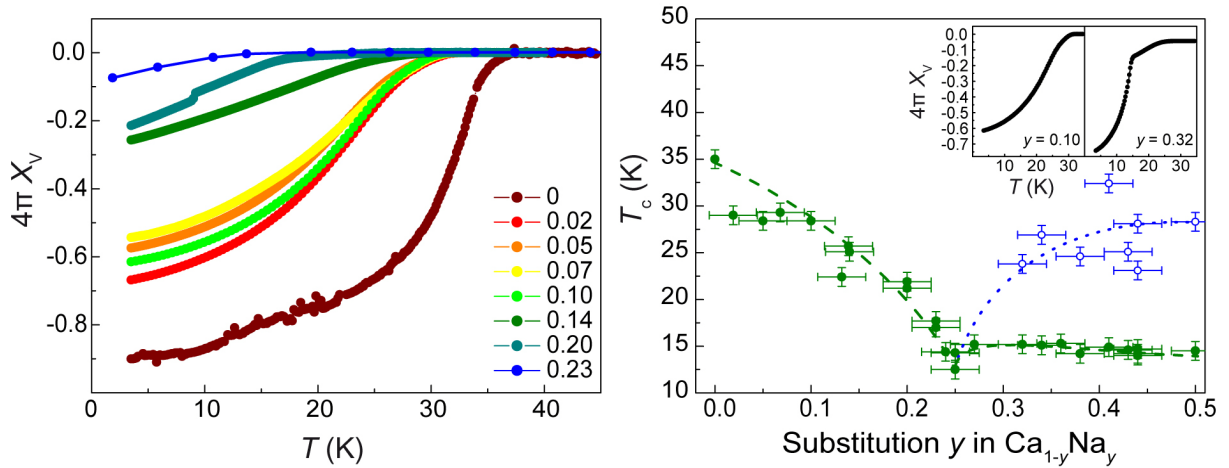
Figure 3. Magnetic susceptibility of (Ca$_{1-y}$Na$_y$FeAs)$_{10}$Pt$_4$As$_8$ with $0 \leq y \leq 0.23$ showing the gradual decrease of T_c and superconducting volume fraction upon Na substitution. Increasing inhomogeneity is conspicuous from transition width (left). Phase diagram of (Ca$_{1-y}$Na$_y$FeAs)$_{10}$Pt$_4$As$_8$ with $0 \leq y \leq 0.5$. Green spots: Superconducting bulk transition. Blue spots: Second superconducting transition arising at higher substitution levels (right).

Investigations on the 1038 and 1048 system so far established the model of 1048 and *RE* doped 1038 compounds being electron doped derivatives of the non-superconducting parent (CaFeAs)$_{10}$Pt$_3$As$_8$, with an optimal electron doping level of 0.13 e^-/FeAs. In this context the structural differences of 1038 and 1048 compounds were found to play a subsidiary role.[15, 23] Density of states calculations for (Ca$_{0.8}$Na$_{0.2}$FeAs)$_{10}$Pt$_4$As$_8$ in Figure 4 highlight the close electronic resemblance to (CaFeAs)$_{10}$Pt$_3$As$_8$.
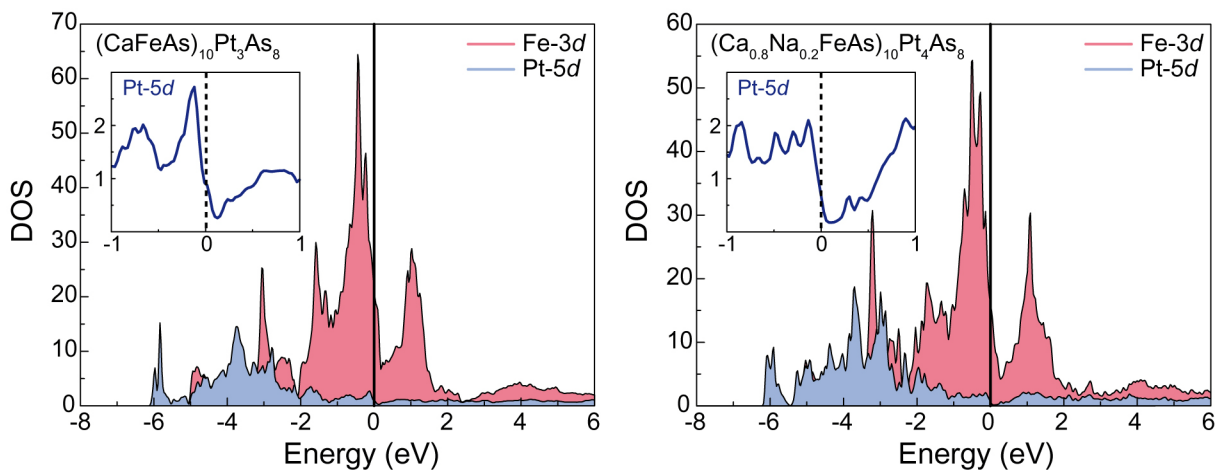
Figure 4. Comparison of density of states (DOS) of stoichiometric (CaFeAs)$_{10}$Pt$_3$As$_8$ (left) and Na substituted (Ca$_{0.8}$Na$_{0.2}$FeAs)$_{10}$Pt$_4$As$_8$ (right).

Both compounds feature almost exclusively Fe-3d states at the Fermi energy with E_F being located just below the Pt-5d pseudo band gap. Thus this calculations impressively

demonstrate that Na substitution allows for a tuning of the iron arsenide layer charge $(FeAs)^{v-}$ similar as found for $(Ca_{1-x}RE_xFeAs)_{10}Pt_3As_8$. Concluding from that a recovery of a parent state similar to stoichiometric $(CaFeAs)_{10}Pt_3As_8$ is expected for hole doped $(Ca_{1-y}Na_yFeAs)_{10}Pt_4As_8$ with $y \approx 0.15$.

Experimental data (Figure 3), however, revealed a minimum of T_c around $y = 0.23$ distinctly different from $y = 0.13 - 0.15$ as expected from the electron doping model and theoretical considerations (Chapter 2.6, 2.7, and 2.9). Moreover no complete suppression of superconductivity was achieved, although Na substitution was proven to be detrimental to superconductivity in this case. Susceptibility measurements on samples with $y = 0.15$ and 0.25 give no indication for a reemergence of magnetic ordering. Corresponding powder data reveal significant reflection broadening at low temperatures, possibly hinting to a small structural distortion. A quantification, however, failed so far. From this results it was concluded, that a recovery of a 1038 parent-like state should be accessible by Na doping in 1048, but the formation of fully charge compensated samples is hindered by the inhomogeneity of the Na distribution within the samples. Although the existence of a fully charge compensated parent state like in $(Ba_{1-x}K_x)(Fe_{0.93}Co_{0.07})_2As_2$ could not be evidenced in this work, the model of intrinsic charge doping in the 1048 compound was experimentally substantiated.

2.10.4 *Conclusion*

In this work the model of intrinsic charge doping suggested for 1048 compound $(CaFeAs)_{10}Pt_4As_8$ with respect to $(CaFeAs)_{10}Pt_3As_8$ was point of focus. Since this model was already experimentally evidenced by electron doped 1038 derivatives $(Ca_{1-y}RE_yFeAs)_{10}Pt_3As_8$,[23] the reverse reasoning of charge doping compensation in Na substituted 1048 was investigated. DFT calculations were consulted to illustrate the close electronic resemblance of stoichiometric 1038 and $(Ca_{1-y}Na_yFeAs)_{10}Pt_4As_8$ also demonstrating Na substitution being an effective instrument to tune E_F. Despite reported difficulties to prepare 1048 samples, Na substituted compounds revealed to be easily synthetically accessible up to $y = 0.5$. Site preference of Na dopants for the lower coordinated Ca sites was found being in line with reported analogue site preferences in $(Ca_{1-y}RE_yFeAs)_{10}Pt_3As_8$. Structural changes upon Na substitution in $(Ca_{1-y}Na_yFeAs)_{10}Pt_4As_8$ are in agreement with the expectations for a reduced ionic interaction between the layers. Magnetic measurements identified a gradual reduction of critical temperatures upon Na substitution, whereby superconductivity was almost completely suppressed at $y = 0.23$. For higher Na content a renewed increase of

superconducting volume fraction along with a second transition was found, with unclear origin so far. Powder data of samples with $y \approx 0.2$ revealed reflection broadening at low temperatures, but neither a reemergence of magnetic ordering nor a structural distortion could be identified. The absence of a complete recovery of a parent-like state as well as the emergence of minimum T_c at $y = 0.2$ instead of 0.15 as predicted from theoretical considerations is probably caused by inhomogeneous sodium substitution. Nevertheless the reduction of critical temperatures up to an almost complete suppression by Na gives direct evidence of the electron doped nature of stoichiometric 1048 and is fully consistent with the model established for the compounds (CaFeAs)$_{10}$Pt$_z$As$_8$ so far.

2.10.5 *References*

[1]   A. D. Christianson, E. A. Goremychkin, R. Osborn, S. Rosenkranz, M. D. Lumsden, C. D. Malliakas, I. S. Todorov, H. Claus, D. Y. Chung, M. G. Kanatzidis, R. I. Bewley, T. Guidi, *Nature* **2008**, *456*, 930.

[2]   H. Ding, P. Richard, K. Nakayama, K. Sugawara, T. Arakane, Y. Sekiba, A. Takayama, S. Souma, T. Sato, T. Takahashi, Z. Wang, X. Dai, Z. Fang, G. F. Chen, J. L. Luo, N. L. Wang, *Europhys. Lett.* **2008**, *83*, 47001.

[3]   I. I. Mazin, D. J. Singh, M. D. Johannes, M. H. Du, *Phys. Rev. Lett.* **2008**, *101*, 057003.

[4]   K. Kuroki, S. Onari, R. Arita, H. Usui, Y. Tanaka, H. Kontani, H. Aoki, *Phys. Rev. Lett.* **2008**, *101*, 087004.

[5]   Y.-Z. Zhang, I. Opahle, H. O. Jeschke, R. Valentí, *Phys. Rev. B* **2010**, *81*, 094505.

[6]   M. Pfisterer, G. Nagorsen, *Z. Naturforsch. B* **1980**, *35*, 703

[7]   M. Rotter, M. Tegel, D. Johrendt, I. Schellenberg, W. Hermes, R. Pöttgen, *Phys. Rev. B* **2008**, *78*, 020503.

[8]   H. Raffius, E. Morsen, B. D. Mosel, W. Mueller-Warmuth, W. Jeitschko, L. Terbuchte, T. Vomhof, *Journal of Physics and Chemistry of Solid* **1993**, *54*, 135.

[9]   M. Rotter, M. Tegel, D. Johrendt, *Phys. Rev. Lett.* **2008**, *101*, 107006.

[10]   Z.-A. Ren, W. Lu, J. Yang, W. Yi, X.-L. Shen, C. Zheng, G.-C. Che, X.-L. Dong, L.-L. Sun, F. Zhou, Z.-X. Zhao, *Chin. Phys. Lett.* **2008**, *25*, 2215.

[11]   V. Zinth, T. Dellmann, H.-H. Klauss, D. Johrendt, *Angew. Chem. Int. Ed.* **2011**, *50*, 7919.

[12]   T. Goltz, V. Zinth, D. Johrendt, H. Rosner, G. Pascua, H. Luetkens, P. Materne, H.-H. Klauss, *arXiv:1402.0711 (unpublished),* **2014**.

[13]   H. Wadati, I. Elfimov, G. A. Sawatzky, *Phys. Rev. Lett.* **2010**, *105*, 157004.

[14]   T. Stürzer, G. M. Friederichs, H. Luetkens, A. Amato, H.-H. Klauss, D. Johrendt, *J. Phys.: Condens. Matter* **2013**, *25*, 122203.

[15]   T. Stürzer, G. Derondeau, D. Johrendt, *Phys. Rev. B* **2012**, *86*, 060516.

[16]   A. Coelho, *TOPAS-Academic*, Version 4.1, Coelho Software, Brisbane, Australia, **2007**.

[17]   a) APEX2, 2009.9 ed., Bruker AXS Inc., Madison, Wisconsin, 2009. b) SAINT, 7.68A ed., Bruker AXS Inc., Madison, Wisconsin, 2009. c) SADABS, 2008/1 ed., Bruker AXS Inc., Madison, Wisconsin, 2008.

[18]   V. Petricek, M. Dusek, L. Palatinus, *Jana2006 Structure Determination Software Programs*, Institute of Physics, Praha, Czech Republic, **2009**.

[19]   K. Schwarz, P. Blaha, *Comp. Mat. Sci.* **2003**, *28*, 259.

[20]   P. Blaha, K. Schwarz, G. K. H. Madsen, D. Kvasnicka, J. Luitz, *WIEN2K-augmented plane wave+local orbitals program for calculating crystal properties* **2001**.

[21]   T. Stürzer, *Masterthesis*, Ludwig-Maximilians-Universität München, **2011**.

[22]   N. Wiberg, E. Wiberg, A. F. Holleman, *Lehrbuch der Anorganischen Chemie* **2007**, de Gruyter.

[23]   T. Stürzer, G. Derondeau, E.-M. Bertschler, D. Johrendt, *Solid State Commun.* **2015**, *201*, 36.

3 New Iron Arsenide Compounds with interconnected FeAs Layers

3.1 Framework Structures of interconnected Layers in Calcium Iron Arsenides

T. Stürzer, C. Hieke, C. Löhnert, F. Nitsche, J. Stahl, C. Maak, R. Pobel, D. Johrendt
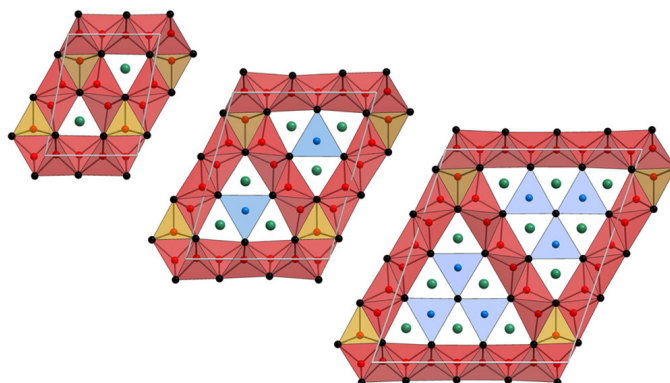
Abstract

The new calcium iron arsenide compounds $Ca_{n(n+1)/2}(Fe_{1-x}M_x)_{(2+3n)}M'_{n(n-1)/2}As_{(n+1)(n+2)/2}$ ($n = 1 - 3$; $M =$ Nb, Pd, Pt; $M' = \square$ Pd, Pt) were synthesized and their crystal structures determined by single crystal X-ray diffraction. The series demonstrates the structural flexibility of iron arsenide materials, which otherwise prefer layered structures, as is known from the family of iron-based superconductors. In the new compounds, iron arsenide tetrahedral layers are bridged by iron-centered pyramids, giving rise to so far unknown frameworks of interconnected FeAs layers. Channels within the structures are occupied with calcium and palladium or platinum, respectively. Common basic building blocks are identified that lead to a better understanding of the building principles of these structures and their relation to $CaFe_4As_3$.

3.1.1 *Introduction*

Layered iron arsenides have earned sweeping prominence in the solid-state chemistry and physics communities during the last years because of the emergence of high-temperature

superconductivity up to 55 K.[1–4] Therewith, the family of layered iron arsenides was found to be a new class of high T_c superconductors beyond the copper oxides discovered in the 1980s.[5] Intensive research has meanwhile identified a growing family of layered compounds each containing two-dimensional FeAs layers.[6] A magnetic instability in the iron layers intertwined with the superconducting properties has been uncovered,[7] which can be manipulated by chemical doping, pressure, or complete replacement of the separating layers by other two-dimensional structure fragments.[6, 8] The presence of layered structures in both high T_c superconductor families has raised the question about the general necessity of low dimensionality, but no final consent has been found on this topic so far. Besides, other structures, featuring fragments of FeAs tetrahedral layers, are also expected to reveal very interesting properties, although it is not clear whether superconductivity could arise in such systems. In 2009, the compound $CaFe_4As_3$ with a structure consisting of interconnected $FeAs_{4/4}$ tetrahedral bands forming channels occupied with calcium was identified.[9] At the band joints, iron is pyramidally coordinated by five arsenic ions connecting two bands. Magnetic measurements identified iron(II) in the $FeAs_{4/4}$ tetrahedra but also remarkably iron(I) in the $FeAs_{5/5}$ pyramids.[10] Also, hints to a spin density wave were reported similar to the layered compounds, but despite diverse substitution attempts, no superconducting properties were achieved.[11] In this paper, we report five new structure types in the iron arsenide family with the general composition $Ca_{n(n+1)/2}(Fe_{1-x}M_x)_{(2+3n)}M'_{n(n-1)/2}As_{(n+1)(n+2)/2}$ (M = Nb, Pd, Pt; M' = □ Pd, Pt) with $n = 1 - 3$, featuring three-dimensional frameworks of interconnected layers. A structural breakdown of these compounds to basic building blocks is given, yielding a systematic understanding of the relationship of these structures to each other and their close relationship to $CaFe_4As_3$ as well as to layered iron pnictides. Finally, the connection to a long-known class of intermetallic compounds with a metal-to-pnictide ratio of 2 : 1 is illustrated.

3.1.2 *Experimental Details*

Polycrystalline samples of the compounds $Ca_{n(n+1)/2}(Fe_{1-x}M_x)_{(2+3n)}M'_{n(n-1)/2}As_{(n+1)(n+2)/2}$ with $n = 2$ and 3 and $(Ca,Na)_3(Fe,Nb)_8As_6$ were synthesized by solid-state methods under ambient pressure. Stoichiometric mixtures of pure elements (> 99.5 %) were heated at $900 - 1000\,°C$ in alumina crucibles or niobium tubes, respectively, and sealed in silica tubes under purified argon. The samples were thoroughly homogenized and annealed twice at $900 - 1000\,°C$. The $α$-polymorphs of the compounds with $n = 1$ and 2 were synthesized from a mixture of binary starting materials and pure elements (> 99.5 %) by high-pressure synthesis in boron nitride crucibles at 6 GPa and 1000 °C, using a modified Walker-type multianvil apparatus.[12, 13]

Bulk α-Ca$_3$Fe$_8$PtAs$_6$ was obtained by both high-pressure and high-temperature synthesis, whereas CaFe$_5$As$_3$ was accessible only by high-pressure synthesis. β-Ca$_3$Fe$_8$PtAs$_6$ was only obtainable as a side phase. In the Ca–Fe–Pd–As system, solid-state synthesis always yielded a mixture of the β- and γ- modifications. An α-type compound has not been identified so far. All samples were characterized by powder X-ray diffraction using a HUBER G670 diffracto-meter with Cu Kα_1 or Co Kα_1 radiation. Singles crystals were selected from the poly-crystalline samples, and X-ray intensity data were measured on a STOE IPDS-I or a BRUKER D8 QUEST diffractometer. Energy dispersive X-ray spectroscopy was used to check the compositions. The structure refinements were performed against F^2 using the JANA2006 program package.[14] Rietveld refinements of the powder diffraction data were performed with the TOPAS package[15] by using the structural data obtained by the single crystal experiments. A typical pattern with a Rietveld fit is exemplarily shown in Figure 1. Up to 10 % of impurity phases were detected in the bulk samples, mostly binary arsenides.
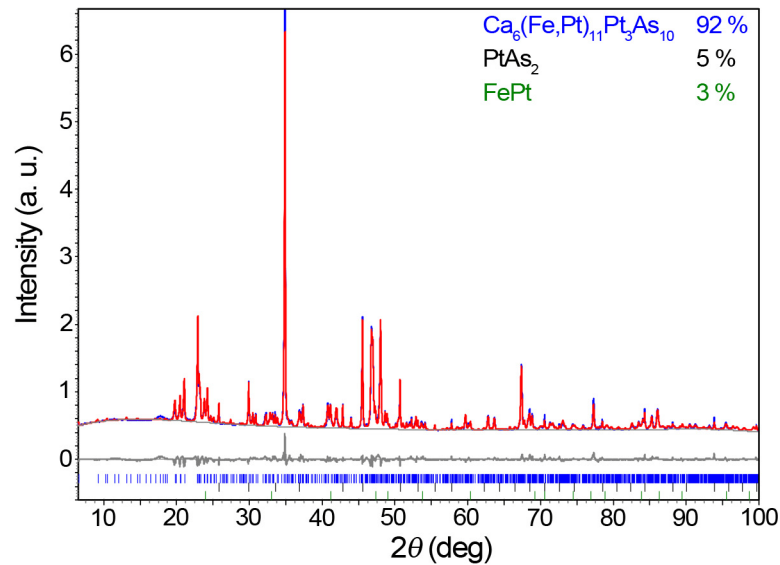
Figure 1. Powder X-ray diffraction pattern (blue) and Rietveld fit (red) of Ca$_6$(Fe,Pt)$_{11}$Pt$_3$As$_{10}$.

Table 1. Crystal data and refinement parameters.

compound	CaFe$_5$As$_3$	Ca$_3$Fe$_8\square$As$_6$	Ca$_3$Fe$_8$PtAs$_6$	Ca$_3$Fe$_8$PdAs$_6$
structure	α-CaFe$_5$As$_3$	α-Ca$_3$Fe$_8\square$As$_6$	α-Ca$_3$Fe$_8$PtAs$_6$	β-Ca$_3$Fe$_8$PdAs$_6$
composition	CaFe$_5$As$_3$	Ca$_{2.56}$Na$_{0.44}$Fe$_{7.49}$Nb$_{0.51}$As$_6$	Ca$_3$Fe$_{7.705}$Pt$_{1.295}$As$_6$	Ca$_3$Fe$_{7.04}$Pd$_{1.96}$As$_6$
space group	$P2_1/m$	$P2_1/m$	$P2_1/m$	$Pnma$
Z	2	2	2	4
a (Å)	7.2734(6)	11.3307(9)	11.3169(5)	26.363(4)
b (Å)	3.8149(3)	3.8078(3)	3.8809(2)	3.8699(5)

c (Å)	9.7577(8)	13.6298(11)	13.7008(6)	11.330(1)
β (deg)	100.704(2)	106.154(3)	105.957(2)	90
Vol (Å^3)	266.04(4)	564.84(8)	578.55(5)	1155.9(2)
R_1(obs/all)	0.033/0.037	0.081/0.134	0.024/0.031	0.038/0.068
wR_2(obs/all)	0.085/0.094	0.178/0.197	0.066/0.072	0.082/0.085

compound	$Ca_3Fe_8PtAs_6$	$Ca_3Fe_8PdAs_6$	$Ca_6Fe_{11}Pd_3As_{10}$	$Ca_6Fe_{11}Pt_3As_{10}$
structure	β-$Ca_3Fe_8PtAs_6$	γ-$Ca_3Fe_8PdAs_6$	α-$Ca_6Fe_{11}Pd_3As_{10}$	α-$Ca_6Fe_{11}Pt_3As_{10}$
composition	$Ca_3Fe_{6.72}Pt_{2.28}As_6$	$Ca_3Fe_{4.74}Pd_{4.26}As_6$	$Ca_6Fe_{7.88}Pd_{6.12}As_{10}$	$Ca_6Fe_{7.62}Pt_{6.38}As_{10}$
space group	$Pnma$	$Pnma$	$P2_1/m$	$P2_1/m$
Z	4	4	2	2
a (Å)	26.435(3)	19.856(3)	15.564(3)	15.499(1)
b (Å)	3.9177(10)	3.9461(5)	3.9679(6)	3.9807(2)
c (Å)	11.345(2)	15.343(2)	17.880(3)	17.814(1)
β (deg)	90	90	108.748(5)	109.169(1)
Vol (Å^3)	1174.9(4)	1202.2(3)	1045.7(3)	1038.1(1)
R_1(obs/all)	0.051/0.137	0.023/0.066	0.064/0.125	0.036/0.058
wR_2(obs/all)	0.103/0.113	0.044/0.049	0.142/0.153	0.076/0.081

3.1.3 Results and Discussion

During the course of exploration in the field of iron arsenides, five so far unknown crystal structures were identified by single crystal X-ray structure determination (Table 1). The compounds obey the general composition of $Ca_{n(n+1)/2}(Fe_{1-x}M_x)_{(2+3n)}M'_{n(n-1)/2}As_{(n+1)(n+2)/2}$ (M = Nb, Pd, Pt; M' = $\square$ Pd, Pt) with $n = 1 - 3$. They crystallize in monoclinic or orthorhombic crystal systems and feature three-dimensional frameworks of interconnected layers forming parallel channels. Figure 2 depicts the triangular shape of the channels for $n = 1 - 3$. With $n > 1$, additional sites occur within the channels, which can be occupied by M'.
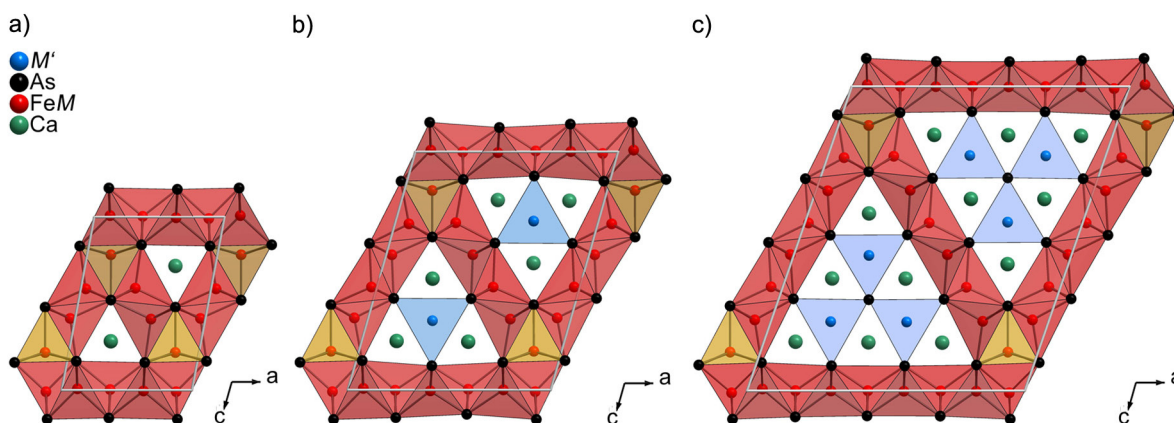
Figure 2. Crystal structures of the monoclinic compounds $Ca_{n(n+1)/2}(Fe_{1-x}M_x)_{(2+3n)}M'_{n(n-1)/2}As_{(n+1)(n+2)/2}$ (M = Pd, Pt; M' = $\square$ Pd, Pt) with $n = 1 - 3$ showing the channel shapes for varying n.

The new structures crystallize in the space groups $P2_1/m$ or $Pnma$, respectively, where they all share a short b-axis of about 3.9 Å with atomic sites exclusively on mirror planes at $y = \frac{1}{4}$ and $\frac{3}{4}$. A three-dimensional framework is formed by covalently bonded and interconnected iron arsenide layers, assembling equilateral triangular channels. Illustrations of the basic building units as well as the designation of labels of distances and angles for a later discussion are depicted in Figure 3. Similar to a scaffold, the framework can be divided into coplanar two-dimensional frames of $^{\infty}_{2}[Fe_{2(n+1)}(As_{4/4})_{2(n-1)}(As_{4/7})_4]$, diagonal braces $^{\infty}_{1}[Fe_{2n}(As_{4/4})_{2(n-1)}(As_{3/7})_2(As_{1/7})_2]$, and joints $^{\infty}_{1}[Fe(As_{2/7})_2As_{1/7}]$, generally keeping in mind their infinite arrangement along the short b-axis. This metaphoric description of the building blocks will be conveniently used for further structure discussion. The channels within the structures are populated with calcium and, depending on the compound composition, as well with arsenic and palladium or platinum in trigonal-planar coordination.
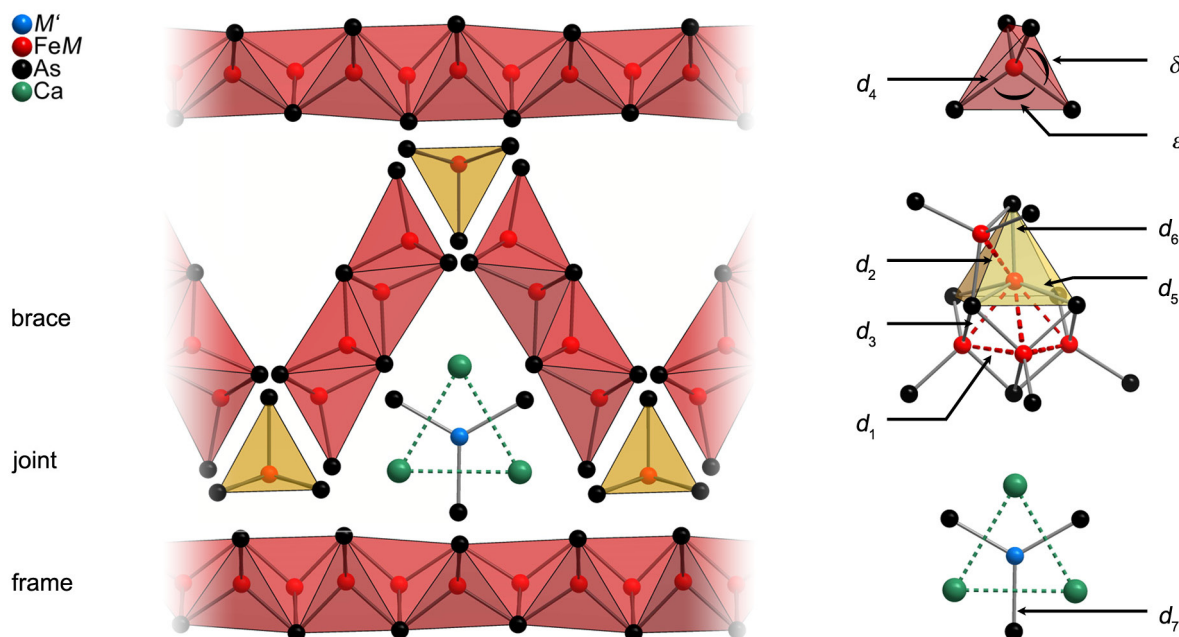
Figure 3. Basic building blocks of the compounds $Ca_{n(n+1)/2}(Fe_{1-x}M_x)_{(2+3n)}M'_{n(n-1)/2}As_{(n+1)(n+2)/2}$ (left) and coordination polyhedra and labels for distances and angles (right).

The frames are formed by edge-sharing $FeAs_{4/4}$ tetrahedral layers corresponding to the *anti*-PbO type. The atomic distances (d_4) and angles (δ and ε) are comparable to the values found in the structures of the layered iron arsenides, including in-plane Fe–Fe metal bonding (d_1).[6] Corresponding features were found for the braces with the mere difference of their restricted extent in the second dimension. A distinctly different situation was found for the joints. There, iron is surrounded by five arsenic atoms in pyramidal coordination. The base plane is formed by a rectangular arrangement of arsenic. Within these pyramids, the Fe As bond lengths (d_5 and d_6) are significantly enlarged compared to the tetrahedral layers (d_4). The same

situation was found regarding Fe–Fe distances (d_2 and d_3). Thus, the interaction of the braces to the frames is decreased, leading to a certain degree of two-dimensionality conserved in this structures, which can be also seen from the presence of continuous frames, being reminiscent of the layered iron arsenide structures. Nevertheless, the rectangular base plane of the joint pyramids leads to a local distortion within the frames. Therefore, each structure features one very small ε angle caused by a frame iron capping the short edge of the pyramid base. Table 2 gives a comparison summary of selected distances and angles for the compounds investigated.

Table 2. Selected interatomic distances (Å) and bond angles (deg).

structure	α-CaFe$_4$As$_3$	α-Ca$_3$Fe$_8\square$As$_6$	α-Ca$_3$Fe$_8$PtAs$_6$	β-Ca$_3$Fe$_8$PdAs$_6$
composition	CaFe$_5$As$_3$	Ca$_{2.56}$Na$_{0.44}$Fe$_{7.49}$Nb$_{0.51}$As$_6$	Ca$_3$Fe$_{7.71}$Pt$_{1.29}$As$_6$	Ca$_3$Fe$_{7.04}$Pd$_{1.96}$As$_6$
d_1(Fe–Fe)	2.5973(9)-2.7634(13)	2.6440(4)-2.8029(4)	2.6023(15)-2.8731(11)	2.6069(5)-2.8500(23)
d_2(Fe–Fe)	2.9824(9)-3.0241(10)	2.9397(3)-2.9582(4)	2.9425(12)-2.9762(17)	2.9481(19)-2.9902(19)
d_3(Fe–Fe)	2.6982(12)-2.7697(14)	2.7800(4)-2.8916(3)	2.7275(22)-2.9591(14)	2.7159(21)-2.9367(21)
d_4(Fe–As)	2.3830(10)-2.4712(11)	2.3983(4)-2.4623(3)	2.3861(9)-2.4767(10)	2.3855(19)-2.4998(16)
d_5(Fe–As)	2.6158(9)-2.6235(9)	2.6753(3)-2.6803(3)	2.6565(12)-2.6718(14)	2.6577(6)-2.6836(7)
d_6(Fe–As)	2.5062(9)	2.6202(4)	2.5703(16)	2.5772(23)
ε(As–Fe–As)	92.468(30)-106.950(34)	96.431(15)-108.352(13)	92.219(62)-111.216(55)	93.918(19)-111.154(94)
δ(As–Fe–As)	109.424(33)-116.309(34)	109.153(4)-115.268(4)	106.464(3)-115.670(3)	107.552(5)-114.892(4)
d_7(M–As)	-	-	2.4785(12)-2.4929(10)	2.4459(22)-2.4592(19)

structure	β-Ca$_3$Fe$_8$PtAs$_6$	γ-Ca$_3$Fe$_8$PdAs$_6$	α-Ca$_6$Fe$_{11}$Pd$_3$As$_{10}$	α-Ca$_6$Fe$_{11}$Pt$_3$As$_{10}$
composition	Ca$_3$Fe$_{6.72}$Pt$_{2.28}$As$_6$	Ca$_3$Fe$_{4.74}$Pd$_{4.26}$As$_6$	Ca$_6$Fe$_{7.88}$Pd$_{6.12}$As$_{10}$	Ca$_6$Fe$_{7.62}$Pt$_{6.38}$As$_{10}$
d_1(Fe–Fe)	2.6232(20)-2.8859(13)	2.6827(14)-2.8766(14)	2.7041(3)-2.8830(3)	2.6409(14)-2.8881(5)
d_2(Fe–Fe)	2.9651(18)-2.9979(20)	2.9881(12)-3.0224(13)	3.0232(3)-3.0299(3)	2.9714(10)-3.0033(14)
d_3(Fe–Fe)	2.6958(29)-2.9675(21)	2.7802(19)-2.9594(14)	2.7879(4)-2.7975(4)	2.7214(17)-3.0074(14)
d_4(Fe–As)	2.3732(21)-2.5513(12)	2.3485(18)-2.5626(11)	2.3618(3)-2.5828(3)	2.3952(12)-2.5775(9)
d_5(Fe–As)	2.6748(18)-2.7123(18)	2.7610(13)-2.7427(12)	2.7520(3)-2.7647(3)	2.7135(12)-2.7443(15)
d_6(Fe–As)	2.5579(27)	2.5700(18)	2.5905(4)	2.5531(17)

ε(As–Fe–As)	93.631(85)- 111.786(64)	99.098(6)- 110.940(53)	98.506(10)- 112.772(10)	94.900(64)- 112.246(49)
δ(As–Fe–As)	105.123(3)- 114.849(8)	107.791(4)- 113.733(3)	107.580(9)- 113.265(10)	107.567(2)- 113.820(2)
d_7(M–As)	2.4496(15)- 2.4594(15)	2.4481(13)- 2.4614(16)	2.4424(3)- 2.4683(4)	2.4305(13)- 2.4478(9)
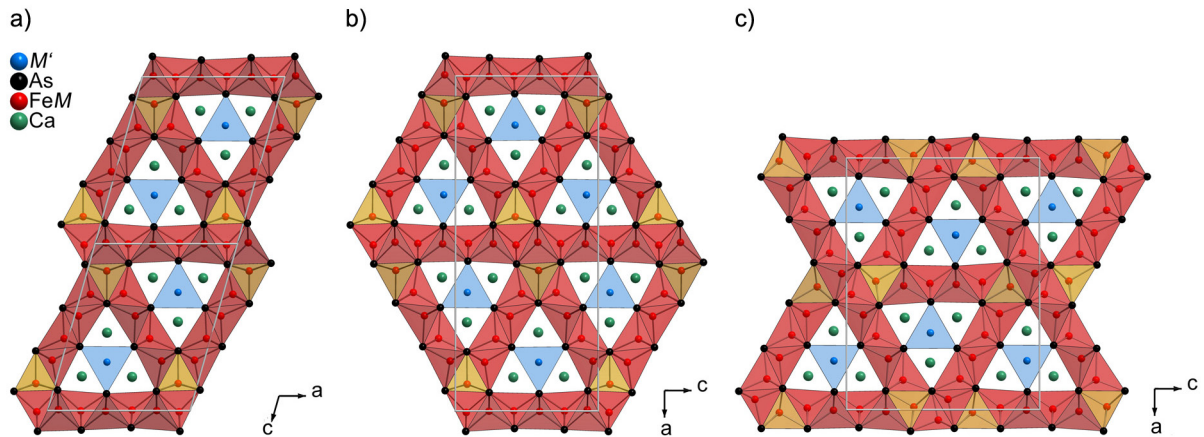
Figure 4. Different polymorphs of $Ca_{n(n+1)/2}(Fe_{1-x}M_x)_{(2+3n)}M'_{n(n-1)/2}As_{(n+1)(n+2)/2}$ with $n = 2$; (a) α-$Ca_3Fe_8M'As_6$; (b) β-$Ca_3Fe_8M'As_6$; (c) γ-$Ca_3Fe_8M'As_6$.

The compounds $Ca_{n(n+1)/2}(Fe_{1-x}M_x)_{(2+3n)}M'_{n(n-1)/2}As_{(n+1)(n+2)/2}$ comprise channels of varying size defined by the iron arsenide framework. Thus, depending on its size, each channel is populated with $n(n + 1)/2$ calcium atoms, each trigonal-prismatically coordinated by arsenic. These $CaAs_6$ prisms share faces, giving rise to strands within the channels. Additionally, compounds with $n \geq 2$ feature the possibility to host further metal atoms M' in each center of three edge connected strands, while this particular site is trigonal-planar coordinated by arsenic. Compounds with a vacancy, palladium, or platinum at this site were found for $n = 2$, and palladium or platinum for a structure with $n = 3$ could be identified so far. Similar planar coordination of palladium and platinum by arsenic was found in CaPtAs and in other compounds.[16, 17] For compounds exceeding $n = 2$, the channel size within the iron arsenide framework cannot coordinate all calcium atoms anymore. Therefore, additional arsenic is incorporated for $n > 2$, saturating the coordination of calcium. Generally, the iron arsenide frames and braces allow for partial palladium and platinum substitution of the iron sites, whereas hardly any mixing was traceable at the joints. However, adding niobium and sodium to the reaction gives rise to significant Fe/Nb mixing exclusively at the joints and Na/Ca mixing within the channels. Similar results were reported for chromium doped $CaFe_4As_3$.[10]

The availability of fundamental structural building blocks as frames, braces, and joints allows for a multitude of different structures, facilitating both different arrangements of the channels

and different channel sizes with a general composition of $Ca_{n(n+1)/2}(Fe_{1-x}M_x)_{(2+3n)}M'_{n(n-1)/2}As_{(n+1)(n+2)/2}$ and $n = 1, 2, 3, \ldots$. So far we could identify homologous structures for $n = 1 - 3$ as well as three different polymorphs for $n = 2$. Figure 2 illustrates the structures with constant channel arrangement and $n = 1 - 3$, while Figure 4 shows the different polymorphs found with constant $n = 2$. The γ-polymorph takes a special position within the presented structure discussion. The frames are intermitted every second channel, therewith losing their infinite extent in one direction. Considering the case $n = 0$, the general formula of this compound yields Fe_2As. The resulting structure for this type should lack any channels. Indeed, the structure of Fe_2As (Cu_2Sb type) reveals layers of edge-connected $FeAs_4$ tetrahedra as well as edge-connected $FeAs_5$ pyramids. Thus, even this long-known binary can be reduced to the basic building units that we described; however, in this special case, braces and channels are absent. Going the other way to the infinite limit $n = \infty$, a hypothetical structure would consist of a mere one "channel" with no iron arsenide frames, braces, and joints presented anymore. CaPtAs might be considered in this context,[18] locally featuring trigonal-planar coordinated platinum sites as well as edge-connected parallel strands of $CaAs_6$. Another more distorted representative would be CaPdAs.[19]

The view of fundamental building blocks described so far even allows for an easy understanding of the close relationship of our new structures to $CaFe_4As_3$ reported in 2009.[9] In this context, the structure of $CaFe_4As_3$ can be interpreted as a defect polymorph of the compound with $n = 1$ with an ordered vacancy of one iron site. A closer view actually reveals $CaFe_4As_3$ as the defect γ-polytype with $n = 1$. With the frames being discontinuous, the γ-type structures can be understood as two connected sawtooth layers, with each formed by one frame fragment, one brace, and two joints. Figure 5 compares both structures with the defect polyhedra of $CaFe_4As_3$ highlighted and contains a schematic illustration of the sawtooth-like motif of the γ-type.
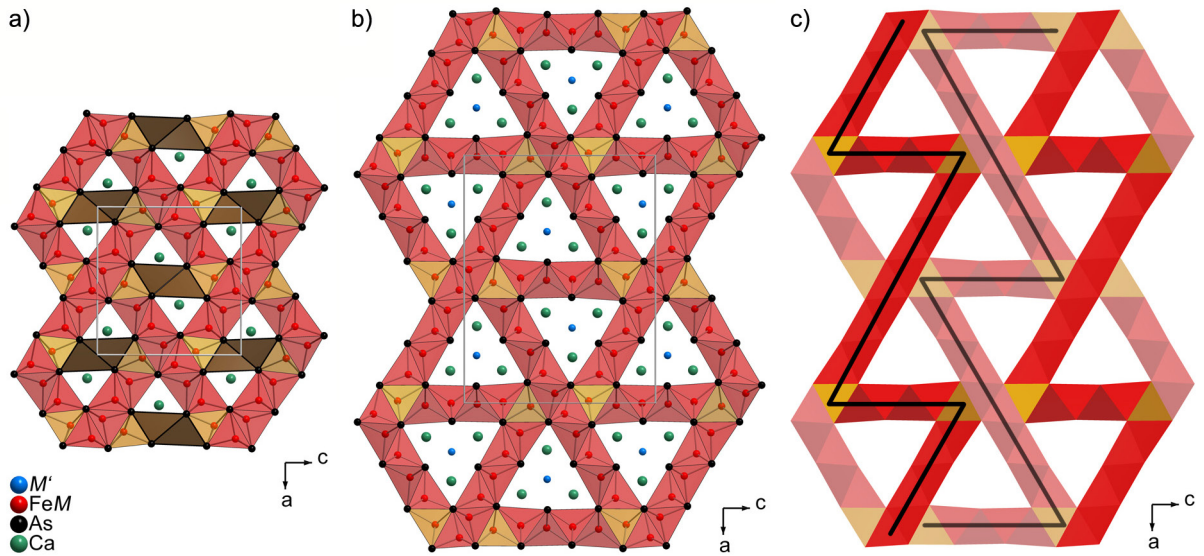
Figure 5. Comparing the structures of CaFe$_4$As$_3$ (left) in terms of a defect variant to γ-Ca$_3$Fe$_8$M'As$_6$ (middle). Defect sites are highlighted in brown. Sawtooth motif in the γ-type structures (right).

Although the existence of frameworks built by tetrahedra frames, braces, and pyramidal joints is quite new in the iron arsenide family, it is not exclusively restricted to this class of compounds. Most recently, *Khatun* et al. reported the structures of Rb$_4$M$_7$Pn$_7$ and Rb$_7$M$_{12}$Sb$_{12}$ with M = Mn, Zn, and Cd featuring coplanar zigzag layers of edge-connected MPn_4 tetrahedra including MPn_5 pyramids at every kink.[20] In terms of the building block concept that we applied on our structures, these structures may be rationalized as frameworks lacking frames and thus forming zigzag layers of braces and joints.
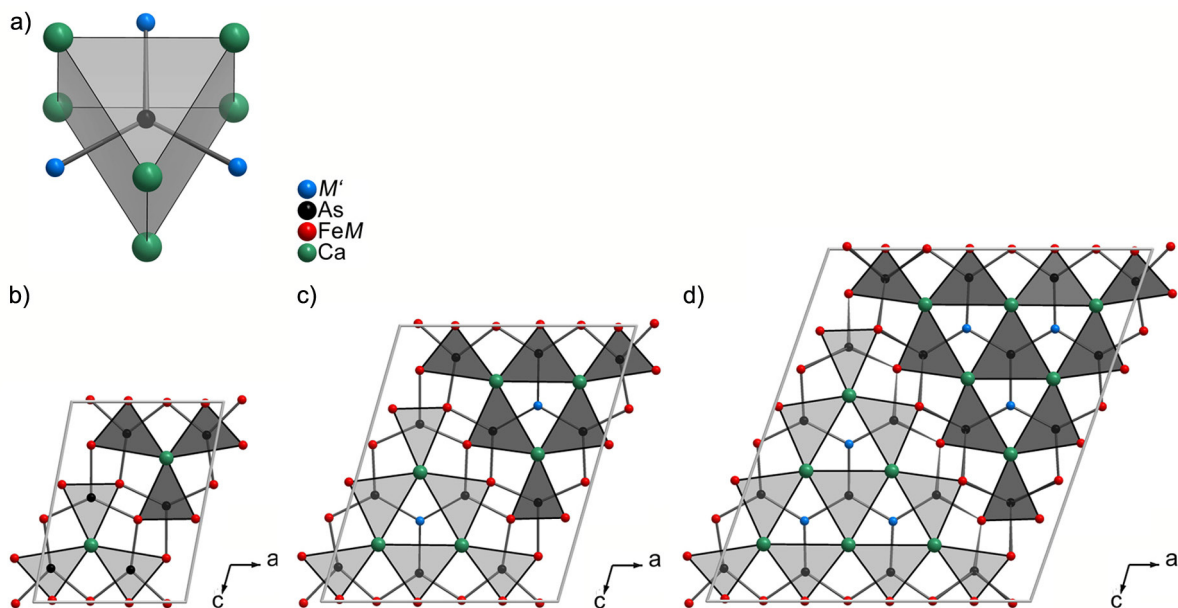
Figure 6. Crystal structures of Ca$_{n(n+1)/2}$(Fe$_{1-x}$M$_x$)$_{(2+3n)}$M'$_{n(n-1)/2}$As$_{(n+1)(n+2)/2}$ with n = 1, 2, 3, emphasizing the tricapped trigonal-prismatic AsM_9 coordination.

107

A different approach of framework transition metal pnictides and related silicides was given earlier by *Jeitschko* and coworkers[21, 22] and other authors,[23, 24] reporting, for instance, rare earth cobalt phosphides featuring structure types very similar to those of our iron arsenides $Ca_{n(n+1)/2}(Fe_{1-x}M_x)_{(2+3n)}M'_{n(n-1)/2}As_{(n+1)(n+2)/2}$. They describe these structures in terms of a frequently reappearing relation of metal to pnictide in nature of 2 : 1, including also metal-rich binaries like Co_2P. The common building unit is a tricapped trigonal-prismatic coordination of the pnictide by metal atoms, whereas the different arrangements of these PnM_9 units yield the large plethora of crystal structures known in this class. The structures of the monoclinic compounds $Ca_{n(n+1)/2}(Fe_{1-x}M_x)_{(2+3n)}M'_{n(n-1)/2}As_{(n+1)(n+2)/2}$ with $n = 1 - 3$ are exemplarily illustrated in Figure 6, emphasizing the tricapped prismatic coordination of the arsenic. In the structures presented in this paper, each arsenic atom is in the center of an AsM_9 unit, with M being all metal atoms present. Within the channels, these units are edge-connected but separated from neighboring channels by FeAs tetrahedra layers. Very similar structures were reported for the compounds $HoCo_3P_2$, $ScCo_5P_3$, and $Sc_5Co_{19}P_{12}$,[21] but with different arrangements of the triangular channels and partial incorporation of different channel sizes as well as other building blocks in the same structure.

The iron arsenide framework structures reported in this paper are supposed to feature interesting magnetic and electronic properties. For $CaFe_4As_3$ iron(II) was evidenced for tetrahedral coordination and iron(I) in the pyramidal environment.[9] We have conducted preliminary density functional theory calculations and found exclusively magnetic ground states for all compounds. Calculated magnetic moments range from ~ 0.3 to $2.0\ \mu_B$ at the iron atoms of the frames and braces and up to $\sim 2.5\ \mu_B$ at the joints. However, detailed magnetic measurements and neutron diffraction experiments are necessary to prove this. For the time being, it seems reasonable to assume a similar situation of two different iron species for our compounds. Because the compounds $Ca_{n(n+1)/2}(Fe_{1-x}M_x)_{(2+3n)}M'_{n(n-1)/2}As_{(n+1)(n+2)/2}$ allow for different distances and arrangements of the iron sites, they present an excellent model system to study the geometry-dependent interplay of a variety of different magnetic centers. Still, no superconductivity was observed yet in any of the compounds described, despite the presence of two-dimensional iron arsenide tetrahedral layers. Nevertheless, these new phases clarify that layered iron arsenide structures are not just restricted to two-dimensional stacking structures but facilitate the formation of complex three-dimensional frameworks.

3.1.4 Conclusion

In conclusion, we reported the eight new calcium iron arsenide compounds $Ca_{n(n+1)/2}(Fe_{1-x}M_x)_{(2+3n)}M'_{n(n-1)/2}As_{(n+1)(n+2)/2}$ with $n = 1, 2, 3$, $M = $ Nb, Pd, Pt, and $M' = \square$ Pd, Pt. The structures reveal three-dimensional frameworks of cross-linked iron arsenide layers with trigonal channels along a short b-axis of 3.9 Å. Thereby the size and arrangement of the channels give rise to the different structures. This relationship was also rationalized by the identification of common structural building blocks and their resemblance to $CaFe_4As_3$. The compounds feature coordination of arsenic typical for compounds with a metal-to-pnictide ratio of 2 : 1. The identification of these new structures elucidates the structural flexibility of iron arsenide layers toward rearrangements. Unlike $CaFe_4As_3$, $Ca_{n(n+1)/2}(Fe_{1-x}M_x)_{(2+3n)}M'_{n(n-1)/2}As_{(n+1)(n+2)/2}$ still feature continuous coplanar $FeAs_{4/4}$ layers and therewith a certain degree of two-dimensionality. Although no superconductivity has been observed in these compounds so far, interesting magnetic and electronic properties are expected.

3.1.5 References

[1] Y. Kamihara, T. Watanabe, M. Hirano, H. Hosono, *J. Am. Chem. Soc.* **2008**, *130*, 3296.

[2] H. Takahashi, K. Igawa, K. Arii, Y. Kamihara, M. Hirano, H. Hosono, *Nature* **2008**, *453*, 376.

[3] Z.-A. Ren, W. Lu, J. Yang, W. Yi, X.-L. Shen, Z.-C. Li, G.-C. Che, X.-L. Dong, L.-L. Sun, F. Zhou, Z.-X. Zhao, *Chin. Phys. Lett.* **2008**, *25*, 2215.

[4] D. Johrendt, *J. Mater. Chem.* **2011**, *21*, 13726.

[5] D. Johrendt, R. Pöttgen, *Angew. Chem. Int. Ed.* **2008**, *47*, 4782.

[6] D. C. Johnston, *Adv. Phys.* **2010**, *59*, 803.

[7] P. Dai, J. Hu, E. Dagotto, *Nat. Phys.* **2012**, *8*, 709.

[8] G. R.Stewart, *Rev. Mod. Phys.* **2011**, *83*, 1589.

[9] I. Todorov, D. Y. Chung, C. D. Malliakas, Q. A. Li, T. Bakas, A. Douvalis, G. Trimarchi, K. Gray, J. F. Mitchell, A. J. Freeman, M. G. Kanatzidis, *J. Am. Chem. Soc.* **2009**, *131*, 5405.

[10] I. Todorov, D. Y. Chung, H. Claus, K. E. Gray, Q. A. Li, J. Schleuter, T. Bakas, A. P. Douvalis, M. Gutmann, M. G. Kanatzidis, *Chem. Mater.* **2010**, *22*, 4996.

[11] Y. Nambu, L. L. Zhao, E. Morosan, K. Kim, G. Kotliar, P. Zajdel, M. A. Green, W. Ratcliff, J. A. Rodriguez-Rivera, C. Broholm, *Phys. Rev. Lett.* **2011**, *106*, 037201.

[12] D. Walker, M. A. Carpenter, C. M. Hitch, *Am. Mineral.* **1990**, *75*, 1020.

[13] H. Huppertz, *Z. Kristallogr.* **2004**, *219*, 330.

[14] V. Petricek, M. Dusek, L. Palatinus, *Jana2006 Structure Determination Software Programs*, Institute of Physics, Praha, Czech Republic, **2006**.

[15] A. Coelho, *TOPAS-Academic*, Version 4.1, Coelho Software, Brisbane, Australia, **2007**.

[16] C. Hieke, J. Lippmann, T. Stürzer, G. Friederichs, F. Nitsche, F. Winter, R. Pöttgen, D. Johrendt, *Philos. Mag.* **2013**, *93*, 3680.

[17] C. Löhnert, T. Stürzer, M. Tegel, R. Frankovsky, G. Friederichs, D. Johrendt, *Angew. Chem. Int. Ed.* **2011**, *50*, 9195.

[18] G. Wenski, A. Mewis, *Z. Anorg. Allg. Chem.* **1986**, *543*, 49.

[19] D. Johrendt, A. Mewis, *Z. Anorg. Allg. Chem.* **1992**, *618*, 30.

[20] M. Khatun, S. S. Stoyko, A. Mar, *Inorg. Chem.* **2013**, *52*, 3148.

[21] W. Jeitschko, E. J. Reinbold, *Z. Naturforsch.* **1985**, *40b*, 900.

[22] Y. M. Prots, W. Jeitschko, *Inorg. Chem.* **1998**, *37*, 5431.

[23] C. Le Sénéchal, V. Babizhets'ky, S. Députier, J. Y. Pivan, R. Guérin, *J. Solid State Chem.* **1999**, *144*, 277.

[24] Y. Kuz'ma, S. Chykhrij, Phosphides In *Handbook on the Physics and Chemistry of Rare Earths*; K. A. Gschneidner, L. Eyring, Eds.; Elsevier Science: Amsterdam, The Netherlands, **1996**, *23*, 285.

3.2 Properties of α-Ca$_3$(Fe,Pt)$_8$PtAs$_6$ and related compounds
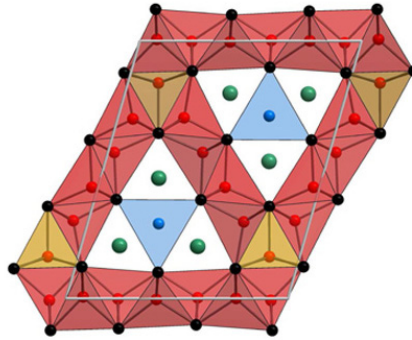
3.2.1 *Introduction*

The proximity of layered iron arsenide compounds to a magnetic instability is considered to be essential for the emergence of superconductivity in this material class. Thereby magnetic fluctuations appear to mediate the interaction of *Cooper* pairs. Although immense progress was made since the discovery of La(O$_{1-x}$F$_x$)FeAs,[1] no thorough understanding of the superconducting mechanism was found so far. While the emergence of superconductivity is restricted to compounds comprising coplanar FeAs$_{4/4}$ tetrahedra sheets at the present stage the structure chemistry of iron arsenides is not. Besides tetrahedral coordination, iron is also found in trigonal pyramidal (Fe$_{12}$As$_5$[2]), square pyramidal (Fe$_2$As,[3] CaFe$_4$As$_3$[4]) or octahedral (FeAs,[5] FeAs$_2$[6]) arsenic environment. Exceptional magnetic properties are reported for all those compounds. Recently a complete series of new iron arsenides Ca$_{n(n+1)/2}$(Fe$_{1-x}$M$_x$)$_{(2+3n)}$M$'_{n(n-1)/2}$As$_{(n+1)(n+2)/2}$ with n = 1, 2, 3, M = Nb, Pd, Pt, and M' = $\square$ Pd, Pt was discovered featuring frameworks of cross linked iron arsenide layers connected by iron in square pyramidal coordination.[7] Further investigations revealed Fe$_2$As (n = 0) being the simplest representative of this series, while CaFe$_4$As$_3$ can be characterized as defect type for n = 1. The new compounds crystallize in differently dense frameworks and form various polymorphs, not just enlarging the family of iron arsenides but also demonstrating an unexpected structural flexibility. As suggested for Fe$_2$As and CaFe$_4$As$_3$ the presence of formal Fe^{2+} in tetrahedral coordination and Fe$^+$ in pyramidal coordination can be assumed for all representatives of Ca$_{n(n+1)/2}$(Fe$_{1-x}$M$_x$)$_{(2+3n)}$M$'_{n(n-1)/2}$As$_{(n+1)(n+2)/2}$.[4, 8] The presence of a multitude of magnetic centers including different iron valences promises interesting magnetic properties. However, earlier investigations revealed, that the preparation of high quality samples of just one representative of Ca$_{n(n+1)/2}$(Fe$_{1-x}$M$_x$)$_{(2+3n)}$M$'_{n(n-1)/2}$As$_{(n+1)(n+2)/2}$ is extremely difficult. In this work the synthesis strategy was optimized and samples of α-Ca$_3$(Fe,Pt)$_8$PtAs$_6$ were

obtained without impurities of other homologs or polymorphs. Temperature dependent properties were studied by X-ray powder diffraction, magnetic, and conductivity measurements. Electronic properties were calculated by DFT methods. The results were compared and discussed in the scope of known $CaFe_4As_3$ to get a first insight into the complex magnetism of the new compounds $Ca_{n(n+1)/2}(Fe_{1-x}M_x)_{(2+3n)}M'_{n(n-1)/2}As_{(n+1)(n+2)/2}$.

3.2.2 *Experimental Details*

Polycrystalline samples of α-$Ca_3Fe_8PtAs_6$ were prepared either by conventional ambient pressure solid-state synthesis or under high-pressure conditions. For conventional synthesis stoichiometric mixtures of pure elements (> 99.5 %) were heated at $900 - 1000\,°C$ in alumina crucibles in silica tubes under purified argon. The samples were thoroughly homogenized and annealed twice at $900 - 1000\,°C$. One step synthesis of α-$Ca_3Fe_8PtAs_6$ was achieved by high-pressure synthesis starting from stoichiometric mixtures of phase pure binaries (FeAs, CaAs, PtAs). Synthesis was carried out in boron nitride crucibles at 6 GPa and $1000\,°C$, using a modified Walker-type multianvil apparatus.[9-10] Both synthesis routes allowed for the preparation of just the α-polymorph, including minor impurity phases $FeAs_2$ or $CaFe_4As_3$. Temperature-dependent X-ray powder diffraction data were collected using a HUBER G670 Guinier imaging plate diffractometer (Cu-Kα_1 radiation, Ge-111 monochromator) equipped with a close-cycle He-cryostat. Structure refinement and determination of composition were performed based on powder diffraction data using the TOPAS package[11] with structural data obtained by the single crystal experiments. A representative powder pattern with Rietveld fit is exemplarily shown in Figure 1. *Dc*-resistivity was measured on a cold pressed pellet which has been annealed at $800\,°C$ for 15 h. Magnetic susceptibility was measured using a QUANTUM DESIGN MPMS-XL5 SQUID magnetometer. Structure relaxation and calculation of magnetic moments in the ground state were performed by DFT methods using the WIEN2K package.[12-13]
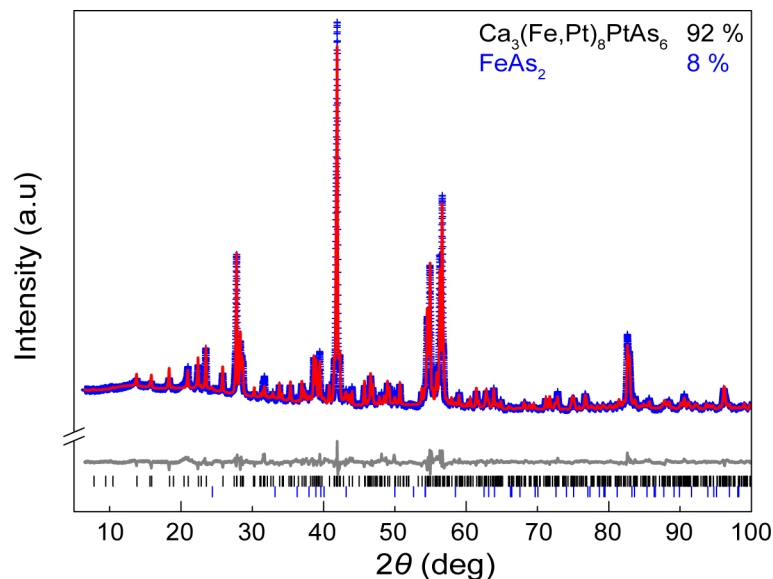
Figure 1. X-ray powder patterns (blue lines) with Rietveld fits (red lines) of α-Ca$_3$(Fe,Pt)$_8$PtAs$_6$.

3.2.3 *Results and Discussion*

The synthesis by ambient pressure as well as high-pressure yielded almost phase pure samples (> 90 wt%) of the α-polymorph of Ca$_3$(Fe,Pt)$_8$PtAs$_6$. The β-polymorph could not be obtained as bulk sample, but just as side phase in form of single crystals. Variations of synthesis conditions lead to the formation of increased amounts of Ca(Fe$_{1-x}$Pt$_x$)$_2$As$_2$, CaFe$_4$As$_3$, (CaFe$_{1-x}$Pt$_x$As)$_{10}$Pt$_3$As$_8$, (CaFe$_{1-x}$Pt$_x$As)$_{10}$Pt$_4$As$_8$, and Ca$_6$(Fe$_{1-x}$Pt$_x$)$_{11}$Pt$_3$As$_{10}$. Analysis of the composition of α-Ca$_3$Fe$_8$PtAs$_6$ samples revealed varying Fe/Pt mixing on the range of $0 \leq x \leq 0.1$, which is in agreement with single crystal studies.

Temperature dependent structure investigations on powder samples give no clear evidence for a structural phase transition in the temperature range between 9 K and 300 K (Figure 2). Structure parameters a and c decrease monotonically upon cooling, whereby a minor flattening of the slope is conspicuous below about 110 K. Only minor shrinkage of monoclinic b-axis was detected, which starts to slightly increase again below about 150 K. The unit cell volume linearly decreases by approximately 1% in the range investigated, but remains almost constant below 100 K.
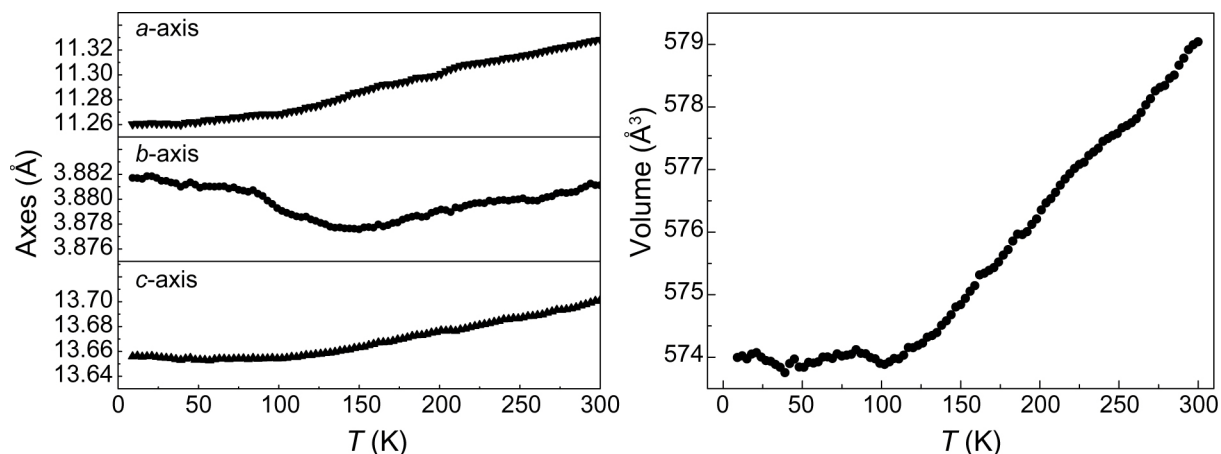
Figure 2. Temperature dependent course of lattice parameters (left) and unit cell volume (right) of α-$Ca_3(Fe,Pt)_8PtAs_6$.

Conductivity measurements in the range of 4 K to 300 K confirmed the metallic properties of $Ca_3(Fe,Pt)_8PtAs_6$ expected from short Fe–Fe contacts in the structure and the metallic luster (Figure 3). Temperature dependent resistivity decreases upon cooling as characteristic for metals but with values around 1 mΩcm being much higher than in conventional conductors like copper or silver. However, this resistivity values are in the typical range of layered iron arsenides, which are referred to as poor conductors. Around 75 K a broad anomaly is conspicuous in the temperature-dependent progress. Resistivity increases below 110 K, passing a maximum at around 75 K and declining again till 4 K.

Field dependent magnetization measurements revealed the presence of a precedent ferromagnetic order already above 300 K, which is in line with high magnetic background in susceptibility and minor *zfc* and *fc* splitting between 300 K and 90 K. The magnitude of the magnetic signal is too strong to originate from magnetic impurities. Below 90 K susceptibility measurement reveal an abrupt splitting of *field cooled* and *zero field cooled* branches, being indicative for ferromagnetic ordering (Figure 3). The absence of a hysteresis in magnetization demonstrates the sensitivity of the magnetic order towards an external magnetic field. This finding substantiates that the conductivity anomaly might be associated with a magnetic phase transition. Also previously mentioned minor changes in the temperature dependent course of cell parameters is in good agreement therewith. With increasing field the anomaly can be gradually suppressed and completely vanishes above 1000 Oe.
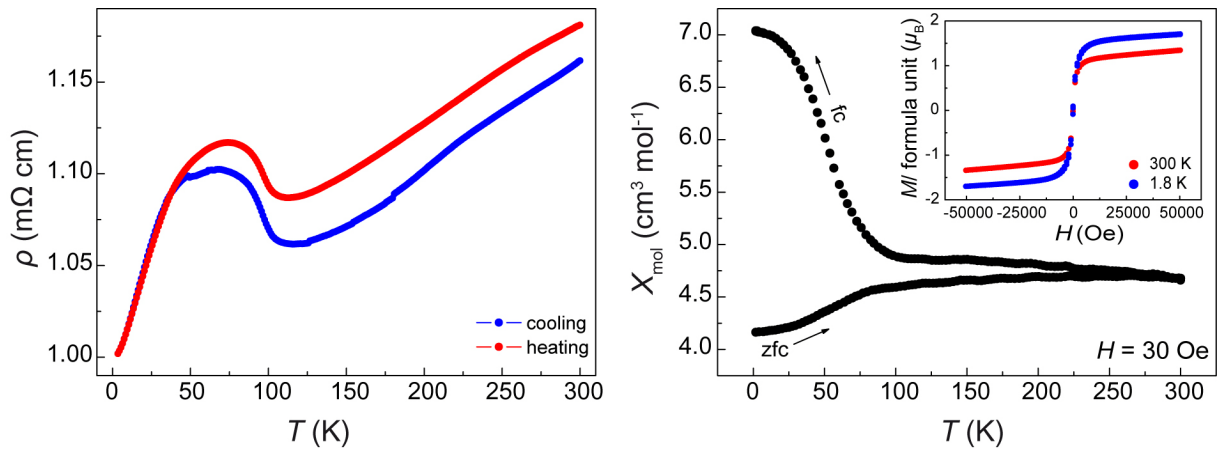
Figure 3. Conductivity (left) and SQUID (right) measurements of α-Ca$_3$(Fe,Pt)$_8$PtAs$_6$.

Calculated density of states confirmed the metallic state as expected from structure investigations and conductivity measurements. Interestingly hardly any Pt states are present at E_F, reducing the role of platinum in this compound to a mere structural one. Similar to the 1038/1048 systems[14] this electronic situation leads to a Fermi surface almost exclusively formed by Fe-3d states. Further investigations revealed rather flat bands and high partial iron density of states at E_F (Figure 4 and Chapter 7.7) being reminiscent of layered iron arsenides. However, the cross linked framework structure creates a very different electronic structure. The Fermi surface is formed by mainly coplanar sheets perpendicular to b^*, as was expected from infinite FeAs layers along b. In this highly anisotropic Fermi surface several k-vectors connecting coplanar Fermi sheets were found, indicating a complex antiferromagnetic ground state rather than a ferromagnetic one. In line with these results ferromagnetic calculations suggest a favorable magnetic ground state, which is in agreement with previous measurements. A summary of DFT data obtained from calculations is listed in the appendix (Chapter 7.7).
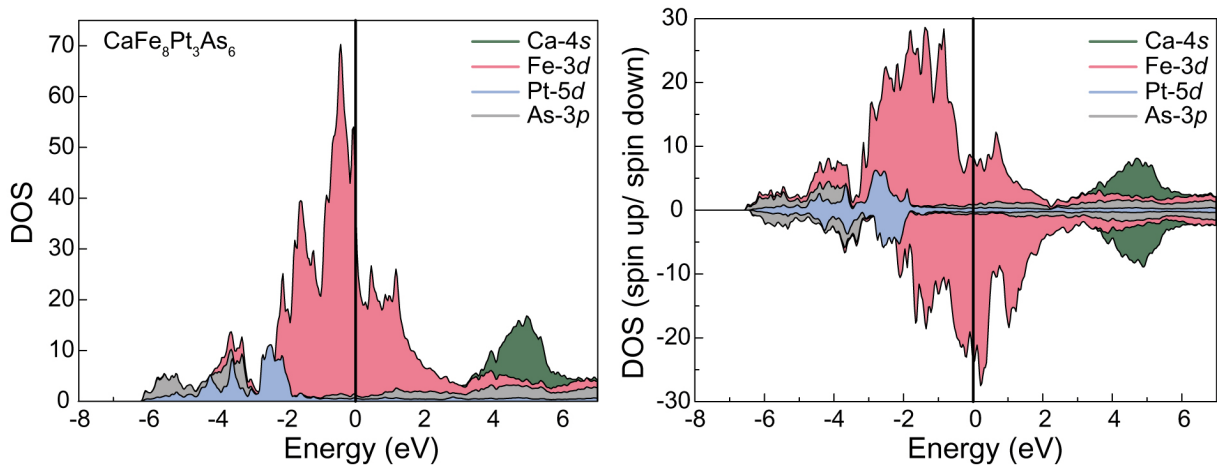
Figure 4. Non-magnetic (left) and spin polarized (right) density of states of α-Ca$_3$Fe$_8$PtAs$_6$.

115

In the previous chapter the structural relation of $Ca_{n(n+1)/2}(Fe_{1-x}M_x)_{(2+3n)}M'_{n(n-1)/2}As_{(n+1)(n+2)/2}$ with $n = 1, 2, 3$, M = Nb, Pd, Pt, and M' = $\square$, Pd, Pt was discussed. Therefore it appears reasonable to compare α-$Ca_3Fe_8PtAs_6$ with known and less complex relatives Fe_2As and $CaFe_4As_3$ to gain a better understanding of the magnetic properties. For both compounds Fe^{2+} was suggested for tetrahedral coordination, but Fe^+ for quadratic pyramidal environment.[4, 8] While antiferromagnetism below 50 °C was found for Fe_2As,[8] a rather complex magnetism was reported for $CaFe_4As_3$.[4, 15] Being Pauli paramagnetic at room temperature, a magnetic phase transition to an incommensurable state similar to $FeAs$[16] occurs at 90 K, followed by reorientation of magnetic moments to a commensurable antiferromagnetic state below 25 K. Magnetic moments estimated for $CaFe_4As_3$ by DFT methods are in very good agreement with moments calculated for the magnetic ground state of α-$Ca_3Fe_8PtAs_6$ within this thesis (Chapter 7.7). Furthermore magnetic measurements of *Todorov* et al. feature a steady divergence of *fc* and *zfc* branch below 300 K at 100 Oe along with abrupt splitting at 90 K, similar to our data. Interestingly magnetic measurements on $CaFe_5As_3$[17] and α-$Ca_6(Fe,Pt)_{11}Pt_3As_{10}$ (not shown) revealed comparable results. Based on this comparison and previously discussed calculations a similar magnetism like in $CaFe_4As_3$ is suggested for α-$Ca_3Fe_8PtAs_6$ and at least for monoclinic compounds $Ca_{n(n+1)/2}(Fe_{1-x}M_x)_{(2+3n)}M'_{n(n-1)/2}As_{(n+1)(n+2)/2}$ with $n \geq 1$. Moreover, comparing susceptibility data of $CaFe_5As_3$, α-$Ca_3Fe_8PtAs_6$ and α-$Ca_6(Fe,Pt)_{11}Pt_3As_{10}$ the magnitude of splitting of the *fc* and *zfc* branch reduces with increasing n, mirroring the dilution of the magnetic lattice by increased channel size. A comparison of DFT data including band structure, density of states, and Fermi surfaces for $CaFe_4As_3$, $CaFe_5As_3$, and α-$Ca_3Fe_8PtAs_6$ is attached to the appendix (Chapter 7.7).

In the field of layered iron arsenides magnetic instabilities and the suppression of spin density wave transitions are considered as crucial ingredients for the emergence of superconductivity. Although spin density wave transitions are also present in $CaFe_4As_3$ substitution experiments to suppress the SDW and induce superconductivity failed so far.[18] From the structural point of view, $CaFe_4As_3$ featuring no infinite FeAs layers, is distinctly different to layered iron arsenides. In contrast the α-polymorphs of $Ca_{n(n+1)/2}Fe_{(2+3n)}M'_{n(n-1)/2}As_{(n+1)(n+2)/2}$ comprise uninterrupted layers of FeAs, moreover allowing for dilution of the magnetic lattice and tuning of the interlayer distance. Further investigations in these materials may help to understand the complicated magnetic interactions in layered iron arsenides.

3.2.4 *Conclusion*

Polycrystalline samples of the α-$Ca_3Fe_8PtAs_6$ were synthesized and low temperature properties studied. Temperature dependent powder X-ray investigations revealed no clear structural phase transition in the range of 9 K to 300 K but minor features around 110 K. Magnetic measurements suggested a transition to a ferromagnetic state at 90 K, which was substantiated by an anomaly in conductivity measurements. DFT calculations revealed exclusively Fe-$3d$ states at E_F and no significant contribution of platinum, similar to the 1038/1048 systems. High density of states at E_F together with coplanar sheets in the Fermi surface indicate a nesting instability. Therefore no simple ferromagnetic ground state is expected but a complicated antiferromagnetic one. In accordance with that a preferred magnetic ground state was found by spin-polarized calculations. Based on the structural relation of $Ca_{n(n+1)/2}Fe_{(2+3n)}M'_{n(n-1)/2}As_{(n+1)(n+2)/2}$ compounds, α-$Ca_3Fe_8PtAs_6$ was discussed in the context of reported results on $CaFe_4As_3$. A variety of similarities concerning experimental and theoretical data was identified suggesting a similar magnetism in both compounds. Although no superconductivity was found in α- $Ca_3Fe_8PtAs_6$ the presence of continuous FeAs layers in the structure renders this compound an ideal system for further studies concerning superconductivity and magnetism in iron arsenide compounds.

3.2.5 *References*

[1]   Y. Kamihara, T. Watanabe, M. Hirano, H. Hosono, *J. Am. Chem. Soc.* **2008**, *130*, 3296.

[2]   S. Maaref, R. Madar, P. Chaudouet, R. Fruchart, J. P. Sénateur, M. T. Averbuch-Pouchot, M. Bacmann, A. Durif, P. Wolfers, *Mater. Res. Bull.* **1983**, *18*, 473.

[3]   M. Elander, G. Haegg, A. Westgren, *Ark. Kem. Mineral. Geol.* **1935**, *12*, 1.

[4]   I. Todorov, D. Y. Chung, C. D. Malliakas, Q. Li, T. Bakas, A. Douvalis, G. Trimarchi, K. Gray, J. F. Mitchell, A. J. Freeman, M. G. Kanatzidis, *J. Am. Chem. Soc.* **2009**, *131*, 5405.

[5]   K. E. Fylking, *Ark. Kem. Mineral. Geol.* **1934**, *11*, 1.

[6]   M. J. Buerger, *Z. Kristallogr. Krist.* **1932**, *82*, 165.

[7]   T. Stürzer, C. Hieke, C. Löhnert, F. Nitsche, J. Stahl, C. Maak, R. Pobel, D. Johrendt, *Inorg. Chem.* **2014**, *53*, 6235.

[8]   H. Katsuraki, K. Suzuki, *J. Appl. Phys.* **1965**, *36*, 1094.

[9]   D. Walker, M. A. Carpenter, C. M. Hitch, *Am. Mineral.* **1990**, *75*, 1020.

[10]   H. Huppertz, *Z. Kristallogr.* **2004**, *219*, 330.

[11]   A. Coelho, *TOPAS-Academic*, Version 4.1, Coelho Software, Brisbane, Australia, **2007**.

[12]   P. Blaha, K. Schwarz, G. K. H. Madsen, D. Kvasnicka, J. Luitz, *WIEN2K-augmented plane wave+local orbitals program for calculating crystal properties* **2001**.

[13]   K. Schwarz, P. Blaha, *Comp. Mat. Sci.* **2003**, *28*, 259.

[14]   C. Löhnert, T. Stürzer, M. Tegel, R. Frankovsky, G. Friederichs, D. Johrendt, *Angew. Chem. Int. Ed.* **2011**, *50*, 9195.

[15]   Y. Nambu, L. L. Zhao, E. Morosan, K. Kim, G. Kotliar, P. Zajdel, M. A. Green, W. Ratcliff, J. A. Rodriguez-Rivera, C. Broholm, *Phys. Rev. Lett.* **2011**, *106*, 037201.

[16]   E. Rodriguez, C. Stock, K. Krycka, C. Majkrzak, P. Zajdel, K. Kirshenbaum, N. Butch, S. Saha, J. Paglione, M. Green, *Phys. Rev. B* **2011**, *83*, 134438.

[17]   R. Pobel, D. Johrendt, *unpublished* **2014**, LMU München.

[18]   I. Todorov, D. Y. Chung, H. Claus, K. E. Gray, Q. Li, J. Schleuter, T. Bakas, A. P. Douvalis, M. Gutmann, M. G. Kanatzidis, *Chemistry of Materials* **2010**, *22*, 4996.

4 Summary

In this thesis the structures and properties of new iron arsenide compounds were investigated, featuring a complex structure chemistry being unprecedented in this material class so far. The main focus was on the newly discovered layered superconductors $(CaFeAs)_{10}Pt_zAs_8$. The structure chemistry of the different branches was elucidated and disorder in the 1048 system analyzed. A new iron arsenide parent compound was identified together with a variety of related superconductors. Low temperature structure and magnetic measurements as well as theoretical calculations were performed to investigate the resemblance of these peculiar compounds to well studied iron arsenides and established theories. The substitution series $(CaFe_{1-x}M_xAs)_{10}Pt_3As_8$ (M = Co, Ni, Cu, Pt), $(CaFe_{1-x}Pt_xAs)_{10}Pt_4As_8$, $(Ca_{1-y}RE_yFeAs)_{10}Pt_3As_8$ (RE = Y, La – Nd, Sm – Lu), $(Ca_{1-y}La_yFe_{1-x}Pt_xAs)_{10}Pt_3As_8$, and $(Ca_{1-y}Na_yFeAs)_{10}Pt_4As_8$ were synthesized to study the influence of structural and electronic modifications upon properties. A schematic overview gives Figure 1. Apart from these layered compounds, a new branch of iron arsenides was discovered featuring three-dimensional frameworks of layer fragments. Structure investigation revealed a general systematization and the relation to known compounds. Magnetic measurements and theoretical calculations were performed to study the complex magnetism presented in this material class. The following chapter gives a brief summary of the key results presented in this thesis.

Superconductivity up to 35 K in the Iron Platinum Arsenides $(CaFe_{1-x}Pt_xAs)_{10}Pt_{4-y}As_8$ with Layered Structures

New layered superconductors $(CaFe_{1-x}Pt_xAs)_{10}Pt_zAs_8$ were discovered, presenting a so far unknown class within the iron arsenide family. While reported compounds form tetragonal structures of alternating iron arsenide and insulating layers, these exceptional representatives comprise the additional metal pnictide layer Pt_zAs_8. These sheets consist of corner sharing $As_{4/2}$ squares stabilized by As–As single bonds, providing Pt sites within the square centers. Two different branches of this structure motive were identified with either $z = 3$ (1038, $P\bar{1}$) or $z = 4$ (1048, polytypic: $P4/n$, $P\bar{1}$) platinum atoms in the Pt_zAs_8 layer. The alternated stacking of CaFeAs and Pt_zAs_8 sheets gives rise to 1038 and 1048 structures with surprisingly low space group symmetry, while local tetragonal symmetry is preserved within each layer. Magnetic and conductivity measurements revealed superconducting properties for all compounds, featuring critical temperatures up to 35 K (α-1048), 13 K (β-1048), and 14 K (1038). DFT

studies on $(CaFeAs)_{10}Pt_zAs_8$ revealed a pseudo band gap of Pt_zAs_8 states close to E_F, giving rise to a typical electronic situation found in other layered iron arsenides. Based on the absence of states of the Pt_zAs_8 subsystem at the E_F a scenario was suggested allowing for intrinsic electron doping in $(Ca^{2+})_{10}[(FeAs)_{10}]^{(10+2y)-}(Pt_{3+y}As_8)^{(10-2y)-}$ in dependency of the Pt content. In the scope of this considerations, the origin of superconductivity in $(CaFe_{1-x}Pt_xAs)_{10}Pt_zAs_8$ was suggested to be intrinsic electron doping in $(CaFeAs)_{10}Pt_4As_8$ (35 K, 1048), direct doping in $(CaFe_{1-x}Pt_xAs)_{10}Pt_3As_8$ (14 K, 1038), and overdoping in $(CaFe_{1-x}Pt_xAs)_{10}Pt_4As_8$ (13 K, 1048), being established concepts known from other iron arsenide systems.

Stacking disorder in the system $(CaFeAs)_{10}Pt_zAs_8$

The structure of the compounds $(CaFeAs)_{10}Pt_zAs_8$ was studied in detail, since strong diffuse contributions and complex twinning were found in earlier structure investigations. Therefore single crystal growth and sample preparation were optimized for further X-ray scattering studies. Stacking disorder was evidenced only in the $\sqrt{5} \times \sqrt{5}$ superstructure of both 1038 and 1048 compounds. For $z = 4$ five basic stacking possibilities were indentified comparing neighboring Pt_4As_8 layers, while order in the CaFeAs sublattice is retained. The presence of partial stacking disorder rather than the existence of distinct polytypes in the 1048 system was substantiated by the study of synthesis conditions, along with empirical X-ray diffraction analysis as well as T- and p-dependent DFT calculations. In this context reported α- ($P4/n$), β- ($P\bar{1}$), and γ-modification ($P2_1/n$) are limiting cases within the disorder model. Based on X-ray scattering measurements and disorder simulations an average ordered domain size of $5 - 10$ unit cells was estimated. Stacking disorder comparable to the 1048 system was also found in 1038 compounds, but with different stacking possibilities. A corresponding disorder model was established for the 1038 system, predicting a potential tetragonal 1038 phase. Ubiquitous twinning in $(CaFeAs)_{10}Pt_zAs_8$ was identified to originate from broken fourfold and twofold rotation symmetry in the superstructure, but still present in the $CaFe_2As_2$ subsystem. Although systematic investigations of the influence of disorder on the properties proved to be difficult, measurements and calculations indicate no significant effect of disorder upon super-conducting properties so far. These results were considered to be in line with the preserved order within the superconducting FeAs substructure.

Structural and magnetic phase transitions in triclinic $(CaFeAs)_{10}Pt_3As_8$

Starting with its discovery $(CaFeAs)_{10}Pt_zAs_8$ featuring unprecedented complex structures, disorder, low symmetry, and violation of accepted structure-property relations, were considered rather exotic representatives of the iron arsenide family. Samples of stoichiometric $(CaFeAs)_{10}Pt_3As_8$ were investigated to study the relation to known compounds. Low temperature X-ray investigations revealed splitting of the in-plane lattice parameter a and b below 120 K with magnitude comparable to $BaFe_2As_2$. In contrast to known iron arsenides, no space group symmetry reduction is associated with this isomorphic (i1) transition, but local tetragonal symmetry in the FeAs layers is broken. Furthermore a magnetic transition from Pauli paramagnetic to static antiferromagnetism was found below 130 K. Detailed μSR investigations revealed no abrupt formation, but a gradual development of static antiferromagnetism reaching 100 % at 5 K. μSR frequencies suggest a first order transition, whereas results from X-ray measurements indicate second order. Both transitions can be suppressed by electron doping in $(Ca_{0.85}La_{0.15}FeAs)_{10}Pt_3As_8$ or direct doping in $(CaFe_{0.97}Pt_{0.03}As)_{10}Pt_3As_8$, facilitating superconductivity. Results from this investigations therewith render $(CaFeAs)_{10}Pt_zAs_8$ a typical iron arsenide system with the parent compound $(CaFeAs)_{10}Pt_3As_8$.

[57]Fe-Mössbauer study on $(CaFeAs)_{10}Pt_3As_8$

Polycrystalline samples of stoichiometric $(CaFeAs)_{10}Pt_3As_8$ were investigated by [57]Fe-Mössbauer spectroscopy to obtain a detailed insight into the magnetic phase transition of this parent compound. Room temperature spectra are well fitted assuming one chemical indistinguishable iron site in $(CaFeAs)_{10}Pt_3As_8$, with values characteristic for layered iron arsenides. Strong signal broadening occurred below 111(4) K, being in good agreement with the reported antiferromagnetic transition at 120 K detected earlier in magnetic and μSR measurements. Hyperfine field of $B_{hyp} = 3.9(1)$ T was determined at 2.2 K with almost 100 % magnetic fraction. Detailed investigations in the paramagnetic regime revealed anisotropic signal broadening already between 245(10) K and T_N indicating magnetic interactions above T_N, possibly associated with nematic order as was also found in other iron arsenide parent systems recently.

Summary

Superconductivity by transition metal doping in (CaFe$_{1-x}$M$_x$As)$_{10}$Pt$_3$As$_8$ (M = Co, Ni, Cu)

Despite its structural peculiarities (CaFeAs)$_{10}$Pt$_z$As$_8$ was shown to be a typical iron arsenide system previously, with the parent compound (CaFeAs)$_{10}$Pt$_3$As$_8$. Substitution of iron by other transition metals is reported to be an effective tool to induce superconductivity in iron arsenides. Samples of the series (CaFe$_{1-x}$M$_x$As)$_{10}$Pt$_3$As$_8$ with M = Co, Ni, Cu were synthesized to probe the portability of known concepts to this system and investigate the influence of different dopants. Therefore synthesis strategies were optimized to achieve substitution exclusively on the Fe sites. Stoichiometric (CaMAs)$_{10}$Pt$_3$As$_8$ were not accessible, but solubility limits were found to be $x_{max}(M)$ = 0.25, 0.25, 0.12 for M = Co, Ni, Cu, respectively. Superconducting properties could be induced for Co, Ni with critical temperatures up to 15 K (M = Co, x = 0.075) and 13 K (M = Ni, x = 0.05) similar to the related system Ba(Fe$_{1-x}$M$_x$)$_2$As$_2$. In accordance with other iron arsenide systems no superconductivity emerged induced in (CaFe$_{1-x}$Cu$_x$As)$_{10}$Pt$_3$As$_8$. Typical dome like $T_c(x)$ phase diagrams were obtained for (CaFe$_{1-x}$M$_x$As)$_{10}$Pt$_3$As$_8$ superconductors showing a decrease of T_c upon overdoping. This study demonstrated the resemblance of (CaFe$_{1-x}$M$_x$As)$_{10}$Pt$_3$As$_8$ to simpler iron arsenides and the portability of the established direct doping concept as general tool to induce superconductivity to more complex systems.

Role of different negatively charged layers in (CaFeAs)$_{10}$Pt$_4$As$_8$ and superconductivity at 30 K in electron doped (Ca$_{0.8}$La$_{0.2}$FeAs)$_{10}$Pt$_3$As$_8$

1038 and 1048 systems demonstrated drastic different properties although the FeAs layers are almost identical in both compounds. Based on DFT calculations and formal charge considerations an intrinsic charge doping scenario was suggested earlier as origin of superconductivity in (CaFeAs)$_{10}$Pt$_4$As$_8$. For experimental validation and quantification considerable synthetic effort was taken to separately obtain high quality mixed series (CaFe$_{1-x}$Pt$_x$As)$_{10}$Pt$_3$As$_8$, and (CaFe$_{1-x}$Pt$_x$As)$_{10}$Pt$_4$As$_8$ as well as stoichiometric (CaFeAs)$_{10}$Pt$_4$As$_8$. Highest critical temperatures of 35 K were found only in (CaFeAs)$_{10}$Pt$_4$As$_8$ while superconductivity decreases in (CaFe$_{1-x}$Pt$_x$As)$_{10}$Pt$_4$As$_8$, but is induced in the first place in (CaFe$_{1-x}$Pt$_x$As)$_{10}$Pt$_3$As$_8$. This results experimentally identified the origin of superconductivity being direct doping in (CaFe$_{1-x}$Pt$_x$As)$_{10}$Pt$_3$As$_8$. In contrast superconductivity in the 1048 system is induced by intrinsic charge transfer from (Pt$_{3+y}$As$_8$)$^{(10-2y)-}$ to [(FeAs)$_{10}$]$^{(10+2y)-}$ due to the additional platinum. The intrinsic electron doping of the FeAs layers in stoichiometric 1048 was

estimated by DFT methods to approximately 0.15 e^-/FeAs, being comparable to other charge doped iron arsenide superconductors. Further evidence for electron doping induced superconductivity in $(CaFeAs)_{10}Pt_zAs_8$ was found experimentally by the emergence of super-conductivity above 30 K in the La doped 1038 compound $(Ca_{0.8}La_{0.2}FeAs)_{10}Pt_3As_8$. This demonstrated that high critical temperatures in the 1038/1048 system only emerge upon electron doping in the FeAs layer, whereby both the Pt_zAs_8 and the Ca layer are suitable as charge donors upon chemical modification.

$(Ca_{1-y}RE_yFeAs)_{10}Pt_3As_8$ with RE = Y, La – Nd, Sm – Lu

Previously discovered electronic equivalency of stoichiometric 1048 and La doped 1038, facilitates a tuning of electron doping level in $(CaFeAs)_{10}Pt_zAs_8$ compounds, according to $[(Ca^{2+})_{1-y}(RE^{3+})_y]_{10}[(FeAs)_{10}]^{(10+y)-}(Pt_3As_8)^{10-}$. Samples of $(Ca_{1-y}RE_yFeAs)_{10}Pt_3As_8$ with RE = Y, La – Nd, Sm – Lu were synthesized to investigate the response of superconductivity to different doping levels and different sized dopants. Structure analysis revealed a distinct preference of RE^{3+} ions to eightfold coordinated Ca positions. Superconductivity was induced in samples with Y, La – Nd, Sm, Gd – Lu, whereas no superconductivity was evident in Eu doped samples. Highest critical temperatures of 35 K were obtained for dopant concentrations of x = 0.13, with this values being almost identical as estimated for stoichiometric 1048 by DFT. Neither structural changes caused by the different radii of the rare earth elements nor strong local magnetic moments showed significant effects on properties. Hence a substituent independent phase diagram was established for electron doping in $(Ca_{1-y}RE_yFeAs)_{10}Pt_3As_8$. The absence of superconductivity in $(Ca_{1-y}Eu_yFeAs)_{10}Pt_3As_8$ was rationalized by the presence of Eu^{2+} in this compounds and verified by magnetic and structural measurements.

Muon spin rotation spectroscopy studies on $(Ca_{1-y}La_yFeAs)_{10}Pt_3As_8$

The superconducting state in electron doped $(Ca_{1-y}La_yFeAs)_{10}Pt_3As_8$ was investigated by μSR spectroscopy. Substitution dependent superconductivity was confirmed reaching a maximal critical temperature of 35 K for optimally doped $(Ca_{0.87}La_{0.13}FeAs)_{10}Pt_3As_8$. Further investigations revealed the development of a magnetic fraction reaching 20 % at 2.2 K in all samples investigated. The origin of this magnetic phase is unclear at the present stage, but precludes a detailed analysis of the superconducting state. The amount of magnetic fraction together

with X-ray powder and susceptibility data as well as kinks in the temperature dependent magnetic fraction close to T_c indicate the magnetism being an intrinsic property of $(Ca_{1-y}La_yFeAs)_{10}Pt_3As_8$ and no impurity effect. Inhomogeneity of the La substitution was suggested as probable origin of the residual magnetism in this compounds.

Phase diagram of $(CaFe_{1-x}Pt_xAs)_{10}Pt_zAs_8$ and the relation of $(Ca_{1-y}La_yFeAs)_{10}Pt_3As_8$ and $(CaFeAs)_{10}Pt_4As_8$

The experimentally found electronic equivalence of $(Ca_{1-y}La_yFeAs)_{10}Pt_3As_8$ and $(CaFeAs)_{10}Pt_4As_8$ despite their structural differences was investigated by DFT methods. For both compounds similar density of states and Fermi surfaces with a Pt-$5d$ pseudo band gap at E_F were found, substantiating the picture of electronic analogy. In this peculiar electronic situation iron is formally more electronegative than platinum, allowing for direct charge manipulations in $(FeAs)^{(1-y)-}$ upon chemical modifications in the Pt_zAs_8 or Ca layer. Poly-crystalline samples of codoped $(Ca_{1-y}La_yFe_{1-x}Pt_xAs)_{10}Pt_zAs_8$ were synthesized to study the different responses of direct substitution on properties compared to $(CaFe_{1-x}Pt_xAs)_{10}Pt_4As_8$. Results revealed an almost identical influence of direct Pt substitution in both compounds, demonstrating that often discussed structural subtleties are of minor importance in terms of superconductivity. Finally the close electronic resemblance of the 1038 and 1048 systems allowed for a consolidation of all experimental data to a general doping phase diagram for the $(CaFe_{1-x}Pt_xAs)_{10}Pt_zAs_8$ system. This compilation highlights the induction of superconductivity by direct or charge doping in the 1038/1048 family, whereby highest T_c only emerge by mere charge doping, a general concept found valid for all iron arsenide superconductors so far.

Suppression of superconductivity by compensation of charge doping in $(Ca_{1-y}Na_yFeAs)_{10}Pt_4As_8$

Samples of $(Ca_{1-y}Na_yFeAs)_{10}Pt_4As_8$ with $0 \leq y \leq 0.5$ were prepared to study the effect of charge manipulations on superconducting properties in the already intrinsically charge doped 1048 system. Structure analyses revealed a distinct preference of Na$^+$ ions for lower coordinated Ca sites, while magnitude of stacking disorder is enhanced in 1048 by Na substitution. The electronic structure of $(Ca_{0.8}Na_{0.2}FeAs)_{10}Pt_4As_8$ was found to be almost identical to $(CaFeAs)_{10}Pt_3As_8$, confirming a direct control of the charge doping in $(FeAs)^{(1-y)-}$ by Na

substitution. Critical temperatures and superconducting volume fractions decrease with increasing Na content between $0 \leq y \leq 0.23$. The intrinsic charge transfer discussed as origin of superconductivity in the 1048 system is gradually compensated by Na hole doping. A full recovery to a non-superconducting 1038 like state was not achieved, due to inhomogeneity within the samples. Na concentrations above $y = 0.23$ result in a renewed increase of super-conducting volume fractions. Although the origin of this phenomenon has not been clarified yet it indicates a hole doped regime in the $(CaFeAs)_{10}Pt_zAs_8$ system.
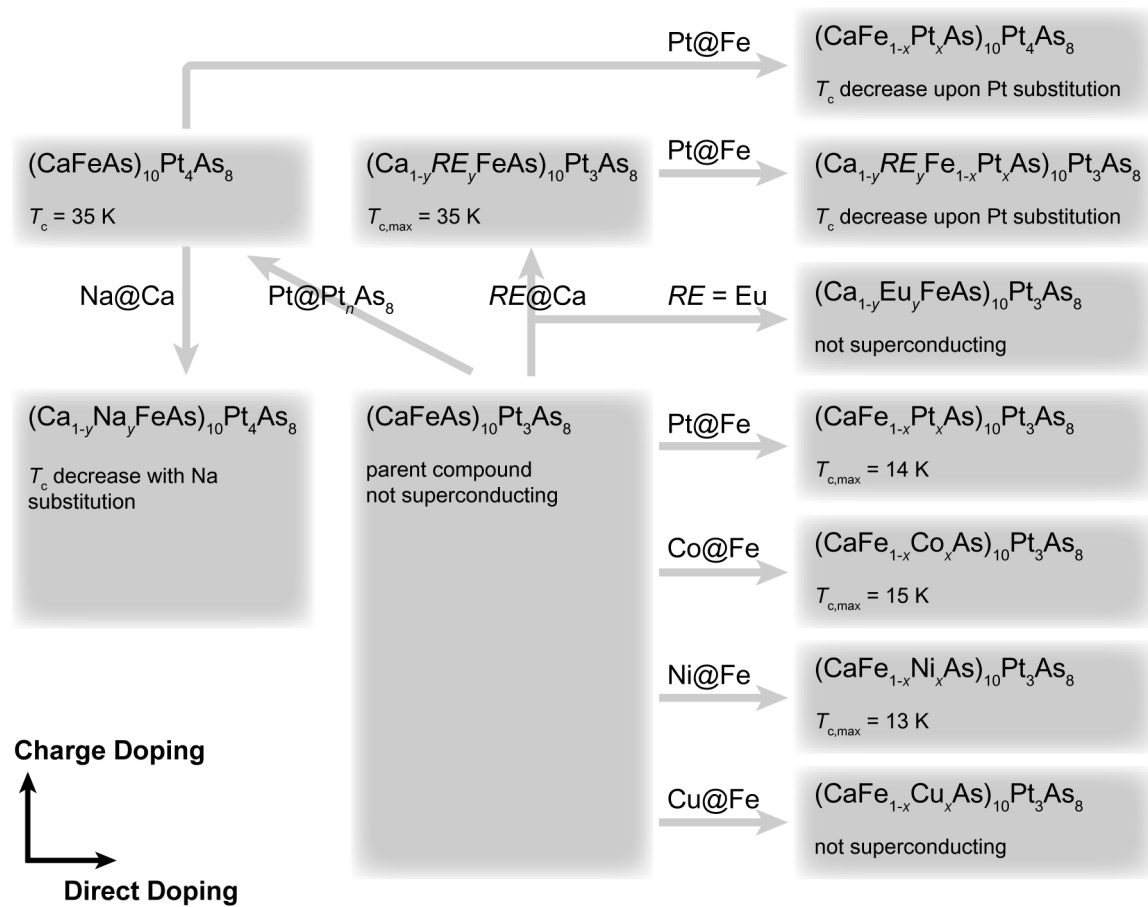
Figure 1. Schematic overview of 1038/1048 family compounds discovered and investigated within this thesis.

Framework structures of interconnected layers in calcium iron arsenides

The study of calcium iron arsenides lead to the discovery of eight new compounds with the general formula $Ca_{n(n+1)/2}(Fe_{1-x}M_x)_{(2+3n)}M'_{n(n-1)/2}As_{(n+1)(n+2)/2}$ with $n = 1, 2, 3$, $M = Nb$, Pd, Pt, and $M' = \square$ Pd, Pt. The structures crystallize in so far unknown structure types and reveal three-dimensional frameworks of cross-linked iron arsenide layer fragments. Iron arsenide

frames, braces, and joints were identified as common structural building blocks allowing for trigonal channels along the short b-axis. These channels are filled with calcium and in dependency of n additionally with vacancy positions, palladium or platinum. Different possible sizes and arrangements of the building units give rise to the various structures and polymorphs identified ($Pnma$, $P2_1/m$). Limiting cases of this homologue series are known Fe_2As ($n = 0$) and $CaPdAs$ or $CaPtAs$ ($n = \infty$), respectively, while related $CaFe_4As_3$ can be described as defect γ-polymorph ($n = 1$). Another characterization approach highlights the relation to a wide material class with a metal-to-pnictide ratio of 2 : 1. In $Ca_{n(n+1)/2}(Fe_{1-x}M_x)_{(2+3n)}M'_{n(n-1)/2}As_{(n+1)(n+2)/2}$ iron was found in typical tetrahedral environment within the layers, but is located in exceptional quadratic pyramidal coordination at the layer junctions. First principle DFT calculations indicated a favorable but complicated antiferromagnetic ground state probably similar to reported $CaFe_4As_3$. The identification of these new structures elucidates the structural flexibility of iron arsenide layers toward rearrangements and appears auspicious in terms of magnetic and superconducting properties.

Electronic and magnetic properties of α-Ca$_3$(Fe,Pt)$_8$PtAs$_6$ and related compounds

To get a first insight into the properties of $Ca_{n(n+1)/2}(Fe_{1-x}Pt_x)_{(2+3n)}Pt_{n(n-1)/2}As_{(n+1)(n+2)/2}$ the synthesis strategy was optimized and polycrystalline samples of α-Ca$_3$(Fe,Pt)$_8$PtAs$_6$ were successfully prepared without impurities of other homologs or polymorphs. Temperature dependent X-ray, magnetic, and conductivity measurements identified a magnetic phase transition in the range of $70 - 80$ K, associated with a minor structural change at about 100 K. DFT studies revealed a Fermi surface exclusively formed by Fe-$3d$ states with no significant Pt-$5d$ contribution. A complicated anisotropic Fermi surface was found, comprising coplanar sheets perpendicular to b^*. The presence of several nesting vectors indicated a complicated antiferromagnetism in α-Ca$_3$Fe$_8$PtAs$_6$. A favorable magnetic ground state was also identified by spin-polarized calculation, which is in line with experimental results. Considering the close structural relation of the $Ca_{n(n+1)/2}(Fe_{1-x}M_x)_{(2+3n)}M'_{n(n-1)/2}As_{(n+1)(n+2)/2}$ compounds, a comparison of reported $CaFe_4As_3$ with α-Ca$_3$(Fe,Pt)$_8$PtAs$_6$ revealed several analogies concerning experimental as well as theoretical results. Further similarities were also reported from preliminary magnetic measurements of the other homologs $CaFe_5As_3$ and $Ca_6(Fe,Pt)_{11}Pt_3As_{10}$. Therefore a similar magnetism was suggested for α-Ca$_3$(Fe,Pt)$_8$PtAs$_6$ and other $Ca_{n(n+1)/2}(Fe_{1-x}Pt_x)_{(2+3n)}Pt_{n(n-1)/2}As_{(n+1)(n+2)/2}$ compounds.

5 Conclusion

The discovery of $(CaFeAs)_{10}Pt_zAs_8$ ($z = 3$, 4) and $Ca_{n(n+1)/2}(Fe_{1-x}M_x)_{(2+3n)}M'_{n(n-1)/2}As_{(n+1)(n+2)/2}$ ($n = 1$, 2, 3, M = Nb, Pd, Pt, and M' = □ Pd, Pt) within this thesis revealed a so far un-expected diversity and complexity in the class of iron arsenide compounds. Several conclusions can be drawn from the results on $(CaFeAs)_{10}Pt_zAs_8$ ($z = 3$, 4). (1) The SDW or-dering and structural phase transition of iron arsenide parent compounds are intrinsic proper-ties of the $(FeAs)^-$ layer. As long as the Fermi surface is formed by exclusively Fe-$3d$ states with formal Fe^{2+} this property is independent from separating layers. At low temperatures a spin density wave transition to a stripe type antiferromagnetic state occurs accompanied with a structural distortion of the square FeAs lattice. The proximity of these systems to a magnetic instability is crucial for the emergence of superconductivity, whereby high space group sym-metry is no prerequisite, but the local tetragonal symmetry of the FeAs subsystem. (2) Manipulation of the magnetic FeAs system by direct substitution or indirect charge modifications in $(FeAs)^{(1+v)-}$ are reliable tools to suppress the spin density wave ordering and induce superconductivity. Highest T_c is achieved by mere charge doping, whereby the "origin" of the doped electrons is arbitrary as long as the FeAs layer is not chemically modified. In contrast superconductivity upon direct substitutions hardly exceeds 20 K. A combination of both charge doping and direct substitution results in a decrease of critical temperatures, which is referred to as "overdoping". (3) Structural subtleties like $FeAs_{4/4}$ tetra-hedra geometry, interlayer distance, or coupling have no significant influence on critical temperatures at least in the electron doped regime. (4) Both, the identification of a magnetic phase above T_N in the 1038 parent compound as well as in the superconducting regime of electron doped 1038 compounds, indicate a more complex magnetism in iron arsenides as expected so far. (5) Broken three-dimensional translation symmetry does not affect super-conducting properties as long as order is retained in the FeAs subsystem. Last but not least the presence of Pt_zAs_8 sheets in $(CaFeAs)_{10}Pt_zAs_8$ ($z = 3$, 4) emphasized, that interlayers in iron arsenides are not restricted to insulating blocks, but can also be formed by metallic layered systems. In this context the discovery of $Ca_{n(n+1)/2}(Fe_{1-x}M_x)_{(2+3n)}M'_{n(n-1)/2}As_{(n+1)(n+2)/2}$ ($n = 1$, 2, 3; M = Nb, Pd, Pt, and M' = □ Pd, Pt) revealed an unprecedented structural flexibility in this material class. The results of this thesis demonstrated not only the still increasing variety in the class of iron arsenides, but also the existence of a complex structure chemistry. Following the example of highest T_c copper oxides it is not unlikely that the final breakthrough in the field of iron arsenides superconductors is to be found in complex stacking structures.

6   Software Development

In the course of this dissertation a variety of time consuming issues frequently reappeared, although being routine work. This issues included creation of structure models and supercells for structure elucidation and DFT calculations, calculation of reciprocal and vectorized unit cell parameters, conversion and correction of structure data, conversion, refinement and temperature dependent evaluation of multiple powder data sets, conversion of EDX data as well as calculation of educt masses for sample synthesis. Therefore a variety of small tools was developed to automatize, accelerate, and facilitate everyday problems like these. *Java* with *Java Runtime Environment 1.7.0.* was used for development of the programs allowing for a usage without installation, since *Java* should be installed by default. All subprograms are compiled to the executable *AKJohrendtToolsVxy.jar* in the current version 2.5. Necessary files are *atoms.dat*, *sg.dat*, *spacegroups.dat*, and *elemente.txt*, which must be located in the same directory as *AKJohrendtToolsVxy.jar*. In the following chapter the main programs will be described briefly.

This software package was developed for internal, noncommercial application at the LMU Munich and must not be distributed without my agreement. Several modules of this software package use the Jama Matrix package and Apache libraries under the Apache license.
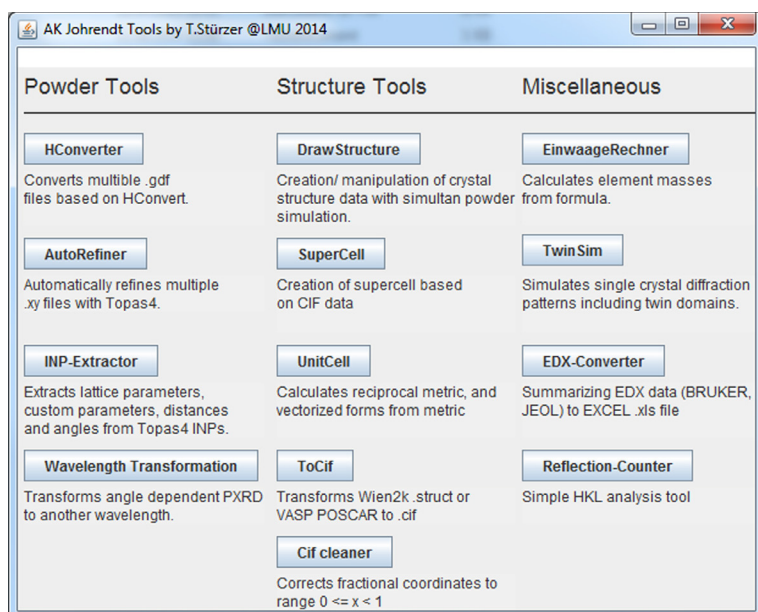
Figure 1. User interface of *AKJohrendtTools*.

6.1   Structure Tools

6.1.1   *DrawStructure*
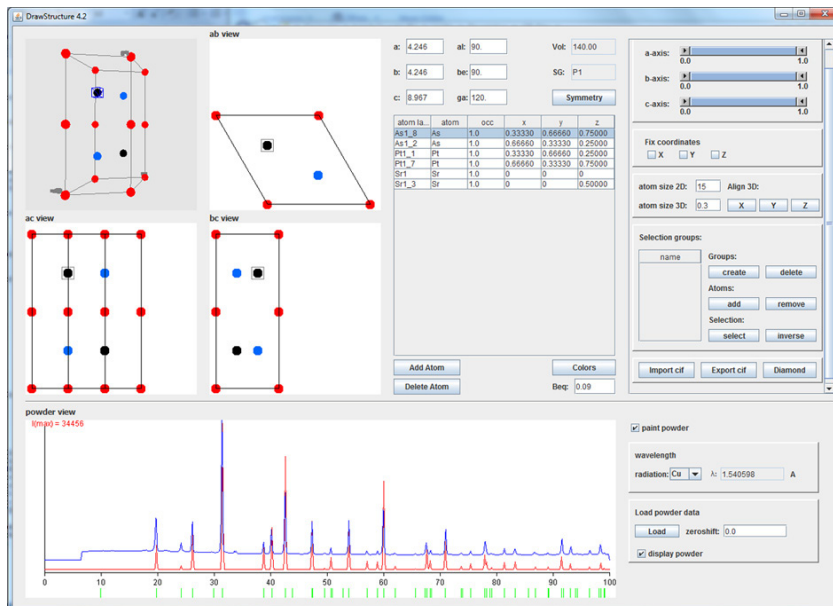
Figure 2. User interface of *DrawStructure*.

DrawStructure was developed to facilitate graphical modifications of structure data in drag and drop like fashion. The two-dimensional projections *XY*, *XZ* and *YZ* along with a light weight 3D viewer were implemented for graphical structure representation. To run *DrawStructure Java3D* is required for 3D structure representation. Orthogonalization of metric and atomic coordinates was performed with alignment of *a*-axis to *x*-axis in orthogonal space.

Structures can be started from scratch or imported from *.cif*. Structure data can be changed manually in the metric panel or atom parameter list. Moreover the 2D views allow for a drag and drop movement of atoms by mouse or arrow keys. Structure update will be performed automatically (If not: A click in one of the 2D views will help). All modifications can be done in symmetry restricted (space group) or unrestricted mode (*P*1), changeable at any time via the *symmetry* button. Moreover *DrawStructure* allows for simultaneous X-ray powder diffraction simulation for the wavelengths Cr, Fe, Cu, Co, and Mo. Reflection positions derived from metric are marked in green ticks, neglecting extinction conditions. Reflection intensity calculation was implemented without symmetry restriction (no inversion), additionally considering global isotropic atomic displacement (*beq*), site occupation, *Lorentz* and polarization factors. To accelerate powder calculation anomalous scattering as well as more

sophisticated powder analysis tools were not implemented. However, for large structures X-ray powder simulation may take several seconds. In such cases simulation can be switched on/off if not needed. Nevertheless, the powder simulation tools was implemented for educational purpose and to get an impression of how structural changes affect X-ray diffraction. This tool is not meant for "rietveld-by-hand ".

Besides additional tools for coloring, grouping, and adjusting the structure representation, DrawStructure allows for exporting structure data directly to *Diamond* (if path is specified correctly in *directory.txt*) or *.cif* file.

6.1.2   *SuperCell*
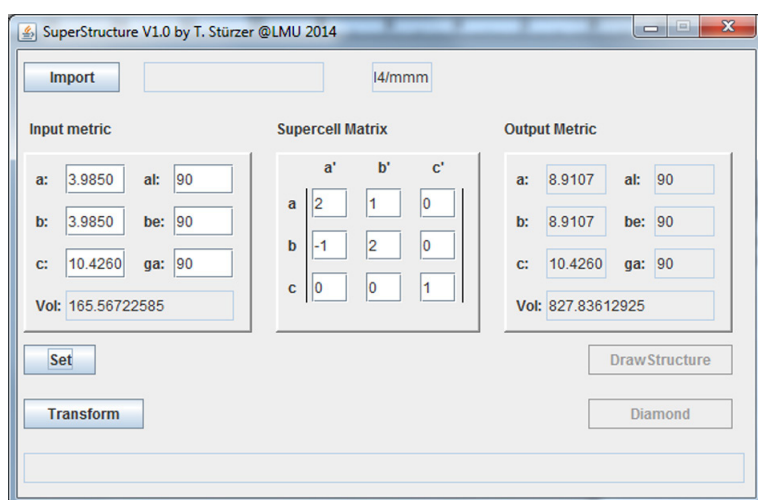
Figure 3. User interface of *SuperCell*.

SuperCell facilitates the creation of supercells based on structure data from *.cif* and a super-structure matrix. The imported structure will be converted to *P*1 and expanded to a supercell defined by the matrix. *Set* calculates superstructure metric for control purpose, whereas *transform* performs the actual conversion. The result is saved in *.cif* format in space group *P*1 and can be additionally exported to *Diamond* or *DrawStructure* for further modifications. Reintroduction of symmetry to the obtained supercell can be achieved for example with *Platon ADDSYM*.

6.1.3   *UnitCell*

UnitCell allows for the conversion of unit cell metric, reciprocal unit cell metric, vectorized unit cell, and vectorized reciprocal unit cell to each other.

6.1.4 *ToCif*

ToCif converts *VASP POSCAR* and *Wien2k .struct* files to *.cif*.

6.1.5 *CifCleaner*

CifCleaner corrects atomic fractional coordinates to the range $0 \leq x,y,z < 1$ and allows for formatting atomic parameters in columns for easier manual editing.

6.2 Powder Tools

6.2.1 *HConverter*

HConverter represents a graphical user interface for *M. Tegels HConvert*, moreover allowing for the automatic conversion of multiple *HUBER .gdf* files to *.xy ASCII* format.

6.2.2 *AutoRefiner*

AutoRefiner allows for the automatic refinement of multiple powder data sets with *Topas4* without prompting a CPU expensive user interface. Therefore a folder containing *.xy* powder data and a template *.inp* have to be defined. Refinement can be carried out in two modes:

Consecutive mode: Each refinement will start from outcome of previous refinement. Suited for set of powder data measured at different temperatures. Results will be saved to corresponding *.inp*. Report will be saved to *report.txt*.

Independent mode: Each refinement will start from template. Suited for independent powder data. Results will be saved to corresponding *.inp*.

6.2.3 *INP-Extractor*

INPExtractor allows for the extraction of structure data from multiple *Topas4 .inp* and *.out* files formatted for *ORIGIN/ MS Excel* import. Unit cell parameters, volume, density, and linear absorption coefficient of the first compound are exported by default. Optionally R_{wp}, temperature, user defined parameters, bonding lengths and angles (if present in .inp file) can be defined for export as well. Accessible data for *INPExtractor* is located between *STR* com-

mand of first and second compound. Requested data beyond this range will be ignored or has to be linked by prm command (e.g. *prm zeroshift = zeroshift_of_2nd_phase;*) for extraction.

6.2.4 *PowderWavelengthConverter*

PowderWavelengthConverter converts powder diffraction intensity data (*.xy*) data from one wavelength to another, based on the *Bragg* equation. Equidistant step size in output file is obtained by linear interpolation.

6.3 Miscellaneous

6.3.1 *EinwaageRechner*
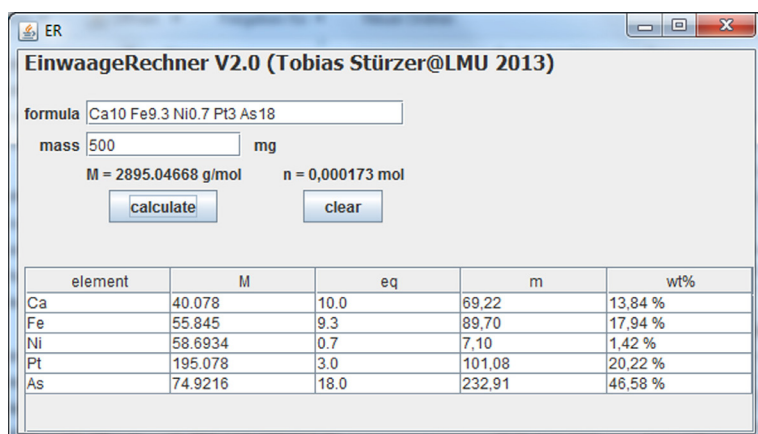
Figure 4. User interface of *EinwaageRechner*.

EinwaageRechner was developed to calculated element masses from sum formula and total weight for sample preparation. The formula has to be defined with spaces between elements. Fractional stoichiometries will be accepted as well. Molar atomic weights are specified in *elemente.txt*. EinwaageRechner calculates molar weight and amount of the target compound as well as weight and mass percent of each element.

6.3.2 *EDXConverter*
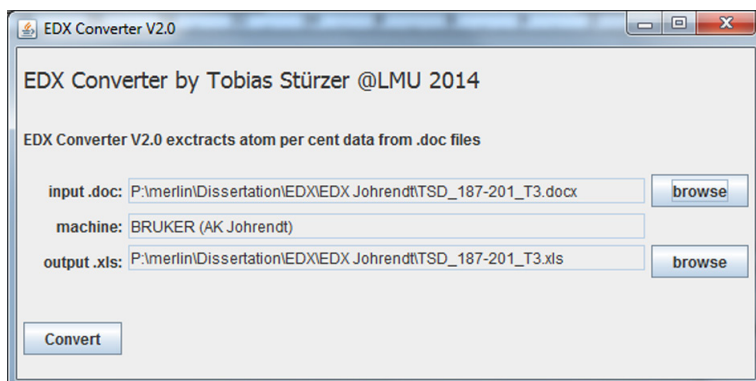
Figure 5. User interface of *EDXConverter*.

EDXConverter converts EDX data from BRUKER and JEOL machines saved in *MS Word .doc/.docx* format in tabular form to *MS Excel .xlsx* file. The type of machine used for measurement will be detected automatically.

6.3.3 *TwinSim*
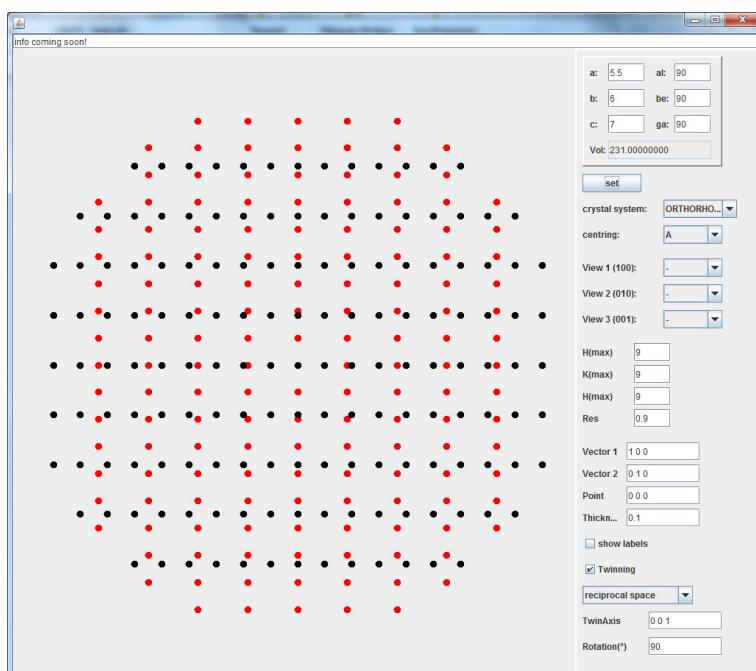
Figure 6. User interface of *TwinSim*.

TwinSim was developed to simulate single crystal diffraction patterns for empirical elucidation of complex twinning problems. Therefore simulations are performed based on geometric diffraction theory without structure factor calculation, whereby twin domains can be included as well. Additional reflection conditions for integral, zonal, and serial extinction can be

defined optionally. Diffraction patterns can be visualized in any desired orientation defined by two vectors and a point of origin. To run *TwinSim* no additional library is required since visualization is based on 2D projections orientated by rotation matrices.

7 Appendix

7.1 Crystallographic Data of $(CaFeAs)_{10}Pt_3As_8$

Table 1. Crystallographic data of $(CaFe_{0.930}Pt_{0.070}As)_{10}Pt_{2.986}As_8$.

Crystal system, space group	Triclinic, $P\overline{1}$, No. 2
a, b, c (Å)	8.7616(5), 8.7726(5), 10.681(1)
α, β, γ (deg.)	75.666(6), 85.412(5), 90.036(5)
Cell volume (Å^3)	792.67(9)
Calculated density (g/cm^3), Z	6.258, 1
Radiation type, λ (Å)	Mo-Kα, 0.71069
2θ range (deg)	9.12 – 72.64
Reflections (total, independent, $I > 3\sigma(I)$)	11595, 4927, 2975
R_{int}, R_{σ}	0.039, 0.1037
GooF (all), GooF ($I > 3\sigma(I)$)	1.01, 0.96
Refined parameters, refinement	202, F^2
$R_1, wR2$ ($I > 3\sigma(I)$)	0.0383, 0.0631
$R_1, wR2$ (all)	0.0797, 0.0979
Largest residual peak, hole $e^-/$Å^3	6.11, -2.79

Site	Wyckoff	SOF	x	y	z	U_{eq}
Pt1	1b	1.000(3)	0.0	0.0	0.5	0.0075(2)
Pt2	1h	1.002(3)	0.5	0.5	0.5	0.0077(2)
Pt3	2i	0.495(2)	0.5056(1)	0.0168(1)	0.4447(1)	0.0150(3)
As1	2i		0.1343(1)	0.9070(1)	0.1378(1)	0.0098(3)
As2	2i		0.3331(1)	0.5091(1)	0.1378(1)	0.0099(3)
As3	2i		0.7637(1)	0.4002(1)	0.5005(1)	0.0089(3)
As4	2i		0.9370(1)	0.3106(1)	0.1384(1)	0.0097(3)
As5	2i		0.5373(1)	0.1110(1)	0.1334(1)	0.0102(3)
As6	2i		0.2603(1)	0.2929(1)	0.8625(1)	0.0103(3)
As7	2i		0.0997(1)	0.2640(1)	0.5000(1)	0.0088(3)
As8	2i		0.3815(1)	0.2445(1)	0.5004(1)	0.0151(3)
As9	2i		0.7446(1)	0.1184(1)	0.5005(1)	0.0144(3)
Fe1/Pt11	2i	0.896(3)	0.4495(1)	0.3522(1)	0.9975(1)	0.0088(4)
Fe2/Pt22	2i	0.902(3)	0.3478(1)	0.0508(1)	0.0002(1)	0.0073(4)
Fe3/Pt33	2i	0.941(3)	0.2476(1)	0.7489(1)	0.0009(1)	0.0091(4)
Fe4/Pt44	2i	0.942(3)	0.0495(1)	0.1501(1)	0.0020(1)	0.0091(4)
Fe5/Pt55	2i	0.976(3)	0.1487(1)	0.4503(1)	0.0002(1)	0.0077(4)
Ca1	2i		0.0202(2)	0.5614(2)	0.2964(2)	0.0118(6)
Ca2	2i		0.5753(2)	0.2257(2)	0.7347(2)	0.0101(6)

Ca3	2i	0.2271(2)	0.1687(2)	0.2665(2)	0.0111(6)
Ca4	2i	0.6218(2)	0.3664(2)	0.2663(2)	0.0107(6)
Ca5	2i	0.1801 (2)	0.0287(2)	0.7331(2)	0.0110(6)

7.2 Crystallographic Data of $(CaFeAs)_{10}Pt_4As_8$ Polymorphs

7.2.1 α-1048

Table 2. Crystallographic data of $(CaFeAs)_{10}Pt_{3.64}As_8$.

Crystal system, space group	Tetragonal, $P4/n$, No. 85
a, c (Å)	8.7145(5), 10.462(1)
Cell volume (Å^3)	794.51
Calculated density (g/cm^3), Z	6.256, 1
Radiation type, λ (Å)	Mo-Kα, 0.71069
2θ range (deg)	6.08 – 60.66
Reflections (total, independent, $I > 3\sigma(I)$)	9264, 1185, 630
R_{int}, R_σ	0.2389, 0.0717
GooF (all), GooF ($I > 3\sigma(I)$)	3.31, 4.58
Refined parameters, refinement	53, F
R_1, $wR2$ ($I > 3\sigma(I)$)	0.0999, 0.1216
R_1, $wR2$ (all)	0.1392, 0.1228

Site	*Wyckoff*	*SOF*	*x*	*y*	*z*	U_{eq}
Pt1	2b	1.03(3)	0	0	0.5	0.0140(10)
Pt2	2c	0.79(2)	0.5	0	0.5658(5)	0.0108(12)
As1	8g		0.2002(6)	0.9003(5)	0.1370(4)	0.0102(11)
As2	8g		0.2633(6)	0.1078(4)	0.4861(6)	0.0128(13)
As3	2c		0	0.5	0.1391(11)	0.0110(20)
Fe1	8g		0.0999(5)	0.6991(6)	0.0006(8)	0.0042(13)
Fe2	2a		0	0	0	0.0030(20)
Ca1	8g		0.0961(10)	0.2046(11)	0.2615(8)	0.0120(20)
Ca2	2c		0.5	0	0.2750(20)	0.0160(50)

7.2.2 β-1048

Table 3. Crystallographic data of $(CaFe_{0.870}Pt_{0.130}As)_{10}Pt_4As_8$.

Crystal system, space group	Triclinic, $P\overline{1}$, No. 2
a, b, c (Å)	8.7382(4), 8.7387(3), 11.225(1)
α, β, γ (deg.)	81.049(3), 71.915(3), 89.980(3)
Cell volume (Å^3)	803.79(6)
Calculated density (g/cm^3), Z	6.7533, 1

Radiation type, λ (Å)	Mo-Kα, 0.71069
2θ range (deg)	6.58 – 68.92
Reflections (total, independent, $I > 3\sigma(I)$)	12485, 6702, 4454
R_{int}, R_σ	0.0603, 0.0598
GooF (all), GooF ($I > 3\sigma(I)$)	2.97, 3.57
Refined parameters, refinement	192, F
R_1, $wR2$ ($I > 3\sigma(I)$)	0.0694, 0.1034
R_1, $wR2$ (all)	0.1093, 0.1060
Largest residual peak, hole $e^-/\text{Å}^3$	18.27, -17.00

Site	*Wyckoff*	*SOF*	*x*	*y*	*z*	*U_{eq}*
Pt1	2i		0.2499(1)	0.2500(1)	0.5004(1)	0.0065(2)
Pt2	2i		0.7243(1)	0.2371(1)	0.5645(1)	0.0093(2)
As1	2i		0.9971(2)	0.3631(2)	0.4824(2)	0.0062(6)
As2	2i		0.5168(2)	0.1439(2)	0.4822(2)	0.0061(6)
As3	2i		0.3527(3)	0.5028(2)	0.5196(2)	0.0094(7)
As4	2i		0.1317(3)	0.9895(2)	0.5195(2)	0.0096(7)
As5	2i		0.2052(3)	0.9763(2)	0.8618(2)	0.0096(7)
As6	2i		0.4030(3)	0.5776(2)	0.8618(2)	0.0100(7)
As7	2i		0.9946(3)	0.6208(2)	0.1388(2)	0.0093(7)
As8	2i		0.8080(3)	0.7782(2)	0.8616(2)	0.0098(7)
As9	2i		0.3947(3)	0.8226(2)	0.1363(2)	0.0098(7)
Fe1/Pt11	2i	0.833(5)	0.5510(2)	0.6498(2)	0.9985(2)	0.0086(7)
Fe2/Pt22	2i	0.879(5)	0.6509(3)	0.9498(2)	0.0002(2)	0.0066(7)
Fe3/Pt33	2i	0.879(5)	0.9502(3)	0.8497(3)	0.0011(3)	0.0086(7)
Fe4/Pt44	2i	0.879(5)	0.2490(3)	0.7495(3)	0.9998(3)	0.0105(7)
Fe5/Pt55	2i	0.879(5)	0.1487(3)	0.4494(3)	0.0001(3)	0.0131(8)
Ca1	2i		0.3576(5)	0.2971(5)	0.7416(4)	0.0104(13)
Ca2	2i		0.8426(5)	0.2960(5)	0.2708(4)	0.0124(14)
Ca3	2i		0.2529(5)	0.5008(5)	0.2574(4)	0.0103(13)
Ca4	2i		0.4428(5)	0.0957(5)	0.2570(4)	0.0102(13)
Ca5	2i		0.9485(5)	0.1072(5)	0.7410(4)	0.0105(13)

7.2.3 γ-1048

Table 4. Crystallographic data of $(CaFe_{0.975}Pt_{0.025}As)_{10}Pt_{3.120}As_8$.

Crystal system, space group	Monoclinic, $P2_1/n$, No. 14
a, b, c (Å)	8.7032(14), 8.7032(14), 21.010(6)
β (deg.)	90
Cell volume (Å^3)	1591.4(6)
Calculated density (g/cm^3), Z	6.143, 1
Radiation type, λ (Å)	Mo-Kα, 0.71069
2Θ range (deg)	5.06 – 60.50
Reflections (total, independent, $I > 3\sigma(I)$)	20477, 4482, 1980

R_{int}, R_σ	0.1049, 0.0958
GooF (all), GooF ($I > 3\sigma(I)$)	3.06, 4.55
Refined parameters, refinement	90, F^2
R_1, $wR2$ ($I > 3\sigma(I)$)	0.0941, 0.2193
R_1, $wR2$ (all)	0.1662, 0.2246
Largest residual peak, hole $e^-/Å^3$	20.26, -8.84

Site	*Wyckoff*	*SOF*	*x*	*y*	*z*	*U_{eq}*
Pt1	2i	0.825(5)	0.9503(5)	0.1515(4)	0.25036(18)	0.0030
Pt2	2i	0.723(5)	0.4499(4)	0.1502(3)	0.21752(9)	0.0026
As1	2i		0.2111(9)	0.2602(8)	0.2587(4)	0.0207(18)
As2	2i		0.8442(8)	0.4195(7)	0.2437(3)	0.0067(14)
As3	2i		0.7521(12)	0.2478(14)	0.9313(7)	0.0060(30)
As4	2i		0.6538(13)	0.5517(15)	0.0696(6)	0.0100(20)
As5	2i		0.0511(16)	0.3494(16)	0.0690(2)	0.0055(7)
As6	2i		0.1481(12)	0.0502(14)	0.9322(5)	0.0022(19)
As7	2i		0.0591(10)	0.8898(5)	0.2404(4)	0.0142(16)
As8	2i		0.4508(17)	0.1500(17)	0.0683(2)	0.0068(7)
As9	2i		0.6889(7)	0.0423(6)	0.2587(4)	0.0058(13)
Fe1/Pt11	2i	0.98(4)	0.2482(17)	0.2540(14)	0.0000(6)	0.0050(60)
Fe2/Pt22	2i	0.96(3)	0.9470(20)	0.1517(18)	0.0001(6)	0.0090(40)
Fe3/Pt33	2i	0.95(3)	0.6481(17)	0.0494(15)	0.9984(9)	0.0100(40)
Fe4/Pt44	2i	0.98(3)	0.5490(20)	0.3496(17)	1.0000(5)	0.0030(40)
Fe5/Pt55	2i	0.97(3)	0.8491(17)	0.4487(15)	0.0015(9)	0.0080(40)
Ca1	2i		0.0490(30)	0.3560(30)	0.3705(4)	0.0077(17)
Ca2	2i		0.1630(20)	0.0580(20)	0.1310(11)	0.0150(40)
Ca3	2i		0.7510(20)	0.2510(20)	0.1279(10)	0.0034(18)
Ca4	2i		0.8620(20)	0.9520(20)	0.3684(9)	0.0060(30)
Ca5	2i		0.9550(30)	0.6510(30)	0.1338(4)	0.0105(16)

The crystal featured typical intense maxima of tetragonal $CaFe_2As_2$ substructure, along with weaker $\sqrt{5} \times \sqrt{5}$ superstructure reflections. Strong diffuse intensities along l for $2h + k \neq 5n$ ($n \in \mathbb{N}$) were evident. With respect to α-/ β-1048 additional intensity maxima occurred for $l/2$ implying a superstructure. Best results were obtained applying a $\sqrt{5} \times \sqrt{5}$ supercell in *ab* together with a doubled *c*-axis and refinement in the monoclinic space group $P2_1/n$ including merohedral twinning (90° around *c**).

7.3 Crystallographic Data of ordered *α*-1048 Derivatives

7.3.1 *α*-(Ca$_{0.875}$Na$_{0.125}$FeAs)$_{10}$Pt$_{3.612}$As$_8$

Table 5. Crystallographic data of (Ca$_{0.875}$Na$_{0.125}$FeAs)$_{10}$Pt$_{3.612}$As$_8$.

Crystal system, space group	Tetragonal, *P*4/*n*, No. 85
a, *c* (Å)	8.6955(2), 10.522(1)
Cell volume (Å^3)	795.59(5)
Calculated density (g/cm^3), *Z*	6.2409, 1
Radiation type, *λ* (Å)	Mo-K*α*, 0.71069
2*θ* range (deg)	6.04 – 74.36
Reflections (total, independent, *I* > 3*σ*(*I*))	33208, 1416, 1269
R$_{int}$, *R*$_σ$	0.0463, 0.0242
GooF (all), GooF (*I* > 3*σ*(*I*))	1.88, 1.56
Refined parameters, refinement	55, *F*^{2}
R$_1$, *wR*2 (*I* > 3*σ*(*I*))	0.0208, 0.0481
R$_1$, *wR*2 (all)	0.0252, 0.0613
Largest residual peak, hole *e*$^-$/Å^3	2.00, -1.63

Site	Wyckoff	SOF	x	y	z	U$_{eq}$
Pt1	2*a*	0.980(2)	0	0	0	0.0035(1)
Pt2	2*c*	0.825(3)	0	0.5	0.93678(4)	0.0076(1)
As1	2*c*		0.5	0	0.36171(10)	0.0104(2)
As2	8*g*		0.09954(5)	0.20159(5)	0.36465(4)	0.0069(1)
As3	8*g*		0.89098(5)	0.25942(6)	0.01584(5)	0.0081(1)
Fe1	8*g*		0	0	0.5	0.0055(2)
Fe2	2*b*		0.30073(7)	0.09978(7)	0.49859(6)	0.0063(2)
Ca1	2*c*		0	0.5	0.22749(18)	0.0104(4)
Ca2/Na22	8*g*	0.843(15)	0.79716(11)	0.09450(11)	0.23954(10)	0.0095(3)

The crystal featured a diffraction pattern which was indexed with $\sqrt{5}$ x $\sqrt{5}$ supercell of the *α*-1048 structure. Hardly any diffuse contribution were evident, indicating ordered stacking. Refinement succeeded with excellent *R* values in the reported space group *P*4/*n*, with Ca/Na mixing refined on one Ca site. Partial merohedral twinning was included into the model to ascribe for additional reflections (180° around (2$\overline{1}$0) in direct space).

7.3.2 α-$(CaFe_{0.869}Ru_{0.131}As)_{10}Pt_{2.92}Ru_{1.08}As_8$

Table 6. Crystallographic data of $(CaFe_{0.869}Ru_{0.131}As)_{10}Pt_{2.92}Ru_{1.08}As_8$.

Crystal system, space group	Tetragonal, $P4/n$, No. 85
a, c (Å)	8.7237(8), 10.393(2)
Cell volume (Å^3)	790.97(18)
Calculated density (g/cm^3), Z	6.3938, 1
Radiation type, λ (Å)	Mo-Kα, 0.71069
2θ range (deg)	6.10 – 63.42
Reflections (total, independent, $I > 3\sigma(I)$)	10862, 920, 671
R_{int}, R_σ	0.0989, 0.0643
GooF (all), GooF ($I > 3\sigma(I)$)	1.38, 1.50
Refined parameters, refinement	55, F^2
R_1, $wR2$ ($I > 3\sigma(I)$)	0.0412, 0.0700
R_1, $wR2$ (all)	0.0689, 0.0761
Largest residual peak, hole $e^-/$Å^3	4.76, -3.98

Site	Wyckoff	SOF	x	y	z	U_{eq}
Pt1/Ru1	2b	0.982(12)	0	0	0.5	0.0085(2)
Pt2/Ru2	2c	0.480(13)	0.5	0	0.5734(1)	0.0141(4)
As1	2c		0	0.5	0.1469(3)	0.0174(7)
As2	8g		0.4006(1)	0.2976(1)	0.1362(1)	0.0115(4)
As3	8g		0.2611(2)	0.1080(1)	0.4884(1)	0.0123(4)
Fe1/Ru11	2a	0.890(19)	0.5	0.5	0	0.0091(8)
Fe2/Ru22	8g	0.863(12)	0.1975(2)	0.4008(2)	0.0037(2)	0.0103(5)
Ca1	2c		0.5	0	0.2738(5)	0.0140(12)
Ca2	8g		0.0970(2)	0.2004(3)	0.2600(2)	0.0134(7)

The crystal featured a diffraction pattern which was indexed with $\sqrt{5} \times \sqrt{5}$ supercell of the α-1048 structure. Hardly any diffuse contribution were evident, indicating ordered stacking. Refinement succeeded in the reported space group $P4/n$, with Fe/Ru mixing and Pt/Ru mixing. Partial merohedral twinning was included into the model to ascribe for additional reflections (180° around ($2\bar{1}0$) in direct space).

7.4   Unit Cell Parameters from Disorder Model

Basis of the disorder model established in Chapter 2.2 were invariant layer setups and interlayer distanced, whereby the one dimensional disorder originates from different layer arrangements. Invariant parameters a, b and (FeAs)–(FeAs) interlayer distance were calculated from single crystal data. To check the models for consistency the unit cell for

triclinic polymorphs of 1038 and β-1048 were then reconstructed based on the invariant parameters and the layer shifts found for disorder. Table 7 shows calculated unit cell parameters being in excellent agreement with single crystal data.

Table 7. Comparison of unit cell metrics of 1038 and β-1048 from single crystal data with calculation based on disorder model layer shifts.

Structure	1038 Single crystal	1038 Disorder model	β-1048 Single crystal	β-1048 Disorder model
a (Å)	8.7616	8.7616	8.7382	8.7382
b (Å)	8.7726	8.7726	8.7387	8.7387
c (Å)	10.681	10.679	11.225	11.228
α (°)	75.666	85.284	81.049	81.045
β (°)	85.412	75.733	71.915	71.863
γ (°)	90.036	90	89.980	90
Volume (Å^3)	792.67	792.67	803.78	803.78

7.5 Fermi Surfaces of $(CaFeAs)_{10}Pt_zAs_8$ (z =3, 4), $(Ca_{0.8}La_{0.2}FeAs)_{10}Pt_3As_8$ and $(Ca_{0.8}Na_{0.2}FeAs)_{10}Pt_4As_8$

Due to the lack of partial Pt_zAs_8 states at E_F all chemical manipulations changing the electronic situation in these compounds exclusively affect the FeAs layers. With identical iron arsenide layers in all compounds a direct comparison of the electronic properties is possible. Fermi surfaces of compounds $(CaFeAs)_{10}Pt_zAs_8$ (z= 3, 4), $(Ca_{0.8}La_{0.2}FeAs)_{10}Pt_3As_8$, and $(Ca_{0.8}Na_{0.2}FeAs)_{10}Pt_4As_8$ calculated by DFT methods using the Wien2k package are depicted in Figure 1. For comparability all surfaces are aligned coplanar to the tetragonal iron arsenide layers in real space. An overview of the relative Fermi energy position of the different compounds is illustrated in Figure 2.
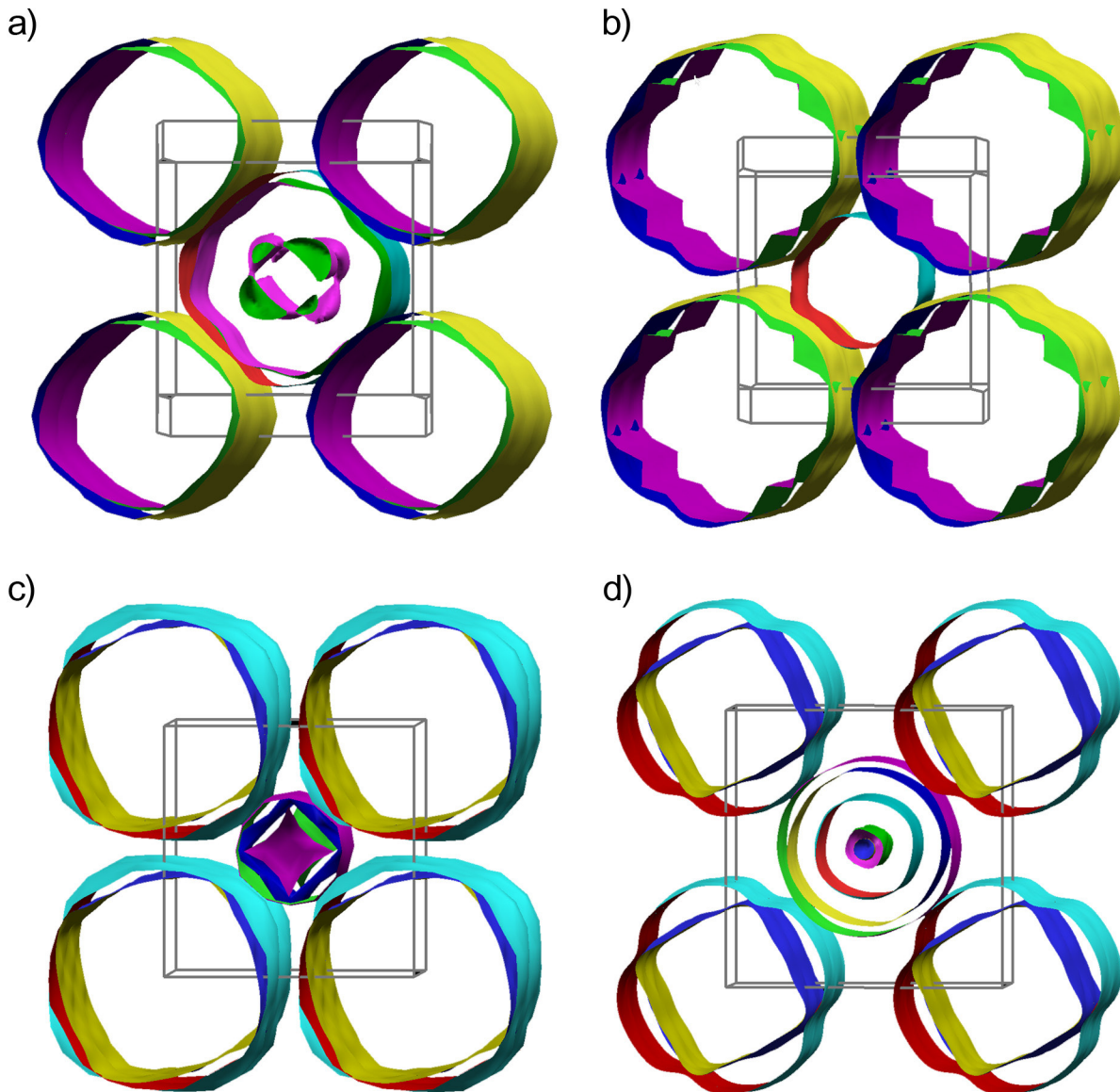

Figure 1. Fermi surfaces of $(CaFeAs)_{10}Pt_3As_8$ (a), $(Ca_{0.8}La_{0.2}FeAs)_{10}Pt_3As_8$ (b), $(CaFeAs)_{10}Pt_4As_8$ (c), and $(Ca_{0.8}Na_{0.2}FeAs)_{10}Pt_4As_8$ (d).
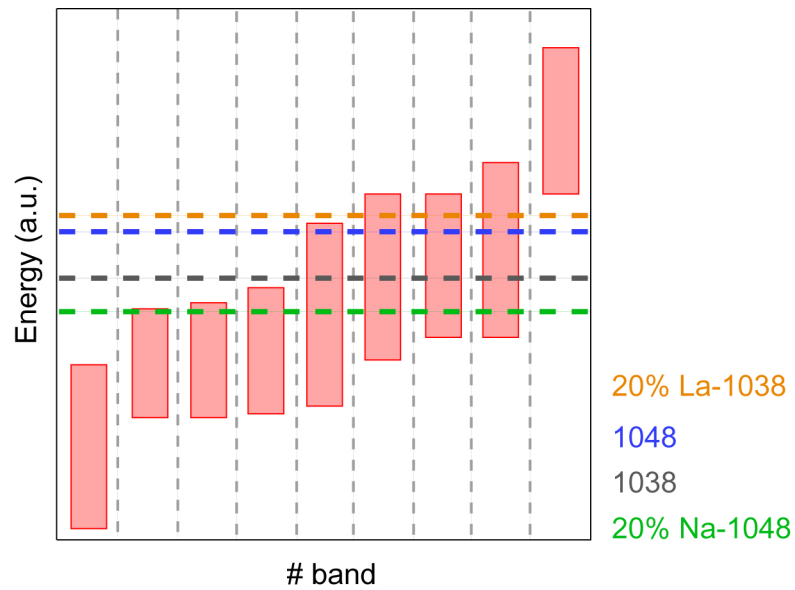
Figure 2. Position of the Fermi niveau for the compounds $(CaFeAs)_{10}Pt_3As_8$ (1038), $(Ca_{0.8}La_{0.2}FeAs)_{10}Pt_3As_8$ (La-1038), $(CaFeAs)_{10}Pt_4As_8$ (1048), and $(Ca_{0.8}Na_{0.2}FeAs)_{10}Pt_4As_8$ (Na-1048).

7.6   Structure-T_c-Correlation in Iron Arsenides

Geometric aspects of the FeAs layer are often discussed to play a significant role for the emergence of high temperature superconductivity in iron arsenides. Especially the As–Fe–As bonding angle and the height of the pnictide layer above the iron sheets are assumed to be critical. A comparison of geometric subtleties and superconducting properties of optimal doped 1038 and 1048 compounds with reported iron arsenides is depicted in Figure 3.
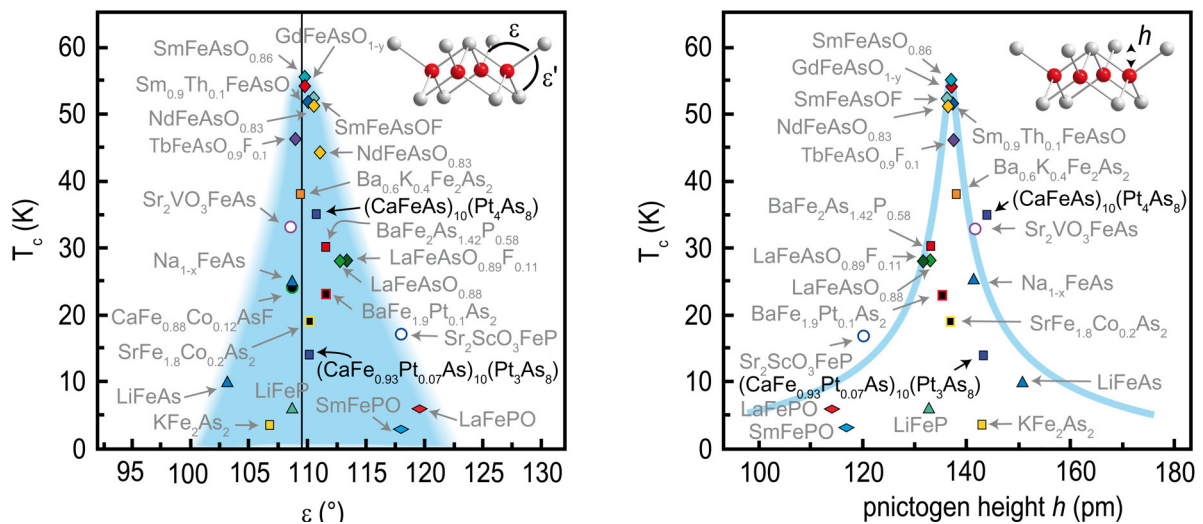

Figure 3. Comparison of critical temperatures in dependency of As–Fe–As bonding angle (left) and pnictogen height (right) of known iron arsenide superconductors.[1]

---

[1] V. Zinth, Dissertation, LMU München, **2012**.

7.7 DFT Data of α-CaFe₅As₃ and α-Ca₃Fe₈PtAs₆

7.7.1 *Non-magnetic Calculations*

α-CaFe$_5$As$_3$ and α-Ca$_3$Fe$_8$PtAs$_6$ are two monoclinic representatives of the newly discovered iron arsenide framework family Ca$_{n(n+1)/2}$(Fe$_{1-x}$M$_x$)$_{(2+3n)}$M$'_{n(n-1)/2}$As$_{(n+1)(n+2)/2}$ ($n = 1 - 3$; $M =$ Nb, Pd, Pt; $M' = \Box$ Pd, Pt). Electronic properties as density of states, bandstructures and Fermi surfaces of non-magnetic, relaxed α-CaFe$_5$As$_3$ and α-Ca$_3$Fe$_8$PtAs$_6$ were calculated by DFT methods using the WIEN2K package.
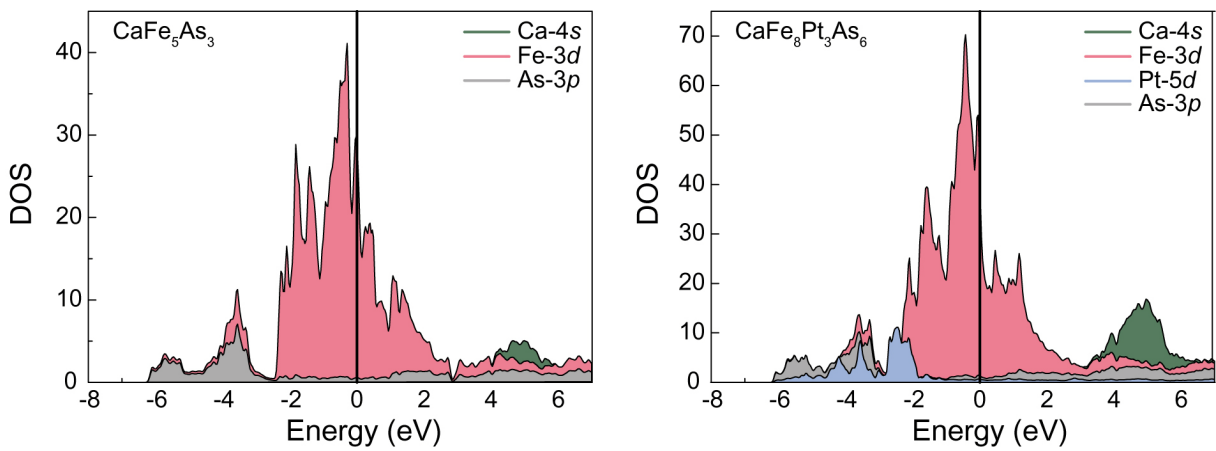

Figure 4. Density of states of relaxed structures α-CaFe₅As₃ (left) and α-Ca₃Fe₈PtAs₆ (right).
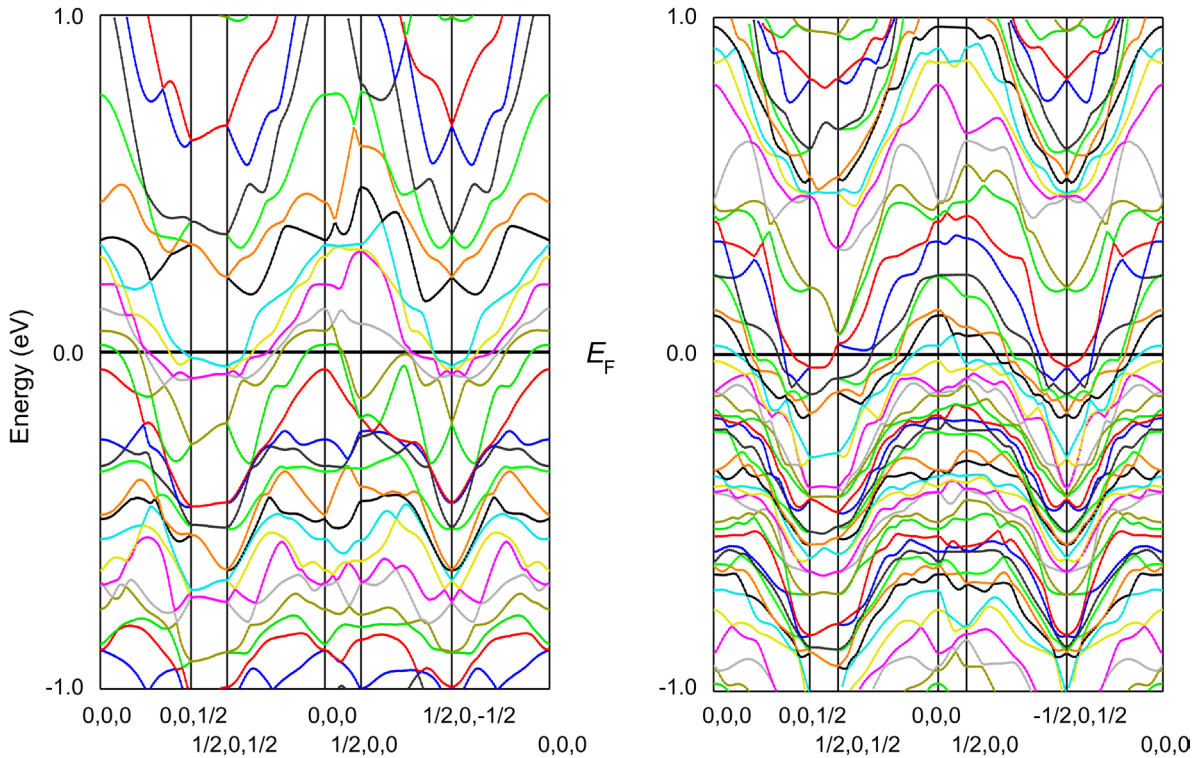

Figure 5. Band structures of relaxed structures α-CaFe₅As₃ (left) and α-Ca₃Fe₈PtAs₆ (right) close to EF.
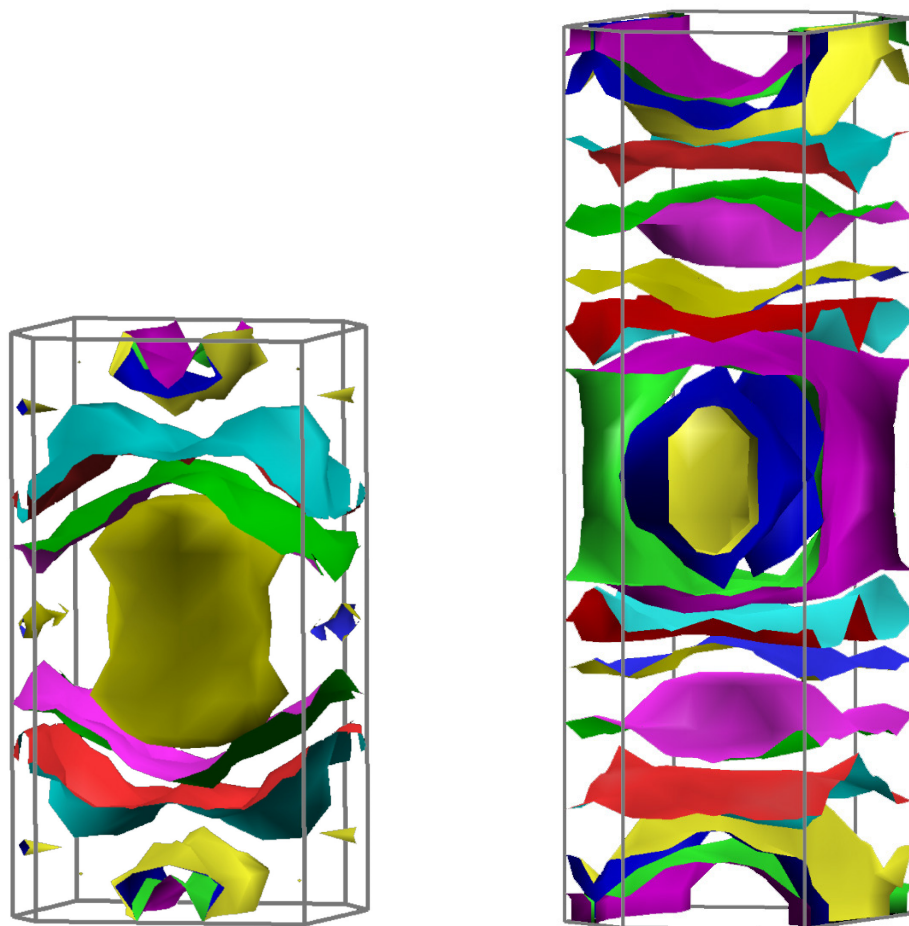
Figure 6. Fermi surfaces of relaxed structures *α*-CaFe$_5$As$_3$ (left) and *α*-Ca$_3$Fe$_8$PtAs$_6$ (right).

7.7.2 *Magnetic Calculations*

Spin polarized calculation revealed a preferable magnetic ground state for both α-CaFe₅As₃ and α-Ca₃Fe₈PtAs₆. Calculated magnetic moments of relaxed magnetic structure are listed in Table 8, together with reported calculated value for $CaFe_4As_3$[1].
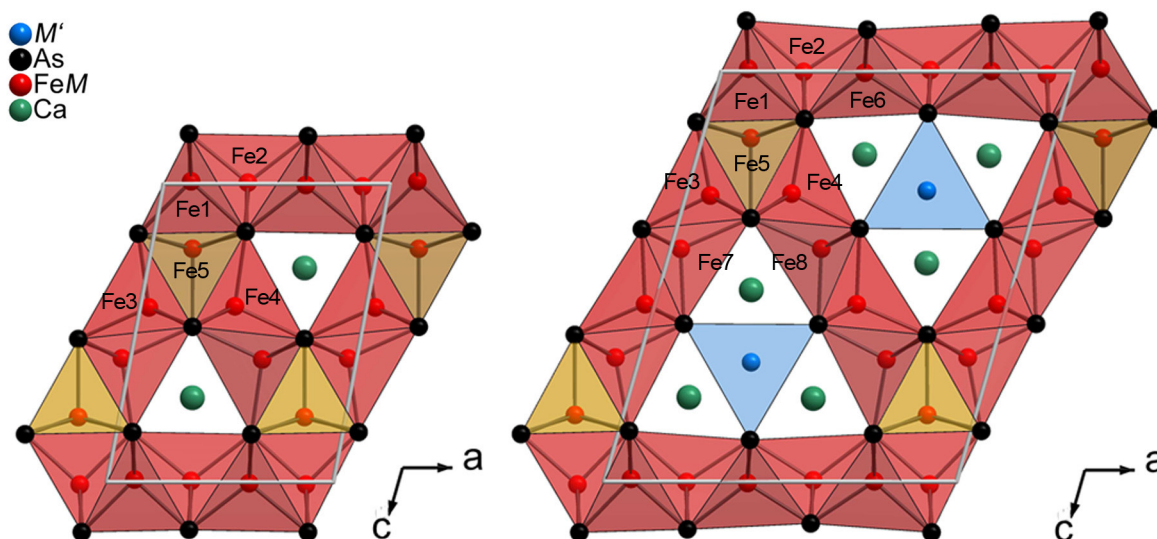
Figure 7. Labels of Fe sites in the asymmetric unit cell of α-CaFe₅As₃ and α-Ca₃Fe₈PtAs₆.

Table 8. Calculated iron moments for the magnetic ground states of CaFe₄As₃, α-CaFe₅As₃ and α-Ca₃Fe₈PtAs₆.

Site	CaFe₄As₃[2]	CaFe₅As₃	Ca₃Fe₈PtAs₆
Fe1	$1.0\,\mu_B$	$0.3\,\mu_B$	$0.7\,\mu_B$
Fe2	$1.7\,\mu_B$	$1.8\,\mu_B$	$1.7\,\mu_B$
Fe3	$1.8\,\mu_B$	$2.0\,\mu_B$	$1.8\,\mu_B$
Fe4	-	$2.0\,\mu_B$	$2.0\,\mu_B$
Fe5	$2.1\,\mu_B$	$2.3\,\mu_B$	$2.5\,\mu_B$
Fe6	-	-	$0.4\,\mu_B$
Fe7	-	-	$1.2\,\mu_B$
Fe8	-	-	$1.4\,\mu_B$

---

[2] I. Todorov, D. Y. Chung, C. D. Malliakas, Q. Li, T. Bakas, A. Douvalis, G. Trimarchi, K. Gray, J. F. Mitchell, A. J. Freeman, M. G. Kanatzidis, *J. Am. Chem. Soc.* **2009**, *131*, 5405.

7.8 CSD Numbers

Crystallographic data (.cif file) of investigated compounds can be obtained from the Fachinformationszentrum Karlsruhe, 76344 Eggenstein-Leopoldshafen, Germany (fax, (+49)7247-808-666; e-mail, crysdata@fiz-karlsruhe.de) by quoting the corresponding depository number.

Table 9. CSD numbers of compounds investigated within this thesis.

Compound	Structure	CSD entry
$Ca_{10}Fe_{9.297}Pt_{3.689}As_{18}$	1038	CSD-423850
$Ca_{10}Fe_{10}Pt_{3.6}As_{18}$	α-1048	CSD-423399
$Ca_{10}Fe_{8.7}Pt_{5.3}As_{18}$	β-1048	CSD-423400
$Ca_{10}Fe_{9.764}Pt_{3.355}As_{18}$	γ-1048	CSD-423851
$CaFe_5As_3$	α-$CaFe_5As_3$	CSD-427443
$Ca_{2.56}Na_{0.44}Fe_{7.49}Nb_{0.51}As_6$	α-$Ca_3Fe_8\square As_6$	CSD-427439
$Ca_3Fe_{7.038}Pd_{1.962}As_6$	β-$Ca_3Fe_8PdAs_6$	CSD-427444
$Ca_3Fe_{4.741}Pd_{4.259}As_6$	γ-$Ca_3Fe_8PdAs_6$	CSD-427446
$Ca_3Fe_{7.705}Pt_{1.295}As_6$	α-$Ca_3Fe_8PtAs_6$	CSD-427440
$Ca_3Fe_{6.75}Pt_{2.25}As_6$	β-$Ca_3Fe_8PtAs_6$	CSD-427445
$Ca_6Fe_{7.879}Pd_{6.121}As_{10}$	α-$Ca_6Fe_{11}Pd_3As_{10}$	CSD-427441
$Ca_6Fe_{7.627}Pt_{6.373}As_{10}$	α-$Ca_6Fe_{11}Pt_3As_{10}$	CSD-427442

8 Abbreviations and Quantities

8.1 Abbreviations

1038	$(CaFeAs)_{10}Pt_3As_8$
1048	$(CaFeAs)_{10}Pt_4As_8$
A	alkaline metal
ac	alternating current
AE	alkaline earth metal
AFM	antiferromagnetic order
ARPES	angle resolved photoelectron spectroscopy
a.u.	arbitrary units
BCS	acronym of *Bardeen*, *Cooper* and *Shrieffer*
CCD	charge coupled device
CDW	charge density wave
CERN	European Organization for Nuclear Research
CN	coordination number
COHP	crystal orbital Hamilton population
CPU	central processing unit
dc	direct current
DFT	density functional theory
DOS	density of states
e^-	electron
EDX	energy dispersive X-ray spectroscopy
EPM	electron probe microanalysis
fc	field cooling
GPS	general purpose surface-muon instrument
$i\mathrm{x}$	isomorphic transition of index x

IPDS	imaging plate diffraction system
Ir1048	$(CaFeAs)_{10}Ir_4As_8$
k	impulse vector
LHC	Large Hadron Collider
LMTO	linear muffin-tin orbital
LMU	Ludwig-Maximillians-Universität
La-Pt-1038	$(Ca_{1-y}La_yFe_{1-x}Pt_xAs)_{10}Pt_3As_8$
Ln	lanthanoid
M	metal
M-1038	$(CaFe_{1-x}M_xAs)_{10}Pt_3As_8$, $M =$ Co, Cu, Ni, Pt
MPMS	magnetic property measurement system
NMR	nuclear magnetic resonance
Pd1038	$(CaFe_{1-x}Pd_xAs)_{10}Pd_3As_8$
PDOS	partial density of states
Pn	pnictide
PSI	Paul Scherrer Institut
PXRD	powder X-ray diffraction
QTAIM	quantum theory of atoms in molecules
RE	rare earth metal
RE-1038	$(Ca_{1-y}RE_yFeAs)_{10}Pt_3As_8$
RT	room temperature
SC	superconductivity
SDW	spin density wave
SG	space group
SOF	site occupation factor
SQUID	superconducting quantum interference device
tx	*translationengleich* transition of index *x*

TF	transversal field
VASP	Vienna ab-initio simulation package
Wyckoff	Wyckoff-Position
ZF	zero field
zfc	zero field cooling
μSR	muon spin rotation

8.2 Magnetic Quantities

$4\pi\chi_V$	magnetic (e.g. superconducting) volume fraction
B	magnetic flux density
B_{hyp}	magnetic hyperfine field splitting (Mössbauer)
C	Curie constant
H	magnetic field
H_c	critical field
M	magnetization
T_N	Néel temperature
T_{nem}	temperature of nematic order
μ	magnetic moment in Bohr magnetons
μ_B	Bohr magneton
μ_{eff}	effective magnetic moment in Bohr magnetons
χ	magnetic susceptibility
χ_V	volume susceptibility

8.3 Crystallografic Quantities

$\square$	vacancy position
A, B_x	layer shift in disorder model
deg	degree
F	structure factor

150

GooF	goodness of fit
h k l	Miller Indices
I	intensity
R...	residual factor
w*R...*	weighted residual factor
U_{eq}	equivalent thermal displacement parameter
w	weighting factor
Z	number for empirical formulas per unit cell
θ	diffraction angle
λ	wave length
$\rho(r)$	electron density

8.4 Other Quantities

a, b, c	unit cell axes
a^*, b^*, c^*	reciprocal unit cell axes
at%	atom percent
E	energy
E_F	Fermi energy
eV	electron Volt
J	Joule
J_c	critical current density
K	Kelvin
M_{eff}	effective mass
mol	mole
p	pressure
q	nesting vector
T	temperature

T_c	critical temperature of a superconductor
T_S	structural transition temperature
V_{ZZ}	main component of the magnetic field gradient tensor (Mössbauer)
wt%	weight percent
α, β, γ	unit cell angles
v	partial charge of a FeAs unit in the FeAs layer
δ	isomer shift (Mössbauer)
δ	structural order parameter
δ-angle	tetrahedra angle (fourfold)
ε-angle	tetrahedra angle (twofold)
ρ	density
ρ	electrical resistivity
σ	standard deviation
Θ_{Debye}	Debye temperature

9 Publications

The major part of results compiled in this thesis were published in scientific journals according to the below-mentioned list. Publications which are not included in this work, as well as talks and poster presentations at scientific conferences are summarized separately.

9.1 Publications within this Thesis

1 **Superconductivity by rare earth doping in the 1038-type compounds $(Ca_{1-x}RE_xFeAs)_{10}Pt_3As_8$ with RE = Y, La – Nd, Sm – Lu**

T. Stürzer, G. Derondeau, E. Bertschler, D. Johrendt

Solid State Commun. **2015**, *201*, 36 – 39.

For this publication, the samples $(Ca_{1-x}RE_xFeAs)_{10}Pt_3As_8$ with RE = Y, La – Nd, Sm – Lu were synthesized by Tobias Stürzer with assistance of Eva-Maria Bertschler and Gerald Derondeau. SQUID data was measured by Gina Friederichs and Simon Peschke. Ac-susceptibility and conductivity measurements, DFT calculations, literature screening, data analysis, Rietveld refinement, writing the manuscript and picture editing were done by Tobias Stürzer. Christine Stürzer (former Hieke) contributed to data analysis and discussion. The manuscript was revised by Christine Stürzer and Dirk Johrendt.

2 **Superconductivity by transition metal doping in $(CaFe_{1-x}M_xAs)_{10}Pt_3As_8$ (M = Co, Ni, Cu)**

T. Stürzer, F. Kessler, D. Johrendt

Philos. Mag. **2014**, *94*, 3632 – 3639.

For this publication, the samples $(CaFe_{1-x}M_xAs)_{10}Pt_3As_8$ with M = Co, Ni, Cu were synthesized by Tobias Stürzer with assistance of Fabian Kessler and Rebekka Erdmann. SQUID data was measured by Gina Friederichs and Simon Peschke. Ac-susceptibility and conductivity measurements, literature screening, data analysis, Rietveld refinement, writing the manuscript and picture editing was done by Tobias Stürzer. Christine Stürzer (former Hieke) contributed to data analysis and discussion. The manuscript was revised by Christine Stürzer and Dirk Johrendt.

3 **Framework structures of interconnected layers in calcium iron arsenides**

T. Stürzer, C. Hieke, C. Löhnert, F. Nitsche, J. Stahl, C. Maak, R. Pobel, D. Johrendt

Inorg. Chem. **2014**, *53*, 6235 – 6240.

For this publication, synthesis of $CaFe_5As_3$ was done by Roman Pobel with the assistance of Christian Maak. Samples of α-$Ca_3(Fe,Pt)_8PtAs_6$, β-$Ca_3(Fe,Pt)_8PtAs_6$, and α-$Ca_6(Fe,Pt)_{11}Pt_3As_{10}$ were prepared by Tobias Stürzer with assistance of Juliane Stahl. Christine Stürzer (former Hieke) prepared samples of β-$Ca_3(Fe,Pd)_8PdAs_6$, γ-$Ca_3(Fe,Pd)_8PdAs_6$ and α-$Ca_6(Fe,Pd)_{11}Pd_3As_{10}$. $(Ca,Na)_3(Fe,Nb)_8As_6$ was prepared by Catrin Löhnert. Structure elucidation of $CaFe_5As_3$, α-$Ca_3(Fe,Pt)_8PtAs_6$, and α-$Ca_6(Fe,Pt)_{11}Pt_3As_{10}$ was done by Tobias Stürzer, of β-$Ca_3(Fe,Pt)_8PtAs_6$ by Dirk Johrendt, of β-$Ca_3(Fe,Pd)_8PdAs_6$, γ-$Ca_3(Fe,Pd)_8PdAs_6$, and α-$Ca_6(Fe,Pd)_{11}Pd_3As_{10}$ by Christine Stürzer and $(Ca,Na)_3(Fe,Nb)_8As_6$ by Fabian Nitsche. Writing the manuscript main part, literature screening, analysis of structural relations, classification of compounds to common family $Ca_{n(n+1)/2}(Fe_{1-x}M_x)_{(2+3n)}M'_{n(n-1)/2}As_{(n+1)(n+2)/2}$ ($n \in \mathbb{N}$; $M =$ Nb, Pd, Pt; $M' = \square$ Pd, Pt), and DFT calculations were done by Tobias Stürzer. Christine Stürzer, Catrin Löhnert, and Fabian Nitsche contributed to data analysis and discussion. Picture editing was done by Christine and Tobias Stürzer. The manuscript was revised by Christine Stürzer, Fabian Nitsche, and Dirk Johrendt.

4 **Structural and magnetic phase transitions in triclinic $(CaFeAs)_{10}Pt_3As_8$**

T. Stürzer, G. M. Friederichs, H. Luetkens, A. Amato, H.-H. Klauss, D. Johrendt

J. Phys.: Condens. Matter **2013**, *25*, 122203.

For this publication, synthesis of $(CaFeAs)_{10}Pt_3As_8$ and sample preparation, writing the manuscript main part, literature screening, Rietveld refinement, measurement and interpretation of ac-susceptibility data, and image editing was done by Tobias Stürzer. EDX analysis was performed by Christian Minke. SQUID and conductivity measurements were done by Gina Friederichs and Rainer Frankovsky. Sample preparation and measurement of low temperature X-ray powder data measurements were performed by Franziska Hummel. Muon spin rotation spectroscopy data measurements, sample preparation as well as data analysis and interpretation were done by Hubertus Luetkens at the Paul Scherrer Institute in Switzerland. Hans-Henning Klauss (TU Dresden) and Alex Amato (PSI Villigen) contributed to data analysis and

discussion. The manuscript was revised by Christine Stürzer (former Hieke), Hubertus Luetkens, and Dirk Johrendt.

5   Role of different negatively charged layers in (CaFeAs)$_{10}$Pt$_4$As$_8$ and superconductivity at 30 K in electron doped (Ca$_{0.8}$La$_{0.2}$FeAs)$_{10}$Pt$_3$As$_8$

T. Stürzer, G. Derondeau, D. Johrendt,

Phys. Rev. B **2012**, *86*, 060516.

For this publication, synthesis of (CaFe$_{1-x}$Pt$_x$As)$_{10}$Pt$_3$As$_8$, (CaFe$_{1-x}$Pt$_x$As)$_{10}$Pt$_4$As$_8$, and with assistance of Gerald Derondeau (Ca$_{0.8}$La$_{0.2}$FeAs)$_{10}$Pt$_3$As$_8$, sample preparation, writing the manuscript main part, literature screening, Rietveld refinement, single crystal growth, measurement and structure elucidation, measurement and interpretation of magnetic data, as well as image editing was done by Tobias Stürzer. EDX analysis was performed by Christian Minke. DFT calculations were done by Dirk Johrendt. The manuscript was revised by Christine Stürzer (former Hieke) and Dirk Johrendt.

6   Superconductivity up to 35 K in the iron platinum arsenides (CaFe$_{1-x}$Pt$_x$As)$_{10}$Pt$_{4-y}$As$_8$ with layered structures

C. Löhnert, T. Stürzer, M. Tegel, R. Frankovsky, G. Friederichs, D. Johrendt

Angew. Chem. Int. Ed. **2011**, *50*, 9195 – 9199.

For this publication, synthesis and samples preparation of (CaFe$_{1-x}$Pt$_x$As)$_{10}$Pt$_z$As$_8$ with z = 3, 4 was done by Catrin Löhnert and Tobias Stürzer. Rietveld refinement of powder data and theoretical calculations were done by Marcus Tegel. Gina Friederichs and Rainer Frankowsky performed conductivity measurements. Magnetic measurements were done by Marcus Tegel and Tobias Stürzer. Literature screening and writing the main part was done by Dirk Johrendt. Marcus Tegel and Tobias Stürzer contributed to data analysis and discussion. The manuscript was revised by Marcus Tegel and Tobias Stürzer.

9.2 Publications beyond this Thesis

7 **Multigap superconductivity in locally non-centrosymmetric SrPtAs: An ^{75}As nuclear quadrupole resonance investigation**

F. Brückner, R. Sarkar, M. Günther, H. Kühne, H. Luetkens, T. Neupert, A. P. Reyes, P. L. Kuhns, P. K. Biswas, T. Stürzer, D. Johrendt, H.-H. Klauss

Phys. Rev. B **2014**, *90*, 220503(R).

8 **Ba$_{1-x}$Rb$_x$Fe$_2$As$_2$ and generic phase behavior of hole doped 122-type superconductors**

S. Peschke, T. Stürzer, D. Johrendt

Z. Anorg. Allg. Chem. **2014**, *640*, 830 − 835.

9 **Evidence for Time-Reversal-Symmetry-Broken Superconductivity in Locally Noncentrosymmetric SrPtAs**

P. K. Biswas, H. Luetkens, T. Neupert, T. Stürzer, C. Baines, G. Pascua, A. P. Schnyder, M. H. Fischer, J. Goryo, M. R. Lees, H. Maeter, F. Brueckner, H.-H. Klauss, M. Nicklas, P. J. Baker, A. D. Hillier, M. Sigrist, A. Amato, D. Johrendt

Phys. Rev. B **2013**, *87*, 180503.

10 **Why T_c of (CaFeAs)$_{10}$Pt$_{3.58}$As$_8$ is twice as high as (CaFe$_{0.95}$Pt$_{0.05}$As)$_{10}$Pt$_3$As$_8$**

S. Thirupathaiah, T. Stürzer, V. B. Zabolotnyy, D. Johrendt, B. Büchner, S. V. Borisenko

Phys. Rev. B **2013**, *88*, 140505.

11 **Superconductivity and crystal structure of the palladium iron arsenides (CaFe$_{1-x}$Pd$_x$As)$_{10}$Pd$_3$As$_8$**

C. Hieke, J. Lippmann, T. Stürzer, G. M. Friederichs, F. Nitsche, F. Winter, R. Pöttgen, D. Johrendt

Philos. Mag. **2013**, *93*, 3680 − 3689.

12   Transition metal Pnictides

D. Johrendt, C. Hieke, T. Stürzer

Comprehensive Inorganic Chemistry II (second edition), Elsevier **2013**, 111 – 135.

13   The specific heat of the electron doped La-1038 compound $(Ca_{0.85}La_{0.15}FeAs)_{10}Pt_3As_8$

J. S. Kim, T. Stürzer, D. Johrendt, G. R. Stewart

J. Phys.: Condens. Matter **2013**, *25*, 135701.

14   Suppression of superconductivity by V doping and possible magnetic order in Sr_2VO_3FeAs

M. Tegel, T. Schmid, T. Stürzer, M. Egawa, Y. Su, A. Senyshyn, D. Johrendt

Phys. Rev. B **2010**, *82*, 140507.

9.3   Conference Contributions

1   Structures, superconductivity, and magnetism in $(CaFeAs)_{10}Pt_zAs_8$ (invited talk)

T. Stürzer, D. Johrendt

Workshop on itinerant magnetism and superconductivity, Dresden, Germany, **2014**.

2   Superconductivity and Crystal Structure of Palladium Iron Arsenides (poster)

C. Hieke, T. Stürzer, G. Friederichs, F. Nitsche, D. Johrendt

SUPER-IRON 2nd Student Workshop, Tsukuba, Japan, **2014**.

3   New Framework Structures with interconnected Iron Arsenide Layers (poster)

T. Stürzer, C. Hieke, C. Löhnert, F. Nitsche, D. Johrendt

SUPER-IRON 2nd Student Workshop, Tsukuba, Japan, **2014**.

4   **Eisenarsenid kann mehr!** (talk)

T. Stürzer, D. Johrendt

Hemdsärmelkolloquium, Köln, Germany, **2014**.

5   **Neue Strukturen mit 3D verknüpften FeAs-Schichten** (talk)

T. Stürzer, D. Johrendt

Erstes Obergurgl-Seminar Festkörperchemie, Obergurgl, Austria, **2014**.

6   **$(CaFeAs)_{10}Pt_zAs_8$ - Eine neue Klasse typischer Eisenarsenid- Supraleiter** (talk)

T. Stürzer, D. Johrendt

Hirschegg-Seminar on solid-state Chemistry, Hirschegg, Austria, **2013**.

7   **Der Einfluss der Ladungsverteilung im neuen Supraleiter $(CaFe_{1-x}Pt_xAs)_{10}Pt_zAs_8$** (talk)

T. Stürzer, D. Johrendt

Hirschegg-Seminar on solid-state Chemistry, Hirschegg, Austria, **2012**.

8   **Polymorphism and phase diagram of $(CaFe_{1-x}Pt_xAs)_{10}Pt_{3+y}As_8$** (poster)

T. Stürzer, C. Löhnert, D. Johrendt

International Workshop on Superconductivity in Iron-based Compounds (SPP 1458), München, Germany, **2012**.

9   **The Role of Stoichiometry and Magnetism in the Superconductor Sr_2VO_3FeAs and Related Compounds** (poster)

M. Tegel, F. Hummel, T. Schmid, T. Stürzer, M. Egawa, Y. Su, A. Senyshyn, D. Johrendt

International Workshop on Novel Superconductors and Super Materials (NS^2_{2011}), Tokyo, Japan, **2011**.

10 Curriculum Vitae